UNIVERSITÉ CÔTE D'AZUR

ÉCOLE DOCTORALE
SCIENCES FONDAMENTALES ET APPLIQUÉES

THÈSE DE DOCTORAT

Méthodes Galerkin discontinues pour la simulation et la calibration de modèles de dispersion non-locaux en nanophotonique

Nikolai SCHMITT

INRIA

Présentée en vue de l'obtention du grade de docteur en science, spécialité mathématiques appliquées **d'Université Côte d'Azur**
Dirigée par : Stéphane Lanteri
Co-encadrée par : Claire Scheid
Soutenue le : 27/09/2018

Devant le jury, composé de :
Herbert De Gersem, Professeur, TUD
Christophe Geuzaine, Professeur, Université de Liège
N. Asger Mortensen, Professeur, University of Southern Denmark
Kurt Busch, Professeur, Humboldt Universität Berlin
Olivier Martin, Professeur, EPFL
Antoine Moreau, Maître de Conférence, Université Clermont Auvergne

Méthodes Galerkin discontinues pour la simulation et la calibration de modèles de dispersion non-locaux en nanophotonique

Devant le jury, composé de :

Président de jury*
Herbert De Gersem, Professeur, Technische Universität Darmstadt, Allemagne

Rapporteurs
Christophe Geuzaine, Professeur, Université de Liège
N. Asger Mortensen, Professeur, University of Southern Denmark, Danemark

Examinateur
Kurt Busch, Professeur, Humboldt Universität Berlin, Allemagne
Olivier Martin, Professeur, École Polytechnique Fédérale de Lausanne, Suisse
Antoine Moreau, Maître de Conférence, Université Clermont Auvergne, France

Titre de la thèse Méthodes Galerkin discontinues pour la simulation et la calibration de modèles de dispersion non-locaux en nanophotonique.....
Sous-titre de la thèse .....
Mots-clés Equations de Maxwell, Discontinuous Galerkin, Nanophotonique.....

Résumé (de 1700 à 4000 caractères espaces compris)
L'objectif principal de cette thèse est l'étude des problèmes et des applications qu'ils se développent dans le domaine de la nanophotonique. Plus précisément, nous considérons les structures de métaux nobles où les modèles de dispersion locaux sont insuffisants et la non-localité doit être incluse dans le modèle. Ici, le système physique sous-jacent est typiquement modélisé comme des équations de Maxwell couplées à des lois de dispersion spatio-temporelles dans le régime des longueurs d'onde optiques. Bien que les solutions analytiques puissent être dérivées pour un petit nombre de problèmes, cela n'est généralement pas possible pour les dispositifs du monde réel, qui présentent souvent des géométries complexes et des compositions de matériaux. Suite à une analyse rigoureuse des propriétés physiques et mathématiques du modèle continu original, nous proposons une méthode de type à éléments finis d'ordre élevé pour discrétiser le modèle continu dans l'espace et le temps. Les méthodes discontinues Galerkin (DG) sont bien établies pour la discrétisation spatiale des équations de Maxwell. Cette thèse prolonge les travaux antérieurs sur les systèmes couplés des équations de Maxwell et les lois de dispersion spatiale. Nous utilisons des méthodes explicites de Runge-Kutta (RK) d'ordre élevé pour la discrétisation temporelle. L'intégration temporelle RK garantit un ordre de convergence espace-temps élevé du schéma entièrement discret, qui repose sur un schéma de preuve de convergence. Parallélisme MPI (Message Passing Interface), éléments curvilignes et PML (Perfectly Matched Layers) autour des aspects d'implémentation et d'évaluation des performances dans le cadre du logiciel développé à Inria Sophia Antipolis-Méditerannée (DIOGENES). La méthode développée est appliquée à de nombreuses simulations nanophotoniques réelles de dispositifs où des observables tels que la réflexion, la section transversale (CS) et la spectroscopie de perte d'énergie électronique (EELS) sont étudiés. Entre autres, nous élaborons une feuille de route pour un étalonnage expérimental robuste du modèle de dispersion non local linéarisé basé sur la solution de problèmes inverses et la quantification d'incertitude (UQ) des paramètres géométriques stochastiques. Nous avons également amélioré les accords de simulations numériques non locales et les résultats expérimentaux pour la résonance des plasmons d'espacement des nano-cubes d'argent. Cela démontre la pertinence de simulations non locales précises.

Thesis title High-order simulations and calibration strategies for spatial dispersion models in nanophotonics

Thesis sub-title .....

Keywords Maxwell's equations, Discontinuous Galerkin, Nanophotonics.....

Abstract (from 1700 to 4000 prints including spaces)

The main objective of this thesis is the study of problems and applications as they arise in the eld of nanophotonics. More speci cally, we consider noble metal structures where local dispersion models are insu cient and nonlocality has to be included in the model.

Here, the underlying physical system is typically modeled as Maxwell's equations coupled to spatio-temporal dispersion laws in the regime of optical wavelengths. While analytical solutions can be derived for a small number of problems, this is typically not possible for real-world devices, which often feature complicated geometries and material compositions.

Following a rigorous analysis of the physical and mathematical properties of the original continuous model, we propose a high order nite element type method for discretizing the continuous model in space and time.

Discontinuous Galerkin (DG) methods are well established for the spatial discretization of Maxwell's equations. This thesis extends previous work on the coupled systems of Maxwell's equations and spatial dispersion laws. We use explicit high-order Runge-Kutta (RK) methods for the subsequent time discretiz- ation. RK time integration guarantees a high space-time convergence order of the fully-discrete scheme, which is underpinned by a sketch of a convergence proof.

Message Passing Interface (MPI) parallelization, curvilinear elements and Perfectly Matched Layers (PMLs) round o implementation aspects and performance assessments in the scope of the Software developed at Inria Sophia Antipolis-Méditerannée (DIOGENeS).

The developed method is applied to numerous real-world nanophotonics simulations of devices where observables like re ectance, Cross Section (CS) and Electron Energy Loss Spectroscopy (EELS) are studied. Inter alia, we elaborate a roadmap for a robust experimental calibration of the linearized nonlocal disper- sion model based on the solution of inverse problems and Uncertainty Quanti cation (UQ) of stochastic geometric parameters. We also nd improved agreements of nonlocal numerical simulations and exper- imental results for the gap-plasmon resonance of silver nano-cubes. This demonstrates the relevance of accurate nonlocal simulations.

Contents

1

Introduction

1.1 Motivation and objectives

Physical and technological context Nanophotonics research has led to astonishing technologies over the last decades. For example, so-called metasurfaces; artificially shaped thin-sheet surfaces, which allow for a systemic phase modulation of the reflected and transmitted waves [49]. Fabrication advances have permitted high-performance solar cells with efficiencies up to 44.7% [35]. In medical research, nano-particles are now used for cancer cell killing thanks to opto-thermal heating [140]. Sophisticated nano-cube based metasurfaces are now being used for nano-scale holography [48] and extremely precise molecule sensing [122]. Figure 1.1 illustrates such a nano-cube metasurface for optical molecule detection and Figure 1.2 shows the world record solar cell from 2014.

Goal-oriented engineering of nanophotonic devices is a challenging task. In the beginning, simplified standard geometries like spheres [99], cylinders [132], half-spaces or gap-structures [8, 96, 105], where analytical or semi-analytical solutions exist, have significantly contributed to the physical understanding and the design of this type of structures. Nevertheless, the experimentalist's experience and 'educated guess' have played and will always play an essential role in the design process as well in the interpretation of measurements [47, 52]. Modern simulation tools now grant access to microscopic insights, which have been sealed even for most modern measurement equipment. For example, exact 3D field distributions, transient wave dynamics and controlled parameter studies or systematic optimizations are almost inaccessible without numerical models.

Of course, a model is only useful if its reliability is ensured. Electromagnetic wave-optical models in nanophotonics are based on Maxwell's equations in vacuum and materials. The considered wavelengths in the visible spectrum lead to dispersive material laws for dielectrics as well as metals. Accurate material models are still an issue today. Historically, Paul Drude proposed a kinetic model for the electron transport, especially in metals, in the early 20^{th} century [36]. His model was extended by Hendrik Antoon Lorentz, commonly known as the Drude-Lorentz model, shortly after. Measurements by Johnson and Christy [70] have been the standard reference of the Drude model parameters for decades. Recently, more specific measurements have been realized taking into account the single-crystalline and evaporated nature of, for example, gold [113].

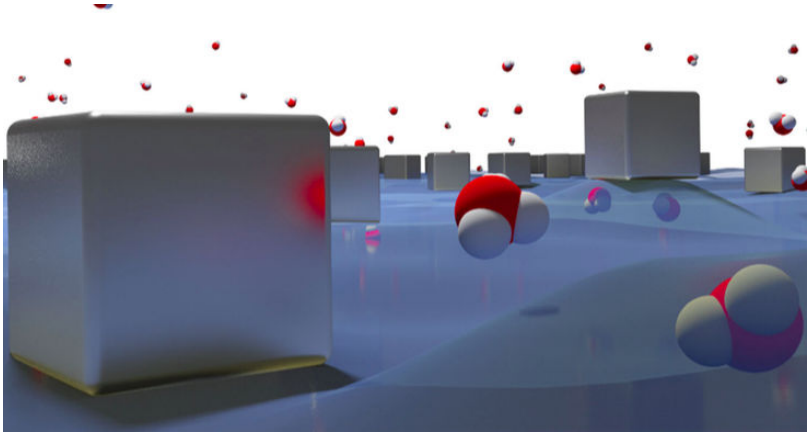

Figure 1.1 | Molecule sensing with nano-cubes. Artistic image showing the nano-cubes resting on a Nafion film interacting with water molecules. Taken from [122].

High-end fabrication technologies nowadays simultaneously enable a minuratization and accuracy down to several nanometers [105, 1, 95]. Such tiny structures [1] tend to host very large wave vectors, which allow the wave to couple incoherently to the free electron gas of the metal. This is since the effective wavelength, which becomes comparable to the mean free path length of the quasi-free electrons. Pauli's exclusion principle then starts to impact the system's response [106, 119, 25]. Clearly, this is a quantum mechanical effect and classical models like Drude, Drude-Lorentz, etc. are insufficient. Boardman [8] has proposed a nonlinear hydrodynamic model with a quantum-mechanical pressure term in order to account for the quantum-mechanical effects in an otherwise classical model.[2] This family of models are called nonlocal because they include the mutual electron interaction of neighboring electrons. Various sub-models have been derived since Boardman, e.g. linearized fluid models [96, 162, 108, 106], linearized fluid models with spill-out [148, 23], i.e. to include the possibility of tunneling, and nonlinear fluid models [60, 103], all of them being characterized nonlocal.

While numerous theoretical studies of the physical properties and their influence on system response [162, 106, 108, 125, 20, 25] have been conducted and many numerical solution strategies [61, 45, 128, 60, 134, 91, 149, 156] have been developed, only a manageable number of experimental evidence has been published [146, 24, 126]. All experimentally observed nonlocal effects have so far relied either on very small spherical geometries [126] or gap structures with extremely thin gaps [24]. However, spherical particles tend to build out a faceted nano-particle shape for radii below $20\ \mathrm{nm}$ and gaps below $2\ \mathrm{nm}$ suffer from tunneling (which is not included in most of the fluid models). This renders it difficult to properly distinguish nonlocal effects from geometric deviations for the sphere setup and from spill-out effects in the gap case. Hence, these results have to be taken with care and may be confirmed by further more robust setups.

Gap-plasmons are naturally good candidates for nonlocality due to their high wavenumber [106]. Silver nano-cubes on gold substrates have proved to nicely couple incident plane waves to their gap mode between the cube and the substrate. Moreau et al. [105] have observed increasing discrepancies between measurements and simulations based on local dispersion models for gap sizes below $5\ \mathrm{nm}$, which is in line with theoretical predictions. Unfortunately, when these experiments were carried out, no simulation tool accounting for spatial dispersion was available yet. Such a desired tool requires the capabilities to

[1] Tiny refers to the overall size or geometric details like gaps.

[2] Alternatively, Density functional theory (DFT) simulations can be used as a full quantum-mechanical approach. DFT is unfortunately restricted to very small systems due to heavy computational costs.

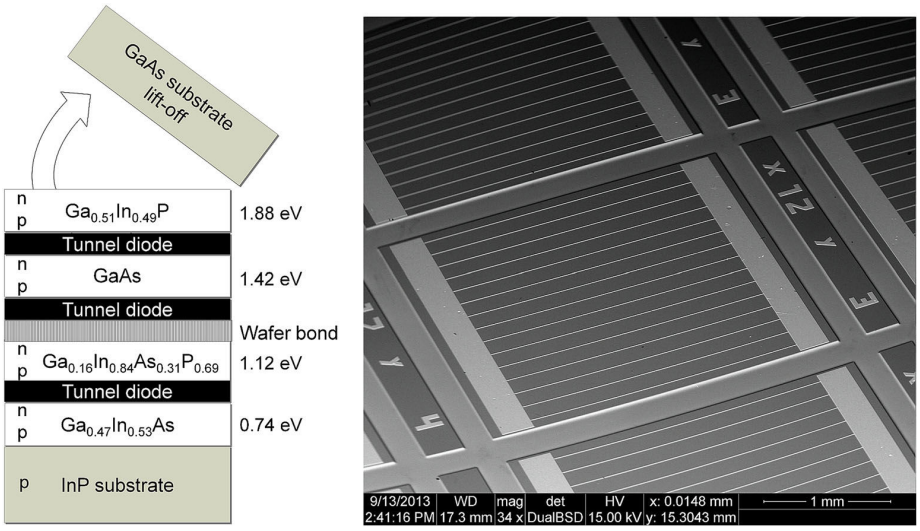

Figure 1.2 | Solar cell. Schematic layer structure of the four-junction wafer bonded solar cell (left) indicating the composition of the subcell materials with bandgap energies, the location of tunnel diodes and the wafer bond. Scanning electron microscopy image of the concentrator cell design with a designated area of $5.2\ \mathrm{mm}^2$ (right). The bonded solar cell had two terminals with parallel grid fingers and two rectangular shaped busbars forming the front contact. Taken from [35].

simulate realistic nano-cubes including appropriate material models and rounded corners and edges, well known to play an important role in the system response [153].

Motivated by the experimental discrepancies between nano-cubes and possibly other systems such as spherical dimers, grating structures and prisms, this thesis has developed and studied a full-wave 3D simulation algorithm, which permits the numerical investigation of arbitrarily shaped nanophotonic devices including spatial dispersion material models. Furthermore, if it turned out that the experimental differences could be explained by a more complex material law, i.e. nonlocal dispersion model, we immediately would have a powerful 3D tool at hand, which was able to predict and quantify the influence of nonlocality in arbitrary systems.

Numerical methods for computational nanophotonics Systematically tailored nanophotonic devices require appropriate and reliable models in the design process. Field solutions and cross-section spectra for basic device components like dielectric and metallic nano-spheres have been developed by Gustav Mie in the early 20^{th} century [99]. His theory has been extended to more general setups [167] as well as EELS spectra [46] in the last decades. The clear advantages of analytical solutions are extremely fast parameter studies and a deep understanding of parameter dependencies.

However, state of the art nanophotonic devices with increasing functionalities exceed the scope of analytical solutions. The Rigorous Coupled Wave Analysis (RCWA) bridges the world of purely analytical solutions and completely general numerical methods. RCWA has been extensively used in nanophotonics for last three decades [93] and has paved the way for many ground-breaking contributions.

Plasmonic simulations with RCWA, however, suffer from slow convergence due to the metallic losses [90] and non-Cartesian geometries. This renders RCWA impractical for curved material interfaces and motivates alternative numerical methods, which are not limited by this restriction.

Limiting this overview to mesh-based numerical methods, key-features of an ideal numerical method for Maxwell's equations in the context of nanoplasmonics would be:

- Locally adaptive mesh-refinement that accounts for small geometric details on large structures;

- Boundary conformity allowing a good resolution of surface plasmonic effects;
- Parallelization-ready for large and multi-scale devices.

Full-wave Maxwell's equations can be formulated in the time-domain or in the frequency-domain. Systems with high quality factors or smallband applications are preferable in frequency-domain. Broadband applications and nonlinear devices are classically more suited to the time-domain.

Frequency-domain methods Well known frequency-domain methods in nanophotonics are for example Finite Element Methods (FEMs) [11, 121, 31, 104] and Boundary Element Methods (BEMs) [156]. These methods have proved to be very efficient for medium size geometries but become costly for increasing amounts of Degree of Freedoms (DoFs) since they require the solution of a sparse (FEM) or dense (BEM) linear system. Especially for nonlocal dispersion models, extreme local mesh refinement is required and leads to high numbers of DoFs. If the system matrix grows to a certain size, iterative methods have to be used. Most nanoplasmonic devices operate in a sub-wavelength configuration and will hence lead to badly-conditioned matrices with high amounts of DoFs. Unless a good preconditioner is available, these systems are very expensive or impossible to solve iteratively.

Time-domain methods Time-domain methods with explicit time integration circumvent the solution of a large linear system and immediately provide a broadband solution. Working in time-domain is only advantageous if the time-domain simulation is more efficient than N frequency-domain solver calls, where N is the number of frequency samples. Additionally, nonlinear effects can be directly addressed in the time-domain.

Finite Differences Time-Domain (FDTD) [143, 64] and Finite Integration Technique (FIT) [157, 158] methods are well established in the microwave regime and also used for optical frequencies. However, these methods suffer from staircase effects at domain interfaces making a boundary conformity more difficult [110]. Additionally, the staggered allocation of primal and dual fields requires extreme mesh-refinements at metal boundaries where the fields are discontinuous.

Discontinuous Galerkin Time-Domain method Local mesh refinement, boundary conformity and broadband simulations can be well treated by Discontinuous Galerkin Time-Domain (DGTD) methods [14, 110, 59, 155, 135]. Based on a local Finite Element (FE) ansatz that leads to block-diagonal mass matrices (easily invertible), they inherit advantages of a FE framework and permit explicit time integration. In direct comparison with FDTD, DGTD further shows improved numerical dispersion properties due to the high order nature of the formulation. The local formulation, which is responsible for the desired block-diagonal matrix, claims doubled DoFs at the interface of mesh cells as depicted in Figure 1.3 (a). This increases the number of DoFs, which obviously is disadvantageous but naturally allows discontinuous field solutions similar to Finite Volume (FV) methods [39, 33].

Managing discontinuous solutions (see Figure 1.3 (b)) is especially important for nonlinear problems where shocks can build up. We predominantly exploit this property at material interfaces in the scope of linear nanophotonics. Additionally to this physically motivated aspect, DGTD is intrinsically suitable for parallel computing due to its local basis functions, i.e. element-wise formulation.

State of the art numerical methods for nonlocal dispersion models Various publications dealing with linear nonlocal dispersion models for nanophotonics in the frequency-domain can be found in literature. All of them consider 2D problems. Most publications rely on COMSOL Multiphysics computations, e.g. [107]. Nevertheless, there are some papers that present a detailed FEM (Nédélec) approach for the

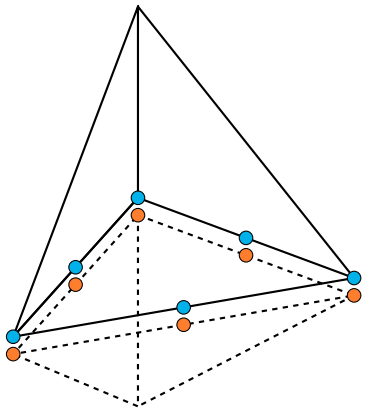

(a) Tetrahedra with DoF on the element interface. Each DoF on the cell interface is doubled for DGTD.

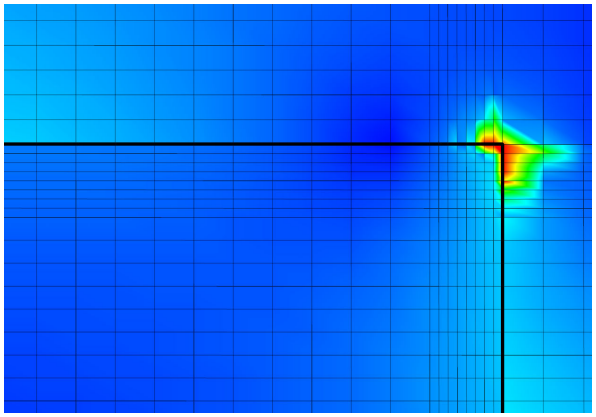

(b) Discontinuous solution. The field solution is obviously discontinuous at the mesh cell interfaces even beyond the material interface.

Figure 1.3 | Discontinuous Galerkin illustration.

hydrodynamic model, e.g. [61]. Beyond volume based methods, BEM has also been successfully applied to nonlocal dispersion models [149, 47]. In the time-domain, a FDTD method has been proposed in [98].

In the DGTD framework, more attention has been given to the nonlinear nonlocal model by Hille et al. [60] and more recently by Moeferdt [102].

Still, to the best of our knowledge a comprehensive numerical analysis together with performance considerations and rigorous comparisons to experimental data has not yet been addressed in the community. These are leading motivations for this thesis.

Challenges and Goals The general goal of this work is the development, analysis, implementation, and application of a robust DGTD method for Maxwell's equations coupled to nonlocal dispersion laws. Classical challenges are to find a stable and convergent formulation. These characteristics have to be proved and accompanied by implementation and validation. Real world simulations that include nonlocal dispersion are very sensitive to inaccurately resolved material interfaces, which we want to tackle with an isoparametric curvilinear formulation.

Physically, the nonlocal model depends on material parameters, which have not yet been thoroughly measured. Our goal is the proposition of a roadmap for a robust calibration strategy based on experiments. Aiming for realistic simulations and experimental evidence of nonlocal effects, the ultimate benchmark of our numerical scheme will be the comparison with experimental data.

1.2 Outline

The remainder of this thesis is structured as follows. We recall the main principles of electrodynamics in Chapter 2. A particular focus is put on the context and motivation of different dispersion models for metals in the visible spectrum. Complementary to a discussion of the physical properties of the models, we have also investigated mathematical aspects of the models. Chapter 3 conducts the derivation and numerical analysis of the DGTD scheme, which we have applied to Maxwell's equations that are simultaneously coupled to a generalized local dispersion model and spatial dispersion model. Towards a simulation tool that is capable of simulating realistic nanophotonic devices, Chapter 4 recalls well known

field sources, domain-truncation techniques and observables. It also proposes and discusses some new aspects of domain-truncation for infinite half-space scattering problems.

After a proper definition of all ingredients and their implementation in the DIOGENeS suite, Chapter 5 presents numerical results. These results range from a thorough validation phase to applied simulations of for example spherical dimers. Beyond pure numerical investigations, a comparison with experiments is done in Chapter 6 metallo-dielectric gratings and nano-cubes. Chapter 7 concludes the main body of this work with propositions for future extensions and research directions.

Achievements The main achievements and scientific contributions of this thesis can be summarized as follows:

- A theoretical study of the continuous Maxwell-hydrodynamic system;
- The proposition of a DGTD formulation for this system and its numerical stability and convergence analysis;
- The demonstration of significant performance improvements for curvilinear elements compared to linear meshes in the context of the linearized fluid model[3];
- An investigation of Scattered Field (SF)-Complex Frequency Shifted (CFS)-PMLs in the time-domain and a workaround with Total Field / Scattered Field (TF/SF)-CFS-PMLs;
- The proposition of a post-fabrication telemetry for metallo-dielectric gratings and a theoretical prediction of the experimental observations. Special attention was given to geometric uncertainties and whether their influence exceeds the impact of nonlocality;
- The accurate 3D simulation of silver nano-cubes and the demonstration of experimental evidence by means of blueshifts on the gap-plasmon;
- The extension of the DIOGENeS software suite by the numerical treatment of the linearized hydrodynamic equations, isoparametric curvilinear elements and MPI parallelization.

[3]Here, we fixed the error level and used different mesh refinements for the linear and curvilinear meshes.

2

Continuous physics

This chapter introduces the physical framework of electrodynamics we will need throughout this thesis. Maxwell's equations hereby play a key role and can be considered as the reference framework for all further investigations. Constitutive relations, accounting for the material responses, are subject to our particular attention, as they build the physical basis of this work. Beyond these two key ingredients, we provide a selection of peripheral aspects and consequences of Maxwell's equations like the conservation of charges, the electromagnetic wave equation, the definition of electromagnetic energy and Poynting's theorem, and Lorentz' force. We will rely on those supplementary results for the definition and explanation of hydrodynamic electron model, i.e. the free electron behavior in metals, as well as several observables like reflectance, CSs or EELS signals.

After the introduction and physical discussion of the material models, a more mathematics oriented study of the full set of equations is carried out. Namely, the proof of existence and uniqueness of the Maxwell's equations, coupled to a linearized fluid model and an energy principle together with hyperbolicity of the same system of equations.

We conclude this chapter with a rich set of analytical solutions. Those will be later used for different purposes. For example, the cavity problem will serve as reference solutions for convergence studies and validation purposes. In the same sense, we use Mie theory in order to provide more complex diffraction problems, which allows to test our numerical implementation against analytical solutions in a most realistic and complex scenario. The free space plane wave solution is also outlined. We conclude with the analytical solution of the electromagnetic field of a moving charge in free space which will be employed as a source term for EELS simulations, afterwards.

2.1 Definitions and notations

For a given open bounded domain $\Omega \subset \mathbb{R}^3$, we use standard notations:

- $\mathcal{L}^2(\Omega)$, the space of square integrable real-valued scalar functions with its canonical scalar product $\langle \cdot, \cdot \rangle_\Omega$ and the associated norm $||\cdot||_\Omega$. $\boldsymbol{\mathcal{L}}^2(\Omega)$ will be its vectorial analogue equipped with the canonical vectorial scalar product (resp. norm) that will be still denoted by $\langle \cdot, \cdot \rangle_\Omega$ (resp $||\cdot||_\Omega$);

- $\mathcal{H}^1(\Omega)$ the space of square integrable functions with square integrable gradient, with $\boldsymbol{\mathcal{H}}^1(\Omega)$ its vectorial analogue;
- $\mathcal{H}_0^1(\Omega)$ the space of square integrable functions with square integrable gradient and vanishing trace on the boundary, with $\boldsymbol{\mathcal{H}}_0^1(\Omega)$ its vectorial analogue;
- $\boldsymbol{\mathcal{H}}(\mathrm{curl}, \Omega)$ the space of square integrable functions with square integrable curl;
- $\boldsymbol{\mathcal{H}}_0(\mathrm{curl}, \Omega)$ the space of square integrable functions with square integrable curl and vanishing tangential trace on the boundary;
- $\boldsymbol{\mathcal{L}}^2(\partial\Omega)$ with its canonical scalar product $\langle \cdot, \cdot \rangle_{\partial\Omega}$ and the associated norm $||\cdot||_{\partial\Omega}$.

Classically, for a given vector field $\mathbf{A}$ of $\mathbb{R}^3$, $\nabla \times \mathbf{A}$, and $\nabla \cdot \mathbf{A}$ respectively denote the curl and the div operator applied to $\mathbf{A}$.

2.2 Transformations

2.2.1 Fourier transformation

The temporal Fourier's transformation allows insights into the frequency spectrum of an arbitrary time domain signal $f(t)$ which is at least an element of the functional space $\mathcal{L}^1(\Omega)$. The transformed signal $F(\omega)$ is defined by

$$F(\omega) := \frac{1}{\sqrt{2\pi}} \int_{-\infty}^{+\infty} f(t) \exp\left(-i\omega t\right) \, \mathrm{d}t =: \mathcal{F}\left\{f\right\}, \tag{2.2.1}$$

with the inverse transformation

$$f(t) := \frac{1}{\sqrt{2\pi}} \int_{-\infty}^{+\infty} F(\omega) \exp\left(i\omega t\right) \, \mathrm{d}\omega =: \mathcal{F}^{-1}\left\{F(\omega)\right\}. \tag{2.2.2}$$

2.2.2 Lorentz transformation

Lorentz' transformation relates space-time of two inertial frames that are moving relatively to each other with a constant velocity. Figure 2.1 depicts relation of the rest (laboratory) frame and the moving frame for an electron in free space. The moving frame is chosen such that the electron does not move within the moving frame and is hence a static and non-moving charge. In order to obtain the trajectory and electromagnetic fields in the rest frame, a Lorentz transformation is required. Comprehensive and didactic discussions on special relativity theory can be found in [42]. Assuming a constant motion of the moving frame $\mathbf{v} = v\mathbf{e}_x$, with $(\mathbf{e}_x, \mathbf{e}_y, \mathbf{e}_z)$ being the canonical basis of $\mathbb{R}^3$, $\mathbf{v} \in \mathbb{R}^3$ and $v = |\mathbf{v}| \in \mathbb{R}$, yields for the space and time in both frames

$$\begin{aligned} t' = \frac{t - vx}{\sqrt{1 - (v/c_0)^2}}, \qquad x' = \frac{x - vt}{\sqrt{1 - (v/c_0)^2}}, \\ y' = y, \qquad z' = z, \end{aligned} \tag{2.2.3}$$

Here, (x, y, z, t) are the coordinates in the rest frame and (x', y', z', t') their counterpart in the moving frame. The electromagnetic fields read similarly

$$\begin{aligned}
\{\mathbf{E}'\}_x &= \{\mathbf{E}\}_x, & \{\mathbf{B}'\}_x &= \{\mathbf{B}\}_x, \\
\{\mathbf{E}'\}_y &= \frac{\{\mathbf{E} + \mathbf{v} \times \mathbf{B})\}_y}{\sqrt{1 - (v/c_0)^2}}, & \{\mathbf{B}'\}_y &= \frac{\{\mathbf{B} - \mathbf{v} \times \mathbf{E})\}_y}{\sqrt{1 - (v/c_0)^2}}, \\
\{\mathbf{E}'\}_z &= \frac{\{\mathbf{E} + \mathbf{v} \times \mathbf{B})\}_z}{\sqrt{1 - (v/c_0)^2}}, & \{\mathbf{B}'\}_z &= \frac{\{\mathbf{B} - \mathbf{v} \times \mathbf{E})\}_z}{\sqrt{1 - (v/c_0)^2}}.
\end{aligned} \tag{2.2.4}$$

Having these transformation rules at hand, we are now able to transform the electromagnetic field from inertial frame to a moving frame and vise versa. Please note that these equations do not hold for accelerated moving frames where $\frac{\mathrm{d}}{\mathrm{d}t}\mathbf{v} \neq 0$.

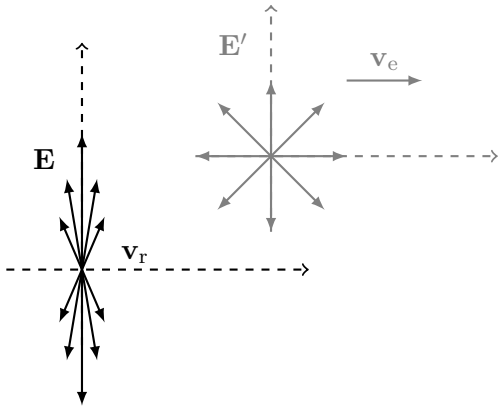

Figure 2.1 | Moving frame for Lorentz transformation. The black frame is the laboratory (rest) frame while the gray frame moves with the relative velocity $\mathbf{v}_e$. Here, the origin of the moving frame is set up in a way that it exactly meets the center of mass of a moving electron. Hence, the electron appears to be at rest in the moving frame.

2.3 Maxwell's equations

The complete set of macroscopic Maxwell's equations that describe the spatio-temporal evolution of electromagnetic waves on a domain $\Omega \subset \mathbb{R}^3$, over a given time interval $[0, T]$ $(T > 0)$, are defined for all $(\mathbf{r}, t) \in \Omega \times [0, T]$ by (see for example [68])

$$\begin{aligned}
\nabla \times \mathbf{E}(\mathbf{r}, t) &= -\partial_t \mathbf{B}(\mathbf{r}, t), & \nabla \cdot \mathbf{D}(\mathbf{r}, t) &= \rho(\mathbf{r}, t), \\
\nabla \times \mathbf{H}(\mathbf{r}, t) &= \partial_t \mathbf{D}(\mathbf{r}, t) + \mathbf{J}(\mathbf{r}, t), & \nabla \cdot \mathbf{B}(\mathbf{r}, t) &= 0,
\end{aligned} \tag{2.3.1}$$

with $\mathbf{E}, \mathbf{D}, \mathbf{H}, \mathbf{B}, \mathbf{J} : \Omega \times [0, T] \to \mathbb{R}^3$ and $\rho : \Omega \times [0, T] \to \mathbb{R}$. Here, $\mathbf{E}$ and $\mathbf{H}$ represent the electric and magnetic field, respectively. The magnetic flux density is denoted by $\mathbf{B}$ and the electric displacement and current density respectively by $\mathbf{D}$ and $\mathbf{J}$, and the charge density by ρ.

Applying Stokes' theorem and Gauss' theorem to (2.3.2), Maxwell's equations can be written in integral form

$$\begin{aligned} \int_{\partial S} \mathbf{E}(\mathbf{r},t)\cdot\mathbf{t}\,\mathrm{d}r &= -\int_S \partial_t \mathbf{B}(\mathbf{r},t)\cdot\mathbf{n}\,\mathrm{d}^2r, & \int_{\mathcal{V}} \mathbf{D}(\mathbf{r},t)\cdot\mathbf{n}\,\mathrm{d}^3r &= \int_{\partial V} \rho\,\mathrm{d}^2r, \\ \int_{\partial S} \mathbf{H}(\mathbf{r},t)\cdot\mathbf{t}\,\mathrm{d}r &= \int_S (\partial_t \mathbf{D}(\mathbf{r},t)+\mathbf{J}(\mathbf{r},t))\cdot\mathbf{n}\,\mathrm{d}^2r, & \int_V \mathbf{B}(\mathbf{r},t)\cdot\mathbf{n}\,\mathrm{d}^3r &= 0, \end{aligned} \tag{2.3.2}$$

Here, the infinitesimal spatial elements $\mathrm{d}r$, d^2r, and d^3r represent the scalar line element, the scalar surface element where the tangential vector $\mathbf{t}$ is in direction of the contour, normal vector $\mathbf{n}$ points outwards the volume $V \subset \Omega$ and $S \subset \mathbb{R}^2$. Figure 2.2 (a) illustrates the geometric relation for Ampère's law and Figure 2.2 (b) for Gauss' law and the absence of magnetic monopoles. Since Maxwell's equations have been discovered individually, they are commonly known as Faraday's law, Ampère's law, Gauss's law and the absence of magnetic monopoles [68]. These equations are supplemented by material laws linking

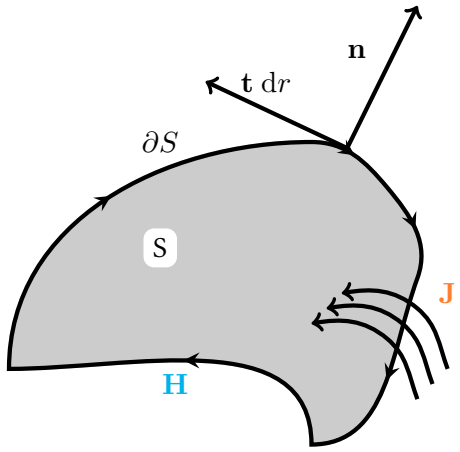

(a) Ampère's law visualized for an arbitrary surface S. Here, $\mathbf{n}$ and $\mathrm{d}r$ respectively illustrate the normal vector and infinitesimal line element for the line integral.

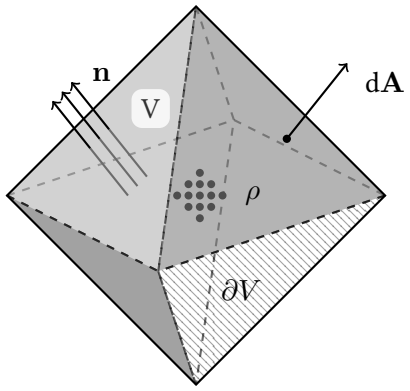

(b) Gauss law. Arbitrary volume V with boundary S (partly marked with a line pattern on the lower side of the volume). The black dots sketch a charge density and the arrows for $\mathbf{A}$ a field like $\mathbf{D}$ and $\mathbf{B}$ for Gauss' law and the absence of magnetic charges, respectively.

Figure 2.2 | Ampère's and Gauss's law. Figure (a) sketches a geometrical interpretation of Ampère's law and (b) Gauss's law, respectively.

$\mathbf{D}$ to $\mathbf{E}$ and $\mathbf{B}$ to $\mathbf{H}$ through the introduction of an electric polarization and a magnetic magnetization

$$\mathbf{D} = \varepsilon_0\mathbf{E} + \mathbf{P}, \qquad \mathbf{B} = \mu_0\left(\mathbf{H} + \mathbf{M}\right). \tag{2.3.3}$$

Here, ε_0 and μ_0 are the vacuum permittivity and permeability, $\mathbf{P} : \Omega \times [0,T] \to \mathbb{R}^3$ the polarization and $\mathbf{M} : \Omega \times [0,T] \to \mathbb{R}^3$ the magnetization. While we here mainly consider metals, we suppose $\mathbf{M} \equiv 0$ throughout the following. In contrast, $\mathbf{P}$ will be of a major importance for the rest of this work.

2.3.1 Conservation of charges

Formally applying the divergence operator $\nabla\cdot\mathbf{A}$ to Faraday's and Ampère's law yields

$$\nabla\cdot\nabla\times\mathbf{E}(\mathbf{r},t) = -\partial_t\nabla\cdot\mathbf{B}(\mathbf{r},t), \qquad \nabla\cdot\nabla\times\mathbf{H}(\mathbf{r},t) = \partial_t\nabla\cdot\mathbf{D}(\mathbf{r},t) + \nabla\cdot\mathbf{J}(\mathbf{r},t), \tag{2.3.4}$$

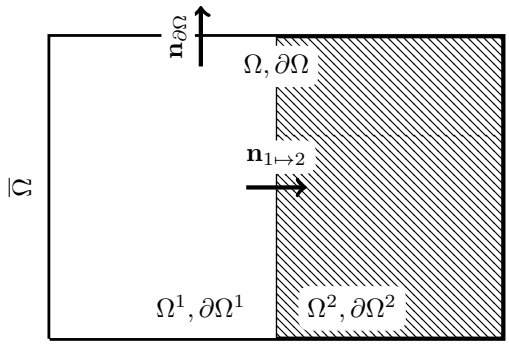

Figure 2.3 | Boundary value problem for Maxwell's equations. Total domain Ω consists of two sub domains Ω^1 and Ω^2. The schematic sketches at the same time the boundary value problem nature and the interface conditions at a material interface between two different materials.

making use of $\nabla \cdot \nabla \times \mathbf{A} = 0$ leads to

$$\mathbf{0} = -\partial_t \nabla \cdot \mathbf{B}(\mathbf{r}, t), \qquad \mathbf{0} = \partial_t \nabla \cdot \mathbf{D}(\mathbf{r}, t) + \nabla \cdot \mathbf{J}(\mathbf{r}, t). \tag{2.3.5}$$

If we now combine this with Gauss's law we get

$$\mathbf{0} = \partial_t \rho(\mathbf{r}, t) + \nabla \cdot \mathbf{J}(\mathbf{r}, t), \tag{2.3.6}$$

which represents the balance of charge density and currents, i.e. a change of the total charge in a given volume is only due to in or out-flowing currents. Equation (2.3.6) is commonly referred to the continuity equation of electromagnetics [68].

2.3.2 Boundary and interface conditions

Considering the entire system of Maxwell's equations (2.3.1) on a bounded closed domain Ω requires additional conditions at the boundary and domain interfaces. The boundary conditions are defined on $\partial\Omega$. Further considering two physically different sub-domains $\Omega^1, \Omega^2 \subset \Omega$ requires a condition on the shared interface $\partial\Omega^{1,2} = \overline{\Omega}^1 \cap \overline{\Omega}^2$. Figure 2.3 outlines the different domains and interfaces.

Interface conditions A standard derivation [68] readily shows conditions for the tangential component of the field quantities $\mathbf{E}$ and $\mathbf{H}$ as well as conditions on the normal component for the flux quantities $\mathbf{D}$ and $\mathbf{B}$. These interface conditions for the electric and magnetic field consequently read

$$\mathbf{n}_{1\to 2} \times (\mathbf{E}_1 - \mathbf{E}_2) = 0, \qquad \mathbf{n}_{1\to 2} \times (\mathbf{H}_1 - \mathbf{H}_2) = \mathbf{J}_{1,2}^{\text{surface}}, \tag{2.3.7}$$

and respectively for the electric and magnetic flux

$$\mathbf{n}_{1\to 2} \cdot (\mathbf{D}_1 - \mathbf{D}_2) = \sigma_{1,2}, \qquad \mathbf{n}_{1\to 2} \cdot (\mathbf{B}_1 - \mathbf{B}_2) = 0. \tag{2.3.8}$$

Here, $\mathbf{n}_{1\to 2}$ is the normal vector at the interface of two domains pointing from domain 1 to domain 2. $\sigma_{1,2}$ is the surface charge that accumulates exactly at the interface due to the (possible) discontinuity of the electric flux. The surface current $\mathbf{J}_{1,2}^{\text{surface}}$ is the magnetic analog to $\sigma_{1,2}$.

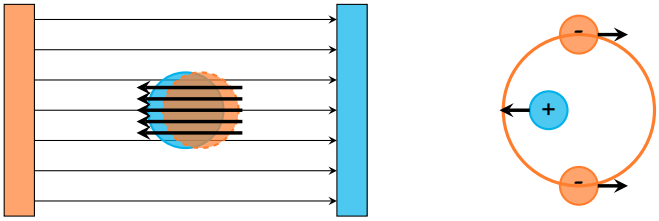

Figure 2.4 | Plate capacitor with dielectric. Left: Charges of the opposite sign (blue and orange) displace relatively to each other. Hence, an additional field that is directed oppositely to the initial one weakens the total field. Right: Cartoon of a single atom where the charge separation happens on a microscopic scale.

Boundary conditions Boundary conditions are deduced from the interface conditions. Applying (2.3.7) on the boundary $\partial\Omega$ and assuming an infinite conductivity outside Ω ($\mathbb{R}^3|_{\overline{\Omega}}$) leads to the Perfect Electrical Conductor (PEC) approximation of metals [4, 72, 42]. Hence, the all field quantities vanish outside Ω. Using (2.3.7) and (2.3.8) yields in this case

$$\begin{aligned} \mathbf{n}_{1\to2} \times \mathbf{E}_1 &= 0, & \mathbf{n}_{1\to2} \cdot \mathbf{D}_1 &= \sigma, \\ \mathbf{n}_{1\to2} \times \mathbf{H}_1 &= \mathbf{J}^{\text{surface}}, & \mathbf{n}_{1\to2} \cdot \mathbf{B}_1 &= 0. \end{aligned} \tag{2.3.9}$$

For closed domains, standard boundary conditions can be for example PEC or Perfect Magnetic Conductor (PMC) conditions.

Radiation conditions Scattering or free space problems, i.e. when Ω is thus not bounded anymore, require special free space radiation conditions. Imagine a scatterer inside Ω. If the observer is sufficiently far away from this scatterer, the scattered fields will converge to a spherical wavefront ($\exp(-i\mathbf{k}\cdot\mathbf{r})/|\mathbf{r}|$ dependence, $\mathbf{k}$ being the wave vector). A first order approximation of this condition is well known as Silver-Müller radiation condition

$$\mathbf{E} \times \mathbf{n} + Z_0\mathbf{H} \underset{+\infty}{=} \mathcal{O}(1/|\mathbf{r}|^2), \qquad \mathbf{H} \times \mathbf{n} - Y_0\mathbf{E} \underset{+\infty}{=} \mathcal{O}(1/|\mathbf{r}|^2) \tag{2.3.10}$$

We refer the interested reader to [160, 4, 72] for details.

2.3.3 Constitutive equations

Polarization The bound polarization $\mathbf{P}$ can be intuitively explained in an electrostatic plate capacitor setup as shown in Figure 2.4. Let the capacitor contain a particle of non-conducting, linear and isotropic material. The initial electric field slightly moves the shell electrons with respect to the positive nucleus and thus shows a dipole like charge distribution. Since we now have a non-uniform charge distribution, electric fields are 'created'. As they are directed in the opposite direction, the total electric field in between the plates is weakened. Casting this effect into formulae gives [42, 68]

$$\begin{aligned} \mathbf{P}_\text{b} &= \varepsilon_0\chi_\text{b}\mathbf{E}, \\ \mathbf{D} &= \varepsilon_0\mathbf{E} + \mathbf{P}_\text{b} = \varepsilon_0 \underbrace{(1+\chi_\text{b})}_{\varepsilon_\text{b}} \mathbf{E}. \end{aligned} \tag{2.3.11}$$

Here, χ_b is the susceptibility of the dielectric material and ε_b the relative permeability subject to vacuum. Obviously, if χ_b equals zero, the material behaves equivalently to vacuum.

Magnetization Although left out in the course of this work, equivalent steps apply to the magnetic flux density and read

$$\begin{aligned} \mathbf{M} &= \chi_\mathrm{m}\mathbf{H}, \\ \mathbf{B} &= \mu_0(\mathbf{H}+\mathbf{M}) = \mu_0 \underbrace{(1+\chi_\mathrm{m})}_{\mu_\infty}\mathbf{H}. \end{aligned} \tag{2.3.12}$$

However, we do not consider magnetic materials in throughout this work which leads to $\chi_\mathrm{m} \equiv 0$.

2.3.4 Electromagnetic wave equation

Maxwell's equations can be brought into a classical wave equation form. For this, we assume the material to be:

- Non dispersive and isotropic: $\mathbf{D} = \varepsilon_0\varepsilon_\mathrm{b}\mathbf{E}$;
- Linear: The material characteristics do not change due to the field amplitudes.

Neglecting currents and charges, i.e. $\mathbf{J} \equiv 0$ and $\rho \equiv 0$, simplifies (2.3.3) to

$$\mathbf{D} = \varepsilon_0\varepsilon_\infty\mathbf{E}. \tag{2.3.13}$$

Consequently, (2.3.1) becomes

$$\begin{aligned} \nabla\times\mathbf{E} &= -\mu_0\partial_t\mathbf{H} \\ \nabla\times\mathbf{H} &= \varepsilon_0\varepsilon_\mathrm{b}\partial_t\mathbf{E}, \end{aligned} \tag{2.3.14}$$

and $\nabla\cdot\mathbf{E} = \nabla\cdot\mathbf{H} \equiv 0$. Applying a standard vector calculus formula $\nabla\times\nabla\times\mathbf{A} = \nabla(\nabla\cdot\mathbf{A}) - \nabla^2\mathbf{A}$ yields the classical wave form of Maxwell's equations

$$\nabla^2\mathbf{A} - \frac{1}{{c_0}^2{c_r}^2}\partial_{tt}\mathbf{A} = 0, \qquad \text{with } \mathbf{A}\in\{\mathbf{E},\mathbf{H}\}. \tag{2.3.15}$$

Here, we defined the speed of light in vacuum $c_0 := (\varepsilon_0\mu_0)^{-1}$ and the relative speed of light $c_r := (\varepsilon_\infty\mu_\infty)^{-1}$

2.3.5 Electromagnetic energy and Poynting's theorem

Poynting's theorem gives an energy balance between the electromagnetic field energy inside a volume V in relation to the in- or out-flowing energy flux and the ohmic (thermal) losses. A comprehensive physical discussion of this phenomenon is given in [42]. The energy flux density is defined by the Poynting vector

$$\mathbf{S} := \mathbf{E}\times\mathbf{H}, \tag{2.3.16}$$

and the energy balance (with w_e is the electric field energy density) equation reads

$$\frac{\mathrm{d}}{\mathrm{d}t}\int_V w_e\,\mathrm{d}^3r = -\int_{\partial V}\mathbf{S}\cdot\mathbf{n}\,\mathrm{d}^2r - \int_V \mathbf{E}\cdot\mathbf{J}\,\mathrm{d}^3r. \tag{2.3.17}$$

Thus, the total change of field energy is driven by in- or out-flowing electromagnetic energy (1st term on the Right Hand Side (RHS)) or by ohmic losses (2nd term on the RHS).

2.3.6 Lorentz force

The force that acts on a single charged particle is called Lorentz force, which is given by

$$\mathbf{F} \quad = \quad q\left(\mathbf{E} + \mathbf{v} \times \mathbf{B}\right). \tag{2.3.18}$$

Here, q is the charge of the particle and $\mathbf{v}$ its velocity.

2.4 Modeling metals in nanoplasmonics

In computational electromagnetics, metals are often assumed to be perfectly conducting. This assumption is usually valid for a vast range of applications, especially in the microwave regime. Classical microwave devices like antennas [4], cavities for particle accelerators [78] or metamaterials [27] operate between MHz frequencies up to several THz for high-end Terahertz technologies. Microwave devices are usually larger than one wavelength (opposite to nanophotonics), leading to characteristic lengths of $l_{\text{device}} > \lambda$. Copper for example, has a skin-depth of 2 μm at 1 GHz that is equivalent to a wavelength $\lambda = 30$ cm. The ratio between the skin depth and the wavelength is $\approx$ 1e$-$3 generally justifying a PEC boundary condition at the metal interface [4].

In nanophotonics, the metamaterial character of metals is the main work-horse which becomes dominant for sub-wavelength structures. As the term photonics already indicate, the frequencies range from the infra-red ($\approx$ 400 THz) to the Ultra Violet (UV) ($\approx$ 800 THz), being equivalent to $\lambda \in [300, 1000]$ nm. Gold for example, appears to have a skin-depth of 100 nm at 500 THz ($\lambda = 600$ nm). Obviously, the wavelength and the skin-depth are of the same order of magnitude and metals cannot be modeled by a simple boundary condition anymore. Hence, a volume material model is required.

2.4.1 Constitutive equations for metals

Throughout the course of this work, we are particularly interested in metals. They are usually seen as a rigid, positive ion-core grid hosting both bound electrons (d-band) and valence electrons (s-band). Hence, the electric polarization $\mathbf{P}$ can be split in two parts: the background polarization of the bound electrons $\mathbf{P}_{\text{b}}$ [77, 105], governing the influence of the background electrons, and $\mathbf{P}_{\text{f}}$, which models the currents in the free electron gas. Exploiting this splitting, the complete polarization can be written as

$$\mathbf{P}(|\mathbf{E}|) = \mathbf{P}_{\text{b}}(|\mathbf{E}|) + \mathbf{P}_{\text{f}}(|\mathbf{E}|). \tag{2.4.1}$$

If $\mathbf{P}$ linearly depends on the electric field $\mathbf{E}$, the material is called linear. Quite often, non-linearities are dominated by a dependence on the magnitude of the electric field $|\mathbf{E}|$. We exclusively consider linear materials in the scope of this thesis. Multiple linear models for the bound electrons $\mathbf{P}_{\text{b}}$ and free electrons $\mathbf{P}_{\text{f}}$ can be found in literature [123].

Bound electron polarization In a linear medium, the polarization of the bounded electrons accounts for the history of the electric field, namely

$$\mathbf{P}_{\text{b}} = \overline{\overline{\chi}}_{\text{b}} \star_t \mathbf{E}, \tag{2.4.2}$$

where the electric susceptibility $\overline{\overline{\chi}}_{\text{b}} : \Omega \times [0, T] \mapsto \mathbb{R}^{3\times3}$ generally is a tensor (anisotropic materials) and $\star_t$ denotes the convolution in time.

Free electron polarization Regarding the polarization of the free electrons, one has to take into account for both the history of the field and its variation over space via the relation

$$\mathbf{P}_{\mathrm{f}} = \overline{\overline{\chi}}_{\mathrm{f}} \star_{(\mathbf{r},t)} \mathbf{E}, \tag{2.4.3}$$

where $\star_{(\mathbf{r},t)}$ denotes the convolution in both space and time. and hence $\overline{\overline{\chi}}_{\mathrm{f}} : \Omega \times [0,T] \mapsto \mathbb{R}^{3\times 3}$ We will assume isotropic materials, i.e. $\overline{\overline{\chi}} := \chi \operatorname{diag}\{1\ 1\ 1\}$ in the following.

Remark 2.4.1. *It is important to note the difference between $\mathbf{P}_{\mathrm{b}}$ and $\mathbf{P}_{\mathrm{f}}$. While $\mathbf{P}_{\mathrm{b}}(\mathbf{r},t)$ only depends on the time history (convolution in time: temporal dispersion) at the same point $\mathbf{r}$, $\mathbf{P}_{\mathrm{f}}(\mathbf{r},t)$ also depends on the surrounding domain (convolution in time and space: temporal and spatial dispersion).*

2.4.2 Dispersion model for bound electrons

In the frequency-domain (for a given frequency ω), equation (2.4.2) reduces to a multiplication of the frequency-dependent quantities associated to ε_{b} and $\mathbf{E}$. Thus prescribing the expression of a frequency-dependent permittivity allows to determine the model equations (performing an inverse Fourier transform to obtain the time-dependent equations).

In the case of bound electrons, inter-band transitions can be modeled by Lorentz oscillators motivated by a simple semi-quantum model of the form

$$\varepsilon_{\mathrm{b}}(\omega) = \sum_{l=1}^{k} \frac{f_l {\omega_{\mathrm{P}}}^2}{(\omega_l^2 - \omega^2) + i\omega\Gamma_l}. \tag{2.4.4}$$

Here, ω_{P} is a physical parameter called the plasma frequency[1] which is related to the electron density and predominantly prescribes the plasmonic behaviour of a metal. The other parameters k (the number of poles), f_i, ω_i and Γ_i are degrees of freedom in the model. These will be fixed in order to fit experimental data of permittivity values. However, this model is limited in accuracy. As an alternative model, we propose to use the Brendel-Bormann (BB) model applied to a wide optical frequency range as developed by Rakic et al. [123]. The advantage of this model is that it is able to distinguish between free and bounded electron contributions in the permittivity and thus allows for an accurate description of the latter ones. However, this model demands the evaluation of relatively complex functions, namely the Kummer functions of the second kind (we refer to [123] for details) and is hence complicated to be formulated in the time-domain. It turns out that the BB model's permittivities can be nicely fitted by a generalized dispersion model which consists of a Padé series of zero, first and second order poles (see [153])

$$\varepsilon_{\mathrm{b}}(\omega) = \varepsilon_\infty - \frac{\sigma}{i\omega} - \sum_{l\in L_1} \frac{a_l}{i\omega - b_l} - \sum_{l\in L_2} \frac{c_l - i\omega d_l}{\omega^2 - e_l + i\omega f_l}, \tag{2.4.5}$$

with $\{\varepsilon_\infty, \sigma, a_l, b_l, c_l, d_l, e_l, f_l\} \in \mathbb{R}$ and $L_{1,2}$ being the number of first and second order poles, respectively. These constants are thus fixed in order to provide a good fit of the values given by the BB model. Figure 2.5 shows an example fit of the bound electron permittivity $\varepsilon_{\mathrm{b}}^{\mathrm{Au}}$ of gold. This fit consists of six second order poles and a constant value ε_∞. Table 2.1 provides the corresponding parameters. Analogous results for Silver are provided in section C. Applying an inverse Fourier transform with the corresponding expression (2.4.5) yields a system of time-domain Ordinary Differential Equations (ODE) driving the evolution of the polarization current which is then coupled to Maxwell's equations via (2.4.1). We refer to [86] for more details on this model and to Chapter 2.5 for the global set of equations.

[1] The plasma frequency is the characteristic oscillation frequency of the electron density with respect to the average electron density.

Table 2.1 | Fit parameters of Au. Coefficients of the generalized dispersion model (2.4.5) with $\varepsilon_\infty = 1.0$ fitted to the BB permittivity of Au. Figure 2.5 depicts the original BB model and the fitted result.

i	c_l [Hz^2]	d_l [Hz]	e_l [Hz^2]	f_l [Hz]
1	0.1244266E+32	0.5443769E+11	0.1710211E+24	0.9838512E+15
2	0.1856766E+32	0.2936716E+12	0.2125471E+32	0.1587780E+16
3	0.1668009E+31	0.3440195E+10	0.1643161E+31	0.9578440E+15
4	0.7350947E+24	0.2222866E+16	0.1296565E+32	0.1400973E+16
5	0.3468661E+32	0.4572497E+11	0.6008717E+32	0.1274194E+16
6	0.8574585E+32	0.8687290E+10	0.4155750E+32	0.2764158E+16

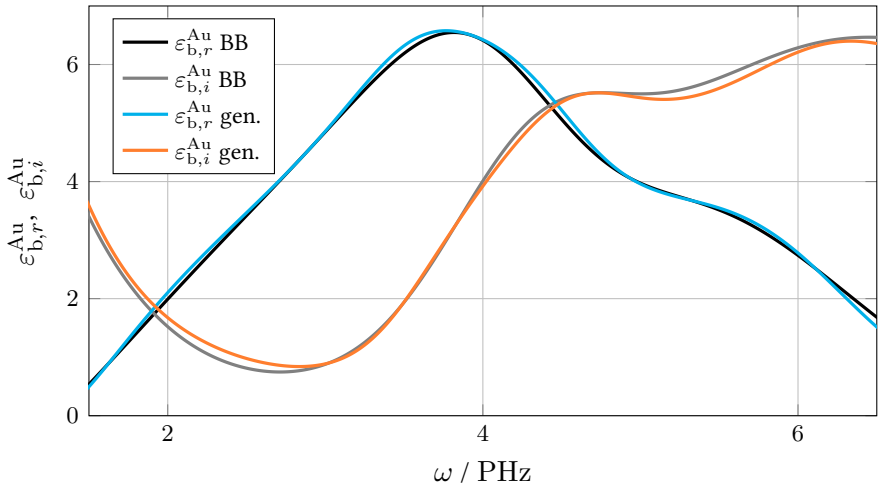

Figure 2.5 | Real and imaginary part of Au's bound permittivity. Black: ε_r and ε_i respectively are the real and imaginary part of the experimentally motivated BB model [123]. Colored: the fitted permittivity with our generalized dispersion model [153]. The corresponding fitting coefficients can be found in Table 2.1.

2.4.3 Quantum hydrodynamic electron response

The free electrons of a metal, leading to the polarization $\mathbf{P}_\mathrm{f}$, can be considered as a free electron gas that is modeled by a nonlinear fluid equation. Given the electron charge $-q_\mathrm{elec}$, its mass m_elec and a damping constant γ, the nonlinear hydrodynamic electron model reads [8]

$$m_\mathrm{elec}\left(\partial_t + \mathbf{v}\cdot\nabla\right)\mathbf{v} \;=\; -q_\mathrm{elec}\left(\mathbf{E} + \mathbf{v}\times\mathbf{B}\right) - m_\mathrm{elec}\gamma\mathbf{v} - \nabla\left(\frac{\delta G[n]}{\delta n}\right), \tag{2.4.6}$$

together with the continuity equation

$$0 \;=\; \partial_t n + \nabla\cdot(n\mathbf{v}), \tag{2.4.7}$$

where $\mathbf{v}$ represents the fluid velocity, n its density and $q_\mathrm{elec}(\mathbf{E}+\mathbf{v}\times\mathbf{B})$ is the Lorentz force. The last term of (2.4.6), containing the quantum pressure $\dfrac{\delta G[n]}{\delta n}$, eventually determines which quantum mechanical effects of the electron gas is taken into account or left out by an explicit form for the energy functional $G[n]$. Following the discussion by Ciraci [23], this term splits up into a sum of kinetic (T), exchange correlation and potential energy (XC). An approximated functional can be formulated as

$$G[n] \approx G_\eta[n] \;=\; T^\mathrm{TF}[n] + \frac{1}{\eta}T^\mathrm{W}[n] + \mathcal{E}_\mathrm{XC}. \tag{2.4.8}$$

where the kinetic contribution consists of the Thomas-Fermi (TF) and the von Weizsäcker (W) part.

A fully nonlinear problem as stated in (2.4.6) is a serious challenge and a reasonably vast range of problems can already be properly modeled by a linearized version of (2.4.6) [23]. Of course, such a model does not account for nonlinear effects like Second Harmonic Generation (SHG) [73], but already includes spatial dispersion [8, 105, 124, 20].

2.4.4 Linear nonlocal dispersion

As a simplified attempt that sticks to functionals of the type (2.4.8), we assume a pure Thomas-Fermi theory and drop the von Weizsäcker contribution as well as the exchange correlation in (2.4.8). Further we assume an equilibrium state with zero background velocity, no static electric and magnetic field, and a constant electron density denoted by n_0. We consider the same expression for the quantum pressure as in [61], which leads to a linear Thomas-Fermi theory [96, 20, 105]. The first order linearized term of the quantum pressure thus expresses as

$$\beta^2 \frac{1}{n_0} \nabla n. \tag{2.4.9}$$

The quantum related parameter β has to be chosen according to the physics of the problem. Its choice is a crucial point in this model and it depends on the Fermi velocity v_F and the spatial dimensionality of the problem. Boardman [8] comprehensively discusses the choice of this parameter and proposes

$$\beta = \sqrt{\frac{3D}{D(D+2)}} v_\mathrm{F}, \tag{2.4.10}$$

for high frequencies where surface plasmons can be excited [8]. In (2.4.10), $D = \{1, 2, 3\}$ is the dimensionality of the Fermi gas. A three dimensional Fermi gas, as we consider it throughout this work, yields $\beta = \sqrt{3/5} v_\mathrm{F}$. Expanding all the fields around an equilibrium state, i.e. $u(\mathbf{r}, t) \approx u_0 + u_1(\mathbf{r}, t)$, $u \in \{n, \mathbf{v}, \mathbf{E}, \mathbf{B}\}$, keeping the linear terms only, and omitting the index $(\cdot)_1$ leads to a first order system

$$\begin{aligned} m_\mathrm{elec} \partial_t \mathbf{v} &= -q_\mathrm{elec} \mathbf{E} - m_\mathrm{elec} \gamma \mathbf{v} + m_\mathrm{elec} \beta^2 \frac{1}{n_0} \nabla n, \\ \partial_t n &= -n_0 \nabla \cdot \mathbf{v}. \end{aligned} \tag{2.4.11}$$

Here, we assumed $\partial_t n_0 = \mathbf{v}_0 = \mathbf{E}_0 = \mathbf{B}_0 = 0$ (non-moving fluid, zero static electric or magnetic fields, and a constant electron density) and constant (in both space and time) background electron density n_0. Differentiating the first equation in (2.4.11) with respect to the time t, exploiting the second equation in (2.4.11), and using $\mathbf{J}_\mathrm{f} = n_0 q_\mathrm{elec} \mathbf{v}$, the current density of the unbound electrons in the fluid formally yields

$$0 = \partial_{tt} \mathbf{J}_\mathrm{f} + \gamma \partial_t \mathbf{J}_\mathrm{f} - \beta^2 \nabla (\nabla \cdot \mathbf{J}_\mathrm{f}) - {\omega_\mathrm{P}}^2 \varepsilon_0 \partial_t \mathbf{E}, \tag{2.4.12}$$

with $\omega_\mathrm{P} = \sqrt{\frac{n_0 q_\mathrm{elec}^2}{\varepsilon_0 m_\mathrm{elec}}}$ being the plasma frequency. Equation (2.4.12) is a second order Partial Differential Equation (PDE) in space and time. As we will see later, this form is impractical for our DGTD framework and we hence want to recast it under a first order system

$$\begin{aligned} 0 &= \partial_t \mathbf{J}_\mathrm{f} + \gamma \mathbf{J}_\mathrm{f} - \beta^2 \nabla Q - {\omega_\mathrm{P}}^2 \varepsilon_0 \mathbf{E}, \\ 0 &= \partial_t Q - \nabla \cdot \mathbf{J}_\mathrm{f}. \end{aligned} \tag{2.4.13}$$

System (2.4.13) can be written as a first order system of hyperbolic PDE (see Section 2.6).

2.4.5 Linear local dispersion

Neglecting nonlocality, i.e. $\beta \equiv 0$, significantly simplifies the model discussed in Section 2.4.4. Hence, (2.4.6) becomes an Ordinary Differential Equation (ODE) of the form

$$\partial_t \mathbf{J} = L(\mathbf{J}, \mathbf{E}), \tag{2.4.14}$$

where L is still a linear but only a local operator now and we dropped the index $(\cdot)_\mathrm{f}$ for the moment. For the well known Drude model [96] we have

$$\partial_t \mathbf{J} = -\gamma \mathbf{J} + {\omega_\mathrm{P}}^2 \varepsilon_0 \mathbf{E}. \tag{2.4.15}$$

Using $\partial_t \mathbf{P} = \mathbf{J}$ in (2.4.15) and $\mathbf{P} = -|q_\mathrm{elec}| n \mathbf{x}$ afterwards, as well as $\omega_\mathrm{P} = \sqrt{\frac{n|q_\mathrm{elec}|^2}{\varepsilon_0 m_\mathrm{elec}}}$ yields

$$m_\mathrm{elec} \partial_{tt} \mathbf{x} + m_\mathrm{elec} \gamma \partial_t \mathbf{x} \quad = \quad -|q_\mathrm{elec}| \mathbf{E}, \tag{2.4.16}$$

which indeed is a simple harmonic oscillator. Here, $\mathbf{x}(t) : \mathbb{R} \mapsto \mathbb{R}^3$ denotes the spatial displacement of an electron in dependence of the time t. Valence electrons are though harmonically oscillating when subject to an external electric field $\mathbf{E}$. Figure 2.6 illustrates a metal bulk irradiated by an incoming electromagnetic wave. Transforming (2.4.15) into the frequency-domain by assuming a harmonic time dependence $f(t) = \Re\{\underline{f} \exp(-i\omega t\}$ and $\underline{f}$ is a phasor, leads to

$$\underline{\mathbf{P}}(\omega) \quad = \quad -\frac{n|q_\mathrm{elec}|^2}{m_\mathrm{elec}(\omega^2 + i\gamma\omega)} \underline{\mathbf{E}}. \tag{2.4.17}$$

Using (2.4.17) in (2.4.1) and subsequently plugging it into (2.3.11) brings us to a frequency dependent permittivity function

$$\underline{\mathbf{D}}(\omega) \quad = \quad \varepsilon_0 \varepsilon(\omega) \underline{\mathbf{E}}. \tag{2.4.18}$$

Equation (2.4.15) is well known in literature as the Drude dispersion model. The performance in terms of fitting accuracy of different materials for both, the real and imaginary part of $\varepsilon(\omega)$ is comprehensively discussed in [153, 152]. Viquerat also proposes a generalized dispersion model based on Padé expansion in order to augment the fitting precision of experimental data over large frequency ranges. This is realized by adding poles up to the second order until the modeled and measured curves sufficiently overlap. We will use this model throughout this work but skip a detailed discussion of the scheme and refer to [153, 86] for further details.

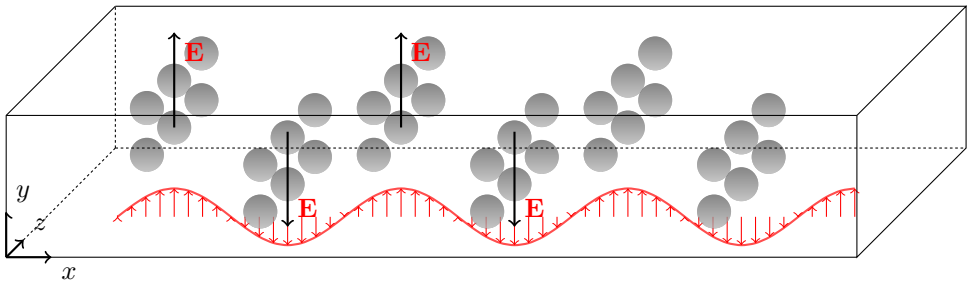

Figure 2.6 | Electron Displacement for the Drude Model. Free electrons (electron gas) inside the metal are excited by an external electric field. The charge displacement causes additional fields in terms of polarization. As this effect is frequency-dependent, a dispersion yields for non-monochromatic illumination.

2.5 Complete system of Maxwell's equations coupled to local and nonlocal dispersion laws

The split of the bound and free polarization in (2.4.1) was necessary in order to apply the quantum hydrodynamic electron response model to the free electrons and to allow a flexible model for the bound electrons at the same time. Coupling both to Maxwell's equations leads to the complete system

Maxwell + local & nonlocal dispersion

$$
\begin{aligned}
\nabla \times \mathbf{E} + \mu_0 \partial_t \mathbf{H} &= 0, \\
\nabla \times \mathbf{H} - \varepsilon_0 \varepsilon_\infty \partial_t \mathbf{E} - \mathbf{J}_\mathrm{f} - \mathbf{J}_\mathrm{b} &= 0, \\
\partial_t \mathbf{J}_\mathrm{f} + \gamma \mathbf{J}_\mathrm{f} - \beta^2 \nabla Q - {\omega_\mathrm{P}}^2 \varepsilon_0 \mathbf{E} &= 0, \\
\partial_t Q - \nabla \cdot \mathbf{J}_\mathrm{f} &= 0, \\
-\mathbf{J}_\mathrm{b} + \boldsymbol{\mathcal{J}}_0 + \sum_{l \in L_1} \boldsymbol{\mathcal{J}}_l + \sum_{l \in L_2} \boldsymbol{\mathcal{J}}_l &= 0, \\
-\boldsymbol{\mathcal{J}}_0 + \left(\sigma + \sum_{l \in L_2} d_l \right) \mathbf{E} &= 0, \\
-\boldsymbol{\mathcal{J}}_l + a_l \mathbf{E} - b_l \boldsymbol{\mathcal{P}}_l &= 0, \quad \forall l \in L_1, \\
-\partial_t \boldsymbol{\mathcal{P}}_l + \boldsymbol{\mathcal{J}}_l &= 0, \quad \forall l \in L_1, \\
-\partial_t \boldsymbol{\mathcal{J}}_l + (c_l - d_l f_l) \mathbf{E} - f_l \boldsymbol{\mathcal{J}}_l - e_l \boldsymbol{\mathcal{P}}_l &= 0, \quad \forall l \in L_2, \\
-\partial_t \boldsymbol{\mathcal{P}}_l + d_l \mathbf{E} + \boldsymbol{\mathcal{J}}_l &= 0, \quad \forall l \in L_2.
\end{aligned}
\tag{2.5.1}
$$

2.5.1 Boundary conditions

The set of equations (2.5.1) is supplemented with initial and boundary conditions. Let us focus on the latter. Regarding the set of pure Maxwell equations, we have to fix boundary conditions for $\mathbf{E}$ and $\mathbf{H}$. We choose not to detail them here since we will use classical boundary conditions that are applied on a PEC or PMC wall or First Order Absorbing Boundary Condition (ABC) as described in Section 2.3.2. We do not prescribe any boundary conditions to the set of unknowns issued from the bound electrons, since their evolution is described by a set of ODEs. Let us focus on the set of unknowns issued from the free electrons model, i.e. $\mathbf{J}_\mathrm{f}$ and Q. We omit the subscript of the free electrons in the following and presume $\mathbf{J} := \mathbf{J}_\mathrm{f}$. System (2.4.13) can be written as a first order hyperbolic equation as expressed in the third and fourth equation of (2.5.1). We refer to [134] for the comprehensive discussion and derivation of this system of hyperbolic PDEs; we simply recall the main results for (2.4.13) in the following. Considering the propagation problem (2.4.13) on a domain Ω we claim continuity for the normal component of the polarization current at any subdomain interface between two disjoint domains Ω_1 and Ω_2, $\Omega_1 \cap \Omega_2 = \partial\Omega_{1,2}$ and $\Omega_{1,2} \subset \Omega$, i.e.

$$
\mathbf{n} \cdot (\mathbf{J}_2 - \mathbf{J}_1)|_{\partial\Omega_{1,2}} = 0. \tag{2.5.2}
$$

Figure 2.7 depicts Ω. In the case of $\beta \neq 0$ on Ω_1 and $\beta \equiv 0$ on Ω_2, $\partial\Omega_{1,2}$ becomes a boundary of the nonlocal domain. Supposing a vanishing polarization current outside the nonlocal domain Ω_1, the resulting boundary condition reads

$$
\mathbf{n} \cdot \mathbf{J}_1|_{\partial\Omega_{1,2}} = 0. \tag{2.5.3}
$$

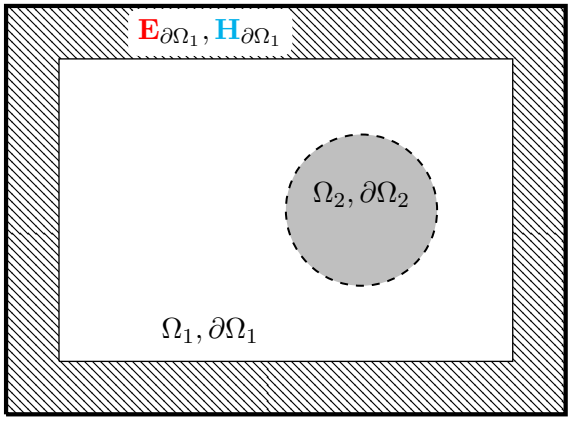

Figure 2.7 | Computational domain Ω. Domain Ω_1 consists of vacuum and hence the electromagnetic fields $\mathbf{E}$ and $\mathbf{H}$ are present. It is surrounded by the boundary $\partial\Omega_{1,2} = \Omega_1 \cup \Omega_2$ where Ω_1 truncates the Maxwell domain and Ω_2 is the interface to the dispersive domain Ω_2 where the additional fields $\mathbf{J}$ and Q are present.

In the special case of $\Omega_1 = \Omega$, (2.5.3) formulates the boundary condition for the entire boundary $\partial\Omega$ of the nonlocal domain Ω. Boundary condition (2.5.3) is often referred to as 'hard-wall' boundary condition because spill-out effects are not modeled.

Remark 2.5.1. *Hard-wall boundary conditions (in the linear case) assume a background electron density which is strictly restricted to the given metal domain, i.e.*

$$n_0 = \begin{cases} n_0(\mathbf{r}) & , \mathbf{r} \in \Omega_2 \\ 0 & , \text{otherwise} \end{cases}. \tag{2.5.4}$$

Here, the domains are presumed to be arbitrarily known. Hence, no electron is allowed to travel out of the predefined metal-domain, which determines the term 'hard-wall'. Differently, if spill-out effects were contained in the model, the boundary of Ω_2 may evolve in time and electrons could travel outside the initially defined metal-domain.

Symmetry conditions Beside the physically interpretable boundary condition (2.5.3) that forbids normal currents at the metal surface, it is useful to define a supplementary symmetry condition. This condition will be used for symmetric simulation setups in order to reduce the computational domain and hence the complexity of the simulation. We define the term 'soft-wall' boundary condition which reads

$$\mathbf{n} Q_1|_{\partial\Omega_{1,2}} = 0. \tag{2.5.5}$$

Condition (2.5.5) is the dual condition of (2.5.3).

2.6 Mathematical characterization

The following part is concerned by a study from a more mathematical point of view. In order to simplify the way of writing down the formulae, we want to cast Maxwell's equations and the linearized fluid model into a more general framework. This requires a multiplication by some constants and hence slightly changes the appearance of the equations. While the actual meaning of the equations is obviously not changed, it allows us to prove existence and uniqueness of the solution as in [65, 21]. Furthermore, we

will exploit this form in order to define bilinear forms in the following chapter. Semi-discrete stability together with classical inverse inequalities meets the requirements for the fully discrete stability and convergence proof. Here, we can re-use the proof in [86]. The following derivations consider the case in (2.5.1) where $\mathbf{J}_\mathrm{b} \equiv 0$. However, the result in [86] and ours yield the result for the whole set of equations in system (2.5.1).

2.6.1 Hydrodynamic system

Casting the four unknown fields $\{\mathbf{E}, \mathbf{H}, \mathbf{J}, Q\}$ into a new vector variable leads to the definition of

$$\boldsymbol{\vartheta} := \begin{bmatrix} \mathbf{H} & \mathbf{E} & \mathbf{J} & Q \end{bmatrix}. \tag{2.6.1}$$

The RHS of the first four equations in system (2.5.1) splits up into a differential operator part $\boldsymbol{\mathcal{L}}$ and $\boldsymbol{\mathcal{K}}$, which represents a compact operator perturbation. These operators are defined by

$$\boldsymbol{\mathcal{L}} := \begin{bmatrix} -\varepsilon_0 {\omega_\mathrm{P}}^2 \nabla \times \{\boldsymbol{\vartheta}\}_2 \\ \varepsilon_0 {\omega_\mathrm{P}}^2 \nabla \times \{\boldsymbol{\vartheta}\}_1 \\ \beta^2 \nabla \{\boldsymbol{\vartheta}\}_4 \\ \beta^2 \nabla \cdot \{\boldsymbol{\vartheta}\}_3 \end{bmatrix}, \quad \boldsymbol{\mathcal{K}} := \begin{bmatrix} 0 \\ -\varepsilon_0 {\omega_\mathrm{P}}^2 \{\boldsymbol{\vartheta}\}_3 \\ -\gamma \{\boldsymbol{\vartheta}\}_3 + \varepsilon_0 {\omega_\mathrm{P}}^2 \{\boldsymbol{\vartheta}\}_2 \\ 0 \end{bmatrix}. \tag{2.6.2}$$

Here, $\{\boldsymbol{\vartheta}\}_1 = \mathbf{H}$, $\{\boldsymbol{\vartheta}\}_2 = \mathbf{E}$, $\{\boldsymbol{\vartheta}\}_3 = \mathbf{J}$ and $\{\boldsymbol{\vartheta}\}_4 = Q$. Eventually, defining a material matrix

$$\boldsymbol{\Lambda} = \mathrm{diag}\left[\varepsilon_0 \mu_0 \mu_\infty {\omega_\mathrm{P}}^2 \mathbf{I}^{3\times 3}, \quad \varepsilon_0 \varepsilon_\infty {\omega_\mathrm{P}}^2 \mathbf{I}^{3\times 3}, \quad \mathbf{I}^{3\times 3}, \quad \beta^2\right], \tag{2.6.3}$$

for the Left Hand Side (LHS) yields the reformulated equation

$$\boldsymbol{\Lambda} \partial_t \boldsymbol{\vartheta} \quad = \quad \boldsymbol{\mathcal{L}}(\boldsymbol{\vartheta}) + \boldsymbol{\mathcal{K}}(\boldsymbol{\vartheta}). \tag{2.6.4}$$

Equation (2.6.4) is rewritten as

$$\boldsymbol{\Lambda} \partial_t \boldsymbol{\vartheta} \quad = \quad \boldsymbol{\mathcal{I}}(\boldsymbol{\vartheta}), \tag{2.6.5}$$

where we have defined $\boldsymbol{\mathcal{I}} := \boldsymbol{\mathcal{L}} + \boldsymbol{\mathcal{K}}$.

2.6.2 Existence and uniqueness

We now want to prove the existence and uniqueness of the solution of system (2.6.4). Following the development in [86], we use classical operator theory and can hence recycle Lemma 3.1 and Theorem 3.2 in [86]. Appropriate spaces for the operators $\boldsymbol{\mathcal{L}}$ and $\boldsymbol{\mathcal{K}}$ are

$$\begin{aligned} \mathcal{D}(\boldsymbol{\mathcal{L}}) \quad &= \quad \boldsymbol{\mathcal{H}}(\mathrm{curl}, \Omega) \times \boldsymbol{\mathcal{H}}_0(\mathrm{curl}, \Omega) \times \boldsymbol{\mathcal{H}}_0(\mathrm{div}, \Omega) \times \mathcal{H}^1(\Omega), \\ \mathcal{D}(\boldsymbol{\mathcal{K}}) \quad &= \quad \left(\boldsymbol{\mathcal{L}}^2(\Omega)\right)^{10}, \end{aligned} \tag{2.6.6}$$

and $\mathcal{D}(\boldsymbol{\mathcal{I}}) = \mathcal{D}(\boldsymbol{\mathcal{K}})$. The complete initial value problem hence reads

$$\begin{aligned} \boldsymbol{\Lambda} \partial_t \boldsymbol{\vartheta} \quad &= \quad \boldsymbol{\mathcal{L}}(\boldsymbol{\vartheta}) + \boldsymbol{\mathcal{K}}(\boldsymbol{\vartheta}), \\ \boldsymbol{\vartheta}(0) \quad &= \quad \boldsymbol{\vartheta}^0, \end{aligned} \tag{2.6.7}$$

with a given $\boldsymbol{\vartheta}^0 \in \mathcal{D}(\boldsymbol{\mathcal{I}})$ We also define the weighted scalar product on $\mathcal{D}(\boldsymbol{\mathcal{K}}) = \left(\boldsymbol{\mathcal{L}}^2(\Omega)\right)^{10}$

$$\langle \boldsymbol{\vartheta}, \boldsymbol{\vartheta}' \rangle_{\boldsymbol{\Lambda}} \quad = \quad \langle \boldsymbol{\Lambda} \boldsymbol{\vartheta}, \boldsymbol{\vartheta}' \rangle \in \left(\mathcal{D}(\boldsymbol{\mathcal{K}})\right)^2, \tag{2.6.8}$$

with the associated norm

$$||\boldsymbol{\vartheta}||_{\boldsymbol{\Lambda}}^2 \quad = \quad \langle \boldsymbol{\vartheta}, \boldsymbol{\vartheta} \rangle_{\boldsymbol{\Lambda}}, \tag{2.6.9}$$

since all the physical constants are ≥ 0. For finite time values $T > 0$, we can adapt the result in [86, 21] and conclude the following lemma and theorem on the existence and uniqueness of the Cauchy problem (2.6.7) on $[0, T]$.

Lemma 2.6.1. *(i) The unbound operator $\boldsymbol{\mathcal{L}}$ is defined on $\mathcal{D}(\boldsymbol{\mathcal{L}}) = \boldsymbol{\mathcal{H}}(curl, \Omega) \times \boldsymbol{\mathcal{H}}_0(curl, \Omega) \times \boldsymbol{\mathcal{H}}_0(div, \Omega) \times \mathcal{H}^1(\Omega)$, which is dense in $\left(\boldsymbol{\mathcal{L}}^2(\Omega)\right)^{10}$. Furthermore, $\boldsymbol{\mathcal{L}}$ is dissipative in $\boldsymbol{\mathcal{L}}(\Omega)^{10}$ and*

$$\langle \boldsymbol{\mathcal{L}}(\boldsymbol{\vartheta}), \boldsymbol{\vartheta} \rangle \quad = \quad 0, \forall \boldsymbol{\vartheta} \in \mathcal{D}(\boldsymbol{\mathcal{L}}). \tag{2.6.10}$$

(ii) The operator $\boldsymbol{\mathcal{K}}$ is defined on $\mathcal{D}(\boldsymbol{\mathcal{K}}) = \left(\boldsymbol{\mathcal{L}}^2(\Omega)\right)^{10}$. Furthermore,

$$\langle \boldsymbol{\mathcal{K}}(\boldsymbol{\vartheta}), \boldsymbol{\vartheta} \rangle \quad \leq \quad 0. \tag{2.6.11}$$

Proof. The proof is straightforward. Performing the scalar product yields

(i)

$$\begin{aligned} \langle \boldsymbol{\mathcal{L}}(\boldsymbol{\vartheta}), \boldsymbol{\vartheta} \rangle \quad = \quad & \varepsilon_0 {\omega_P}^2 \left(-\langle \nabla \times \{\boldsymbol{\vartheta}\}_2, \{\boldsymbol{\vartheta}\}_1 \rangle + \langle \nabla \times \{\boldsymbol{\vartheta}\}_2, \{\boldsymbol{\vartheta}\}_1 \rangle - \langle \mathbf{n} \times \{\boldsymbol{\vartheta}\}_2, \{\boldsymbol{\vartheta}\}_1 \rangle \right) \\ & \beta^2 \left(\langle \nabla \{\boldsymbol{\vartheta}\}_4, \{\boldsymbol{\vartheta}\}_3 \rangle - \langle \nabla \{\boldsymbol{\vartheta}\}_4, \{\boldsymbol{\vartheta}\}_3 \rangle + \langle \{\boldsymbol{\vartheta}\}_4 \{\boldsymbol{\vartheta}\}_3, \mathbf{n} \rangle \right), \end{aligned} \tag{2.6.12}$$

where we exploited the definition of $\mathcal{D}(\boldsymbol{\mathcal{L}})$.

(ii)

$$\begin{aligned} \langle \boldsymbol{\mathcal{K}}(\boldsymbol{\vartheta}), \boldsymbol{\vartheta} \rangle \quad = \quad & \varepsilon_0 {\omega_P}^2 \left(-\langle \{\boldsymbol{\vartheta}\}_3, \{\boldsymbol{\vartheta}\}_2 \rangle + \langle \{\boldsymbol{\vartheta}\}_2, \{\boldsymbol{\vartheta}\}_3 \rangle \right) \\ & -\gamma \langle \{\boldsymbol{\vartheta}\}_3, \{\boldsymbol{\vartheta}\}_3 \rangle \\ = \quad & -\gamma ||\{\boldsymbol{\vartheta}\}_3||^2. \end{aligned} \tag{2.6.13}$$

□

Theorem 2.6.1. *If $\boldsymbol{\vartheta}^0 \in \left(\mathbf{H}^0, \mathbf{E}^0, \mathbf{J}^0, Q^0\right) \in \mathcal{D}(\boldsymbol{\mathcal{I}})$, then there exists a unique weak solution*

$$\boldsymbol{\vartheta} \quad = \quad (\mathbf{H}, \mathbf{E}, \mathbf{J}, Q) \in \mathcal{C}^0 \left([0, T], \mathcal{D}(\boldsymbol{\mathcal{I}})\right) \cap \mathcal{C}^1 \left([0, T], \left(\boldsymbol{\mathcal{L}}^2(\Omega)\right)^{10}\right), \tag{2.6.14}$$

of (2.6.7).

2.6.3 Energy

An energy principle can be understood as a figure of merit of a physical model, as the total energy stored in a physically motivated system must never increase. Additionally, preserving this property when it comes to numerical algorithms would be a nice feature of the latter. Formally defining the energy in system (2.6.4) at any time $t \in [0, T]$ by

$$\mathcal{E}(t) \quad = \quad \frac{1}{2} ||\boldsymbol{\vartheta}||_{\boldsymbol{\Lambda}}^2, \tag{2.6.15}$$

leading to the following result.

Theorem 2.6.2. *If* $\boldsymbol{\vartheta} \in \mathcal{C}^0([0,T],\mathcal{D}(\boldsymbol{\mathcal{I}})) \cap \mathcal{C}^1\left([0,T],\left(\boldsymbol{\mathcal{L}}^2(\Omega)\right)^{10}\right)$, $\mathcal{E}(t)$ *is bounded on* $[0,T]$.

Proof. Dot multiplying (2.6.4) with $\boldsymbol{\vartheta}$ and assuming sufficiently regular fields, leads to

$$\langle \boldsymbol{\Lambda}\partial_t\boldsymbol{\vartheta},\boldsymbol{\vartheta}\rangle \quad = \quad \langle \boldsymbol{\mathcal{L}}(\boldsymbol{\vartheta}),\boldsymbol{\vartheta}\rangle + \langle \boldsymbol{\mathcal{K}}(\boldsymbol{\vartheta}),\boldsymbol{\vartheta}\rangle. \tag{2.6.16}$$

Simplifying the result by using (i) and (ii) of Lemma 2.6.1 yields

$$\partial_t\mathcal{E}(t) \quad \leq \quad 0, \tag{2.6.17}$$

for all $t \in [0,T]$.

Here, where we have assumed that $\partial\Omega$ is a perfectly electric conducting boundary and that currents vanish outside Ω. □

The result obtained in (2.6.16) shows the strict preservation of the energy $\partial_t\mathcal{E}(t) = 0$ for a collision free model, i.e. $\gamma \equiv 0$ and also drives dissipation if collisions (damping), i.e. $\gamma \neq 0$ is taken into account.

2.6.4 Study of the hyperbolicity

If we focus on the Maxwell-hydrodynamic part of (2.5.1) (i.e. the first four equations, neglecting the ODEs contributions, i.e. $\mathbf{J}_\mathrm{b} \equiv 0$), one can study its hyperbolicity. We here recall the associated eigenvalues and again refer to [134] for details. For $\xi = \{\xi_1,\xi_2,\xi_3\}^T \in \mathbb{R}^3$, the eigenvalues of the Maxwell-hydrodynamic system are given by

$$\boldsymbol{\lambda}(||\xi||) = \left\{0 \quad 0 \quad 0 \quad 0 \quad -c_0c_r||\xi|| \quad -c_0c_r||\xi|| \quad c_0c_r||\xi|| \quad c_r||\xi|| \quad -\beta||\xi|| \quad \beta||\xi||\right\}. \tag{2.6.18}$$

These will be of importance when discussing the numerical fluxes in the numerical sections that follow.

2.7 Analytical solutions

This chapter is concerned with the definition of several analytical solutions of Maxwell's equations and Maxwell's equations coupled to dispersion laws. Such solutions are provided in order to serve as reference solutions to our numerically computed results in the coming chapters.

Most of them are well known textbook examples like respectively cubic and spherical PEC cavities or free space solutions for Maxwell's equations. More advanced solution techniques for scattering problems of individual rods or spheres have been done by Mie [99] in the beginning of the 20^{th} century. We briefly recall the physical setup of this type of problems and give the main results we need for our validation purposes.

2.7.1 Cavity problem

Rectangular cavities consist of a domain $\Omega = \{\mathbf{r} \in [0,a_l]^3\}$, where a_l with $l \in \{x,y,z\}$ respectively denote the edge lengths in the Cartesian $\{x,y,z\}$ direction. Assuming PEC boundary conditions on $\partial\Omega$ and bringing (2.3.15) to the frequency-domain yields the eigenvalue problem

$$\nabla^2\underline{\mathbf{E}} + \frac{\omega^2}{{c_0}^2{c_r}^2}\underline{\mathbf{E}} = 0, \tag{2.7.1}$$

with the time-domain solution

$$\mathbf{E}(x,y,z,t) = \begin{bmatrix} \{\mathbf{E}_0\}_x \cos\left(\frac{\pi n_x}{a_x}x\right) \sin\left(\frac{\pi n_y}{a_y}y\right) \sin\left(\frac{\pi n_z}{a_z}z\right) \\ \{\mathbf{E}_0\}_y \sin\left(\frac{\pi n_x}{a_x}x\right) \cos\left(\frac{\pi n_y}{a_y}y\right) \sin\left(\frac{\pi n_z}{a_z}z\right) \\ \{\mathbf{E}_0\}_z \sin\left(\frac{\pi n_x}{a_x}x\right) \sin\left(\frac{\pi n_y}{a_y}y\right) \cos\left(\frac{\pi n_z}{a_z}z\right) \end{bmatrix} \cos\left(\omega_{\mathrm{res}}t\right). \tag{2.7.2}$$

Here, $n_l \in \mathbb{N}$ with $l \in \{x,y,z\}$ is the mode number and ω_{res} the resonance angular frequency resulting from the dispersion relation. The solution of the magnetic field is analogous. Additionally, we have to avoid unphysical solutions which can be guaranteed by Gauss' law

$$\nabla \cdot \mathbf{E} = 0. \tag{2.7.3}$$

Assuming a cubic cavity with $a_l = a$ and the mode $n_l = 1$ for all l simplifies the equations Without Loss Of Generality (w.l.o.g.). The resonance frequency hence reads

$$\omega_{\mathrm{res}} = c_0 c_r \pi \sqrt{3}, \tag{2.7.4}$$

We skip simple algebraic steps [68] and directly provide the result for $\mathbf{E}_0 = \begin{pmatrix} -1 & 0 & 1 \end{pmatrix}^{\mathsf{T}}$

$$\begin{aligned} \mathbf{E}(x,y,z,t) &= \begin{bmatrix} -\cos(\pi x)\sin(\pi y)\sin(\pi z) \\ 0 \\ \sin(\pi x)\sin(\pi y)\cos(\pi z) \end{bmatrix} \cos\left(\omega_{\mathrm{res}}t\right), \\ \mathbf{H}(x,y,z,t) &= \pi c_0 c_r \begin{bmatrix} -\sin(\pi x)\cos(\pi y)\cos(\pi z) \\ 2\cos(\pi x)\sin(\pi y)\cos(\pi z) \\ -\cos(\pi x)\cos(\pi y)\sin(\pi z) \end{bmatrix} \sin\left(\omega_{\mathrm{res}}t\right). \end{aligned} \tag{2.7.5}$$

Equally, the linear hydrodynamic Drude model (2.4.13) has a similar form if $\gamma = \omega_{\mathrm{P}} \equiv 0$. We hence obtain

$$\begin{aligned} \beta^2 \nabla Q - \partial_t \mathbf{J} &= 0, \\ \nabla \cdot \mathbf{J} - \partial_t Q &= 0. \end{aligned} \tag{2.7.6}$$

Proceeding equivalently to the Maxwell case leads to

$$\left(\beta^2\left(\underline{K}_x + \underline{K}_y + \underline{K}_z\right) + \omega^2\right)\underline{Q} = 0, \tag{2.7.7}$$

where the $\beta^2\left(\underline{K}_x + \underline{K}_y + \underline{K}_z\right) + \omega^2 = 0$ is the dispersion relation. In case of a nontrivial solution we claim $Q \neq 0$. Solving the separated ODE for each separation constant $\underline{K}_l = (i\{\mathbf{k}\}_l)^2$ that verifies the

dispersion relation and with the appropriate boundary conditions $\partial_{\mathbf{n}} Q|_{\partial\Omega}$ as discussed in Chapter 2.4.4 gives

$$\underline{K}_l = -\left(\frac{n_l \pi}{a_l}\right)^2, \tag{2.7.8}$$

as previously for the Maxwell case. The resonance angular frequency for the hydrodynamic case reads

$$\omega_{\text{res,fluid}} = \pi\beta\sqrt{\left(\frac{n_x}{a_x}\right)^2 + \left(\frac{n_y}{a_y}\right)^2 + \left(\frac{n_z}{a_z}\right)^2}. \tag{2.7.9}$$

Eventually, we obtain the time-domain solution of of Q and $\mathbf{J}$

$$\begin{aligned} Q(x,y,z,t) &= Q_0 \cos\left(\frac{\pi n_x}{a_x}x\right)\cos\left(\frac{\pi n_y}{a_y}y\right)\cos\left(\frac{\pi n_z}{a_z}z\right)\sin\left(\omega_{\text{res,fluid}}t\right), \\ \mathbf{J}(x,y,z,t) &= -\frac{\beta^2 \text{diag}(\mathbf{J}_0)}{\omega_{\text{res,fluid}}} \begin{bmatrix} \frac{\pi n_x}{a_x}\sin\left(\frac{\pi n_x}{a_x}x\right)\cos\left(\frac{\pi n_y}{a_y}y\right)\cos\left(\frac{\pi n_z}{a_z}z\right) \\ \frac{\pi n_y}{a_y}\cos\left(\frac{\pi n_x}{a_x}x\right)\sin\left(\frac{\pi n_y}{a_y}y\right)\cos\left(\frac{\pi n_z}{a_z}z\right) \\ \frac{\pi n_z}{a_z}\cos\left(\frac{\pi n_x}{a_x}x\right)\cos\left(\frac{\pi n_y}{a_y}y\right)\sin\left(\frac{\pi n_z}{a_z}z\right) \end{bmatrix} \cos\left(\omega_{\text{res,fluid}}t\right). \end{aligned} \tag{2.7.10}$$

If $n_l = 1$ and $a_l = a\ \forall l$ the solution simplifies analogously to the Maxwell case.

2.7.2 Plane wave propagation in free space

Moving from the setup of an enclosed convex domain Ω with boundary conditions on $\partial\Omega$, we now consider a free space problem in the infinite space. This is a particularly useful setup as we will use this field solution as excitation for the scattering problems considered in the following chapters.

Starting from Maxwell's equations in a homogeneous infinite space filled with a linear, isotropic and non dispersive medium and respectively switching to the temporal and spatial Fourier space

$$\partial_l \rightarrow i\{\mathbf{k}\}_l, \quad \forall l \in \{x,y,z\}, \tag{2.7.11}$$

leads to

$$\begin{aligned} -\omega\varepsilon_0\varepsilon_r\mathbf{E} &= \mathbf{k}\times\mathbf{H}, \\ \omega\mu_0\mu_\infty\mathbf{H} &= \mathbf{k}\times\mathbf{E}. \end{aligned} \tag{2.7.12}$$

The combination of Ampère's and Faraday's law yields

$$\begin{aligned} \omega^2(c_0c_r)^{-1/2}\mathbf{E} &= \mathbf{k}\times(\mathbf{k}\times\mathbf{E}), \\ &= -(\mathbf{k}\cdot\mathbf{E})\cdot\mathbf{k} + (\mathbf{k}\cdot\mathbf{k})\mathbf{E}. \end{aligned} \tag{2.7.13}$$

and due to the orthogonality $\mathbf{k}\perp\mathbf{E}$ we eventually get

$$(\omega^2(c_0c_r)^{-1/2} - \mathbf{k}\cdot\mathbf{k})\mathbf{E} = 0. \tag{2.7.14}$$

In order to fulfill the dispersion relation

$$\omega^2(c_0c_r)^{-1/2} = \{\mathbf{k}\}_x^2 + \{\mathbf{k}\}_y^2 + \{\mathbf{k}\}_z^2, \tag{2.7.15}$$

the individual components of the wave vector read

$$\begin{aligned} \{\mathbf{k}\}_x &= \frac{\omega}{c_0 c_r}\sin(\theta)\cos(\phi), \\ \{\mathbf{k}\}_y &= \frac{\omega}{c_0 c_r}\sin(\theta)\sin(\phi), \\ \{\mathbf{k}\}_z &= \frac{\omega}{c_0 c_r}\cos(\theta), \end{aligned} \tag{2.7.16}$$

with $\theta \in [0, \pi)$ and $\phi \in [0, 2\pi)$ (see Figure B.1). This leads to the final *monochromatic* solution

$$\begin{aligned} \mathbf{E}(\mathbf{r}) &= \mathbf{E}_0 \exp(-i\omega t)\exp(i\mathbf{k}\cdot\mathbf{r}), \\ \mathbf{H}(\mathbf{r}) &= \frac{\mathbf{k}\times\mathbf{E}_0}{\omega\mu_0\mu_\infty}\exp(-i\omega t)\exp(i\mathbf{k}\cdot\mathbf{r}). \end{aligned} \tag{2.7.17}$$

Time-domain simulations are not restricted to monochromatic excitations and it is hence beneficial to account for the whole frequency spectrum in one simulation run. In order to excite a broad frequency spectrum, we use a Gaussian windowed monochromatic plane wave as an incident pulse. The resulting frequency spectrum is controlled by an appropriate choice of the temporal variance of the Gaussian signal

$$\mathbf{E}_{\mathrm{inc}}(\mathbf{r}, t) = \mathbf{E}_0 \sin\left(\omega_\mathrm{c}\left(t - t_0 - \frac{\mathbf{k}\cdot\mathbf{r}}{|\mathbf{k}|}\right)\right)\exp\left[-\frac{\left(t - t_0 - \frac{\mathbf{k}\cdot\mathbf{r}}{|\mathbf{k}|}\right)^2}{2\sigma^2}\right]. \tag{2.7.18}$$

Here, $\mathbf{E}_0$ is the transverse electric field amplitude, ω_c is the central frequency, t_0 an initial time delay, and σ the variance of the Gaussian window. For one particular field source in the scope of our numerical code (see Section 4.1.2), time derivatives of the source signal are required. By this means, we here provide the time derivative as well

$$\begin{aligned} \partial_t \mathbf{E}_{\mathrm{inc}}(\mathbf{r}, t) = \mathbf{E}_0 \Bigg\{ & \omega_\mathrm{c}\cos\left(\omega_\mathrm{c}\left(t - t_0 - \frac{\mathbf{k}\cdot\mathbf{r}}{|\mathbf{k}|}\right)\right)\exp\left[-\frac{\left(t - t_0 - \frac{\mathbf{k}\cdot\mathbf{r}}{|\mathbf{k}|}\right)^2}{2\sigma^2}\right] \\ & - \frac{t - t_0 - \frac{\mathbf{k}\cdot\mathbf{r}}{|\mathbf{k}|}}{\sigma^2}\sin\left(\omega_\mathrm{c}\left(t - t_0 - \frac{\mathbf{k}\cdot\mathbf{r}}{|\mathbf{k}|}\right)\right) \\ & \cdot\exp\left[-\frac{\left(t - t_0 - \frac{\mathbf{k}\cdot\mathbf{r}}{|\mathbf{k}|}\right)^2}{2\sigma^2}\right]\Bigg\}. \end{aligned} \tag{2.7.19}$$

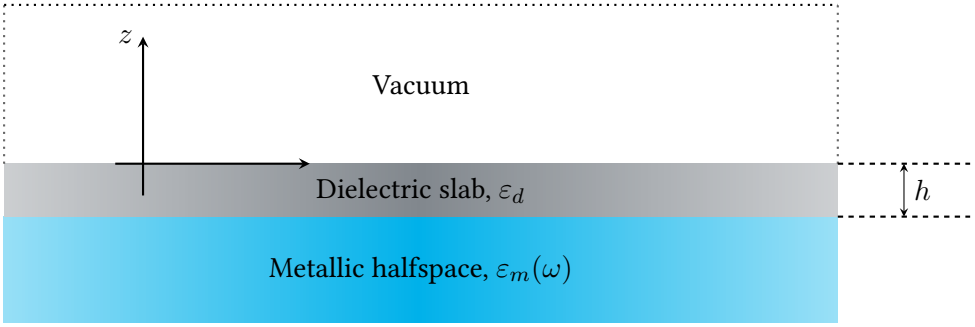

Figure 2.8 | Three layer system. Our three layer system consists of an infinite metallic half-space, a dielectric layer on top of the metal, and vacuum.

For the sake of completeness, we also want to provide the spatial derivative of $\mathbf{E}_{\text{inc}}$. Spatial derivation with respect to $l \in \{x, y, z\}$ yields

$$\begin{aligned} \partial_l \mathbf{E}_{\text{inc}}(\mathbf{r}, t) &= -\frac{\mathbf{E}_0 \mathbf{k} \cdot \mathbf{e}_l}{\sigma^2 |\mathbf{k}|^2} \exp\left[-\frac{\left(t - t_0 - \frac{\mathbf{k}\cdot\mathbf{r}}{|\mathbf{k}|} \right)^2}{2\sigma^2} \right] \\ &\quad \cdot \left[\omega_c \sigma^2 |\mathbf{k}| \cos\left(\omega_c \left(t - t_0 - \frac{\mathbf{k}\cdot\mathbf{r}}{|\mathbf{k}|} \right) \right) \right. \\ &\quad \left. + \left((\mathbf{k}\cdot\mathbf{r} - (t - t_0)|\mathbf{k}|) \sin\left(\omega_c \left(t - t_0 - \frac{\mathbf{k}\cdot\mathbf{r}}{|\mathbf{k}|} \right) \right) \right) \right]. \end{aligned} \tag{2.7.20}$$

2.7.3 Three layer system

An important setup in nanophotonics is illustrated in Figure 2.8. The metallic ground plane is covered by a dielectric layer. Further obstacles like nano cubes, nano spheres, etc. are often placed on top of the dielectric layer. Such setups may require the analytical solution of the three layer system without the obstacle in order to impose the correct incident field in our numerical simulation. We will derive this solution in the following.

Due to symmetry reasons, we consider the solution to be invariant in x and y direction, i.e. we neglect the derivatives $\partial_x = \partial_y = 0$, and only consider the incident wave propagating in $-\mathbf{e}_z$ direction. Hence, we only solve for $\{\mathbf{E}\}_y$ and $\{\mathbf{H}\}_x$. Making an ansatz for the solution in all three sub domains in the frequency-domain

$$\begin{aligned} \{\underline{\mathbf{E}}^{\text{v}}\}_y &= \exp(-ik_0 z) + \underline{r} \exp(ik_0 z), \\ \{\underline{\mathbf{E}}^{\text{d}}\}_y &= \underline{A} \exp\left(-ik_0 \sqrt{\underline{\varepsilon}_{\text{d}}} z\right) + \underline{B} \exp\left(ik_0 \sqrt{\underline{\varepsilon}_{\text{d}}} z\right), \\ \{\underline{\mathbf{E}}^{\text{m}}\}_y &= \underline{C} \exp\left(-ik_0 \sqrt{\underline{\varepsilon}_{\text{m}}} z\right), \end{aligned} \tag{2.7.21}$$

with $k_0 = \omega\sqrt{\varepsilon_0 \mu_0}$. Analogous relations are obtained for $i\omega\mu_0 \{\mathbf{H}\}_x = -\partial_z \{\mathbf{E}\}_y$. Solving this system obviously requires additional conditions which are given at the material interfaces. First, we claim the continuity of the tangential electric field and the continuity of the tangential magnetic field subsequently. This is justified by vanishing surface currents due to a finite permeability. Exploiting these conditions at

$z = 0$ yields

$$\begin{aligned} 1 + \underline{r} &= \underline{A} + \underline{B}, \\ \underline{r} - 1 &= \sqrt{\varepsilon_\mathrm{d}}(\underline{B} - \underline{A}), \end{aligned} \tag{2.7.22}$$

which gives

$$\begin{aligned} \underline{A} &= \frac{2}{1+\sqrt{\varepsilon_\mathrm{d}}} + \frac{\sqrt{\varepsilon_\mathrm{d}}-1}{\sqrt{\varepsilon_\mathrm{d}}+1}\underline{B} = t + \underline{r}_+\underline{B}, \\ t &:= \frac{2}{1+\sqrt{\varepsilon_\mathrm{d}}}, \\ r_+ &:= \frac{\sqrt{\varepsilon_\mathrm{d}}-1}{\sqrt{\varepsilon_\mathrm{d}}+1} \end{aligned} \tag{2.7.23}$$

Performing equivalent steps at $z = -h$ eventually leads to

$$\begin{aligned} \underline{B} &= \underline{A}\frac{\sqrt{\varepsilon_\mathrm{d}} - \sqrt{\underline{\varepsilon}_\mathrm{m}}}{\sqrt{\varepsilon_\mathrm{d}} + \sqrt{\underline{\varepsilon}_\mathrm{m}}} \exp\left(i2k_0\sqrt{\varepsilon_\mathrm{d}}h\right) \\ &= \underline{r}_m\underline{A} \exp\left(i2k_0\sqrt{\varepsilon_\mathrm{d}}h\right), \\ \underline{r}_\mathrm{m} &:= \frac{\sqrt{\varepsilon_\mathrm{d}} - \sqrt{\underline{\varepsilon}_\mathrm{m}}}{\sqrt{\varepsilon_\mathrm{d}} + \sqrt{\underline{\varepsilon}_\mathrm{m}}}. \end{aligned} \tag{2.7.24}$$

Combining these two equations gives

$$\begin{aligned} \underline{A} &= \frac{t}{1 - r_+\underline{r}_\mathrm{m}\exp\left(i2k_0\sqrt{\varepsilon_\mathrm{d}}h\right)}, \\ \underline{B} &= \frac{\underline{r}_\mathrm{m}t}{1 - r_+\underline{r}_\mathrm{m}\exp\left(i2k_0\sqrt{\varepsilon_\mathrm{d}}h\right)} \exp\left(i2k_0\sqrt{\varepsilon_\mathrm{d}}h\right). \end{aligned} \tag{2.7.25}$$

As we now have $\underline{A}$ and $\underline{B}$ we are able to straightforwardly obtain $\underline{r}$ and $\underline{C}$

$$\begin{aligned} \underline{r} &= \frac{t}{1 - r_+\underline{r}_\mathrm{m}\exp\left(i2k_0\sqrt{\varepsilon_\mathrm{d}}h\right)}\left(1 + \underline{r}_\mathrm{m}\exp\left(i2k_0\sqrt{\varepsilon_\mathrm{d}}h\right)\right) - 1, \\ \underline{C} &= \frac{t(1+\underline{r}_\mathrm{m})}{1 - r_+\underline{r}_\mathrm{m}\exp\left(i2k_0\sqrt{\varepsilon_\mathrm{d}}h\right)} \exp\left(ik_0\sqrt{\varepsilon_\mathrm{d}}h\right)\exp\left(-ik_0\sqrt{\underline{\varepsilon}_\mathrm{m}}h\right). \end{aligned} \tag{2.7.26}$$

This completes the Ansatz in (2.7.21) and allows for the explicit evaluation of the fields. However, the solution is still in frequency-domain and we would like to derive the corresponding time-domain signal. Unfortunately, it turns out that a closed form of (2.7.21) in the time-domain is a challenging task or perhaps even impossible. This issue is due to the dispersive material $\underline{\varepsilon}_\mathrm{m}(\omega)$ which hence shows different phase and group velocities depending on the frequency. Such a dispersion degenerates the initially Gaussian shaped pulse. A possible work around is to reconstruct a time-domain signal from a discrete evaluation of (2.7.21), i.e. by a discrete inverse Fourier transform.

2.7.4 Mie scattering of a dispersive rod

Ruppin has provided an analytic solution for the electromagnetic scattering of small metallic nano-wires [132]. The metal is modeled by linearized hydrodynamic Drude model. We here recall the main results

that are of concern to our work. The physical setup is depicted in Figure 2.9. This system is modeled by (2.5.1) with $\mathbf{J}_\mathrm{b} \equiv= 0$. Following [132], the extinction cross-section CS_ext is given by

$$CS_\mathrm{ext}(\omega) \quad = \quad -\frac{2}{k_0 R} \sum_{n=-\infty}^{\infty} \Re\{a_n\}. \tag{2.7.27}$$

Here, R is the rod's radius, and a_n the nth Mie coefficient

$$\begin{aligned}
\varepsilon_\mathrm{T}(\omega) &= 1 - \frac{{\omega_\mathrm{P}}^2}{\omega(\omega + i\gamma)}, \\
k_0(\omega) &= \sqrt{\varepsilon_\infty}\frac{\omega}{c_0}, \\
k_\mathrm{T}(\omega) &= \sqrt{\varepsilon(\omega)}\frac{\omega}{c_0}, \\
k_\mathrm{L}(\omega) &= \sqrt{\frac{\omega(\omega + i\gamma) - {\omega_\mathrm{P}}^2}{\beta^2}}, \\
c_n(\omega) &= \frac{n^2}{k_\mathrm{L} R}\frac{J_n(k_\mathrm{L})}{J_n'(k_\mathrm{L})} J_n(k_\mathrm{T} R)\left(\frac{\sqrt{\varepsilon_\mathrm{T}}}{k_0 R} - \frac{\sqrt{\varepsilon_\infty}}{k_\mathrm{T} R}\right), \\
a_n(\omega) &= -\frac{c_n J_n(k_0 R) + \sqrt{\varepsilon_\infty} J_n(k_0 R) J_n'(k_\mathrm{T} R) - \sqrt{\varepsilon_\mathrm{T}} J_n'(k_0 R) J_n(k_\mathrm{T} R)}{c_n H_n(k_0 R) + \sqrt{\varepsilon_\infty} H_n(k_0 R) J_n'(k_\mathrm{T} R) - \sqrt{\varepsilon_\mathrm{T}} H_n'(k_0 R) J_n(k_\mathrm{T} R)},
\end{aligned} \tag{2.7.28}$$

where we stuck to previously defined notations of the ω_P and β. Here, $J(\cdot)$ and $H(\cdot)$ are the cylindrical Bessel and Hankel functions and $(\cdot)'$ their derivatives, respectively. We will exploit this analytical result for the validation of our 2D implementation in Section 5.2.3. Please note that for $\beta = 0$ the additional Mie coefficients c_n vanish and we recover the standard Mie solution for the local Drude model.

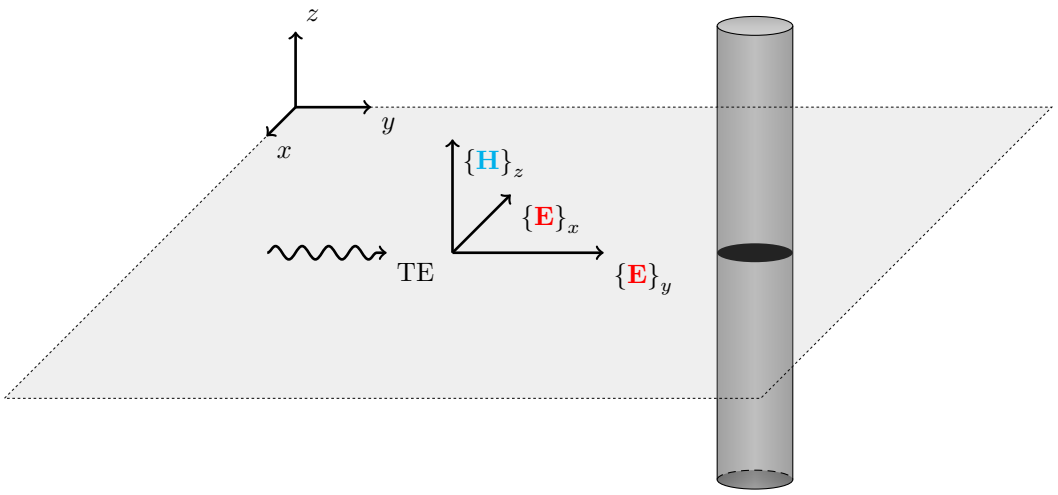

Figure 2.9 | Infinitely long dispersive rod. The rod is illuminated by an electric field that is polarized perpendicular to the cylinder axis. Due to the translational invariance in the y direction, the 3D geometry is reduced to a 2D problem.

2.7.5 Mie scattering of a dispersive sphere

Analogously to the 2D Mie solution in the previous section we now provide an analytical Mie solution in 3D. The following results are taken from [28]. We only summarize the main equations that are necessary

in order to implement the solution of CS_{ext}. All material and dispersion model related functions read

$$\begin{aligned} k_0 &= \frac{\omega}{c_0}, \\ \varepsilon_{\text{L}} &= \varepsilon_\infty - \frac{{\omega_{\text{P}}}^2}{\omega(\omega + i\gamma)}, \\ a_{\text{v}} &:= k_0 R\sqrt{\varepsilon_{\text{v}}}, \\ a_{\text{L}} &:= k_0 R\sqrt{\varepsilon_{\text{L}}}, \\ a_{\text{N}} &:= \frac{1}{\beta}\left(\omega(\omega + i\gamma) - \frac{{\omega_{\text{P}}}^2}{\varepsilon_\infty}\right). \end{aligned} \tag{2.7.29}$$

Here, ε_{v} is the permittivity of the surrounding material. Subsequently, the Mie coefficients are given by

$$\begin{aligned} t_n^{\text{M}} &:= \frac{a_{\text{v}}\mathrm{J}_n'(a_{\text{v}})\mathrm{J}_n(a_{\text{L}}) - \mathrm{J}_n(a_{\text{v}})a_{\text{L}}\mathrm{J}_n'(a_{\text{L}})}{\mathrm{H}_n(a_{\text{v}})a_{\text{L}}\mathrm{J}_n'(a_{\text{L}}) - a_{\text{v}}\mathrm{H}_n'(a_{\text{v}})\mathrm{J}_n(a_{\text{L}})}, \\ t_n^{\text{E}} &:= \frac{\varepsilon_{\text{L}}\left(\mathrm{J}_n(a_{\text{v}}) + a_{\text{v}}\mathrm{J}_n'(a_{\text{v}})\right)\mathrm{J}_n(a_{\text{L}}) - \mathrm{J}_n(a_{\text{v}})\left((\mathrm{J}_n(a_{\text{L}}) + a_{\text{L}}\mathrm{J}_n'(a_{\text{L}})) + t_n^{\text{N}}\right)}{-\varepsilon_{\text{L}}\left(\mathrm{H}_n(a_{\text{v}}) + a_{\text{v}}\mathrm{H}_n'(a_{\text{v}})\right)\mathrm{J}_n(a_{\text{L}}) + \mathrm{H}_n(a_{\text{v}})\left((\mathrm{H}_n(a_{\text{L}}) + a_{\text{L}}\mathrm{H}_n'(a_{\text{L}})) + t_n^{\text{N}}\right)}, \end{aligned} \tag{2.7.30}$$

where

$$t_n^{\text{N}} := \frac{n(n+1)\mathrm{J}_n(a_{\text{L}})\mathrm{J}_n(a_{\text{N}}R)}{a_{\text{N}}R\mathrm{J}_n(a_{\text{N}}R)}\left(\frac{\varepsilon_{\text{L}}}{\varepsilon_\infty} - 1\right). \tag{2.7.31}$$

In case of a $\beta \equiv 0$, the nonlocal contribution vanishes and $t_n^{\text{N}} = 0$ which gives the standard Mie coefficients [131]. Eventually, the extinction CS in a vacuum surrounded nonlocal nano-sphere reads

$$CS_{\text{ext}} = \frac{-2}{(k_0 R)^2}\sum_{n=1}^{\infty}(2n+1)\Re\left(t_n^{\text{M}} + t_n^{\text{E}}\right), \tag{2.7.32}$$

We will use the analytically calculated extinction cross section CS_{ext} in order to validate our 3D implementation of the system (2.6.4).

2.7.6 Electromagnetic field of a moving point charge in the free space

A second category of open space setups is the electromagnetic field generated by a moving point charge. We assume a constant velocity of the electron and hence no change in the moving direction. Liénard-Wiechert potentials allow for a field solution of more complicated trajectories including acceleration [68]. For our purposes a shortcut can be taken via the Lorentz transformation of an electrostatic field as we leave out acceleration. Applying (2.2.4) to the electrostatic field of a point charge yields

$$\mathbf{E}_{\text{elec}}(\mathbf{r}, t) = \frac{q\gamma}{4\pi\varepsilon_0}\frac{\mathbf{d}(\mathbf{r}, t)}{\left(|\mathbf{d}(\mathbf{r}, t)|^2 + \frac{\gamma^2 - 1}{|\mathbf{v}|^2}(\mathbf{v}\cdot\mathbf{d}(\mathbf{r}, t))^2\right)^{3/2}}. \tag{2.7.33}$$

Here, q is the particle's charge, $\mathbf{v}$ the velocity of the electron, $\mathbf{r}_{\text{elec}}(t) = (x_{\text{elec}}(t), y_{\text{elec}}(t), z_{\text{elec}}(t))^{\text{T}}$ the electron's position, $\mathbf{d}(\mathbf{r}, t) =: \mathbf{r}_{\text{elec}}(t) - \mathbf{r}$ the distance vector from $\mathbf{r}$ to the electron, and the relativistic

factor $\gamma = 1/\sqrt{1-(|v|/c_0)^2}$. The partial time derivative equally reads

$$\begin{aligned}\partial_t \mathbf{E}_{\text{elec}}(\mathbf{r},t) &= \frac{q\gamma}{4\pi\varepsilon_0}\frac{\mathbf{v}}{\left(|\mathbf{d}(\mathbf{r},t)|^2+\frac{\gamma^2-1}{|\mathbf{v}|^2}(\mathbf{v}\cdot\mathbf{d}(\mathbf{r},t))^2\right)^{3/2}} \\ &- \frac{3q\gamma}{4\pi\varepsilon_0}\frac{(\mathbf{v}\cdot\mathbf{d}(\mathbf{r},t))\gamma^2\mathbf{d}(\mathbf{r},t)}{\left(|\mathbf{d}(\mathbf{r},t)|^2+\frac{\gamma^2-1}{|\mathbf{v}|^2}(\mathbf{v}\cdot\mathbf{d}(\mathbf{r},t))^2\right)^{5/2}}.\end{aligned} \tag{2.7.34}$$

2.7.7 Electromagnetic field of a moving Gaussian charge distribution in the free space

Section 2.7.6 was concerned with the analytic solution of a moving point charge in free space. However, with regards to our essential intents that are the simulation of EELS or Cathodoluminescence (CL), we envisage penetrating beams, i.e. an electron that penetrates the material.

We would need, the incident field and its time derivative will have to be evaluated on the volume where the electron flies through. A sharp look at (2.7.33) and (2.7.34) shows a singularity for $\mathbf{r} = \mathbf{r}_{\text{elec}}$. Of course, this leads to accuracy issues at and close to the singularity due to the finite machine precision. For this reason, we propose to regularize the field with a Gaussian charge distribution. Proceeding in a similar fashion as in Section 2.7.6, we perform a Lorentz transformation of the electrostatic field.

We start the derivation with the electrostatic field generated by a Gaussian charge distribution which can be expressed by

$$\rho_{\text{gauss}}(\mathbf{r}) := \frac{q}{\sqrt{8\pi^3\sigma^6}}\exp\left[-\frac{|\mathbf{r}|^2}{2\sigma^2}\right], \tag{2.7.35}$$

centered at the coordinate origin and with q the total charge and σ the variance. If we now take Gauss' law from (2.3.2), we obtain

$$\begin{aligned}\int_{\partial\Omega}\mathbf{D}_{\text{gauss}}\cdot\mathbf{n}\ \mathrm{d}^2r &= \int_{\Omega}\rho_{\text{gauss}}\ \mathrm{d}^3r, \\ \mathbf{D}_{\text{gauss}}(\mathbf{r}) &= \frac{q\mathbf{e}_r}{4\pi|\mathbf{r}|^2\sqrt{8\pi^3\sigma^6}}\int_0^{2\pi}\int_0^{\pi}\int_0^{|\mathbf{r}|}\exp\left[-\frac{r^2}{2\sigma^2}\right]\ \mathrm{d}r\ \mathrm{d}\theta\ \mathrm{d}\phi, \\ &= \frac{q\mathbf{e}_r}{|\mathbf{r}|^2\sqrt{8\pi^3\sigma^6}}\left(\sqrt{\frac{\pi}{2}}\sigma^3\mathrm{erf}\left[\frac{|\mathbf{r}|}{\sqrt{2}\sigma}\right]-\sigma^2|\mathbf{r}|\exp\left[-\frac{|\mathbf{r}|^2}{2\sigma^2}\right]\right)\Bigg|_0^{|\mathbf{r}|}.\end{aligned} \tag{2.7.36}$$

Consequently, we obtain

$$\mathbf{E}_{\text{gauss}}(\mathbf{r}) = \frac{q\mathbf{e}_r}{\varepsilon_0|\mathbf{r}|^2\sqrt{8\pi^3\sigma^6}}\left(\sqrt{\frac{\pi}{2}}\sigma^3\mathrm{erf}\left[\frac{|\mathbf{r}|}{\sqrt{2}\sigma}\right]-\sigma^2|\mathbf{r}|\exp\left[-\frac{|\mathbf{r}|^2}{2\sigma^2}\right]\right). \tag{2.7.37}$$

Equation (2.7.37) now needs to be transformed to Cartesian coordinates in order to make it suitable for the later implementation in our DGTD framework. Performing a coordinate transformation leads to the

electric field

$$
\begin{aligned}
\{\mathbf{E}_{\text{gauss}}\}_x &= x\frac{q\left(-\frac{\sqrt{2}}{\sigma}\exp\left[-\frac{x^2+y^2+z^2}{2\sigma^2}\right]\sqrt{x^2+y^2+z^2}+\sqrt{\pi}\text{erf}\left[\frac{\sqrt{x^2+y^2+z^2}}{\sqrt{2}\sigma}\right]\right)}{4\pi^{3/2}\left(x^2+y^2+z^2\right)^{3/2}\varepsilon_0}\\
\{\mathbf{E}_{\text{gauss}}\}_y &= y\frac{q\left(-\frac{\sqrt{2}}{\sigma}\exp\left[-\frac{x^2+y^2+z^2}{2\sigma^2}\right]\sqrt{x^2+y^2+z^2}+\sqrt{\pi}\text{erf}\left[\frac{\sqrt{x^2+y^2+z^2}}{\sqrt{2}\sigma}\right]\right)}{4\pi^{3/2}\left(x^2+y^2+z^2\right)^{3/2}\varepsilon_0}\\
\{\mathbf{E}_{\text{gauss}}\}_z &= z\frac{q\left(-\frac{\sqrt{2}}{\sigma}\exp\left[-\frac{x^2+y^2+z^2}{2\sigma^2}\right]\sqrt{x^2+y^2+z^2}+\sqrt{\pi}\text{erf}\left[\frac{\sqrt{x^2+y^2+z^2}}{\sqrt{2}\sigma}\right]\right)}{4\pi^{3/2}\left(x^2+y^2+z^2\right)^{3/2}\varepsilon_0}
\end{aligned}
\tag{2.7.38}
$$

Here, the distribution is centered at the coordinate system's origin. Having a closer look to the electric field at $\{x, y, z\} = 0$ shows a finite field

$$
\lim_{\{x,y,z\}\to 0}|\mathbf{E}_{\text{gauss}}| = 0. \tag{2.7.39}
$$

However, (2.7.38) is numerically difficult to evaluate due to the singular denominators. Although analytically speaking the numerator dominates, (2.7.38) remains challenging in terms of floating point precision. We hence propose a linearization of (2.7.38) around $\{x, y, z\} = 0$ and a piecewise assembled reformulation of (2.7.38) by means of

$$
\mathbf{E}_{\text{gauss}}(x,y,z) = \begin{cases} \dfrac{q}{6\sqrt{2}\pi^{3/2}\varepsilon_0\sigma^3}\{x,y,z\}, & |\{x,y,z\}| \leq \dfrac{\sigma}{\mathrm{s}} \\ (2.7.38), & \text{otherwise} \end{cases}, \tag{2.7.40}
$$

where s denotes the splitting parameter which tunes the linearized sphere around $\{x, y, z\} = 0$. Figure 2.10 depicts (2.7.40) for four example values of σ.

Having the electrostatic field at hand, we can now perform a Lorentz transformation in order to obtain the field of a moving charge in the laboratory frame. w.l.o.g., we assume a trajectory in $\mathbf{e}_z$ direction $\mathbf{r}_{\text{gauss}}(t) := \mathbf{r}_0 + \mathbf{v}t$ with $\mathbf{v} = |\mathbf{v}|\mathbf{e}_z$. Applying the Lorentz transformation to (2.7.40) and rewriting the

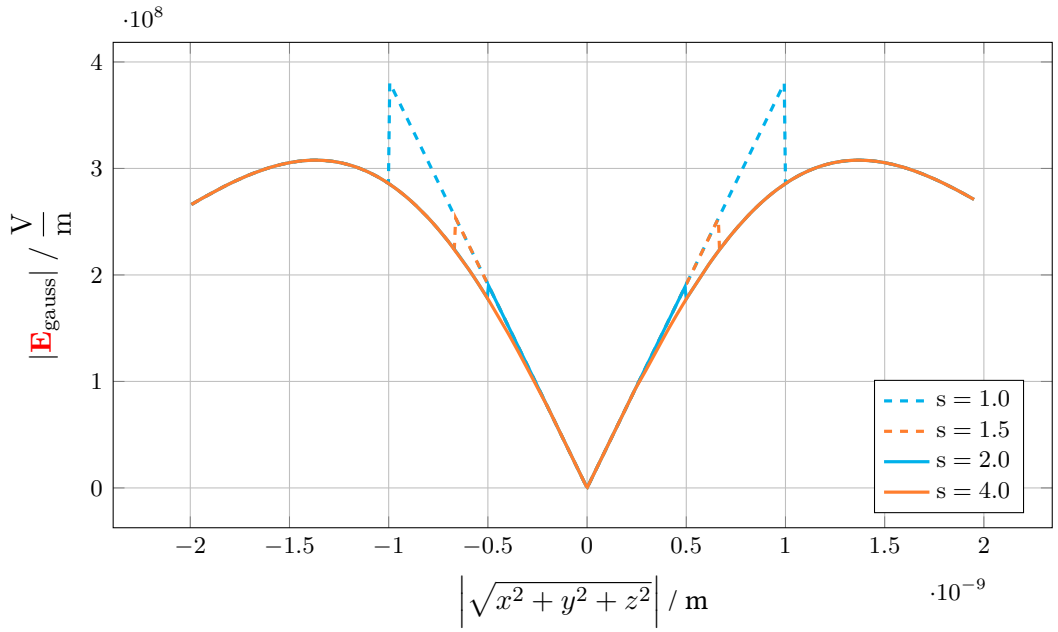

Figure 2.10 | Piece-wisely defined electric field of a Gaussian distributed charge. Here, $\sigma = 1$ nm and we plot the absolute value $|\mathbf{E}_{\text{gauss}}|$ for $\mathrm{s} = \{1, 1.5, 2, 4\}$. The transition between the linearized and the original region is almost invisible for $\mathrm{s} \geq 4$.

formula in laboratory frame coordinates reads

$$\begin{aligned} \{\mathbf{E}_{\text{gauss,lab}}\}_i &:= \{\mathbf{E}_{\text{gauss}}\}_i \left(x, y, \frac{z + t\,|\mathbf{v}|}{\sqrt{1 - \left(\frac{|\mathbf{v}|}{c_0}\right)^2}} \right), \qquad i = \{x, y\}, \\ \{\mathbf{E}_{\text{gauss,lab}}\}_z &:= \gamma\,\{\mathbf{E}_{\text{gauss}}\}_z \left(x, y, \frac{z + t\,|\mathbf{v}|}{\sqrt{1 - \left(\frac{|\mathbf{v}|}{c_0}\right)^2}} \right). \end{aligned} \tag{2.7.41}$$

If we additionally allow an arbitrary starting position $\mathbf{r}_e = \{x_e, y_e, z_e\}$ for the electron, (2.7.41) becomes

$$\tilde{\mathbf{E}}_{\text{gauss,lab}}\,(x, y, z) := \mathbf{E}_{\text{gauss,lab}}\,(x_e - x, y_e - y, z_e - z) \tag{2.7.42}$$

Inserting all quantities finally yields the explicit incident field which is ready to be implemented in our DGTD framework

$$\tilde{\mathbf{E}}_{\text{gauss,lab}}(x, y, z) = \begin{cases} a_2\{\Delta x, \Delta y, \Delta z\}, & |\{\Delta x, \Delta y, \gamma\Delta z\}| \leq \dfrac{\sigma}{\mathrm{s}} \\ a_3\{\Delta x, \Delta y, \Delta z\}, & \text{otherwise} \end{cases}, \tag{2.7.43}$$

with

$$
\begin{aligned}
\Delta x &= x_e - x, \\
\Delta y &= y_e - y, \\
\Delta z &= z_e - z + |\mathbf{v}|t, \\
\Delta r &= \Delta x^2 + \Delta y^2 + (\gamma \Delta z)^2, \\
a_1 &= -\frac{\sqrt{2\Delta r}}{\sigma} \exp\left[-\frac{\Delta r}{2\sigma^2}\right] + \sqrt{\pi}\mathrm{erf}\left[\sqrt{\frac{\Delta r}{2\sigma^2}}\right], \\
a_2 &= \frac{\gamma q}{6\sqrt{2}\pi^{3/2}\varepsilon_0 \sigma^3}, \\
a_3 &= \frac{a_1 \gamma q}{4\pi^{3/2}\Delta r^{3/2}\varepsilon_0}.
\end{aligned}
\tag{2.7.44}
$$

Figure 2.11 illustrates the Lorentz transformed fields in the vicinity of the center of mass of the charge

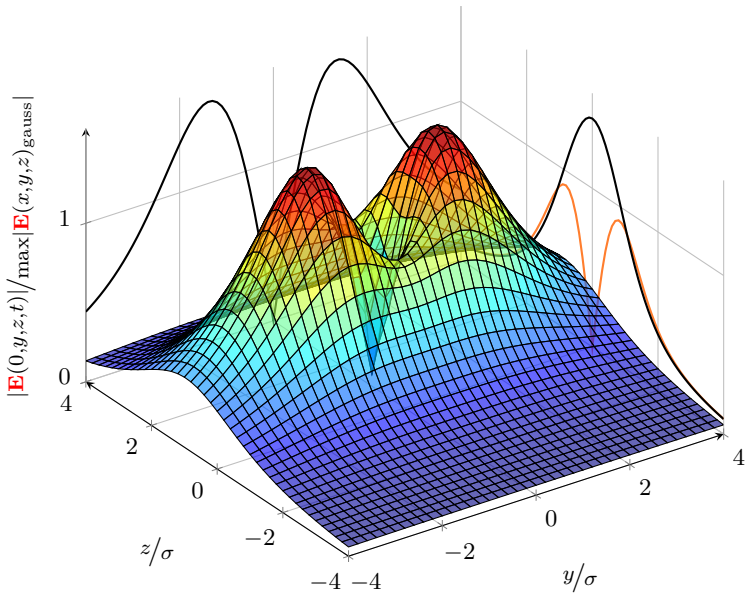

Figure 2.11 | Lorentz transformed field of Gaussian charge. Here, the velocity $|\mathbf{v}| = 0.8 \cdot c_0$, the splitting factor $\mathrm{s} = 4$, and the charge is moving in $\mathbf{e}_z$ direction.

distribution. The corresponding time derivative reads

$$
\partial_t \tilde{\mathbf{E}}_{\mathrm{gauss,lab}}(x,y,z) = \begin{cases} \{0, 0, \dfrac{|\mathbf{v}|\gamma q}{6\sqrt{2}\pi^{3/2}\varepsilon_0\sigma^3}\}, & |\{\Delta x, \Delta y, \gamma \Delta z\}| \leq \dfrac{\sigma}{\mathrm{s}} \\ \{\Delta x \Delta z a_4 a_5,\ \Delta y \Delta z a_4 a_5,\ a_4(\Delta z^2 a_5 + a_6)\}, & \text{otherwise} \end{cases},
\tag{2.7.45}
$$

with

$$\begin{aligned} a_4 &= -\frac{q\nu\gamma^3 \exp\left[-\dfrac{\Delta r}{2\sigma^2}\right]}{4\pi^{3/2}\Delta r^{5/2}\varepsilon_0\sigma^3}, \\ a_5 &= -\sqrt{2}\Delta r^{3/2} + 3a_1\sigma^3 \exp\left[\frac{\Delta r}{2\sigma^2}\right], \\ a_6 &= \frac{a_1\sigma^3}{\gamma^2}\Delta r \exp\left[\frac{\Delta r}{2\sigma^2}\right]. \end{aligned} \tag{2.7.46}$$

We now evaluate the relative error of the Gaussian electron with respect to a point charge. Defining the relative error by

$$\Delta\mathbf{E}_{\text{rel}}(\mathbf{r}) := \frac{\mathbf{E}_{\text{dirac}}(\mathbf{r}) - \mathbf{E}_{\text{gauss}}(\mathbf{r})}{\mathbf{E}_{\text{dirac}}(\mathbf{r})}, \tag{2.7.47}$$

and respectively plugging in (2.7.33) for $\mathbf{E}_{\text{dirac}}$ and (2.7.37) for $\mathbf{E}_{\text{gauss}}$ yields

$$\Delta\mathbf{E}_{\text{rel}}(\mathbf{r}) = \sqrt{\frac{2|\mathbf{r}|}{\pi\sigma^2}} \exp\left[-\frac{|\mathbf{r}|^2}{2\sigma^2}\right] + \operatorname{erf}\left[\frac{|\mathbf{r}|}{\sqrt{2}\sigma}\right]. \tag{2.7.48}$$

Evaluating the overall relative error by means of the $\boldsymbol{\mathcal{L}}^1(\Omega)$-norm reads

$$\begin{aligned} \Delta\mathbf{E}_{\text{rel}} &= \int_\Omega |\Delta\mathbf{E}_{\text{rel}}(\mathbf{r})| \, \mathrm{d}^3 r, \\ &= \sqrt{\frac{8}{\pi}}\sigma. \end{aligned} \tag{2.7.49}$$

This result shows a linear convergence for the Gaussian smeared-out electron.

3
Discrete physics

Apart from basic nanophotonic devices like rods, spheres or spherical dimers for which we have analytical solutions thanks to standard and advanced Mie theories, more complicated setups are highly difficult or even impossible to solve by hand. Numerical methods that allow for the solutions of PDEs, more precisely in the context of this work, of Maxwell's equations, have gained tremendous attention in the last fifty years. This development has mainly been driven by the extremely rapid improvement of computing capacities of modern machines.

For the full set of Maxwell's equations, i.e. without approximations of static type or quasi-static type, two complementary formulations are possible. They can either be (naturally) formulated in the time-domain or in the frequency-domain. The latter intrinsically assumes a time-harmonic dependency $\exp[-i\omega t]$ of the solution and the time derivatives transform to a multiplication with $-i\omega$. Frequency-domain methods are particularly useful for monochromatic simulations or if a fairly low amount of frequency samples is needed (one solver call per frequency). In the context of nanophotonics, Maxwell's equations in the frequency-domain are nowadays predominantly solved with RCWA [55, 83], FEM [104, 12] and BEM [63]. RCWA has originally been developed for periodic gratings and has now been extended to infinite structures including PMLs and coordinate stretching for metals [29]. Since the standard RCWA is a layer-wise method, it is not well suited for any non-Cartesian geometry. An additional limitation occurs if the periodicity of the structure becomes large with respect to the wavelength requiring a significant amount of modes that leads to large matrices. FEM and BEM can overcome this limitation. These methods are formulated on a volume (FEM) and on a surface (BEM) discretization, which is well suited for more general geometries. Among others, common domain tessellations are for example tetrahedra and triangles for FEM and BEM, respectively. Both methods are somewhat complementary. FEM is usually better suited for volume dominated problems with many geometrical details while BEM is preferable for large domains with a relatively small amount of surfaces. These qualitative geometrical arguments are based on the fact that FEM leads to larger but sparse matrices while the BEM matrices are dense and more difficult to solve.

Considering Maxwell's equations in the time-domain is usually favorable if one wants to simulate broad frequency bands, nonlinear effects or large computational domains. The latter may lead to prohibitive linear systems of the FEM discretization (this argument is only valid if one uses an explicit time integration scheme). Historically, Yee [166] proposed a FDTD scheme in 1966 and Weiland [157] the FIT

in 1977 for time-domain Maxwell's equations. Both methods rely on staggered Cartesian grids. These schemes and various extensions have become very popular especially because of their simplicity and non-dissipative nature. However, the efficiency of both methods is intrinsically limited due to the regular Yee grid that is not suitable for geometries that are non Cartesian. Cartesian Yee grids are subject to a staircasing effect that pollutes the solution. Additionally, the electromagnetic fields at material interfaces may in this case loose smoothness, which is difficult to handle with FDTD and FIT for example. This is a severe issue for nanophotonics where many effects are confined to the material interfaces.

Ideally, a numerical method would combine the broadband character of time-domain methods with the unstructured mesh flexibility and the high-order nature of FEM. A promising approach is the family of so called DGTD methods. Equally to FEM, DGTD methods rely on a weak formulation and work very well on unstructured meshes. However, instead of continuous basis functions, a discontinuous approximation space is used that decouples the neighbored mesh elements. Such an approach leads to discontinuities at the cell interfaces and hence to a global discontinuous solution. This is why that family of methods is commonly referred to as DG methods. Interestingly, the decoupling of the mesh elements changes the structure of the mass matrix, which now becomes block-diagonal. A block-diagonal mass matrix is easily invertible and hence provides a well-suited setting for explicit time integration schemes.

Beyond the spatial discretization, the selected time integration scheme plays an important role in the overall performance of the algorithm. FDTD methods usually employ a second order Leap-Frog (LF) scheme due to its simplicity and energy conservation property. In the FDTD case, a higher order time integration scheme would even not be advantageous since the overall convergence order is dictated by the minimum of the spatial and temporal order. Despite various efforts [41, 30, 114] that involve severe complications of the original algorithm, increased accuracy of FDTD on computational domains with discontinuous materials remains challenging. The situation changes for DGTD as high spatial convergence orders are now achievable. In this prospect, high-order order explicit RK methods are promising candidates, especially the family of Low Storage Runge-Kutta (LSRK) methods. In other words, DGTD combines the mesh flexibility and high-order nature of FEM with a possible explicit time integration scheme as for FDTD methods.

This chapter proposes a DGTD discretization of system (2.5.1). More precisely, we develop the spatial discretization, referred to as semi-discrete scheme, provide a semi-discrete stability result and conclude by sketching a convergence proof on quasi-uniform tetrahedral meshes. A brief reminder on more technical aspects concerning the assembly of the local matrices, the mapping from a reference element and the extension to curvilinear elements is conducted. After having discretized in space, we proceed with the discretization in time resulting in a fully-discrete scheme. Here, we rely on a second order LF scheme and RK-type methods. We provide stability results of the fully-discrete schemes for LF and RK time discretizations. Further, we sketch the convergence proof of the DG-RK version.

3.1 Discontinuous Galerkin method

The DG method was first proposed in the context of neutron transport problems by Reed and Hill [129] in 1973. In the following years, the method has become very popular and has been applied to a vast field of computational physics and engineering topics. A very popular example is the field of computational fluid dynamics where discontinuous formulations are well adapted to shocks. Although most publications on DG are journal papers, the books of Hesthaven and Warburton [58] as well as Di Pietro and Ern [33] give a comprehensive study of DG methods.

The starting point of the DG formulation is a local weak formulation of system (2.5.1). Spatial discretization with the DG method requires a special choice of FE spaces, i.e. special polynomial basis functions

on a given mesh. This choice clearly distinguishes DG methods from conforming FEM. While Nédélec based FEM uses basis function from conforming discretization spaces, DG relies on element-wise local basis functions. The use of local basis functions implies that the continuity of the fields is not enforced and discontinuities at the cell interfaces may arise. The treatment of those discontinuities provides an additional design parameter for the final algorithm. As we will see later, the discontinuities at the mesh element interfaces will be handled by a *numerical flux* (similar to FV methods). Further, the choice of this flux is not unique and will strongly influence numerical properties such as the numerical dissipation and dispersion as well as the existence of spurious solutions [14]. Different polynomial basis expansions are possible, but in this work, we concentrate on nodal Lagrange based basis functions on a triangular (2D) or a tetrahedral (3D) mesh. As mentioned earlier, the associated block-diagonal mass matrix allows an efficient explicit time integration. The introduced discontinuity in the approximation induces an increasing amount of discrete unknowns, which is an obvious drawback of the method. It can be overcome by exploiting the locality of the approach with a distributed memory parallel implementation strategy.

We now want to apply the DG method to system (2.6.4). To do so, we will first define an approximation space that leads to a local weak formulation and which is the reason for the discontinuous nature of the method. In order to re-establish a communication between the (local) cells, we require the definition of a numerical flux (also known as numerical trace) that provides a unique definition of the fields on the cell interfaces. Coupling the local formulations via the numerical flux eventually allows a global weak formulation. All notations are consistent with Chapter 2 and we refer to the previous chapter for definitions.

Remark 3.1.1. *We have decided to skip the full derivation of a DG scheme for system* (2.5.1) *for the sake of readability and restrict ourselves to Maxwell's equations coupled to the hydrodynamic equations, i.e.* (2.6.4)*. The interested reader is referred to [86] for the analysis of the generalized local dispersion model. An extension to the analysis of the full system* (2.5.1) *is straightforward due to linearity.*

3.1.1 Domain discretization and approximation space

The following derivations can be seen as an extension of the work in [86]. We have used the same notations as far as possible. This first part sets up the discrete version of the computational domain and the corresponding approximation space.

Tessellated domain Let us consider a polyhedral domain Ω that can be tessellated. The tessellation is defined by $\mathcal{T}_h = (\tau_i)_{i\in[\![0,N_{\mathcal{T}_h}]\!]}$ tetrahedra with $N_{\mathcal{T}_h} \in \mathbb{N}$ such that $\overline{\Omega}_h = \cup_{i\in[\![0,N_{\mathcal{T}_h}]\!]}\overline{\tau}_i \equiv \Omega$. A characteristic size parameter $h_i > 0$ with $i \in [\![0, N_{\mathcal{T}_h}]\!]$ is associated to each tessellated sub domain and we define a global mesh parameter $h = \max_{i\in[\![0,N_{\mathcal{T}_h}]\!]} h_i$. This characteristic size parameter h_i can be understood as the diameter of the tetrahedron τ_i.

We further define the overlap of two tetrahedra as an internal face $a_{i,k} := \tau_i \cup \tau_k$ for $i \neq k$. The corresponding outward-oriented normal vector of the triangle $a_{i,k}$ is denoted by $\mathbf{n}_{i,k}$ pointing from the element τ_i to its neighbor τ_k. The set of neighbors of element τ_i $\forall i \in [\![0, N_{\mathcal{T}_h}]\!]$ is cast into $\mathcal{V}_i$ (the indices of the neighboring tetrahedra). All inner faces between tetrahedra are gathered in $\mathcal{F}_{\text{int}}$ and the boundary faces $a_{i,\partial\Omega} := \overline{\tau}_i \cap \partial\Omega$ for all $i \in [\![0, N_{\mathcal{T}_h}]\!]$ are cast into $\mathcal{F}_{\partial\Omega}$.

The anisotropy of the mesh is limited by a quasi-uniformity assumption, i.e. there exists a positive and mesh-independent constant η such that for all h, for all $\tau_i \in \mathcal{T}_h$ and for all $k \in \mathcal{V}_i$; $h_i/h_k \leq \eta$ holds.

Approximation space We aim for an approximate solution $\boldsymbol{\vartheta}_h$ of the actual solution $\boldsymbol{\vartheta}$ on each finite element $\tau_i,\ i \in [\![0, N_{\mathcal{T}_h}]\!]$. Here, we rely on a polynomial ansatz and $\boldsymbol{\vartheta}_h$ are hence piecewise polynomials.

The polynomial degree of $\boldsymbol{\vartheta}_h$ may generally vary for different finite elements τ_i. Keeping this element-dependency in mind, for a given $i \in [\![0, N_{\mathcal{T}_h}]\!]$, we denote by $d_i > 0$ the number of DoFs per τ_i and by $\mathcal{P}_i$ the associated polynomial space. Let $(\varphi_{i,j})_{1 \leq j \leq d_i}$ be a set of linearly independent basis functions such that $\mathcal{P}_i := \mathrm{Span}\{\varphi_{i,j}, 1 \leq j \leq d_i\}$. The corresponding approximation space is finally defined by

$$\begin{aligned} \mathbb{V}_h &:= \left\{ \mathbf{W}_h \in \boldsymbol{\mathcal{L}}^2(\Omega), \mathbf{W}|_{\tau_i} \in (\mathcal{P}_i)^3, \forall\, \tau_i \in \mathcal{T}_h \right\}, \\ V_h &:= \left\{ W_h \in \mathcal{L}^2(\Omega), W|_{\tau_i} \in \mathcal{P}_i, \forall\, \tau_i \in \mathcal{T}_h \right\}. \end{aligned} \tag{3.1.1}$$

We additionally claim for $\mathbf{W}_h \in \mathbb{V}_h$ and $W_h \in V_h$ that

- $\mathbf{W}_i$ and W_i denote their restriction to the $\tau_i-\mathrm{th}$ element;
- Their average on an arbitrary face $a_{i,k} \in \mathcal{F}_{\mathrm{int}}$ is defined by

$$\begin{aligned} \{\mathbf{W}_h\}_{ik} &:= \mathbf{W}_i + \mathbf{W}_k, \\ \{W_h\}_{ik} &:= W_i + W_k \end{aligned} \tag{3.1.2}$$

- Their jump at a given face $a_{i,k} \in \mathcal{F}_{\mathrm{int}}$ is similarly defined as

$$\begin{aligned} [\![\mathbf{W}_h]\!]_{ik} &:= \mathbf{W}_i - \mathbf{W}_k, \\ [\![W_h]\!]_{ik} &:= W_i - W_k. \end{aligned} \tag{3.1.3}$$

In other words, we are searching for a polynomial representation $\boldsymbol{\vartheta}_h \in \mathbb{V}_h$ of $\boldsymbol{\vartheta}$, where

$$\mathbb{V}_h := \mathbb{V}_h^3 \times V_h, \tag{3.1.4}$$

being defined on the set of all sub domains and hence the total domain.

Remark 3.1.2. *Since our approximation space is completely element-wise, no continuity of the global solution $\boldsymbol{\vartheta}_h$ is guaranteed. The potential discontinuity at a cell interface has to be properly handled. This is commonly solved by considering a Riemann problem.*

3.1.2 Riemann problem at a cell interface

As previously mentioned, each cell has strictly local basis functions. Without an additional treatment, each individual cell is isolated from each other. The global solution is consequently discontinuous on the cell interfaces (see Figure 3.1 (a) and (b)) and a unique definition of the field values on the face $\overline{\tau}_- \cap \overline{\tau}_+$ is lacking. In order to overcome this dilemma, a numerical flux is used, which weakly reinforces the tangential continuity of the solution. Finding the appropriate numerical flux is subject to solving a local Riemann problem at each cell interface. The driving idea is outlined in Figure 3.1. Each cell interface is subject to a discontinuity coming from the element-wise definition of our approximation space. Keeping only the leading term of the generalized Riemann problem (see Figure 3.1 (b) and (c)) leads to a standard Riemann problem with a constant solution on each side. Such a problem can be solved with the methods of characteristics (see Figure 3.1 (d)). Means and jumps at the cell interface between element τ_- and its neighbor τ_+ are defined by

$$\{\mathbf{A}\}_{-+} := \mathbf{A}^- + \mathbf{A}^+, \; [\![\mathbf{A}]\!]_{-+} := \mathbf{A}^- - \mathbf{A}^+, \tag{3.1.5}$$

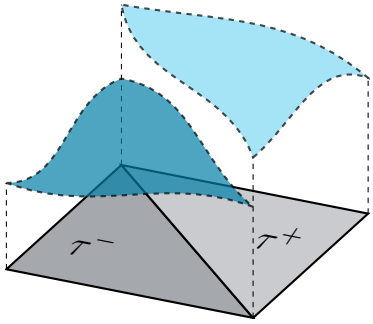

(a) Field discontinuity at the interface of two mesh cells.

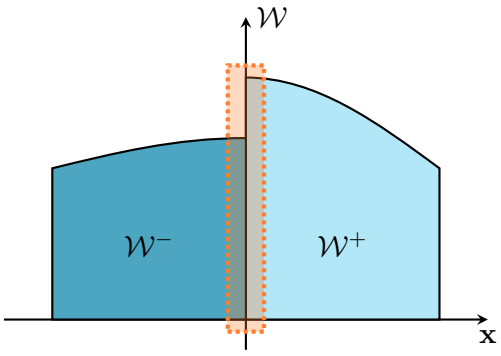

(b) Generalized Riemann problem at a cell interface.

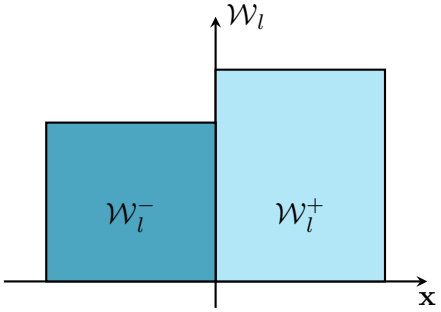

(c) Leading Riemann problem at the cell interface.

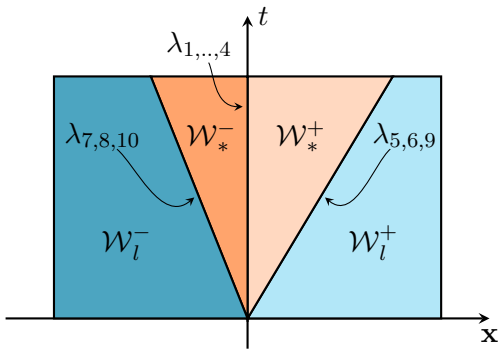

(d) Solution of the leading term Riemann problem.

Figure 3.1 | Riemann problem. Figure (a) illustrates a field discontinuity at the interface of two mesh cells. Generally, this is subject to a generalized Riemann problem as shown in (b). Considering only the leading term within the vicinity of the interface (orange region), simplifies the generalized Riemann problem to a standard Riemann problem with a piecewise constant solution (c). Its solution in the $(\mathbf{x} - t)$ space is shown in (d). With kind permission from [153].

analogously to (3.1.2) and (3.1.3). Here, $\mathbf{A}_{-,+}$ can be an operator, a field $\mathbf{E}$, $\mathbf{H}$, $\mathbf{J}$, Q or physical parameters like Z (impedance), Y (admittance) and β on the left (-) and right (+) side of the cell interface, respectively. Since this is very classical, we skip the details of the derivation of the numerical flux for Maxwell's equations and refer to the literature [58, 14, 153] for details. Let us directly recall the general upwind flux for the $\mathbf{E}$ and $\mathbf{H}$ fields [135]

$$\begin{aligned} \mathbf{n} \times \mathbf{H}_*^- &= \frac{1}{Z^- + Z^+} \left(\mathbf{n} \times \{Z\mathbf{H}\}_{-+} - \alpha \mathbf{n} \times (\mathbf{n} \times [\![\mathbf{E}]\!]_{-+}) \right), \\ \mathbf{n} \times \mathbf{E}_*^- &= \frac{1}{Y^- + Y^+} \left(\mathbf{n} \times \{Y\mathbf{E}\}_{-+} + \alpha \mathbf{n} \times (\mathbf{n} \times [\![\mathbf{H}]\!]_{-+}) \right), \end{aligned} \tag{3.1.6}$$

where $\mathbf{n}_{-+} = -\mathbf{n}_{+-}$. The scalar $\alpha \in [0, 1]$ weights the upwinding. The case $\alpha = 0$ is called centered flux and in the case $\alpha = 1$ the scheme is fully upwind. Regarding the hydrodynamic part $\mathbf{J}$ and Q, centered fluxes have already been considered in [134], and we now propose to derive the formulation of the upwind fluxes. Let us ignore the coupling to Maxwell's equations, neglect the damping term in (2.4.13), and focus

on the hydrodynamic equations

$$\begin{aligned} \partial_t \mathbf{J} &= \beta^2 \nabla Q, \\ \beta^2 \partial_t Q &= \beta^2 \nabla \cdot \mathbf{J}. \end{aligned} \tag{3.1.7}$$

Proposition 3.1.1. *The upwind flux for* (3.1.7) *is given by*

Numerical flux

$$\begin{aligned} (\beta^-)^2 Q_\star^- &= \frac{\beta^-\beta^+}{\beta^- + \beta^+} \left(\{\beta Q\}_{-+} - \alpha \left(\mathbf{n} \cdot [\![\mathbf{J}]\!]_{-+} \right) \right), \\ (\beta^-)^2 \mathbf{n} \cdot \mathbf{J}_\star^- &= \frac{(\beta^-)^3 (\beta^+)^3}{(\beta^-)^3 + (\beta^+)^3} \left(\mathbf{n} \cdot \left\{ \frac{\mathbf{J}}{\beta} \right\}_{-+} - \alpha [\![Q]\!]_{-+} \right), \end{aligned} \tag{3.1.8}$$

and on the boundary of the nonlocal dispersive domain

$$\begin{aligned} Q_\star^- |_{\partial\Omega_{\mathrm{NL}}} &= Q^-, \\ \mathbf{n} \cdot \mathbf{J}_\star^- |_{\partial\Omega_{\mathrm{NL}}} &= 0. \end{aligned} \tag{3.1.9}$$

Proof. Casting (3.1.7) into a conservative form leads to:

$$\boldsymbol{\mathcal{Q}} \partial_t \mathcal{W} + \nabla \cdot \mathcal{F}(\mathcal{W}) = 0, \tag{3.1.10}$$

with

$$\begin{aligned} \mathcal{W} &= \begin{bmatrix} \{\mathbf{J}\}_x \\ \{\mathbf{J}\}_y \\ \{\mathbf{J}\}_z \\ Q \end{bmatrix}, \qquad \boldsymbol{\mathcal{Q}} = \begin{bmatrix} 1 & 0 & 0 & 0 \\ 0 & 1 & 0 & 0 \\ 0 & 0 & 1 & 0 \\ 0 & 0 & 0 & \beta^2 \end{bmatrix}, \\ \mathcal{F}_x &= \begin{bmatrix} -\beta^2 Q \\ 0 \\ 0 \\ -\beta^2 \{\mathbf{J}\}_x \end{bmatrix}, \quad \mathcal{F}_y = \begin{bmatrix} 0 \\ -\beta^2 Q \\ 0 \\ -\beta^2 \{\mathbf{J}\}_y \end{bmatrix}, \quad \mathcal{F}_z = \begin{bmatrix} 0 \\ 0 \\ -\beta^2 Q \\ -\beta^2 \{\mathbf{J}\}_z \end{bmatrix}. \end{aligned} \tag{3.1.11}$$

The Rankine-Hugoniot jump conditions read

$$\begin{aligned} \beta^- \boldsymbol{\mathcal{Q}}^- (\mathcal{W}_\star^- - \mathcal{W}^-) + \mathbf{n}_{-+} \cdot (\mathcal{F}_\star^- - \mathcal{F}^-) &= 0, \\ \mathbf{n}_{-+} \cdot (\mathcal{F}_\star^- - \mathcal{F}_\star^+) &= 0, \\ -\beta^+ \boldsymbol{\mathcal{Q}}^+ (\mathcal{W}_\star^+ - \mathcal{W}^+) + \mathbf{n}_{-+} \cdot (\mathcal{F}_\star^+ - \mathcal{F}^+) &= 0. \end{aligned} \tag{3.1.12}$$

Here, we have used the eigenvalues that correspond to the hydrodynamic part (see section 2.6.4). For the sake of simplicity, we omit the direction of $\mathbf{n}_{-+}$ and fix the normal vector to point from "-" to "+", i.e. $\mathbf{n} := \mathbf{n}_{-+}$. Subtracting the second from the first equation and summing up the second and third equation of (3.1.12) gives

$$\begin{aligned} \beta^- \boldsymbol{\mathcal{Q}}^- (\mathcal{W}_\star^- - \mathcal{W}^-) + \mathbf{n} \cdot (\mathcal{F}_\star^+ - \mathcal{F}^-) &= 0, \\ -\beta^+ \boldsymbol{\mathcal{Q}}^+ (\mathcal{W}_\star^+ - \mathcal{W}^+) + \mathbf{n} \cdot (\mathcal{F}_\star^- - \mathcal{F}^+) &= 0, \end{aligned} \tag{3.1.13}$$

respectively multiplying with $\beta^+\boldsymbol{\mathcal{Q}}^+$ and $\beta^-\boldsymbol{\mathcal{Q}}^-$ (that are commuting) and summing yields

$$\begin{aligned}\beta^-\beta^+\boldsymbol{\mathcal{Q}}^-\boldsymbol{\mathcal{Q}}^+\left(\mathcal{W}_\star^- - \mathcal{W}^- - \mathcal{W}_\star^+ + \mathcal{W}^+\right)\\ +\left(\beta^-\boldsymbol{\mathcal{Q}}^- + \beta^+\boldsymbol{\mathcal{Q}}^+\right)\mathbf{n}\cdot\mathcal{F}_\star^-\\ -\beta^-\boldsymbol{\mathcal{Q}}^-\mathbf{n}\cdot\mathcal{F}^+ - \beta^+\boldsymbol{\mathcal{Q}}^+\mathbf{n}\cdot\mathcal{F}^- &= 0.\end{aligned} \tag{3.1.14}$$

The normal flux is given by

$$\mathbf{n}\cdot\mathcal{F} = \begin{bmatrix}-\beta^2\mathbf{n}Q\\ -\beta^2\mathbf{n}\cdot\mathbf{J}\end{bmatrix}. \tag{3.1.15}$$

Inserting the flux gives for the $\mathbf{J}$ part

$$\begin{aligned}\beta^-\beta^+\left(\mathbf{J}_\star^- - \mathbf{J}^- - \mathbf{J}_\star^+ + \mathbf{J}^+\right)\\ +\left(\beta^+ + \beta^-\right)\mathbf{n}\left(-\left(\beta^-\right)^2 Q_\star^-\right)\\ +\beta^+\left(\beta^-\right)^2\mathbf{n}Q^- + \beta^-\left(\beta^+\right)^2\mathbf{n}Q^+ &= 0.\end{aligned} \tag{3.1.16}$$

Performing the cross product with $\mathbf{n}$ and together with (3.1.12) yields

$$\begin{aligned}\mathbf{n}\times\left(\mathbf{J}_\star^- - \mathbf{J}_\star^+\right) &= \mathbf{n}\times\left(\mathbf{J}^- - \mathbf{J}^+\right),\\ \mathbf{n}\cdot\left(\mathbf{J}_\star^- - \mathbf{J}_\star^+\right) &= 0.\end{aligned} \tag{3.1.17}$$

The vector identity $\mathbf{A} = (\mathbf{n}\cdot\mathbf{A})\mathbf{n} - \mathbf{n}\times(\mathbf{n}\times\mathbf{A})$ applied to $\mathbf{A} = \mathbf{J}_\star^- - \mathbf{J}_\star^+$ reads

$$\begin{aligned}\mathbf{J}_\star^- - \mathbf{J}_\star^+ &= \underbrace{\left(\mathbf{n}\cdot\left(\mathbf{J}_\star^- - \mathbf{J}_\star^+\right)\right)}_{=0}\mathbf{n} - \mathbf{n}\times\left(\mathbf{n}\times\left(\mathbf{J}_\star^- - \mathbf{J}_\star^+\right)\right),\\ \mathbf{J}_\star^- - \mathbf{J}_\star^+ &= -\mathbf{n}\times\left(\mathbf{n}\times\left(\mathbf{J}_\star^- - \mathbf{J}_\star^+\right)\right).\end{aligned} \tag{3.1.18}$$

and similarly for $\mathbf{A} = \mathbf{J}^- - \mathbf{J}^+$

$$\begin{aligned}\mathbf{J}^- - \mathbf{J}^+ &= \left(\mathbf{n}\cdot\left(\mathbf{J}^- - \mathbf{J}^+\right)\right)\mathbf{n} - \mathbf{n}\times\left(\mathbf{n}\times\left(\mathbf{J}^- - \mathbf{J}^+\right)\right),\\ \mathbf{J}_\star^- - \mathbf{J}_\star^+ &= \mathbf{J}^- - \mathbf{J}^+ - \left(\mathbf{n}\cdot\left(\mathbf{J}^- - \mathbf{J}^+\right)\right)\mathbf{n}.\end{aligned} \tag{3.1.19}$$

Plugging (3.1.19) into (3.1.16) leads to

$$\begin{aligned}\left(\beta^-\right)^2\mathbf{n}Q_\star^- &= \frac{\beta^-\beta^+}{\beta^- + \beta^+}\left(\mathbf{n}\left(Q^-\beta^- + Q^+\beta^+\right) - \mathbf{n}\left(\mathbf{n}\cdot\left(\mathbf{J}^- - \mathbf{J}^+\right)\right)\right),\\ \left(\beta^-\right)^2\mathbf{n}Q_\star^- &= \frac{\beta^-\beta^+}{\beta^- + \beta^+}\left(\mathbf{n}\{\beta Q\}_{-+} - \mathbf{n}\left(\mathbf{n}\cdot[\![\mathbf{J}]\!]_{-+}\right)\right).\end{aligned} \tag{3.1.20}$$

Similar steps for the Q part give

$$\begin{aligned}\beta^-\beta^+\left(\beta^-\right)^2\left(\beta^+\right)^2\left(Q_\star^- - Q^- - Q_\star^+ + Q^+\right)\\ -\left(\left(\beta^-\right)^3 + \left(\beta^+\right)^3\right)\left(\left(\beta^-\right)^2\mathbf{n}\cdot\mathbf{J}_\star^-\right)\\ +\beta^-\left(\beta^-\right)^2\left(\mathbf{n}\cdot\mathbf{J}^+\left(\beta^+\right)^2\right) + \beta^+\left(\beta^+\right)^2\left(\mathbf{n}\cdot\mathbf{J}^-\left(\beta^-\right)^2\right) &= 0.\end{aligned} \tag{3.1.21}$$

Using (3.1.20) simplifies (3.1.21) to

$$(\beta^-)^2\,\mathbf{n}\cdot\mathbf{J}_\star^+ \;=\; \frac{(\beta^-)^3\,(\beta^+)^3}{(\beta^-)^3+(\beta^+)^3}\left(\mathbf{n}\cdot\left\{\frac{\mathbf{J}}{\beta}\right\}_{-+}-[\![Q]\!]_{-+}\right). \tag{3.1.22}$$

If we now allow the contribution of the jump value $[\![\cdot]\!]$ to be tunable by a real tuning parameter $\alpha\in[0,1]$ we obtain (3.1.8). □

The eventual choice of α heavily influences the numerical properties of the final discretized version of (2.5.1). Properties like numerical dissipation and the occurrence of spurious solutions are particularly sensitive to the fluxes as we will see later for the numerical results.

3.1.3 Weak form

Towards the discretization of space, we now derive a weak form. We will use the above defined element-wise polynomial approximation space to define a local weak form on each element τ_i for all $i\in[\![0,N_{\mathcal{T}_h}]\!]$. A global form will be constructed from the local form afterwards.

Definitions For the sake of readability, we define

- An element-wise $\boldsymbol{\mathcal{L}}^2$-scalar product for all $i\in[\![0,N_{\mathcal{T}_h}]\!]$ $\langle\cdot,\cdot\rangle_{\tau_i}$;
- Its global counterpart $\langle\cdot,\cdot\rangle_h := \sum_{i\in[\![0,N_{\mathcal{T}_h}]\!]}\langle\cdot,\cdot\rangle_{\tau_i}$;
- And the $\boldsymbol{\mathcal{L}}^2$-scalar product on a face F, $\langle\cdot,\cdot\rangle_F$, together with the global version on all internal faces $\langle\cdot,\cdot\rangle_{\mathcal{F}_h^{\text{int}}} := \sum_{F\in\mathcal{F}_h^{\text{int}}}\langle\cdot,\cdot\rangle_F$;
- And finally the $\boldsymbol{\mathcal{L}}^2$-scalar product $\langle\cdot,\cdot\rangle_{\partial\tau_i}$ on the boundary of τ_i, which is equal to $\sum_{k\in\mathcal{V}_i}\langle\cdot,\cdot\rangle_{a_{ik}}$.

Further, for all $\boldsymbol{\vartheta}\in\boldsymbol{\mathcal{L}}^2(\Omega)^{10}$, we write $\boldsymbol{\vartheta}=\begin{pmatrix}\boldsymbol{\vartheta}_1 & \boldsymbol{\vartheta}_2 & \boldsymbol{\vartheta}_3 & \vartheta_4\end{pmatrix}^T\in\boldsymbol{\mathcal{L}}^2(\Omega)\times\boldsymbol{\mathcal{L}}^2(\Omega)\times\boldsymbol{\mathcal{L}}^2(\Omega)\times\mathcal{L}^2(\Omega)$. For the sake of readability, we temporarily redefine the normal vector $\mathbf{n}_{ik}$ for each cell τ_i with $i\in[\![0,N_{\mathcal{T}_h}]\!]$ and for all neighbors $k\in\mathcal{V}_i$ as $\mathbf{n}:=\mathbf{n}_i$.

Element-wise weak form In the same fashion as for Maxwell's equations without the supplementary hydrodynamic model, we now develop an element-wise weak form of (2.6.4). First, we multiply (2.6.4) with a test function $\boldsymbol{\vartheta}'\in\mathbb{V}_h$ and perform the $\boldsymbol{\mathcal{L}}^2$-scalar product on a sub domain τ_i. This procedure includes an integration by parts, which leads to an ambiguity in our discontinuous framework on the boundary $\partial\tau_i$. The field values on the element boundary, commonly referred to as numerical flux, will be recovered by the solution of the Riemann problem. Simultaneously, the numerical fluxes are the communication channel of two neighboring elements. The local problem is formulated as: find $\boldsymbol{\vartheta}_h\in\mathcal{C}^1(0,T,\mathbb{V}_h)$ such that for all $i\in[\![0,N_{\mathcal{T}_h}]\!]$ for all $\boldsymbol{\vartheta}_h'\in\mathbb{V}_h$

Local weak form

$$\langle\boldsymbol{\Lambda}\partial_t\boldsymbol{\vartheta}_h,\boldsymbol{\vartheta}'\rangle_{\tau_i} \;=\; \langle\boldsymbol{\vartheta}_h,\boldsymbol{\mathcal{L}}_i^\star(\boldsymbol{\vartheta}')\rangle_{\tau_i}-\langle\boldsymbol{\mathcal{F}}_{i,h}^\alpha(\boldsymbol{\vartheta}_h),\boldsymbol{\vartheta}_h'\rangle_{\partial\tau_i}+\langle\boldsymbol{\mathcal{K}}(\boldsymbol{\vartheta}_h),\boldsymbol{\vartheta}_h'\rangle_{\tau_i}, \tag{3.1.23}$$

on $[0,T]$. Here, integration by parts splits the differential operators into their volumic and surfacic part, i.e.

$$\begin{aligned}
\langle \boldsymbol{\Lambda}\partial_t \boldsymbol{\vartheta}_h, \boldsymbol{\vartheta}'_h\rangle_{\tau_i} = \quad & -{\varepsilon_0\omega_{\mathrm{P}}}^2 \quad \left(\left\langle \{\boldsymbol{\vartheta}_h\}_2, \nabla\times\{\boldsymbol{\vartheta}'_h\}_1\right\rangle_{\tau_i} + \left\langle \mathbf{n}_i\times\boldsymbol{\vartheta}^\star_2, \{\boldsymbol{\vartheta}_h\}'_1\right\rangle_{\partial\tau_i}\right)\\
& +{\varepsilon_0\omega_{\mathrm{P}}}^2 \quad \left(\left\langle \{\boldsymbol{\vartheta}_h\}_1, \nabla\times\{\boldsymbol{\vartheta}'_h\}_2\right\rangle_{\tau_i} + \left\langle \mathbf{n}_i\times\boldsymbol{\vartheta}^\star_1, \{\boldsymbol{\vartheta}_h\}'_2\right\rangle_{\partial\tau_i}\right)\\
& +\beta^2 \quad \left(-\left\langle \{\boldsymbol{\vartheta}_h\}_4\nabla, \{\boldsymbol{\vartheta}'_h\}_3\right\rangle_{\tau_i} + \left\langle \mathbf{n}_i\boldsymbol{\vartheta}^\star_4, \{\boldsymbol{\vartheta}_h\}'_3\right\rangle_{\partial\tau_i}\right)\\
& +\beta^2 \quad \left(-\left\langle \{\boldsymbol{\vartheta}_h\}_3, \nabla\{\boldsymbol{\vartheta}'_h\}_4\right\rangle_{\tau_i} + \left\langle \{\boldsymbol{\vartheta}_h\}'_4\mathbf{n}_i, \boldsymbol{\vartheta}^\star_3\right\rangle_{\partial\tau_i}\right)\\
& + \quad \left(-\gamma\left\langle \{\boldsymbol{\vartheta}_h\}_3, \{\boldsymbol{\vartheta}_h\}'_3\right\rangle_{\tau_i} + {\varepsilon_0\omega_{\mathrm{P}}}^2\left\langle \{\boldsymbol{\vartheta}_h\}_2, \{\boldsymbol{\vartheta}_h\}'_3\right\rangle_{\tau_i}\right).
\end{aligned} \tag{3.1.24}$$

The local volumic operator in (3.1.23) is defined by

$$\boldsymbol{\mathcal{L}}^\star_i(\boldsymbol{\vartheta}') = \begin{bmatrix} {\varepsilon_0\omega_{\mathrm{P}}}^2\nabla\times\boldsymbol{\vartheta}_2|_{\tau_i} \\ -{\varepsilon_0\omega_{\mathrm{P}}}^2\nabla\times\boldsymbol{\vartheta}_1|_{\tau_i} \\ -\beta^2\nabla\boldsymbol{\vartheta}_4|_{\tau_i} \\ -\beta^2\nabla\cdot\boldsymbol{\vartheta}_3|_{\tau_i} \end{bmatrix}, \tag{3.1.25}$$

and the local surfacic trace operator reads

$$\begin{aligned}
\boldsymbol{\mathcal{F}}^\alpha_{i,h}(\boldsymbol{\vartheta}_h)|_{\partial\tau_i} &= \begin{bmatrix} {\varepsilon_0\omega_{\mathrm{P}}}^2\mathbf{n}_i\times\boldsymbol{\vartheta}^*_2|_{\tau_i} \\ -{\varepsilon_0\omega_{\mathrm{P}}}^2\mathbf{n}_i\times\boldsymbol{\vartheta}^*_1|_{\tau_i} \\ -\beta^2\mathbf{n}_i\boldsymbol{\vartheta}^*_4|_{\tau_i} \\ -\beta^2\mathbf{n}_i\cdot\boldsymbol{\vartheta}^*_3|_{\tau_i} \end{bmatrix},\\
&= \begin{bmatrix} \mathbf{n}_i\times\left(\dfrac{{\varepsilon_0\omega_{\mathrm{P}}}^2}{Y^-+Y^+}\left(\{Y\boldsymbol{\vartheta}_2\}_{-+} - \alpha\left(\mathbf{n}_i\times[\![\boldsymbol{\vartheta}_1]\!]_{-+}\right)\right)\right) \\ \mathbf{n}_i\times\left(\dfrac{{\varepsilon_0\omega_{\mathrm{P}}}^2}{Z^-+Z^+}\left(-\{Y\boldsymbol{\vartheta}_1\}_{-+} - \alpha\left(\mathbf{n}_i\times[\![\boldsymbol{\vartheta}_2]\!]_{-+}\right)\right)\right) \\ \left(\dfrac{\beta^-\beta^+}{\beta^-+\beta^+}\left(-\mathbf{n}_i\{\beta\boldsymbol{\vartheta}_4\}_{-+} + \alpha\mathbf{n}_i\left(\mathbf{n}_i\times[\![\boldsymbol{\vartheta}_3]\!]_{-+}\right)\right)\right) \\ \left(\dfrac{(\beta^-)^3(\beta^+)^3}{(\beta^-)^3+(\beta^+)^3}\left(-\mathbf{n}_i\cdot\left\{\dfrac{\boldsymbol{\vartheta}_3}{\beta}\right\}_{-+} + \alpha[\![\boldsymbol{\vartheta}_4]\!]_{-+}\right)\right) \end{bmatrix}.
\end{aligned} \tag{3.1.26}$$

Here, we have used the flux definitions in (3.1.6) and (3.1.8) for the numerical trace, seen from element τ_i, i.e. the "-" is equivalent to i and "+" represents the neighboring elements k for all $k\in\mathcal{V}_i$ if $a_{ik}\in\mathcal{F}_{\mathrm{int}}$. The upwind parameter $\alpha\in[0,1]$ remains variable and tunes the flux formulation from centered fluxes for $\alpha=0$ to fully upwind fluxes $\alpha=1$. We want to emphasize that we keep an element-dependent material definition β^i, Y^i and Z^i. As commonly known, heterogeneous materials (different materials in each cell τ_i) do not cause any problems for a DGTD discretization of Maxwell's equations with local dispersion laws. However, coupling the Maxwell system with the linearized fluid model reveals a constraint on the material parameter β. From a numerical analysis point of view, we cannot prove stability for the linearized hydrodynamic fluid model if $\beta^-\neq\beta^+$ as we will see later.

Remark 3.1.3. *A constant value for β is somewhat physically intuitive. One of our initial physical assumptions was a constant background electron density. Allowing two different values of β at a material interface can be seen as a varying electron density and hence a violation of the initial assumption. In other words, different values for β (in the context of the here studied model) are only valid if the nonlocal dispersive domains are separated and do not share any interfaces.*

Global weak form Aiming for a global weak formulation, which we express with bilinear forms, we need global operators. In this sense, we define a global weak volumic operator

$$\boldsymbol{\mathcal{L}}_h(\boldsymbol{\vartheta}) \;=\; -\boldsymbol{\mathcal{L}}_h^*(\boldsymbol{\vartheta}) = \begin{bmatrix} -\varepsilon_0 {\omega_\mathrm{P}}^2 \nabla_h \times \{\boldsymbol{\vartheta}\}_2 \\ \varepsilon_0 {\omega_\mathrm{P}}^2 \nabla_h \times \{\boldsymbol{\vartheta}\}_1 \\ \beta^2 \nabla_h \{\boldsymbol{\vartheta}\}_4 \\ \beta^2 \nabla_h \cdot \{\boldsymbol{\vartheta}\}_3 \end{bmatrix}, \tag{3.1.27}$$

for all $\boldsymbol{\vartheta} \in \mathbb{V}_h$, with the piecewise operators $(\nabla_h\,)$ on each sub domain τ_i for $i \in [\![0, N_{\tau_i}]\!]$. In other words for all $\mathbf{p}_h \in \mathbf{V}_h$ and for all $q_h \in V_h$

$$\begin{aligned} (\nabla_h \times \mathbf{p}_h)|_{\tau_i} &= \nabla \times (\mathbf{p}_h|_{\tau_i})\,, \\ (\nabla_h \cdot \mathbf{p}_h)|_{\tau_i} &= \nabla \cdot (\mathbf{p}_h|_{\tau_i})\,, \\ (\nabla_h q_h)|_{\tau_i} &= \nabla\,(q_h|_{\tau_i})\,. \end{aligned} \tag{3.1.28}$$

Casting the global form into the bilinear forms m, a, b_α and k, which are defined on $\mathbb{V}_h \times \mathbb{V}_h$, yields for all $(\boldsymbol{\vartheta}, \boldsymbol{\vartheta}') \in \mathbb{V}_h \times \mathbb{V}_h$

$$\begin{aligned} m(\boldsymbol{\vartheta}, \boldsymbol{\vartheta}') &= \langle \boldsymbol{\vartheta}, \boldsymbol{\vartheta}' \rangle_{\boldsymbol{\Lambda}}, \\ a(\boldsymbol{\vartheta}, \boldsymbol{\vartheta}') &= \langle \boldsymbol{\vartheta}, \boldsymbol{\mathcal{L}}_h^*(\boldsymbol{\vartheta}') \rangle_h, \\ b_\alpha(\boldsymbol{\vartheta}, \boldsymbol{\vartheta}') &= \varepsilon_0 {\omega_\mathrm{P}}^2 \left(-\left\langle \frac{\{Y \boldsymbol{\vartheta}_2\}}{\{Y\}}, [\![\boldsymbol{\vartheta}_1']\!] \times \mathbf{n} \right\rangle_{\mathcal{F}_h^{\mathrm{int}}} - \alpha \left\langle \frac{[\![\boldsymbol{\vartheta}_1]\!] \times \mathbf{n}}{\{Y\}}, [\![\boldsymbol{\vartheta}_1']\!] \times \mathbf{n} \right\rangle_{\mathcal{F}_h^{\mathrm{int}}} \right) \\ &\quad \varepsilon_0 {\omega_\mathrm{P}}^2 \left(+\left\langle \frac{\{Z \boldsymbol{\vartheta}_1\}}{\{Z\}}, [\![\boldsymbol{\vartheta}_2']\!] \times \mathbf{n} \right\rangle_{\mathcal{F}_h^{\mathrm{int}}} - \alpha \left\langle \frac{[\![\boldsymbol{\vartheta}_2]\!] \times \mathbf{n}}{\{Y\}}, [\![\boldsymbol{\vartheta}_2']\!] \times \mathbf{n} \right\rangle_{\mathcal{F}_h^{\mathrm{int}}} \right) \\ &\quad \left(+\left\langle \tilde{\beta} \{\beta \boldsymbol{\vartheta}_4\} \mathbf{n}, [\![\boldsymbol{\vartheta}_3']\!] \right\rangle_{\mathcal{F}_h^{\mathrm{int}}} - \alpha \left\langle \tilde{\beta} [\![\boldsymbol{\vartheta}_3]\!], \mathbf{n} \right\rangle_{\mathcal{F}_h^{\mathrm{int}}} \langle [\![\boldsymbol{\vartheta}_3']\!], \mathbf{n} \rangle_{\mathcal{F}_h^{\mathrm{int}}} \right) \\ &\quad \left(+\left\langle \hat{\beta} \left\{ \frac{\boldsymbol{\vartheta}_3}{\beta} \right\} [\![\boldsymbol{\vartheta}_4']\!], \mathbf{n} \right\rangle_{\mathcal{F}_h^{\mathrm{int}}} - \alpha \left\langle \hat{\beta} [\![\boldsymbol{\vartheta}_4]\!], [\![\boldsymbol{\vartheta}_4']\!] \right\rangle_{\mathcal{F}_h^{\mathrm{int}}} \right) \\ &\quad + \mathrm{BoundaryConditions}(\boldsymbol{\vartheta}), \\ k(\boldsymbol{\vartheta}, \boldsymbol{\vartheta}') &= \langle \boldsymbol{\mathcal{K}}(\boldsymbol{\vartheta}), \boldsymbol{\vartheta}' \rangle_h. \end{aligned} \tag{3.1.29}$$

For the sake of readability, we have defined

$$\begin{aligned} \tilde{\beta} &= \frac{\beta^- \beta^+}{\beta^- + \beta^+}, \\ \hat{\beta} &= \frac{(\beta^-)^3 (\beta^+)^3}{(\beta^-)^3 + (\beta^+)^3}, \end{aligned} \tag{3.1.30}$$

where $\beta^{-,+}$ respectively is the material parameter left and right of the interior face $a_{ik} \in \mathcal{F}_{\mathrm{int}}$ with $(i,k) \in [\![0, \mathcal{N}_h]\!] \times [\![0, \mathcal{N}_h]\!]$ in direction of the normal vector $\mathbf{n}_{ik}$. Hence, β^+ describes the material in cell k. Obviously, the bilinear form $b_\alpha(\boldsymbol{\vartheta}, \boldsymbol{\vartheta}')$, which contains the surfacic terms, is slightly more complicated to derive. Since its derivation is a bit lengthy, we only sketch the idea for the hydrodynamic contribution.

Presuming to start on element τ_-, the total surface contribution reads

$$\mathfrak{b}_- \quad := \quad \beta_-^2 \sum_{+} \int_{s_{-+}} \boldsymbol{\vartheta}_{4-}^{\star} \boldsymbol{\vartheta}_{3-}' \cdot \mathbf{n} + \boldsymbol{\vartheta}_{3-}^{\star} \cdot \mathbf{n}\, \boldsymbol{\vartheta}_{4-}', \tag{3.1.31}$$

with $\sum_{+}$ being the sum over all faces, which do *not* belong to the physical boundary $\partial\Omega$ of the total domain Ω. Summing up over all elements (all internal faces) leads to

$$\begin{aligned} \mathfrak{b} &= \sum_{i \in [\![0, \mathcal{N}_h]\!]} \mathfrak{b}_i \\ \mathfrak{b} &= \sum_{s_j \in \mathcal{F}^{\text{int}}} \int_{s_j} \quad +\tilde{\beta} \left(\{\beta \boldsymbol{\vartheta}_4\}_{-+} \mathbf{n} \cdot [\![\boldsymbol{\vartheta}_3']\!]_{-+} - \alpha \left(\mathbf{n} \cdot [\![\boldsymbol{\vartheta}_3]\!]_{-+} \right) \left(\mathbf{n} \cdot [\![\boldsymbol{\vartheta}_3']\!]_{-+} \right) \right) \\ &\qquad\qquad +\hat{\beta} \left(\left(\mathbf{n} \cdot \left\{ \frac{\boldsymbol{\vartheta}_3}{\beta} \right\}_{-+} \right) [\![\boldsymbol{\vartheta}_4']\!]_{i+} - \alpha [\![\boldsymbol{\vartheta}_4]\!]_{-+} [\![\boldsymbol{\vartheta}_4']\!]_{-+} \right), \end{aligned} \tag{3.1.32}$$

and immediately to the bilinear form $b_\alpha(\boldsymbol{\vartheta}, \boldsymbol{\vartheta}')$. We postpone the treatment of the boundary faces for a moment, and keep it in mind as an additional contribution called $\mathrm{BoundaryConditions}(\boldsymbol{\vartheta})$.

The previously defined bilinear forms now allow us to recast the global semi-discrete problem as: Find $\boldsymbol{\vartheta}_h \in \mathcal{C}^1(0, T, \mathbb{V}_h)$ such that

Global weak form

$$m(\partial_t \boldsymbol{\vartheta}_h, \boldsymbol{\vartheta}_h') \quad = \quad a(\boldsymbol{\vartheta}_h, \boldsymbol{\vartheta}_h') + b_\alpha(\boldsymbol{\vartheta}_h, \boldsymbol{\vartheta}_h') + k(\boldsymbol{\vartheta}_h, \boldsymbol{\vartheta}_h'), \tag{3.1.33}$$

for all $\boldsymbol{\vartheta}_h' \in \mathbb{V}_h$ on $[0, T]$. We further establish a consistency result.

Proposition 3.1.2. *(Consistency) The exact solution $\boldsymbol{\vartheta}$ of (2.6.4) verifies*

$$m(\partial_t \boldsymbol{\vartheta}, \boldsymbol{\vartheta}_h') \quad = \quad a(\boldsymbol{\vartheta}, \boldsymbol{\vartheta}_h') + b_\alpha(\boldsymbol{\vartheta}, \boldsymbol{\vartheta}_h') + k(\boldsymbol{\vartheta}, \boldsymbol{\vartheta}_h'), \quad \forall \boldsymbol{\vartheta}_h' \in \mathbb{V}_h. \tag{3.1.34}$$

Proof. The proof is straightforward. Due to the continuous tangential trace of the electromagnetic fields, the continuous normal trace of the current density and the continuous trace of the charge density, the expression $a(\boldsymbol{\vartheta}, \boldsymbol{\vartheta}_h') + b(\boldsymbol{\vartheta}, \boldsymbol{\vartheta}_h') = \langle \boldsymbol{\mathcal{L}}(\boldsymbol{\vartheta}), \boldsymbol{\vartheta}_h' \rangle$ is verified. The result follows. □

In terms of boundary conditions, we allow five different kinds: (i) PEC, (ii) PMC, (iii) ABC for Maxwell's equations and (iv) Hard Wall (HW), (v) Soft Wall (SW) for the hydrodynamic part. They respectively read

$$\begin{aligned} \mathbf{n} \times \boldsymbol{\vartheta}_2^{\star}|_{\partial\tau_{\text{PEC}}} &= 0, \\ \mathbf{n} \times \boldsymbol{\vartheta}_1^{\star}|_{\partial\tau_{\text{PMC}}} &= 0, \\ \mathbf{n} \times \boldsymbol{\vartheta}_1^{\star}|_{\partial\tau_{\text{ABC}}} &= \frac{1}{2}(\boldsymbol{\vartheta}_2^- - Z^-(\mathbf{n} \times \boldsymbol{\vartheta}_1^-)), \\ \mathbf{n} \times \boldsymbol{\vartheta}_2^{\star}|_{\partial\tau_{\text{ABC}}} &= \frac{1}{2}(\boldsymbol{\vartheta}_1^- + Y^-(\mathbf{n} \times \boldsymbol{\vartheta}_2^-)), \\ \mathbf{n} \cdot \boldsymbol{\vartheta}_3^{\star}|_{\partial\tau_{\text{HW}}} &= 0, \\ \mathbf{n} \boldsymbol{\vartheta}_4^{\star}|_{\partial\tau_{\text{SW}}} &= 0. \end{aligned} \tag{3.1.35}$$

All of these conditions turn out to be energy conserving except for the ABC contribution. The overall boundary contribution hence reads

$$\text{BoundaryConditions}(\boldsymbol{\vartheta}_h) \quad = \quad -\frac{1}{2}\left(||Z\mathbf{n}\times\boldsymbol{\vartheta}_1||^2_{\mathcal{F}^{\text{ABC}}} + ||Y\mathbf{n}\times\boldsymbol{\vartheta}_2||^2_{\mathcal{F}^{\text{ABC}}}\right). \tag{3.1.36}$$

Lemma 3.1.1. *If the material parameter β is constant and $\alpha \in [0,1]$, then for all $\boldsymbol{\vartheta}_h \in \mathbb{V}_h$,*

$$a(\boldsymbol{\vartheta}_h, \boldsymbol{\vartheta}_h) + b_\alpha(\boldsymbol{\vartheta}_h, \boldsymbol{\vartheta}_h) \quad = \quad -\alpha|\boldsymbol{\vartheta}_h|^2_{\text{S}} \leq 0, \tag{3.1.37}$$

where we have defined

$$\begin{aligned} |\boldsymbol{\vartheta}_h|^2_{\text{S}} \quad := \quad & {\varepsilon_0\omega_{\text{P}}}^2\left(\left|\left|\frac{[\![\boldsymbol{\vartheta}_1]\!]\times\mathbf{n}}{\{Y\}}\right|\right|^2_{\mathcal{F}^{\text{int}}} + \left|\left|\frac{[\![\boldsymbol{\vartheta}_2]\!]\times\mathbf{n}}{\{Z\}}\right|\right|^2_{\mathcal{F}^{\text{int}}}\right) \\ & + \left(\frac{\beta}{2}||[\![\boldsymbol{\vartheta}_3]\!]\cdot\mathbf{n}||_{\mathcal{F}^{\text{int}}} + \frac{\beta^3}{2}||[\![\boldsymbol{\vartheta}_4]\!]||_{\mathcal{F}^{\text{int}}}\right) \\ & + \text{BoundaryConditions}(\boldsymbol{\vartheta}_h). \end{aligned} \tag{3.1.38}$$

Proof. First, we choose as test function $\boldsymbol{\vartheta}' = \boldsymbol{\vartheta}$, which leads to

$$\begin{aligned} a(\boldsymbol{\vartheta}_h, \boldsymbol{\vartheta}_h) + b_\alpha(\boldsymbol{\vartheta}_h, \boldsymbol{\vartheta}_h) \quad &= \quad \varepsilon_0 {\omega_\mathrm{P}}^2 \left(-\left\langle \boldsymbol{\vartheta}_1^+ \times \mathbf{n}, \boldsymbol{\vartheta}_2^+ \right\rangle_{\mathcal{F}^\mathrm{int}} + \left\langle \boldsymbol{\vartheta}_1^- \times \mathbf{n}, \boldsymbol{\vartheta}_2^+ \right\rangle_{\mathcal{F}^\mathrm{int}} \right) \\ &\quad -\left\langle (\beta^-)^2 \boldsymbol{\vartheta}_4^- \boldsymbol{\vartheta}_3^-, \mathbf{n} \right\rangle_{\mathcal{F}^\mathrm{int}} + \left\langle (\beta^+)^2 \boldsymbol{\vartheta}_4^+ \boldsymbol{\vartheta}_3^+, \mathbf{n} \right\rangle_{\mathcal{F}^\mathrm{int}} \\ &\quad + b_\alpha(\boldsymbol{\vartheta}_h, \boldsymbol{\vartheta}_h), \end{aligned} \tag{3.1.39}$$

where we have exploited an integration by parts. Expanding the surface contribution yields

$$\begin{aligned} & a(\boldsymbol{\vartheta}_h, \boldsymbol{\vartheta}_h) + b_\alpha(\boldsymbol{\vartheta}_h, \boldsymbol{\vartheta}_h) \\ = \quad & \varepsilon_0 {\omega_\mathrm{P}}^2 (\quad -\left\langle \boldsymbol{\vartheta}_1^+ \times \mathbf{n}, \boldsymbol{\vartheta}_2^+ \right\rangle_{\mathcal{F}^\mathrm{int}} + \left\langle \boldsymbol{\vartheta}_1^- \times \mathbf{n}, \boldsymbol{\vartheta}_2^+ \right\rangle_{\mathcal{F}^\mathrm{int}} \\ & -\left\langle \frac{Z^- \boldsymbol{\vartheta}_2^-}{\{Z\}}, \boldsymbol{\vartheta}_1^- \times \mathbf{n} \right\rangle_{\mathcal{F}^\mathrm{int}} - \left\langle \frac{Y^- \boldsymbol{\vartheta}_2^-}{\{Y\}}, \boldsymbol{\vartheta}_1^- \times \mathbf{n} \right\rangle_{\mathcal{F}^\mathrm{int}} - \left\langle \boldsymbol{\vartheta}_2^-, \boldsymbol{\vartheta}_1^- \times \mathbf{n} \right\rangle_{\mathcal{F}^\mathrm{int}} \\ & +\left\langle \frac{Z^+ \boldsymbol{\vartheta}_2^+}{\{Z\}}, \boldsymbol{\vartheta}_1^+ \times \mathbf{n} \right\rangle_{\mathcal{F}^\mathrm{int}} + \left\langle \frac{Y^+ \boldsymbol{\vartheta}_2^+}{\{Y\}}, \boldsymbol{\vartheta}_1^+ \times \mathbf{n} \right\rangle_{\mathcal{F}^\mathrm{int}} + \left\langle \boldsymbol{\vartheta}_2^+, \boldsymbol{\vartheta}_1^+ \times \mathbf{n} \right\rangle_{\mathcal{F}^\mathrm{int}} \\ & -\left\langle \frac{Z^+ \boldsymbol{\vartheta}_2^-}{\{Z\}}, \boldsymbol{\vartheta}_1^+ \times \mathbf{n} \right\rangle_{\mathcal{F}^\mathrm{int}} + \left\langle \frac{Y^- \boldsymbol{\vartheta}_2^-}{\{Y\}}, \boldsymbol{\vartheta}_1^+ \times \mathbf{n} \right\rangle_{\mathcal{F}^\mathrm{int}} \\ & +\left\langle \frac{Z^- \boldsymbol{\vartheta}_2^+}{\{Z\}}, \boldsymbol{\vartheta}_1^- \times \mathbf{n} \right\rangle_{\mathcal{F}^\mathrm{int}} + \left\langle \frac{Y^+ \boldsymbol{\vartheta}_2^+}{\{Y\}}, \boldsymbol{\vartheta}_1^- \times \mathbf{n} \right\rangle_{\mathcal{F}^\mathrm{int}} \Big) \\ & +\left\langle \tilde{\beta} \beta^- \boldsymbol{\vartheta}_4^- \mathbf{n}, \boldsymbol{\vartheta}_3^- \right\rangle_{\mathcal{F}^\mathrm{int}} + \left\langle \frac{\hat{\beta} \boldsymbol{\vartheta}_4^-}{\beta^-} \mathbf{n}, \boldsymbol{\vartheta}_3^- \right\rangle_{\mathcal{F}^\mathrm{int}} - \left\langle (\beta^-)^2 \boldsymbol{\vartheta}_4^- \mathbf{n}, \boldsymbol{\vartheta}_3^- \right\rangle_{\mathcal{F}^\mathrm{int}} \\ & -\left\langle \tilde{\beta} \beta^+ \boldsymbol{\vartheta}_4^+ \mathbf{n}, \boldsymbol{\vartheta}_3^+ \right\rangle_{\mathcal{F}^\mathrm{int}} - \left\langle \frac{\hat{\beta} \boldsymbol{\vartheta}_4^+}{\beta^+} \mathbf{n}, \boldsymbol{\vartheta}_3^+ \right\rangle_{\mathcal{F}^\mathrm{int}} + \left\langle (\beta^+)^2 \boldsymbol{\vartheta}_4^+ \mathbf{n}, \boldsymbol{\vartheta}_3^+ \right\rangle_{\mathcal{F}^\mathrm{int}} \\ & +\left\langle \tilde{\beta} \beta^+ \boldsymbol{\vartheta}_4^+ \mathbf{n}, \boldsymbol{\vartheta}_3^- \right\rangle_{\mathcal{F}^\mathrm{int}} - \left\langle \frac{\hat{\beta} \boldsymbol{\vartheta}_4^+}{\beta^-} \mathbf{n}, \boldsymbol{\vartheta}_3^- \right\rangle_{\mathcal{F}^\mathrm{int}} \\ & -\left\langle \tilde{\beta} \beta^- \boldsymbol{\vartheta}_4^- \mathbf{n}, \boldsymbol{\vartheta}_3^+ \right\rangle_{\mathcal{F}^\mathrm{int}} + \left\langle \frac{\hat{\beta} \boldsymbol{\vartheta}_4^-}{\beta^+} \mathbf{n}, \boldsymbol{\vartheta}_3^+ \right\rangle_{\mathcal{F}^\mathrm{int}} \\ & -\alpha \varepsilon_0 {\omega_\mathrm{P}}^2 \left(\left|\left| \frac{[\![\boldsymbol{\vartheta}_1]\!] \times \mathbf{n}}{\{Y\}} \right|\right|^2_{\mathcal{F}^\mathrm{int}} + \left|\left| \frac{[\![\boldsymbol{\vartheta}_2]\!] \times \mathbf{n}}{\{Z\}} \right|\right|^2_{\mathcal{F}^\mathrm{int}} \right) \\ & -\alpha \left(\left\langle \tilde{\beta} [\![\boldsymbol{\vartheta}_3]\!], \mathbf{n} \right\rangle_{\mathcal{F}^\mathrm{int}} \langle [\![\boldsymbol{\vartheta}_3]\!], \mathbf{n} \rangle_{\mathcal{F}^\mathrm{int}} + \left\langle \hat{\beta} [\![\boldsymbol{\vartheta}_4]\!], [\![\boldsymbol{\vartheta}_4]\!] \right\rangle_{\mathcal{F}^\mathrm{int}} \right) \\ & +\mathrm{BoundaryConditions}(\boldsymbol{\vartheta}_h). \end{aligned} \tag{3.1.40}$$

If β is a constant parameter, i.e. $\beta^- = \beta^+ = \beta$ for all cells, basic algebraic simplifications lead to

$$\begin{aligned} a(\boldsymbol{\vartheta}_h, \boldsymbol{\vartheta}_h) + b_\alpha(\boldsymbol{\vartheta}_h, \boldsymbol{\vartheta}_h) \quad &= \quad -\alpha \varepsilon_0 {\omega_\mathrm{P}}^2 \left(\left|\left| \frac{[\![\boldsymbol{\vartheta}_1]\!] \times \mathbf{n}}{\{Y\}} \right|\right|^2_{\mathcal{F}^\mathrm{int}} + \left|\left| \frac{[\![\boldsymbol{\vartheta}_2]\!] \times \mathbf{n}}{\{Z\}} \right|\right|^2_{\mathcal{F}^\mathrm{int}} \right) \\ &\quad -\alpha \left(\frac{\beta}{2} ||[\![\boldsymbol{\vartheta}_3]\!] \cdot \mathbf{n}||_{\mathcal{F}^\mathrm{int}} + \frac{\beta^3}{2} ||[\![\boldsymbol{\vartheta}_4]\!]||_{\mathcal{F}^\mathrm{int}} \right) \\ &\quad + \mathrm{BoundaryConditions}(\boldsymbol{\vartheta}_h). \end{aligned} \tag{3.1.41}$$

The result follows. □

Remark 3.1.4. *The assumption on β is completely justified and even necessary because we have assumed a constant electron equilibrium density for our linearized fluid model.*

We complete this series of useful lemma by the so-called inverse inequalities and an energy principle.

Lemma 3.1.2. *Let $\alpha \in [0,1]$. Then, for all $\boldsymbol{\vartheta} \in \mathbb{V}_h$,*

$$\begin{aligned} \sup_{\boldsymbol{\vartheta}' \in \mathbb{V}_h} \frac{|a(\boldsymbol{\vartheta}, \boldsymbol{\vartheta}') + b_\alpha(\boldsymbol{\vartheta}, \boldsymbol{\vartheta}')|}{||\boldsymbol{\vartheta}'||} &\leq Ch^{-1}\eta||\boldsymbol{\vartheta}||, \\ \sup_{\boldsymbol{\vartheta}' \in \mathbb{V}_h} \frac{|k(\boldsymbol{\vartheta}, \boldsymbol{\vartheta}')|}{||\boldsymbol{\vartheta}'||} &\leq C||\boldsymbol{\vartheta}||, \\ \sup_{\boldsymbol{\vartheta}' \in \mathbb{V}_h} \frac{|b_\alpha(\boldsymbol{\vartheta}, \boldsymbol{\vartheta}')|}{||\boldsymbol{\vartheta}'||} &\leq Ch^{-1}\eta||\boldsymbol{\vartheta}||, \end{aligned} \tag{3.1.42}$$

as well as

$$|b_\alpha(\boldsymbol{\vartheta}, \boldsymbol{\vartheta}')| \leq Ch^{-1}\eta||\boldsymbol{\vartheta}||\,|\boldsymbol{\vartheta}'|_S, \tag{3.1.43}$$

for all $(\boldsymbol{\vartheta}, \boldsymbol{\vartheta}') \in \mathbb{V}_h \times \mathbb{V}_h$. Here, η is the mesh regularity parameter indicating the quasi uniformity as defined previously.

Proof. The proof is classical and only extends the proof in [86] using the divergence and gradient operator inverse estimates, similar to [134]. □

Proposition 3.1.3. *If $\boldsymbol{\vartheta}_h \in \mathbb{V}_h$ is a solution of the semi-discrete scheme, the semi-discrete energy $\mathcal{E}_h$ defined on $[0,T]$ by*

Semi-discrete energy

$$\mathcal{E}_h(t) = \frac{1}{2}m(\boldsymbol{\vartheta}_h, \boldsymbol{\vartheta}_h) = \frac{1}{2}||\boldsymbol{\vartheta}_h||^2_{\boldsymbol{\Lambda}}, \tag{3.1.44}$$

is strictly non-increasing in time.

Proof. By the help of Lemma 3.1.1 and $k(\boldsymbol{\vartheta}_h, \boldsymbol{\vartheta}_h) = -\left|\left|\sqrt{\gamma}\boldsymbol{\vartheta}_3\right|\right|^2 \leq 0$, with $\gamma \geq 0$, directly follows

Semi-discrete stability

$$\partial_t \mathcal{E}_h(t) = \frac{1}{2}m(\partial_t\boldsymbol{\vartheta}_h, \boldsymbol{\vartheta}_h) \leq 0. \tag{3.1.45}$$

□

Remark 3.1.5. *Due to linearity, the total semi-discrete energy of system (2.5.1) is the superposition of the nonlocal dispersion and generalized dispersion contribution [134]. The total energy hence reads*

$$\mathcal{E}_{\text{tot}}(t) = \mathcal{E}_{\text{NL}}(t) + \mathcal{E}_{\text{gen}}(t). \tag{3.1.46}$$

The stability for the generalized model follows readily [86] and is not further detailed here. Consequently, the stability of the complete semi-discrete version of (2.5.1) follows via classical arguments.

3.1.4 Convergence of the semi-discrete scheme

The semi-discrete convergence proof of system (2.6.4) turns out to be a combination of arguments from [85] and [86]. On the one hand, we allow more general fluxes than in [85], on the other hand, $\langle \boldsymbol{\mathcal{K}}\boldsymbol{\vartheta}, \boldsymbol{\vartheta}\rangle$ is strictly non-positive. Based on these conditions, the proof in [86] also holds in our case.

Supposing sufficiently regular initial conditions, such that there exists $\boldsymbol{\vartheta} \in \mathcal{C}^0(0, T, \mathcal{H}^s(\Omega)^{10})$ with $s > 1$. We skip the details of the (lengthy) proof and directly provide the result.

Semi-discrete convergence

(i) For $\alpha = 0$, the error $||\boldsymbol{\vartheta} - \boldsymbol{\vartheta}_h||$ is of the order $O\left(h^{\min(s,k)}\right)$, if $||\boldsymbol{\vartheta}_h(0) - \pi_h(\boldsymbol{\vartheta}(0))||^2_{\boldsymbol{\Lambda}} = O\left(h^{\min(s,k)}\right)$;

(ii) For $\alpha \in (0, 1]$, the error $||\boldsymbol{\vartheta} - \boldsymbol{\vartheta}_h||$ is of the order $O\left(h^{\min(s,k)+\frac{1}{2}}\right)$, if $||\boldsymbol{\vartheta}_h(0) - \pi_h(\boldsymbol{\vartheta}(0))||^2_{\boldsymbol{\Lambda}} = O\left(h^{\min(s,k)+\frac{1}{2}}\right)$.

Here, π_h denotes the $\boldsymbol{\mathcal{L}}^2$ projection on $\mathbb{V}_h$ and k the polynomial order. We can conclude from these results that the dissipative upwind scheme shows improved convergence rates compared to centered fluxes.

3.2 DG matrices and mappings from a reference element

Chapter 3.1.1 has set up the polynomial approximation space, which has led to the global weak formulation (3.1.34). The bilinear forms in (3.1.34) consists of three different types of integrals commonly referred to as mass- (m), stiffness- (a) and surface-terms (b_α). An element-wise matrix formulation of the semi-discrete problem reads

$$\mathbb{M}_i \partial_t \boldsymbol{\Theta}_i(t) \quad = \quad \mathbb{A}_i \boldsymbol{\Theta}_i(t) + \mathbb{B}_i \boldsymbol{\Theta}_i(t) + \mathbb{K}_i \boldsymbol{\Theta}_i(t). \tag{3.2.1}$$

Here, $\boldsymbol{\Theta}_i \in \mathbb{R}^{10 d_i}$ denotes the vector of unknowns. We omit a detailed derivation of the matrices since it is quite classic (see [58, 134]) and restrict ourselves to the type of matrix entries.

Global matrix The global mass-terms $\mathbb{M}$ and $\mathbb{K}$ are of the same kind. They share the important property of block-diagonality. Block-diagonality for $\mathbb{M}$ easily allows the computation of $\mathbb{M}^{-1}$, which is the main reason why DGTD is efficient with explicit time-integration schemes.

In general, the assembly of the sub matrices provides the global formulation. We derive the sub matrices in the following.

Mass matrix Due to the local definition of $\mathbf{W}_i,\ i \in [\![0, N_{\mathcal{T}_h}]\!]$ the sub blocks read for all $j, k \in d_i$

$$(\mathbb{M}_{ii})_{jk} \quad = \quad \int_{\tau_i} \mathfrak{m} \varphi_{ij} \varphi_{ik} \, \mathrm{d}^3 r. \tag{3.2.2}$$

Here, $\mathfrak{m} \in \{\boldsymbol{\Lambda}_{ll}, -\varepsilon_0 {\omega_\mathrm{P}}^2, -\gamma, \varepsilon_0 {\omega_\mathrm{P}}^2\}$ with $l = 1, \ldots, 4$ are the different materials that appear in the mass matrix. Throughout the course of this manuscript, we consider constant material parameters $\mathfrak{m}$ per element $\tau_i,\ i \in [\![0, N_{\mathcal{T}_h}]\!]$. Considering the element $\tau_i,\ i \in [\![0, N_{\mathcal{T}_h}]\!]$ with a local DoF vector $\boldsymbol{\Theta}_i$ that

contains the DoFs of the electric and magnetic field, the polarization current and charge density leads to the element-wise mass matrix multiplication $\mathbb{M}_i \partial_t \mathbf{\Theta}_i(t)$ with

$$\mathbb{M}_i \quad = \quad \mathrm{diag}\{\mathbb{M}_{ii}, \ldots, \mathbb{M}_{ii}\}, \quad \in \mathbb{R}^{10d_i \times 10d_i}, \tag{3.2.3}$$

where each block contains the corresponding $\mathfrak{m}$.

Stiffness matrix In the same way we proceeded for the mass matrices, we define a material dependent stiffness matrix as

$$\left(\mathbb{A}_{ii}^{l}\right)_{jk} \quad = \quad \mathfrak{m} \int_{\tau_i} \varphi_{ij} \partial_l \varphi_{ik} \, \mathrm{d}^3 r, \quad l \in \{x, y, z\}, \tag{3.2.4}$$

with $\mathfrak{m} \in \{-\varepsilon_0 {\omega_\mathrm{P}}^2, \varepsilon_0 {\omega_\mathrm{P}}^2, -\beta^2, -\beta^2\}$. Each $\mathbb{A}_i^l$ is associated to ∂_l and we can assemble discrete differential operators

$$\begin{aligned} \mathbb{A}_i^{\mathrm{curl}} \quad &= \quad \begin{bmatrix} 0 & -\mathbb{A}_i^z & \mathbb{A}_i^y \\ \mathbb{A}_i^z & 0 & -\mathbb{A}_i^x \\ -\mathbb{A}_i^x & \mathbb{A}_i^y & 0 \end{bmatrix}, \\ \mathbb{A}_i^{\mathrm{grad}} \quad &= \quad \begin{bmatrix} \mathbb{A}_i^x & \mathbb{A}_i^y & \mathbb{A}_i^z \end{bmatrix}^T, \\ \mathbb{A}_i^{\mathrm{div}} \quad &= \quad \left(\mathbb{A}_i^{\mathrm{grad}}\right)^T. \end{aligned} \tag{3.2.5}$$

The operation on $\tau_i, \ i \in [0, N_{\mathcal{T}_h}]$ with a local DoF vector $\mathbf{\Theta}_i$ hence reads $\mathbb{A}_i \mathbf{\Theta}_i(t)$ with

$$\mathbb{A}_i \quad = \quad \mathrm{diag}\{\mathfrak{m}_1 \mathbb{A}_i^{\mathrm{curl}}, \mathfrak{m}_2 \mathbb{A}_i^{\mathrm{curl}}, \mathfrak{m}_3 \mathbb{A}_i^{\mathrm{grad}}, \mathfrak{m}_3 \mathbb{A}_i^{\mathrm{div}}\}, \quad \in \mathbb{R}^{10d_i \times 10d_i}, \tag{3.2.6}$$

with $(\mathfrak{m}_1, \mathfrak{m}_2, \mathfrak{m}_3, \mathfrak{m}_4) = (-\varepsilon_0 {\omega_\mathrm{P}}^2, \varepsilon_0 {\omega_\mathrm{P}}^2, -\beta^2, -\beta^2)$.

Surface matrix Integration by parts in the weak formulation has split the differential operators into a volumic stiffness part and the surfacic contribution where the DG flux definitions were required. The surface integral reads

$$\left(\mathbb{B}_{iv}^{l}\right)_{jk} \quad = \quad \mathfrak{m} \int_{a_{iv}} \varphi_{ij} \varphi_{vk} \mathbf{e}_l \cdot \mathbf{n}_{iv} \, \mathrm{d}^2 r, \quad l \in \{x, y, z\}, \tag{3.2.7}$$

with $v \in \mathcal{V}_i$ and $\mathfrak{m} \in \{-\varepsilon_0 {\omega_\mathrm{P}}^2, \varepsilon_0 {\omega_\mathrm{P}}^2, \beta^2, \beta^2\}$. In a similar manner as for the volumic part, we assemble

$$\begin{aligned} \mathbb{B}_{iv}^{\mathrm{curl}} \quad &= \quad \begin{bmatrix} 0 & -\mathbb{B}_{iv}^z & \mathbb{B}_{iv}^y \\ \mathbb{B}_{iv}^z & 0 & -\mathbb{B}_{iv}^x \\ -\mathbb{B}_{iv}^x & \mathbb{B}_{iv}^y & 0 \end{bmatrix}, \\ \mathbb{B}_{iv}^{\mathrm{grad}} \quad &= \quad \begin{bmatrix} \mathbb{B}_{iv}^x & \mathbb{B}_{iv}^y & \mathbb{B}_{iv}^z \end{bmatrix}^T, \\ \mathbb{B}_{iv}^{\mathrm{div}} \quad &= \quad \left(\mathbb{B}_{iv}^{\mathrm{grad}}\right)^T. \end{aligned} \tag{3.2.8}$$

The operation on $\tau_i, \ i \in [\![0, N_{\mathcal{T}_h}]\!]$ with a local DoF vector of the fluxes $\mathbf{\Theta}_i^\star$ leads to $\mathbb{B}_i \mathbf{\Theta}_i$ with

$$\mathbb{B}_i \mathbf{\Theta}_i^\star(t) \quad = \quad \sum_{v \in \mathcal{V}_i} \mathrm{diag}\{\mathfrak{m}_1 \mathbb{B}_{iv}^{\mathrm{curl}}, \mathfrak{m}_2 \mathbb{B}_{iv}^{\mathrm{curl}}, \mathfrak{m}_3 \mathbb{B}_{iv}^{\mathrm{grad}}, \mathfrak{m}_3 \mathbb{B}_{iv}^{\mathrm{div}}\} \mathbf{\Theta}_{iv}^\star. \tag{3.2.9}$$

Here, $\mathbf{\Theta}_{iv}^\star$ denotes the numerical flux at the cell interface between τ_i and τ_v.

3.2.1 Linear elements

For linear triangles and tetrahedra, i.e. elements with straight edges and plane surfaces, we can define affine mappings from a reference element to the physical elements. Deploying affine mappings for the integrals of the mass-, stiffness-, and flux-matrix computations shrinks down the memory consumptions[1]. The integrals are evaluated on a reference element and then transformed to the physical one. Hence, only the transformation from the reference element to the physical element has to be stored. This is possible due to a constant Jacobian matrix as we will see now.

Figure 3.2 depicts the mapping $\boldsymbol{\psi}_{\tau_i}(\boldsymbol{\xi})$ from a reference element $\hat{\tau}$ to a physical tetrahedron τ_i. Please note that this figure illustrates a second order mapping while we only consider linear mappings for the moment. Let us define the reference tetrahedron as $\hat{\tau} := \{(\xi, \eta, \zeta) \in \mathbb{R}^+, \xi+\eta+\zeta \leq 1\}$ and $\boldsymbol{\xi} = (\xi, \eta, \zeta)$. The mapping from the reference element to the physical element is defined by the affine mapping

$$\boldsymbol{\psi}_{\tau_i} : \hat{\tau} \rightarrow \tau_i, \quad \text{such that } \forall\, \boldsymbol{\xi} \in \hat{\tau} \;\; \mathbf{x} = \boldsymbol{\psi}_{\tau_i}(\boldsymbol{\xi}), \tag{3.2.10}$$

with $\mathbf{x} = (x, y, z)$. Applying this transformation to the integrals of the previous section yields [104]

$$\begin{aligned}
\left(\mathbb{M}_{ii}\right)_{jk} &= \int_{\hat{\tau}} \hat{\varphi}_j \hat{\varphi}_k \det\left(\mathbf{J}_{\boldsymbol{\psi}_{\tau_i}}\right) \, \mathrm{d}\boldsymbol{\xi}, \\
\left(\mathbb{A}^l_{ii}\right)_{jk} &= \int_{\hat{\tau}} \hat{\varphi}_j \left\{ \det\left(\mathbf{J}_{\boldsymbol{\psi}_{\tau_i}}\right) \mathbf{J}^{-1}_{\boldsymbol{\psi}_{\tau_i}} \nabla_{\boldsymbol{\xi}} \hat{\varphi}_k \right\}_l \mathrm{d}\boldsymbol{\xi}, \\
\left(\mathbb{B}_{il}\right)_{jk} &= \int_{\hat{t}} \hat{\varphi}_j \hat{\varphi}_k \det\left(\mathbf{J}_{\boldsymbol{\psi}_{\tau_i}}\right) \det\left(\mathbf{J}^{-1}_{\boldsymbol{\psi}_{\tau_i}} \hat{\mathbf{n}}\right) \, \mathrm{d}\hat{\mathbf{s}},
\end{aligned} \tag{3.2.11}$$

where we dropped the material parameters $\mathfrak{m}$ and denote the reference triangle by $\hat{t}$. The Jacobian matrix of the transformation $\boldsymbol{\psi}_{\tau_i}$ is defined by

$$\left(\mathbf{J}_{\boldsymbol{\psi}_{\tau_i}}\right)_{jl} = \left(\frac{\partial \mathbf{x}_j}{\partial \boldsymbol{\xi}_l}\right)_{jl}. \tag{3.2.12}$$

For linear tetrahedra, the mapping's implementation and consequently its Jacobian matrix become

$$\begin{aligned}
\boldsymbol{\psi}_{\tau_i}(\boldsymbol{\xi}) &= \mathbf{v}_1 + (\mathbf{v}_2 - \mathbf{v}_1)\xi + (\mathbf{v}_3 - \mathbf{v}_1)\eta + (\mathbf{v}_4 - \mathbf{v}_1)\zeta, \\
\mathbf{J}_{\boldsymbol{\psi}_{\tau_i}}(\boldsymbol{\xi}) &= \begin{bmatrix} \{\mathbf{v}_2 - \mathbf{v}_1\}_x & \{\mathbf{v}_3 - \mathbf{v}_1\}_x & \{\mathbf{v}_4 - \mathbf{v}_1\}_x \\ \{\mathbf{v}_2 - \mathbf{v}_1\}_y & \{\mathbf{v}_3 - \mathbf{v}_1\}_y & \{\mathbf{v}_4 - \mathbf{v}_1\}_y \\ \{\mathbf{v}_2 - \mathbf{v}_1\}_z & \{\mathbf{v}_3 - \mathbf{v}_1\}_z & \{\mathbf{v}_4 - \mathbf{v}_1\}_z \end{bmatrix}.
\end{aligned} \tag{3.2.13}$$

Since the Jacobian matrix is constant, the integrals in (3.2.11) can be simplified. Each element only needs to store the Jacobian matrix instead of the whole mass-, stiffness-, and surface-matrix.

3.2.2 Curvilinear elements

Although non-uniform tetrahedral meshes are well adapted to large simulation domains that contain small geometrical details, they require significant local refinements for curved material interfaces. Especially in nanoplasmonics, where most effects rely on surface waves, an accurate field solution at the metal-dielectric interfaces is crucial.

[1] In a DGTD implementation, we do not actually assemble global matrices. Each element is treated locally. This is commonly referred to as a matrix-free implementation. Thus, during the update of each cell τ_i, we transform the matrix entries from the reference element $\hat{\tau}$ to τ_i.

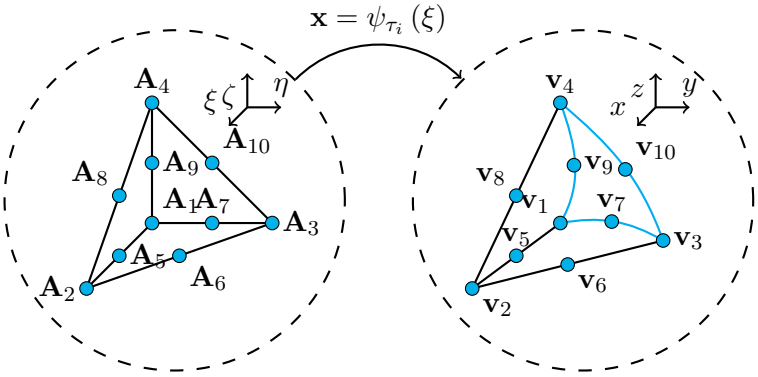

Figure 3.2 | High-order mapping. Second order mapping from the reference element $\hat{\tau}$ to the physical element τ_i. With kind permission from [153].

Typically, technical schematics and plans are done by the help of Computer Aided Design (CAD) software. At the end of the design phase, the engineer obtains a geometric computer model of the desired devices. Common computer based geometry representations are for example Boundary Representation (BREP)[142] and Non-Uniform Rational Basis Spline (NURBS)[117]. If one wants to solve a PDE on a geometry, which is given by a CAD software, classical methods like FDTD, Finite Volume Method (FVM) or FEM require an intermediate meshing step. For Maxwell's equations, FDTD is usually formulated on regular Cartesian grids that may suffer from the staircasing effect. Complex geometrical details are often better approximated by unstructured tetrahedral meshes, well suited to FE methods. However, once a CAD geometry has been tessellated, the original geometric description is lost. Later mesh refinement iterations may require a communication step with the CAD system and can be problematic. A relatively new approach that directly uses the NURBS representation of a given geometry is the so-called Isogeometric Analysis (IGA)[67]. IGA directly employs the geometric basis functions as approximation space and is hence intrinsically boundary conforming. This family of methods has significantly gained attention in the last decade [10]. Although IGA seems to be very promising, it requires fairly drastic changes for existing implementations. An alternative approach, which incorporates more sophisticated geometry approximations are isoparametric elements. Even though they still rely on a mesh, the clear advantage of isoparameteric elements is a fairly easy extension of the existing implementation.

For nanophotonics, the authors in [110] have investigated the importance of a proper surface approximation of metallic nano-spheres. They compared a Cartesian mesh FDTD implementation with a DGTD formulation on linear elements. The latter out-performed the FDTD because FDTD suffers from the staircasing effect. However, the author still experienced limited convergence rates for curved geometries and proposed an implementation of curvilinear elements for nanophotonic metal structures. These predictions have been confirmed meanwhile in the context of nonlinear hydrodynamic dispersion models [59] and for local dispersion laws [155].

In the scope of this manuscript, we extend the formulation proposed in [155] to the linearized hydrodynamic fluid model. Our main motivation is the extremely thin penetration layer of nonlocal effects at the metal boundary [119], which leads to an enormous surface-sensitivity of the solution. Compared to simulations with a local dispersion model, the weight of surface effects will increase and further mesh refinements would be necessary. As a result, the obtained numerical solution shows unwanted artefacts like spurious resonances or numerical dissipation when compared to the analytical reference solution. We refer to section 5.2.4 for a numerical evidence.

In other words, the nonlocal dispersion model even impairs the performance of linear elements with

respect to local dispersion models since all nonlocal effects below the plasma frequency predominantly appear at the metal surface[2]. Additionally, the DGTD convergence rate of simulations with curved geometries on a linear mesh is intrinsically limited to the second order with regards to the approximation of the geometry. This is polynomial order independent of the DG approximation space [40, 155]. For this reason, we extend our DGTD method by curvilinear elements allowing us to significantly reduce the computational costs. Hereby, the performance gain can be explained by a combination of a reduced amount of mesh cells and the full high-order nature due to curvilinear elements.

One clear drawback of curvilinear elements appears in the mapping from the reference element to the physical tetrahedron. In the previous section, we defined a linear mapping with a constant Jacobian. As we will see in the following, the mapping for high-order elements is non-linear. This prevents the 'easy' storage of the DG matrices, where only the Jacobian is needed. Now, a numerical integration on each physical element is indispensable and we have to store the full local DG matrices on each element. According to our experience, the net gain due to curvilinear elements is still strictly overbalanced.

High-order mapping If curvilinear elements are present in the computational mesh, the procedure remains similar as for a purely linear mesh. The only difference is a change in the mapping from the reference element $\hat{\tau}$ to the physical curvilinear element τ_i. In order to account for the curved physical element, additional control points are introduced as depicted in Figure 3.2. This leads to a non-linear mapping $\boldsymbol{\psi}_{\tau_i}$ if they do not lie on a straight line between two edges. For DG with Lagrange basis functions, the procedure is straightforward and the mapping consists in a sum of weighted Lagrange polynomials defined on $\hat{\tau}$. In this sense, we define the usual DoFs $(A_l)_{l=1,\dots,M_n}$ with $M_n = 1/6(n+1)(n+2)(n+3)$ the amount of DoFs on the reference element $\hat{\tau}$. This leads to an n-th order mapping ${\boldsymbol{\psi}_{\tau_i}}^{(n)}$ and reads

$$ {\boldsymbol{\psi}_{\tau_i}}^{(n)}(\boldsymbol{\xi}) = \sum_{0\leq j+k+l\leq n} a_{jkl}^{(n)} \xi^j \eta^k \zeta^l. \tag{3.2.14} $$

Here, $a_{jkl}^{(n)}$ are the weighting coefficients of the n-th order mapping. A second order mapping for example, as we consider throughout the course of this work, becomes

$$ \begin{aligned} {\boldsymbol{\psi}_{\tau_i}}^{(2)}(\boldsymbol{\xi}) \quad = \quad & a_1^{(2)} + \\ & a_2^{(2)}\xi + a_3^{(2)}\eta + a_4^{(2)}\zeta + \\ & a_5^{(2)}\xi\eta + a_6^{(2)}\xi\zeta + a_7^{(2)}\eta\zeta + \\ & a_8^{(2)}\xi^2 + a_9^{(2)}\eta^2 + a_{10}^{(2)}\zeta^2. \end{aligned} \tag{3.2.15} $$

The Jacobian matrix of a second order mapping already contains first order polynomials and its determinant third order polynomials. Consequently, we cannot simplify the integrals in (3.2.11), i.e. we cannot take the Jacobian out of the integral. A space-dependent Jacobian thus requires numerical integration of the DG matrices and prevents a simple mapping coefficient as it was possible for linear elements. This involves the storage of the DG matrices for each curvilinear element and significantly increases the memory consumption. We spare out the details of the determination of $a_{jkl}^{(2)}$ and the numerical integration strategies since they are equivalent to the procedure for Maxwell's equation in [155].

Adding curvilinear elements to our DGTD implementation of the nonlocal dispersion model reuses the already integrated volumic matrices of the Maxwell part. However, the surface terms have changed

[2] We focus on the physics below the plasma frequency since the regime beyond ω_P is dominated by losses and less interesting for real-world applications.

due to the different surface integrals of the hydrodynamic part and have to be added. These additional matrices arise for the normal flux of the current density $\int_{\partial\tau_i} \mathbf{J}^\star \nabla\phi_{ik} \cdot \mathbf{n}$ and the scalar flux of charge density $\int_{\partial\tau_i} Q^\star \boldsymbol{\phi}_{ik} \cdot \mathbf{n}$. As a reminder, since the surface normals are not constant anymore (due to the curved surface, $n = 2$ in our case), a separate computation of each integral-type is necessary. In total, four additional matrices have to be stored when the curvilinear tetrahedron τ_i is subject to a nonlocal dispersion law.

Remark 3.2.1. *Despite advantages like a lower amount of mesh cell, a highly accurate surface approximation, the overall performance of the simulation is constrained by and increased memory-consumption and the quality of a valid curvilinear mesh. Valid and invalid curvilinear meshes have been discussed in [69, 50]. We here rely on available software like http://gmsh.info/ (GMSH) and www.meshgems.com (Distene) for the mesh generation.*

3.3 Time discretization

System (3.1.34) has been discretized in space. However, the time axis is still continuous and needs to be discretized. A key-advantage of a spatial DG discretization clearly is the local formulation that leads to weakly coupled elements. The weakness of the coupling can rather be seen as a communication of neighboring cells via the numerical fluxes. Such a weak coupling yields a block-diagonal mass matrix that is issued from the $m(\boldsymbol{\vartheta}_h, \boldsymbol{\vartheta}'_h)$ for all $\boldsymbol{\vartheta}_h, \boldsymbol{\vartheta}'_h \in \mathbb{V}_h$ term. This particular property of the mass matrix is the reason why DG is efficient in combination with an explicit time integration. (The inversion of the mass matrix that is required by any explicit time integrator is easily attainable due to the block-diagonality.)

Generally, various explicit time integration schemes could be employed for the time discretization in (3.1.34). However, the overall convergence order of the space-time scheme is limited by the order of the space *and* time scheme (as we will see later). In other words, if a spatial discretization of order k is combined with a time integration scheme of order l, the overall order shall be $\min(k, l)$.

Maxwell's equations in time-domain have predominantly been solved with the well established Yee scheme [166], i.e. staggered finite differences. Efficient and simple FDTD implementations are intrinsically limited by a second order convergence (in optimal conditions). A second order LF scheme is hence sufficient and does not limit the overall convergence of the scheme. As DG provides a high spatial convergence order (see Chapter 3.1.4), a second order LF scheme would dramatically limit the overall convergence order. Motivated to fully exploit the high spatial order in combination with a well adapted time integration scheme, we couple our DG discretization with explicit high order RK methods.

We first provide a stability result of the fully-discrete DGTD scheme when the time is discretized with a second order LF scheme. Afterwards, we introduce classical RK methods and an optimized LSRK variant which is particularly tailored to the discrete Maxwell operator. A stability and convergence result of DGTD with a standard RK-4 scheme is sketched and concludes this part.

3.3.1 Second order leap-frog

We consider (3.1.34) on the time interval $[0, T]$ with $T > 0$ and discretize the latter by a uniform subdivision $(t_n)_{n\in[\![0,N]\!]}$, $N \in \mathbb{N}^\star$ of size Δt. The dual grid is shifted in time by $\Delta t/2$ with respect to the primary one. Applying a second order LF scheme to system (3.1.34) we obtain the following fully discrete scheme

$$m\left(\frac{\boldsymbol{\vartheta}_h^{n+1} - \boldsymbol{\vartheta}_h^n}{\Delta t}, \boldsymbol{\vartheta}'_h\right) = a(\boldsymbol{\vartheta}_h^{n+\frac{1}{2}}, \boldsymbol{\vartheta}'_h) + b_\alpha(\boldsymbol{\vartheta}_h^{n+\frac{1}{2}}, \boldsymbol{\vartheta}'_h) + k(\boldsymbol{\vartheta}_h^n, \boldsymbol{\vartheta}'_h), \tag{3.3.1}$$

with

$$\begin{aligned}
\boldsymbol{\vartheta}_h^{n+1} &= \left(\boldsymbol{\vartheta}_{h,1}^{n+\frac{3}{2}} \quad \boldsymbol{\vartheta}_{h,2}^{n+1} \quad \boldsymbol{\vartheta}_{h,3}^{n+\frac{3}{2}} \quad \boldsymbol{\vartheta}_{h,4}^{n+1}\right)^T, \\
\boldsymbol{\vartheta}_h^{n+1/2} &= \left(\boldsymbol{\vartheta}_{h,1}^{n+\frac{1}{2}} \quad \boldsymbol{\vartheta}_{h,2}^{n+1} \quad \boldsymbol{\vartheta}_{h,3}^{n+\frac{1}{2}} \quad \boldsymbol{\vartheta}_{h,4}^{n+1}\right)^T, \\
\boldsymbol{\vartheta}_h^{n} &= \left(\boldsymbol{\vartheta}_{h,1}^{n+\frac{1}{2}} \quad \boldsymbol{\vartheta}_{h,2}^{n} \quad \boldsymbol{\vartheta}_{h,3}^{n+\frac{1}{2}} \quad \boldsymbol{\vartheta}_{h,4}^{n}\right)^T.
\end{aligned} \tag{3.3.2}$$

We only recall the Courant Friedrichs Lewy (CFL)-type stability criterion and refer to [134] for details.

Proposition 3.3.1. Positivity of the energy. *The corresponding energy to* (3.3.1) *is positive under the following condition*

LF stability

$$\frac{\Delta t}{4} \leq \min\left\{\frac{1}{9{\omega_\mathrm{P}}^2\varepsilon_0 C}, \frac{\varepsilon_0\varepsilon_\infty}{2h+9C}, \frac{1}{2h\varepsilon_0{\omega_\mathrm{P}}^2+9\beta^2 C}, \frac{1}{9C}\right\}, \tag{3.3.3}$$

where C is a generic constant independent of Δt and h.

Proof. See [134]. □

Its low order nature and the staggered formulation makes it unhandy to extend this scheme to a generalized dispersion model [153]. We will not further pursue the investigation of this scheme.

3.3.2 Runge-Kutta methods

The semi-discrete system (3.1.34) is a system of ODEs and can be cast into

$$\partial_t \mathbf{y}(t) = \mathbf{F}(t, \mathbf{y}(t)), \tag{3.3.4}$$

to which standard time integration methods directly apply. Here, $\mathbf{y} \in \mathbb{R}^M$ is the vector of unknowns, M the number of coupled ODEs, and $\mathbf{F} : \mathbb{R}^\star \times \mathbb{R}^M \mapsto \mathbb{R}^M$ the RHS. Using the same discretization of the time interval $[0, T]$ with $T > 0$ (a uniform subdivision $(t_n)_{n\in[\![0,N]\!]}$, $N \in \mathbb{N}^\star$ of size Δt). We further define $\mathbf{y}_n$ to be the approximated solution of $\mathbf{y}(t_n)$ at the time t_n. A classical RK scheme [15] of order s with $s \in \mathbb{N}^*$ stages for (3.3.4) reads

$$\begin{aligned}
\mathbf{y}_{n+1} &= \mathbf{y}_n + \Delta t \sum_{i=1}^{s} b_i \mathbf{K}_i, \\
\mathbf{K}_i &= \mathbf{F}\left(t_n + c_i\Delta t, \mathbf{y}_n + \Delta t \sum_{j=1}^{s} a_{ij}\mathbf{K}_j\right)
\end{aligned} \tag{3.3.5}$$

Here, s denotes the number of stages and a_{ij}, b_i, c_i the so-called Butcher coefficients. The Butcher coefficients eventually determine the characteristics of the scheme and tailors properties like its implicit or explicit character, stability criteria and its convergence and order. The following considerations are restricted to conditionally stable explicit schemes, i.e. $a_{i,j} = 0$ for $j \geq i$. We omit a deeper analysis of classical explicit RK schemes and refer the interested reader to [15].

However, we want to point out the memory consumption of (3.3.5). The recursive sum requires a storage of $s+1$ vectors of the same size as $\mathbf{y}_n$. Since DG type methods avoid the storage of a large matrix

and rely on a transformation from a reference element, memory limitations are directly related to the size of the vector of DoFs. This, in turn, means that a multiple storage of the DoF vector is preferably avoided.

Nevertheless, we will make use of the scheme (3.3.5) for the numerical analysis of the fully-discrete scheme where we will use an explicit RK scheme of order 4.

3.3.3 Low storage Runge-Kutta methods

Specialized LSRK methods overcome the memory constraint of classical RK schemes. As a matter of fact, these schemes only need a storage of two full DoF vectors independently of the number of stages. We follow [111] where the authors have focused on a scheme that was originally proposed by Williamson [161]. Different implementations have been proposed in [150, 75]. The Williamson formulation reads

$$\begin{aligned}
&\mathbf{K}_1 = \mathbf{y}_1, \\
&\left.\begin{aligned}
\mathbf{K}_2 &= A_i \mathbf{K}_2 + \Delta t \mathbf{F}(t_n + c_i \Delta t, \mathbf{K}_1) \\
\mathbf{K}_1 &= \mathbf{K}_1 + B_i \mathbf{K}_2
\end{aligned}\right\} \quad \text{for all } i = [\![1, s]\!], \\
&\mathbf{y}_{n+1} = \mathbf{K}_1.
\end{aligned} \tag{3.3.6}$$

Obviously, this scheme only requires one additional DoF vector. Looking for a scheme which is self-starting requires $A_1 = 0$ and we hence end up with $2s-1$ free variables that tailor the scheme. A reduced amount of free variables comes with more restrictive general convergence behaviour. As a consequence, at least 5 LSRK stages are required in order to guarantee 4th-order convergence [16].

Niegemann et al. [111] have recently proposed a LSRK scheme algorithm with optimized stability regions. The proposed scheme has been designed for advection-dominated problems and works particularly well for Maxwell's equations solved by a DGTD formalism. Optimized LSRK methods in combination with Maxwell-DGTD coupled to a Padé-type generalized dispersion model have been studied recently [153]. Throughout this work, we rely on an LSRK with an optimized stability region of order 4 and 12 or 14 stages for centered or upwind fluxes, respectively.

Extending Maxwell's equations coupled to a linearized hydrodynamic model in combination with a generalized dispersion model (see (2.5.1)), may impact the stability criterion. However, we have never experienced any stability issues due to the nonlocal dispersion model. A rigorous stability analysis has not been done and will be part of a future work.

Nevertheless, the hyperbolicity analysis in Chapter 2.6.4 allows a qualitative explanation. The eigenvalues of the pure Maxwell case correspond to the speed of light which is the propagation velocity of the electromagnetic wave. Coupling Maxwell's equations to a linearized fluid model enriches the set of solutions by the bulk plasmon waves. These bulk plasmons, however, appear to have a propagation velocity which is about two orders of magnitude slower than the speed of light. If the original time step Δt has thus been determined by the CFL criterion of Maxwell's equations, the coupled system should still be stable.

Of course, Maxwell's equations and the hydrodynamic model are not equivalent and our qualitative explanation lacks the impact of the discrete grad, div and curl operators. Numerical experiments (cubic cavity and the scattering of a sphere in vacuum) have shown that we can artificially increase the nonlocal parameter up to $\beta = 0.85 c_0$ without experiencing stability issues. Such a value for β is almost two orders of magnitude higher than physically acceptable values.

3.3.4 Stability of the fully-discrete scheme

It turns out that the analysis of the semi-discrete scheme (3.1.34) appears to have similar properties as for Maxwell's equations only coupled to a generalized dispersion law. Indeed, since the energy is not only bounded in finite time but is strictly decreasing, the scheme is even more favorable. Luckily, our case fulfills the requirements of the proof in [86] and the result hence equally holds for (3.1.34). We use a standard explicit RK time integrator instead of the previously presented LSRK scheme. Following [86], we define the operator $\mathfrak{L}_h$ by

$$\mathfrak{L}_h : \quad \mathbb{V}_h \mapsto \mathbb{V}_h \tag{3.3.7}$$

with for all $(\boldsymbol{\varsigma}, \boldsymbol{\xi}) \in \mathbb{V}_h \times \mathbb{V}_h$,

$$(\mathfrak{L}_h \boldsymbol{\varsigma}, \boldsymbol{\xi}) = a(\boldsymbol{\varsigma}, \boldsymbol{\xi}) + b_\alpha(\boldsymbol{\varsigma}, \boldsymbol{\xi}). \tag{3.3.8}$$

We further define the operator $\mathfrak{K}_h : \mathbb{V}_h \mapsto \mathbb{V}_h$ with for all $(\mathfrak{K}_h \boldsymbol{\varsigma}, \boldsymbol{\xi}) = k(\boldsymbol{\varsigma}, \boldsymbol{\xi})$. The overall RHS is packed together and we define

$$\mathfrak{D}_h := \mathfrak{L}_h + \mathfrak{K}_h, \tag{3.3.9}$$

which permits to recast the semi-discrete scheme as: Find $\boldsymbol{\vartheta}_h \in \mathbb{V}_h$ such that

$$\boldsymbol{\Lambda} \partial_t \boldsymbol{\vartheta}_h = \mathfrak{D}_h(\boldsymbol{\vartheta}_h). \tag{3.3.10}$$

Equation (3.3.12) is of the same form as (3.3.4) an we apply a 4th order RK discretization. We still consider (3.3.12) on the time interval $[0, T]$ with $T > 0$ and discretize the latter by a uniform subdivision $(t_n)_{n \in [\![0,N]\!]}$, $N \in \mathbb{N}^\star$ of size Δt. Here, all components of $\boldsymbol{\vartheta}_h^n$ share the same time grid, i.e.

$$\boldsymbol{\vartheta}_h^n = \begin{pmatrix} \boldsymbol{\vartheta}_{h,1}^n & \boldsymbol{\vartheta}_{h,2}^n & \boldsymbol{\vartheta}_{h,3}^n & \boldsymbol{\vartheta}_{h,4}^n \end{pmatrix}^T. \tag{3.3.11}$$

The stability condition follows. We recall from [86]:

Proposition 3.3.2. *Let $\alpha \in]0, 1]$. Under a $4/3-$CFL condition, i.e. $\Delta t \lesssim h^{4/3}$, the scheme is stable in finite time, in the sense that there exists $C > 0$ (independent of h and Δt) such that*

RK stability

$$\max_{n \in \{0,\dots,N\}} ||\boldsymbol{\vartheta}_h^n||_{\boldsymbol{\Lambda}}^2 \leq \exp(CT) \left|\left|\boldsymbol{\vartheta}_h^0\right|\right|_{\boldsymbol{\Lambda}}^2. \tag{3.3.12}$$

Remark 3.3.1. *Proposition 3.3.2 states a controlled increase of energy. This is due to the generalized dispersion model contribution. In other words, if we only couple Maxwell's equations to the linearized fluid model, the exponential term drops and the stability result changes to*

$$\max_{n \in \{0,\dots,N\}} ||\boldsymbol{\vartheta}_h^n||_{\boldsymbol{\Lambda}}^2 \leq \left|\left|\boldsymbol{\vartheta}_h^0\right|\right|_{\boldsymbol{\Lambda}}^2. \tag{3.3.13}$$

Proof. Since we are in a very similar situation as in [86], the proof is almost equivalent and we spare out a thorough reproduction of the details. □

3.3.5 Convergence of the fully-discrete scheme

Thanks to the successful stability analysis, a conducting convergence proof relies on similar steps. We refer the interested reader to [13, 85] for inspirations on the convergence proof. The result reads

Proposition 3.3.3. *There exists $C > 0$ (independent of h and Δt, but that depends on T and $\boldsymbol{\vartheta}$) such that*

RK convergence

$$\max_{n\in\{0,\dots,N\}} ||\boldsymbol{\vartheta}(t_n) - \boldsymbol{\vartheta}_h^n||_{\boldsymbol{\Lambda}} \leq C\left(h^{\min(s,k)+1/2} + \Delta t^4\right), \tag{3.3.14}$$

under the CFL-type condition.

4
Technicalities

Chapter 2 has set up the physical context in terms of model equations, boundary conditions and source terms. Aiming for complex nanophotonic geometries, where analytical solutions are either extremely elaborate or do not exist, we have proposed a spatial and temporal discretization scheme in Chapter 3. While Chapter 3 deals with the description of the numerical scheme, its stability analysis and a convergence result, an exhaustive numerical simulation of nanophotonic scattering problems still requires additional functionalities.

We name the lacking ingredients 'Technicalities', containing specific field sources, sophisticated free-space boundary conditions and physically interpretable observables.

More precisely, we will recall the TF/SF-interface approach enabling an intuitive manner to impose incident fields. A complementary approach, the so called SF-formulation, will lead to a formulation of Maxwell's equations, where only scattered fields remain. Such a formulation is well suited for EELS simulations due to its very flexible source term formulation [97, 34].

In terms of domain truncation, we provide a CFS-PML boundary condition that has proven to be very efficient for DGTD methods [82, 153].

Correspondingly to their formulation, CFS-PMLs easily allow arbitrary materials inside the PML region. This feature will be of particular importance for simulation examples like nano-cubes, where an infinite half-space (metallo-dielectric substrate) is mandatory. We refer to Chapter 5 for concrete application examples.

Sophisticated domain truncation thanks to PMLs and appropriate field source formulations will allow 3D time-domain simulations of system (2.5.1). However, most physical interpretation are very often based on frequency-domain observables like optical CSs of a scatterer, reflectance or transmission spectra (for periodic unit-cells) and absorption spectra inside a certain sub domain of a device. In the context of EELS simulations, physicists are commonly interested in the Electron Energy Loss Probability (EELP), which is equally defined in frequency-domain. Adding those observables to our DGTD implementation grants access to comparisons of the simulated observables and their experimental counterparts.

i

4.1 Field sources

Nanophotonic scattering simulations generally rely on any kind of incident signal, except for eigenvalue problems. Such signals can for instance be a plane wave pulse, a Gaussian laser beam [92] or electron beams in EELS [46, 159], Electron Energy Gain Spectroscopy (EEGS) [116, 115] and CL [151] microscopy. The question arises, how to impose these excitations to system (2.5.1). This section briefly recalls already established techniques like the TF/SF approach and the SF technique as these principles are used throughout the course of this work in different situations later on.

4.1.1 Total field / scattered field interface

TF/SF interface will serve for two different purposes at the same time. On the one hand side, a TF/SF interface allows incident fields for PML truncated domains and on the other hand they provide an elegant possibility to evaluate physical observables based on Poynting's theorem (2.3.17).

The here presented techniques are well established in the FDTD and also more recently in the DGTD community. Comprehensive details can be found in [143, 14, 153] and we only provide a condensed version of the references. The TF/SF approach splits the total fields

$$\boldsymbol{\vartheta}_{\mathrm{tot}} \quad = \quad \boldsymbol{\vartheta}_{\mathrm{inc}} + \boldsymbol{\vartheta}_{\mathrm{sca}}, \tag{4.1.1}$$

into their incident and scattered components. Usually, the incident field is known a priori since it is part of the simulation setup definition. Splitting-up the overall computational domain into two sub domains: the scattered field domain Ω_{sca} (where we only compute the scattered field) and the total field domain Ω_{tot} which containing the scatterers and where we compute the total field, leads to two sets of the semi-discrete problem in (3.1.34)

$$\begin{aligned} m(\partial_t \boldsymbol{\vartheta}_{h,\mathrm{tot}}, \boldsymbol{\vartheta}'_h) &= a(\boldsymbol{\vartheta}_{h,\mathrm{tot}}, \boldsymbol{\vartheta}'_h) + b_\alpha(\boldsymbol{\vartheta}_{h,\mathrm{tot}}, \boldsymbol{\vartheta}'_h) + \\ &\quad k(\boldsymbol{\vartheta}_{h,\mathrm{tot}}, \boldsymbol{\vartheta}'_h), \qquad \forall \boldsymbol{\vartheta}'_h \in \mathbb{V}_h, \ \ \mathrm{supp}(\boldsymbol{\vartheta}_{h,\mathrm{tot}}) = \Omega_{\mathrm{tot}}, \\ m(\partial_t \boldsymbol{\vartheta}_{h,\mathrm{sca}}, \boldsymbol{\vartheta}'_h) &= a(\boldsymbol{\vartheta}_{h,\mathrm{sca}}, \boldsymbol{\vartheta}'_h) + b_\alpha(\boldsymbol{\vartheta}_{h,\mathrm{sca}}, \boldsymbol{\vartheta}'_h) + \\ &\quad k(\boldsymbol{\vartheta}_{h,\mathrm{sca}}, \boldsymbol{\vartheta}'_h), \qquad \forall \boldsymbol{\vartheta}'_h \in \mathbb{V}_h, \ \ \mathrm{supp}(\boldsymbol{\vartheta}_{h,\mathrm{sca}}) = \Omega_{\mathrm{sca}}. \end{aligned} \tag{4.1.2}$$

Although the unknowns of each sub domain now represent different fields, the DG formalism remains exactly the same inside each domain. However, the flux at the interface $\partial\Omega_{\mathrm{tot,sca}} = \partial\overline{\Omega}_{\mathrm{tot}} \cap \partial\overline{\Omega}_{\mathrm{sca}}$ has to be adapted in order to take the different field formulations into account. We refer to [14, 153] for further details. Please note that the presented approach is only valid for linear Maxwell's equations. Figure 4.1 shows a sphere inside Ω_{tot}, surrounded by the TF/SF interface. The domain outside the TF/SF interface thus is Ω_{sca} being truncated by PMLs. Figure 4.2 depicts a numerical example of the TF/SF approach. In Figure 4.2 (a) no scatterer is present (vacuum sphere) and hence no scattered fields appear in the SF domain. Assuming a metallic sphere in Figure 4.2 (b) leads to the classic Surface Plasmon Polariton (SPP) resonance and hence to scattered waves in the SF domain.

4.1.2 Scattered field formulation

The SF formulation is based on a similar approach as the TF/SF interface formulation. However, the slight difference arises due to the strict absence of the total field in the solution. The TF/SF formulation divides the computational domain into a total field domain Ω_{tot} and a scattered field domain Ω_{sca}. While the

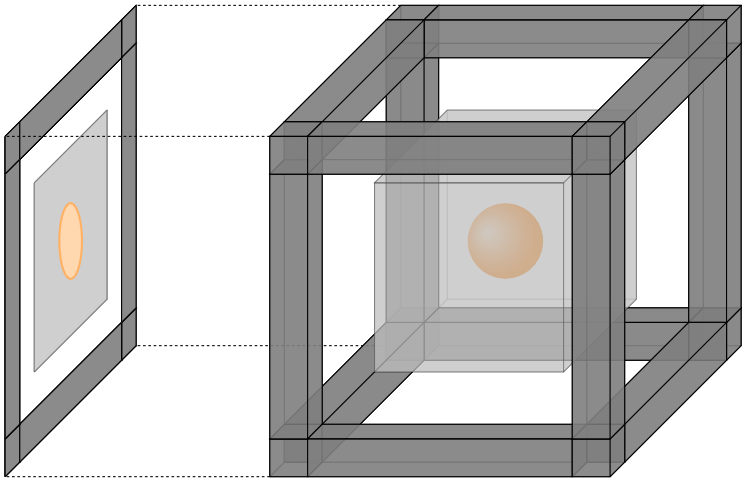

Figure 4.1 | Mesh configuration including a scatterer, a TF/SF interface, and a PML layer. The scatterer (orange) is enclosed by the TF/SF interface in (light gray). The faces of the PML (gray) are removed for clarity. Courtesy of [153].

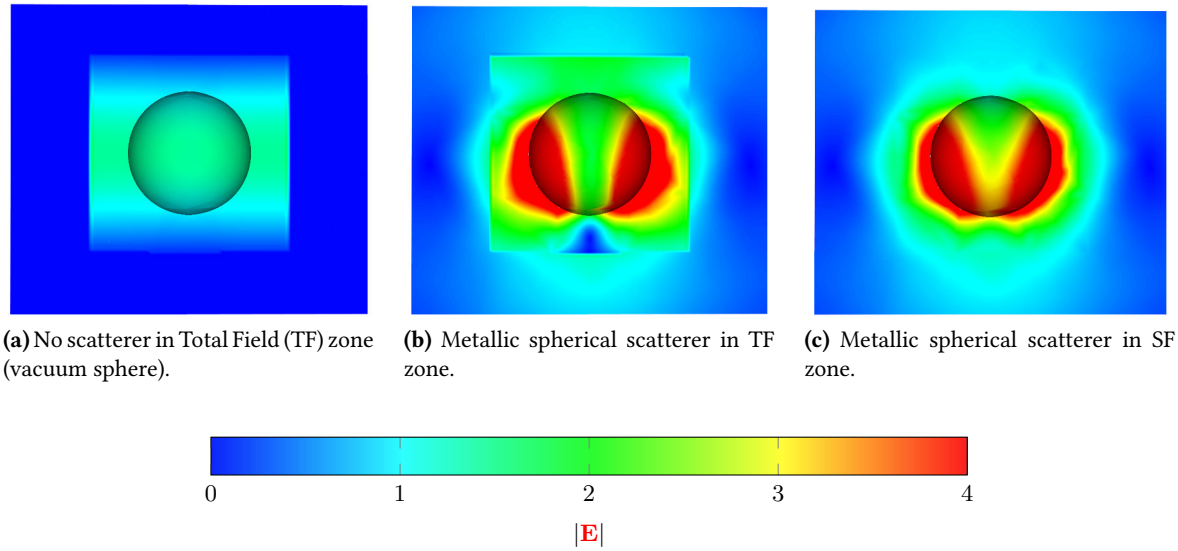

(a) No scatterer in Total Field (TF) zone (vacuum sphere).

(b) Metallic spherical scatterer in TF zone.

(c) Metallic spherical scatterer in SF zone.

Figure 4.2 | TF/SF and SF field plot. Figure (a) shows the incident field in the TF domain and no field in the SF domain. Putting a metal sphere into the TF zone causes scattered fields hence fields in the SF zone. The solution in Figure (c) has been obtained with the SF source formulation and does not contain any incident field which makes the TF/SF interface invisible for the solution.

solution on Ω_{tot} is composed of the incident plus the scattered field, the solution on Ω_{sca} only consists in the scattered field without the incident field. In contrast, the SF formulation does not have any total field region, i.e. $\Omega = \Omega_{\text{sca}}$. If wanted, the total solution can be reconstructed by $\boldsymbol{\vartheta}_{\text{tot}} = \boldsymbol{\vartheta}_{\text{sca}} + \boldsymbol{\vartheta}_{\text{inc}}$.

Benefits of the SF formulation System (3.1.34) in the SF form turns out to be a very flexible option for EELS simulations that rely on an incident electron beam excitation. Such a simulation requires a fairly complicated TF/SF approach guaranteeing a convex TF domain for non-penetrating electron beams [97, 153]. Penetrating electron beams are unfortunately impossible in combination with TF/SF interfaces.

Employing a SF formulation intrinsically overcomes this drawback due to its volume based formulation (instead of a TF/SF interface). Additionally, re-meshing is not required for different electron trajectories, since different electron beam positions only manifest in different parameters of the analytical source term ϑ_{inc}. This paves the way for multiple simulation runs with various electron beam trajectories on the same mesh that avoids mesh noise.

Maxwell's equations in the SF formulation Inspired by Diehl [34], we extend the frequency-domain SF formulation to a purely time-domain derivation (leading to an equivalent result) and considering arbitrary dispersion models, e.g. the generalized dispersion model coupled to a linearized hydrodynamic dispersion model (2.5.1). Extending the SF formulation to nonlocal dispersion models is very straightforward thanks to the fact that the entire dispersion is cast into a dispersion current. For linear dispersion laws and linear Maxwell's equations, the actually implemented form of $\mathbf{J}_{\mathrm{f}}$ does not affect the SF derivation and can hence be kept general.

Remark 4.1.1. *Although throughout the course of this thesis we neglect any magnetization effects, i.e.* $\mathbf{M} \equiv 0$*, the following derivation preserves the generalization* $\mathbf{M} \neq 0$ *for the sake of completeness.*

We assume a vacuum domain Ω^1 and a dispersive domain Ω^2 as depicted in Figure 4.3. The electric and magnetic fields are equivalently decomposed as in (4.1.1). Ampère's and Faraday's law for the dispersive materials and for vacuum on the same domain Ω^2 respectively read

$$\begin{aligned}
\nabla \times \mathbf{E}^{\mathrm{tot}} &= -\partial_t(\mu_0 \mathbf{H}^{\mathrm{tot}}) - \partial_t(\mu_0 \mathbf{M}(\mathbf{H}^{\mathrm{tot}})),\\
\nabla \times \mathbf{H}^{\mathrm{tot}} &= \partial_t \varepsilon_0 \varepsilon_\infty \mathbf{E}^{\mathrm{tot}} + \mathbf{J}_{\mathrm{b}}(\mathbf{E}^{\mathrm{tot}}) + \mathbf{J}_{\mathrm{f}}(\mathbf{E}^{\mathrm{tot}}),\\
\nabla \times \mathbf{E}^{\mathrm{inc}} &= -\mu_0 \partial_t \mathbf{H}^{\mathrm{inc}},\\
\nabla \times \mathbf{H}^{\mathrm{inc}} &= \varepsilon_0 \partial_t \mathbf{E}^{\mathrm{inc}}.
\end{aligned} \tag{4.1.3}$$

Simple algebraic steps immediately lead to

$$\begin{aligned}
\nabla \times \mathbf{E}^{\mathrm{sca}} &= -\partial_t(\mu_0 \mathbf{H}^{\mathrm{sca}}) - \partial_t(\mu_0 \mathbf{M}(\mathbf{H}^{\mathrm{tot}})),\\
\nabla \times \mathbf{H}^{\mathrm{sca}} &= \partial_t \varepsilon_0 \varepsilon_\infty \mathbf{E}^{\mathrm{sca}} + \partial_t \varepsilon_0 (\varepsilon_\infty - 1)\mathbf{E}^{\mathrm{inc}} + \mathbf{J}_{\mathrm{b}}(\mathbf{E}^{\mathrm{tot}}) + \mathbf{J}_{\mathrm{f}}(\mathbf{E}^{\mathrm{tot}}),
\end{aligned} \tag{4.1.4}$$

and eventually

SF formulation

$$\begin{aligned}
\partial_t \mathbf{H}^{\mathrm{sca}} &= -\frac{1}{\mu_0} \nabla \times \mathbf{E}^{\mathrm{sca}} - \partial_t(\mathbf{M}(\mathbf{H}^{\mathrm{tot}})),\\
\partial_t \mathbf{E}^{\mathrm{sca}} &= \frac{1}{\varepsilon_0 \varepsilon_\infty} \left(\nabla \times \mathbf{H}^{\mathrm{sca}} - \mathbf{J}_{\mathrm{b}}(\mathbf{E}^{\mathrm{tot}}) + \mathbf{J}_{\mathrm{f}}(\mathbf{E}^{\mathrm{tot}}) \right) - (1 - \varepsilon_\infty^{-1}) \partial_t \mathbf{E}^{\mathrm{inc}}.
\end{aligned} \tag{4.1.5}$$

We can conclude from (4.1.5):

- In case of vacuum, i.e. $\varepsilon_\infty = \mathbf{J}_{\mathrm{f}} \equiv 0$, we recover Maxwell's equations without any source terms, leading to the absence of scattered fields if no materials are present (equivalent if (4.1.5) was considered on Ω^1);

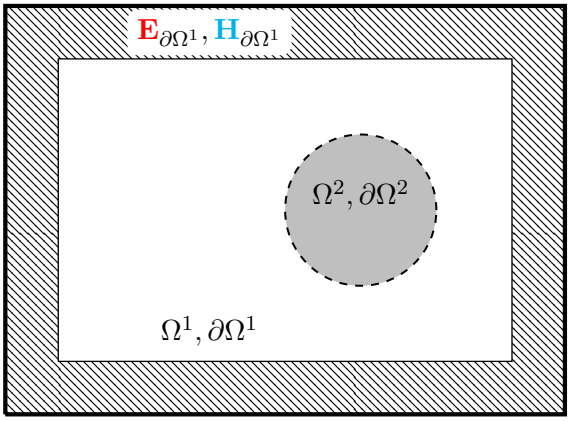

Figure 4.3 | SF computational domain. Ω^1 consists of vacuum and Ω^2 is dispersive. $\mathbf{E}_{\partial\Omega^1}, \mathbf{H}_{\partial\Omega^1}$ symbolize the boundary conditions for $\mathbf{E}$ and $\mathbf{H}$ where the vacuum domain is truncated.

- Either non-dispersive dielectric ε_∞ or/and bound electron polarization current $\mathbf{J}_\mathrm{b}$ or/and a free electron polarization current $\mathbf{J}_\mathrm{f}$ can cause scattered fields.

Regarding the computational costs, the SF formulation requires the evaluation of the incident field on every non-vacuum volume, i.e. where $\mathbf{J}_\mathrm{b}(\mathbf{E}_\mathrm{tot}) \neq 0$ or/and $\mathbf{J}_\mathrm{f}(\mathbf{E}_\mathrm{tot}) \neq 0$ due to $\mathbf{E}_\mathrm{tot} = \mathbf{E}_\mathrm{inc} + \mathbf{E}_\mathrm{sca}$. If the material's background permittivity ε_∞ is non-vanishing, an additional evaluation of the incident field's time derivative is also necessary. Figure 4.2 (b) and (c) illustrate the difference between the TF/SF and SF source formulation.

4.2 Domain truncation

This chapter outlines different domain truncation techniques. First, Silver-Müller (first-order radiation conditions), often referred to as ABC, are given for completeness. We then sketch the main ideas of CFS-PMLs and proceed with a special formulation of Maxwell's equation based on a combination of the SF formulation and CFS-PMLs. This formulation will turn out to be impractical in time-domain what motivates our proposition of a combination of TF/SF surfaces and CFS-PMLs.

4.2.1 Silver-Müller absorbing condition

The Silver-Müller radiation condition [104] reads

$$\lim_{\rho\to\infty} \rho((\nabla \times \mathbf{E}_\mathrm{sca}) \times \mathbf{n} - ik_0\mathbf{E}_\mathrm{sca}) = 0, \tag{4.2.1}$$

which can also be expressed as [44]

$$\mathbf{n} \times \mathbf{E} = -Z\mathbf{n} \times (\mathbf{n} \times \mathbf{H}). \tag{4.2.2}$$

This first order radiation condition assumes outward-travelling waves and its performance significantly decreases for oblique incidence angles [22].

4.2.2 Perfectly matched layers

Overcoming the incident angle limitation of Silver-Müller boundary *conditions*, an artificial boundary *layer* can be employed, commonly known as PMLs. PMLs have first been proposed by Berenger in 1994

[5]. The leading idea is to truncate a free space simulation setup with a layer filled by an artificial material that attenuates the outward-travelling waves. Such an artificial material has to be designed in a way that it optimally absorbs all radiation coming from the actual computational domain (for example the scattered fields of a sphere). Perfect absorption also means no back reflection into the simulation domain and would hence mimic an infinite space for the solution on the domains Ω^1 and Ω^2 according to Figure 4.3.

König et al. [82] have recently proposed the CFS-PML in the context of DGTD. For details and performance assessments of standard PMLs, Uniaxial Perfectly Matched Layers (UPMLs) and CFS-PMLs we refer to [6, 82, 153]. In the following, we restrict ourselves to CFS-PMLs.

CFS-PML formulation CFS-PMLs rely on a complex coordinate stretching in the PML domain $\tilde{\Omega}$ [19], see Figure 4.4 (b). Such a stretching transforms the spatial derivatives

$$\partial_l \quad \rightarrow \quad \frac{1}{s_l(\omega)}\partial_l, \tag{4.2.3}$$

in the frequency-domain. Here, $s_l(\omega) := \kappa_l - \dfrac{\sigma_l}{i\omega - \alpha_l}$ and $l \in \{x, y, z\}$. We refer to [153] for a quantitative study about appropriate choices of the numerical values of $\kappa_l, \sigma_l, \alpha_l$. Applying the PML strategy to Maxwell's equations in frequency-domain yields

Maxwell's equations on $\tilde{\Omega}$

$$\begin{aligned} -i\omega\varepsilon_0\varepsilon_\infty \mathbf{E} &= \widetilde{\nabla} \times \mathbf{H}, \\ i\omega\mu_0\mu_\infty \mathbf{H} &= \widetilde{\nabla} \times \mathbf{E}, \end{aligned} \tag{4.2.4}$$

with the transformed operator

$$\widetilde{\nabla} = \left(\frac{1}{s_x(\omega)}\partial_x, \frac{1}{s_y(\omega)}\partial_y, \frac{1}{s_z(\omega)}\partial_z \right)^T, \tag{4.2.5}$$

and for $\tilde{\Omega}$ being filled with vacuum.

Time-domain CFS-PML An inverse Fourier transform leads to the time-domain version of (4.2.4). The $\mathbf{e}_x$ component of Ampère's law for example reads

$$\begin{aligned} \varepsilon_0\varepsilon_\infty \partial_t \{\mathbf{E}\}_x &= \frac{1}{s_y}\partial_y \{\mathbf{H}\}_z - \frac{1}{s_z}\partial_z \{\mathbf{H}\}_y, \\ \varepsilon_0\varepsilon_\infty \partial_t \{\mathbf{E}\}_x &= \frac{1}{\kappa_y}\partial_y \{\mathbf{H}\}_z - \frac{1}{\kappa_z}\partial_z \{\mathbf{H}\}_y - \{\mathbf{G}^\mathbf{E}\}_{xy} - \{\mathbf{G}^\mathbf{E}\}_{xz}, \\ \partial_t \{\mathbf{G}^\mathbf{E}\}_{xy} &= \frac{\sigma_y}{\kappa_y^2}\partial_y \{\mathbf{H}\}_z - \left(\alpha_y + \frac{\sigma_y}{\kappa_y}\right) \{\mathbf{G}^\mathbf{E}\}_{xy}, \\ \partial_t \{\mathbf{G}^\mathbf{E}\}_{xz} &= -\frac{\sigma_z}{\kappa_z^2}\partial_z \{\mathbf{H}\}_y - \left(\alpha_z + \frac{\sigma_z}{\kappa_z}\right) \{\mathbf{G}^\mathbf{E}\}_{xz}. \end{aligned} \tag{4.2.6}$$

Here, $\mathbf{G}$ is the auxiliary PML quantity due to the artificial material. We refer to [82, 153] for details about the derivation and more technical aspects like the split-flux formulation. DG-based CFS-PMLs crucially rely on split-fluxes.

CFS-PML and SF formulation Beside rather academic studies like isolated spheres in vacuum, most nanophotonic devices are deposited on an infinite metal or dielectric substrate. A scatterer, e.g. a nanocube or a sphere, etc. is subsequently deposited on the substrate surface. This infinite substrate, however, has to be truncated in volume-based numerical methods, similar to the infinite vacuum domain in Figure 4.1. Figure 4.5 (b) depicts such a setup.

In the context of CFS-PMLs, materials inside the PML domain do not change the PML formulation [81] and hence provide a very efficient way to incorporate non-vacuum materials in $\tilde{\Omega}$. An intuitive approach may be to put a TF/SF interface around a scatterer as outlined in Figure 4.4 (a). However, this requires the analytical solution of a three-layer system, see Section 2.7.3 and is easily achievable in frequency-domain. In broad-band time-domain simulations, where the incident signal is a Gaussian pulse for example, no analytic closed form inverse Fourier transform of such a signal exists. We would require a discrete inverse Fourier transform of the incident field on the entire TF/SF interface. This is certainly possible but involves high computational costs.

Trying to circumvent this issue, we propose the combination of the SF formulation in combination with material-filled CFS-PMLs. As we will see soon, such an approach encounters a pitfall which potentially leads to a complete failure if done incorrectly. We will provide both, the wrong and correct formulation.

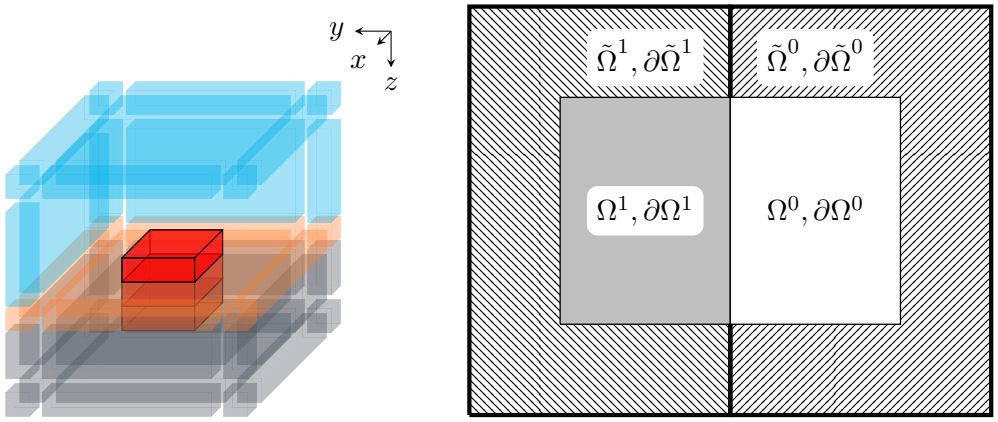

(a) Infinite metallic and dielectric slab with TF/SF and PML. The two lower layers respectively illustrate metallic ground plane and the dielectric slab which equally enter the PMLs and hence act like an infinite plane. Additionally, a TF/SF surface surrounds a volume that contains metal, dielectric, and vacuum.

(b) SF-PML domain. Domain Ω^0 consists of vacuum and Ω^1 of an arbitrary material. The PML domains $\tilde{\Omega}^0$ and $\tilde{\Omega}^1$ are respectively filled with the same material as their corresponding domains Ω^i for $i = \{1, 2\}$.

Figure 4.4 | TF/SF-PML and SF-PML. Figure (a) shows TF/SF interface for infinite substrates and (b) sketches the SF-PML domain setup.

CFS-PML and SF formulation - the naive approach In order to provide a general derivation, we define 4 different domains as outlined in Figure 4.4 (b). Domain Ω^0 and Ω^1 represent the 'inner' domain, i.e. the actual computational domain. Consistently with previous notations, $\tilde{\Omega}^i$, $i \in \{0, 1\}$ denote the PML extension of Ω^i. The term 'extension' means a constant material transition from the inner domain Ω^i to the PML domain $\tilde{\Omega}^i$. In other words, if Ω^1 consists of a gold, the gold will be continued in the $\tilde{\Omega}^1$

and mimic an infinite gold volume. Defining Maxwell's equations on the inner domains Ω^i reads

$$\begin{aligned} \nabla \times \mathbf{H}^0_{\text{tot}} &= \varepsilon_0 \partial_t \mathbf{E}^0_{\text{tot}}, & \nabla \times \mathbf{H}^1_{\text{tot}} &= \varepsilon_0 \varepsilon_\infty \partial_t \mathbf{E}^1_{\text{tot}}, \\ \nabla \times \mathbf{E}^0_{\text{tot}} &= -\mu_0 \partial_t \mathbf{H}^0_{\text{tot}}, & \nabla \times \mathbf{E}^1_{\text{tot}} &= -\mu_0 \mu_\infty \partial_t \mathbf{H}^1_{\text{tot}}. \end{aligned} \tag{4.2.7}$$

accompanied by the interface condition on $\overline{\Omega}^0 \cap \overline{\Omega}^1$

$$\begin{aligned} \mathbf{n}_{01} \times (\mathbf{E}^1_{\text{tot}} - \mathbf{E}^0_{\text{tot}}) &= 0, \\ \mathbf{n}_{01} \cdot (\varepsilon_\infty \mathbf{E}^1_{\text{tot}} - \mathbf{E}^0_{\text{tot}}) &= 0, \end{aligned} \tag{4.2.8}$$

as well as for the domain PML interfaces $\overline{\Omega}^0 \cap \overline{\tilde{\Omega}}^0$ and $\overline{\Omega}^1 \cap \overline{\tilde{\Omega}}^1$

$$\begin{aligned} \mathbf{n}_{0\tilde{0}} \times (\tilde{\mathbf{E}}^0_{\text{tot}} - \mathbf{E}^0_{\text{tot}}) &= 0, & \mathbf{n}_{1\tilde{1}} \times (\tilde{\mathbf{E}}^1_{\text{tot}} - \mathbf{E}^1_{\text{tot}}) &= 0, \\ \mathbf{n}_{0\tilde{0}} \cdot (\tilde{\mathbf{E}}^0_{\text{tot}} - \mathbf{E}^0_{\text{tot}}) &= 0, & \mathbf{n}_{1\tilde{1}} \cdot (\varepsilon_\infty \tilde{\mathbf{E}}^1_{\text{tot}} - \mathbf{E}^1_{\text{tot}}) &= 0. \end{aligned} \tag{4.2.9}$$

Applying the SF procedure on each inner domain yields on Ω^i

$$\begin{aligned} \nabla \times \mathbf{H}^0_{\text{sca}} &= \varepsilon_0 \partial_t \mathbf{E}^0_{\text{sca}}, & \nabla \times \mathbf{H}^1_{\text{sca}} &= \varepsilon_0 \varepsilon_\infty \partial_t \mathbf{E}^1_{\text{sca}} + \varepsilon_0 (\varepsilon_\infty - 1) \partial_t \mathbf{E}^1_{\text{inc}}, \\ \nabla \times \mathbf{E}^0_{\text{sca}} &= -\mu_0 \partial_t \mathbf{H}^0_{\text{sca}}, & \nabla \times \mathbf{E}^1_{\text{sca}} &= -\mu_0 \mu_\infty \partial_t \mathbf{H}^1_{\text{sca}} - \mu_0 (\mu_\infty - 1) \partial_t \mathbf{H}^1_{\text{inc}}. \end{aligned} \tag{4.2.10}$$

Equivalent steps apply for the PML domains and subsequently the CFS-PML coordinate transform which changes the derivatives and hence $\nabla \mapsto \tilde{\nabla}$, leads to

$$\begin{aligned} \tilde{\nabla} \times \mathbf{H}^0_{\text{sca}} &= \varepsilon_0 \partial_t \mathbf{E}^0_{\text{sca}}, & \tilde{\nabla} \times \mathbf{H}^1_{\text{sca}} &= \varepsilon_0 \varepsilon_\infty \partial_t \mathbf{E}^1_{\text{sca}} + \varepsilon_0 (\varepsilon_\infty - 1) \partial_t \mathbf{E}^1_{\text{inc}}, \\ \tilde{\nabla} \times \mathbf{E}^0_{\text{sca}} &= -\mu_0 \partial_t \mathbf{H}^0_{\text{sca}}, & \tilde{\nabla} \times \mathbf{E}^1_{\text{sca}} &= -\mu_0 \mu_\infty \partial_t \mathbf{H}^1_{\text{sca}} - \mu_0 (\mu_\infty - 1) \partial_t \partial \mathbf{H}^1_{\text{inc}}. \end{aligned} \tag{4.2.11}$$

Here, we have applied a standard PML strategy to Maxwell's equations in SF form.

A straightforward implementation of (4.2.11) with the incident plane wave solution (2.7.18) and (2.7.20) yields a wrong formulation and hence a wrong solution. Where does the error come from? During the SF derivation, we have used the fact, that the incident field in free space fulfills Maxwell's equations (see Section 4.1.2). However, the free space solution of (4.2.4) is not equivalent to (2.7.18).

CFS-PML and SF formulation - the correct approach Let us compare (4.2.11) with a different formulation, where we commute the application of the SF formulation and the coordinate stretching $\nabla \mapsto \tilde{\nabla}$. In other words, we start with the total field equations, apply the PML transformation and switch to the SF form, afterwards. As a matter of fact, the equations for vacuum remain the same as there is no incident field due to $\varepsilon_\infty = 1$. On $\tilde{\Omega}^1$ the PML-transformed equations read

$$\begin{aligned} \tilde{\nabla} \times \mathbf{H}^1_{\text{tot}} &= \varepsilon_0 \varepsilon_\infty \partial_t \mathbf{E}^1_{\text{tot}}, \\ \tilde{\nabla} \times \mathbf{E}^1_{\text{tot}} &= -\mu_0 \mu_\infty \partial_t \mathbf{H}^1_{\text{tot}}. \end{aligned} \tag{4.2.12}$$

w.l.o.g., we omit the polarization current for the sake of readability. Splitting into scattered and incident fields yields

$$\begin{aligned} \tilde{\nabla} \times \mathbf{H}^1_{\text{tot}} &= \varepsilon_0 \varepsilon_\infty \partial_t \mathbf{E}^1_{\text{tot}} + \tilde{\nabla} \times \mathbf{H}^1_{\text{inc}} - \varepsilon_0 \partial_t \mathbf{E}^1_{\text{inc}}, \\ \tilde{\nabla} \times \mathbf{E}^1_{\text{tot}} &= -\mu_0 \mu_\infty \partial_t \mathbf{H}^1_{\text{tot}} + \tilde{\nabla} \times \mathbf{E}^1_{\text{inc}} - \mu_0 \partial_t \mathbf{H}^1_{\text{inc}}. \end{aligned} \tag{4.2.13}$$

As we cannot decompose or simplify the term $\varepsilon_0\varepsilon_\infty\partial_t\tilde{\mathbf{E}}^1_{\text{inc}} - \varepsilon_0\partial_t\mathbf{E}^1_{\text{inc}}$, we have to use the incident field $\tilde{\mathbf{E}}$ and $\tilde{\mathbf{H}}$ of an entirely filled PML domain for the SF approach. Maxwell's equations on a material-filled PML domain in the SF formulation hence become

$$\begin{aligned} \varepsilon_0\varepsilon_\infty\partial_t\tilde{\mathbf{E}}^1_{\text{sca}} &= \tilde{\nabla}\times\tilde{\mathbf{H}}^1_{\text{sca}} + \tilde{\nabla}\times\tilde{\mathbf{H}}^1_{\text{inc}} - \varepsilon_0(\varepsilon_\infty-1)\partial_t\tilde{\mathbf{E}}^1_{\text{inc}}, \\ -\mu_0\mu_\infty\partial_t\tilde{\mathbf{H}}^1_{\text{sca}} &= \tilde{\nabla}\times\tilde{\mathbf{E}}^1_{\text{sca}} + \tilde{\nabla}\times\tilde{\mathbf{E}}^1_{\text{inc}} + \mu_0(\mu_\infty-1)\partial_t\tilde{\mathbf{H}}^1_{\text{inc}}, \end{aligned} \tag{4.2.14}$$

or in a simplified form

Maxwell's equations on $\tilde{\Omega}$ in SF form

$$\begin{aligned} \varepsilon_0\varepsilon_\infty\partial_t\tilde{\mathbf{E}}^1_{\text{sca}} &= \tilde{\nabla}\times\tilde{\mathbf{H}}^1_{\text{sca}} + \varepsilon_0(1-\varepsilon_\infty)\partial_t\tilde{\mathbf{E}}^1_{\text{inc}}, \\ -\mu_0\mu_\infty\partial_t\tilde{\mathbf{H}}^1_{\text{sca}} &= \tilde{\nabla}\times\tilde{\mathbf{E}}^1_{\text{sca}} - \mu_0(1-\mu_\infty)\partial_t\tilde{\mathbf{H}}^1_{\text{inc}}. \end{aligned} \tag{4.2.15}$$

Non-vacuum SF-PMLs in frequency-domain The implementation of (4.2.15) is in principal possible. Of course, the analytic solution of the incident field in a PML 'material' is needed.

Analytical solution of a plane wave on $\tilde{\Omega}$ We refer to (2.7.17) for the plane wave solution in the free space and simply extend the derivation in terms of the transformation of the spatial derivatives (4.2.3) [6]. Taking into account the PML-transformed derivative operator, i.e. $\mathbf{k}$ becomes $\tilde{\mathbf{k}}$. The solution of a plane wave in an infinite PML medium hence reads

$$\begin{aligned} \tilde{\mathbf{E}}(\mathbf{r}) &= \mathbf{E}_0\exp(-i\omega t)\exp(i\tilde{\mathbf{k}}\cdot\mathbf{r}), \\ \tilde{\mathbf{H}}(\mathbf{r}) &= \frac{\mathbf{k}\times\mathbf{E}_0}{\omega}\exp(-i\omega t)\exp(i\tilde{\mathbf{k}}\cdot\mathbf{r}), \end{aligned} \tag{4.2.16}$$

with the dispersion relation

$$\left(\frac{\omega}{c_0c_r}\right)^2 - \left|\tilde{\mathbf{k}}\right|^2 = 0, \tag{4.2.17}$$

which leads to

$$\begin{aligned} \left\{\tilde{\mathbf{k}}\right\}_x &= \frac{\omega}{c_0c_r}s_x\sin(\theta)\cos(\phi), \\ \left\{\tilde{\mathbf{k}}\right\}_y &= \frac{\omega}{c_0c_r}s_y\sin(\theta)\sin(\phi), \\ \left\{\tilde{\mathbf{k}}\right\}_z &= \frac{\omega}{c_0c_r}s_z\cos(\theta). \end{aligned} \tag{4.2.18}$$

Let us assume an incident angle $\theta = 0$ and $\phi = 0$ finally leading to the frequency-domain free space solution of a plane wave

Plane wave in CFS-PML

$$\tilde{\mathbf{E}}(\mathbf{r}) = \mathbf{E}_0\exp(-i\omega t)\exp\left(i\omega\frac{z}{c_0c_r}\left(\kappa_z + \frac{\alpha_z\sigma_z}{\alpha_z^2+\omega^2}\right) - \frac{z}{c_0c_r}\omega^2\frac{\sigma_z}{\alpha_z^2+\omega^2}\right). \tag{4.2.19}$$

Remark 4.2.1. *A technical complication arises if the plane wave is obliquely incident with respect to the domain-PML interface. In such a case, the damping at each point $\mathbf{r}$ has to be computed as a function of the distance that the wave will have travelled through the PML domain.*

Non-vacuum SF-PMLs in time domain A rigorous and exact use of (4.2.15) is more complicated in the time-domain. The difficulties arise due to the dispersive behavior of the PML. Dispersive incident fields usually lack analytic inverse Fourier transforms for Gaussian pulses in the sense of (2.7.18) which involve a poly-chromatic signal. Due to dispersion, one has to account for frequency-dependent propagation velocities.

Especially the second term of the propagative part in the exponent is problematic. Hoping for a way out of this dilemma, we have tried an approximated incident field. Assuming realistic material parameters and CFS-PML parameters justifies $\kappa >> \frac{\alpha\sigma}{\alpha^2+\omega^2}$ and we hence neglect the second term of the exponent. The resulting time-harmonic incident signal hence reads

$$\tilde{\mathbf{E}}(\mathbf{r}) \quad = \quad \mathbf{E}_0 \exp(-i\omega t) \exp\left(i\omega \frac{z}{c_0 c_r} (\kappa_z) - \omega^2 \frac{z}{c_0 c_r} \frac{\sigma_z}{\alpha_z^2 + \omega^2} \right), \tag{4.2.20}$$

which easily transforms to

$$\tilde{\mathbf{E}}(\mathbf{r}, t) \quad = \quad \mathbf{E}_0 \sin\left(-i\omega \left(t - \frac{z\kappa_z}{c_0 c_r} \right) \right) \exp\left(-\omega^2 \frac{z}{c_0 c_r} \frac{\sigma_z}{\alpha_z^2 + \omega^2} \right), \tag{4.2.21}$$

in the monochromatic case. However, as soon as we want to use an incident broadband Gaussian pulse, the damping term also becomes problematic due to the varying angular frequency ω. Replacing the frequency dependency in the damping term by a constant frequency, e.g. the central frequency ω_c, introduces wrong decays of the incident field and leads to spuriously reduced or increased incident fields in the SF-PML formulation. In practice, such a 'tweaking' does not work.

4.2.3 Total field / scattered field interfaces inside perfectly matched layers

We have motivated and outlined the PML domain truncation in Section 4.2.2. As a result, we have concluded that scatterers on infinite substrates can neither be efficiently simulated with PMLs in combination with the TF/SF interface nor with the SF formulation (in time-domain).

A sharp look at Figure 4.5 (b) gives rise to a third possibility. If an incident plane wave travels in $\mathbf{e}_z$ direction, i.e. vertically, no PML attenuation appears in the lateral PML zones where $s_z \equiv 0$. In other words, a TF/SF interface can be easily combined with PMLs for normal incidence.

Additionally, appropriate boundary conditions behind the PMLs are either periodic boundaries or PEC plus PML (depending on the polarization of the incident wave).

Proof. The proof is trivial. Insert the incident plane wave with $\mathbf{E}_{\text{inc}} \perp \mathbf{e}_z$ and $\mathbf{H}_{\text{inc}} \perp \mathbf{e}_z$ into (4.2.4). The result follows. □

Comparison of the 'naive' SF-PML formulation and TF/SF interfaces inside PMLs Figure 4.5 (a) shows the absolute value of the electric field $|\mathbf{E}|$ for a single nano cube on an infinite metal substrate. We can clearly see a very suspicious behavior at the domain-PML interface which is due to the incorrect SF-PML time-domain formulation. In contrast, Figure 4.6 depicts the field solution for the setup in Figure 4.5 (b) without a scatterer. The pulse obviously travels correctly inside the domain and the PML domain. This result concludes our chapter on field sources and PMLs. We have now developed a methodology which allows infinite substrates and non-periodic scatterers at the same time.

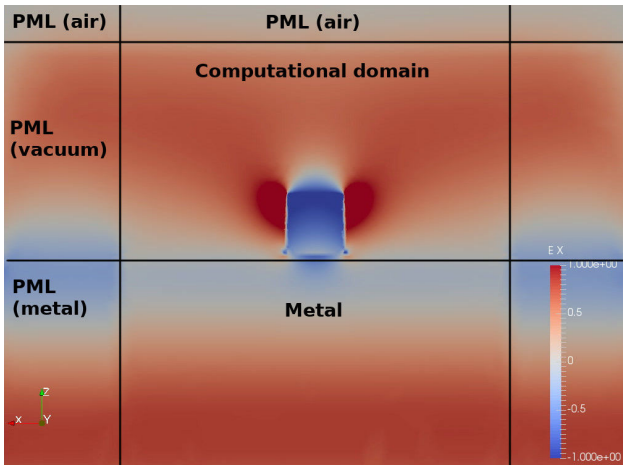

(a) Erroneous incident field for SF-PML The incorrect incident field in the PML regions (left and right outside the black line) leads among less visible errors to artificial wave-fronts at the domain-PML interface. A perfectly matched incident field would lead to plane wave-fronts.

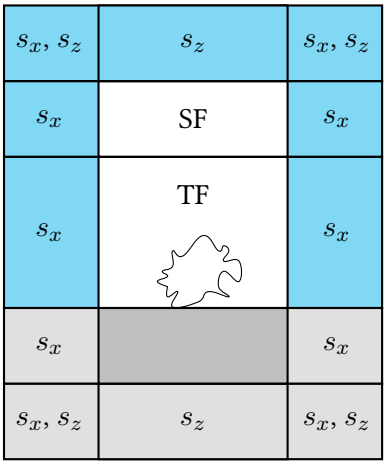

(b) TF/SF-PML setup with scatterer. The TF/SF enters the PML region. It is important to note the position of the TF/SF interface, which is chosen to only penetrate the PMLs in the s_x layer.

Figure 4.5 | SF-PML time domain snapshot and TF/SF-PML setup. Figure (a) shows a field snapshot of the incorrect SF-PML and (b) sketches the TF/SF-PML setup with dispersive metals inside the PML zone.

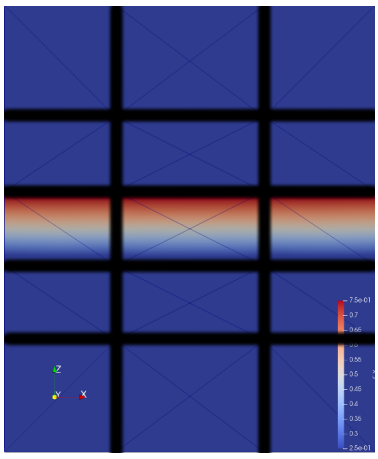

(a) Electric field at t_1. The TF/SF surface 'emits' a plane in $-\mathbf{e}_z$ direction.

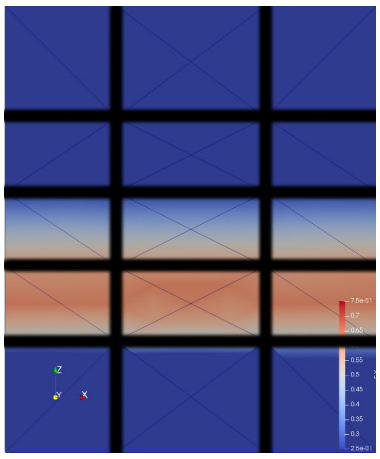

(b) Electric field at t_2. The pulse arrives at the vacuum-dielectric interface without any spurious reflections or wave-fronts at the PML interface.

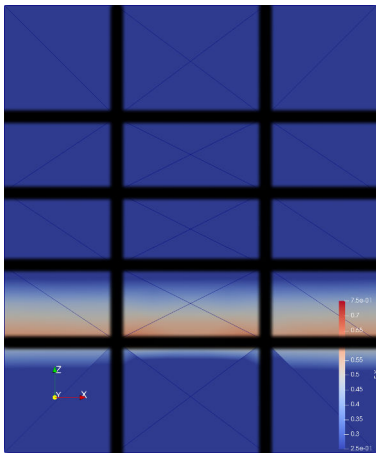

(c) Electric field at t_3. The pulse passes the vacuum-dielectric and interface is evenly attenuated inside along the s_z layer.

Figure 4.6 | TF/SF-PML time domain snapshots. Field plots at different simulation times in a TF/SF-PML setup according to Figure 4.5 (b) (here without scatterer and a dielectric instead of a metal in order to better show the PML attenuation).

4.3 Observables

This section is dedicated to observables which are extractable from 3D time-domain field solutions. We briefly recall these observables for the purpose of readability of this manuscript and to avoid any ambiguities in their definitions whenever our results are compared with external results.

4.3.1 Scattered power - the optical cross section

The optical CS reveals the optical response of a scatterer. We define the real part time averaged Poynting vector

$$\mathbf{S} \quad = \quad \frac{1}{2}\Re\{\underline{\mathbf{E}} \times \underline{\mathbf{H}}^*\}. \tag{4.3.1}$$

Again, splitting the *fields* $\mathbf{E}$ and $\mathbf{H}$ in the same way as we did in (4.1.1), we define an incident, scattered and total field Poynting vector, i.e.

$$\mathbf{S}_l \quad = \quad \frac{1}{2}\Re\{\underline{\mathbf{E}}_l \times \underline{\mathbf{H}}_l^*\}, \qquad \text{with } l \in \{\text{inc}, \text{sca}, \text{tot}\}. \tag{4.3.2}$$

According to Section 2.3.5, the total and scattered time-averaged absorbed powers respectively read

$$\begin{aligned} P_{\text{abs}} \quad &= \quad -\int\limits_{\partial\Omega_{\text{TF/SF}}} \mathbf{S}_{\text{tot}} \cdot \mathbf{n}\, \mathrm{d}^2 r, \\ P_{\text{sca}} \quad &= \quad \int\limits_{\partial\Omega_{\text{TF/SF}}} \mathbf{S}_{\text{sca}} \cdot \mathbf{n}\, \mathrm{d}^2 r. \end{aligned} \tag{4.3.3}$$

The three different Quantity of Interest (QoI), namely the absorption CS, the scattering CS, and the extinction CS are finally defined by

Cross-section

$$\begin{aligned} CS_{\text{abs}} \quad &:= \quad \frac{P_{\text{abs}}}{|\mathbf{S}_{\text{inc}}|}, \\ CS_{\text{sca}} \quad &:= \quad \frac{P_{\text{sca}}}{|\mathbf{S}_{\text{inc}}|}, \\ CS_{\text{ext}} \quad &:= \quad CS_{\text{abs}} + CS_{\text{sca}}. \end{aligned} \tag{4.3.4}$$

Here, $\partial\Omega_{\text{TF/SF}}$ is a closed surface as depicted in Figure 4.1. The incident power $|\mathbf{S}_{\text{inc}}|$ is analytically available if $\mathbf{E}_{\text{inc}}$ is analytically known together with its temporal Fourier transform. We can derive it from the incident Gaussian pulse (2.7.18) by the help of the temporal Fourier transform (2.2.1)

$$\underline{\mathbf{E}}_{\text{inc}} \quad = \quad \mathbf{E}_0 \frac{i\sigma}{2} \exp\left[i\omega(t_0 + \mathbf{k}\cdot\mathbf{r})\right] \left(\exp\left[-\frac{1}{2}\sigma^2(\omega-\omega_{\text{c}})^2\right] - \exp\left[-\frac{1}{2}\sigma^2(\omega+\omega_{\text{c}})^2\right] \right), \tag{4.3.5}$$

where t_0 determines the temporal arrival of the pulse. Eventually, we obtain

$$|\mathbf{S}_{\text{inc}}| = |\mathbf{E}_{\text{inc}}|^2. \tag{4.3.6}$$

4.3.2 Reflection and transmission coefficient in a unit-cell

Periodic structures allow for the definition of reflection and absorption coefficients. These coefficients provide a spectral information about the frequency-depend reflection and transmission properties of a structure. Reusing the already defined expressions, we define the reflection coefficient by

Reflectance

$$R := \frac{P_{\text{sca}}}{\int_{\partial\Omega_{\text{TF/SF}}} \mathbf{S}_{\text{inc}} \cdot \mathbf{n} \, \mathrm{d}^2 r}, \tag{4.3.7}$$

and analogously

Transmission

$$T := \frac{P_{\text{abs}}}{\int_{\partial\Omega_{\text{TF/SF}}} \mathbf{S}_{\text{inc}} \cdot \mathbf{n} \, \mathrm{d}^2 r} \tag{4.3.8}$$

for the transmission coefficient. Here, $\partial\Omega_{\text{TF/SF}}$ is a pseudo-closed surface as shown in Figure 4.7 (a). If lossy materials are involved, the definition of an additional absorption coefficient

$$A := 1 - R - T, \tag{4.3.9}$$

may be useful.

4.3.3 Ohmic losses

Heat losses or Ohmic losses have already been mentioned in Section 2.3.5 (Poynting's theorem). The definition of the time-averaged Ohmic-loss inside a closed volume $\Omega_{\text{ohm}} \subset \Omega$ is given by

Ohmic-loss

$$P_{\text{ohm}} := \frac{\int_{\Omega_{\text{ohm}}} \underline{\mathbf{J}}^{\star} \cdot \underline{\mathbf{E}} \, \mathrm{d}^3 r}{2|\mathbf{S}_{\text{inc}}|}. \tag{4.3.10}$$

4.3.4 Electron energy loss probability

EELS signals mimic the energy loss of an electron beam due to its electromagnetic interaction with a Device Under Test (DUT). Let us suppose such an EELS electron beam in the vicinity of a metallic sphere as depicted Figure 4.7 (b). When the electron gets sufficiently close to the sphere, the electromagnetic field of the moving charge induces a scattered field on the sphere. For metallic spheres, a SPP will be excited. This excitation is an energy transfer from the kinetic electron energy to the SPP resonance. Hence, after the electron-sphere interaction, the electron will be slowed down due to its energy loss.

Typical EELS devices, however, provide electron beams at beam energies of about $0.6c_0$ in combination with extremely low currents of the order of nA, leading to quasi-single electron beams [151]. Such high energy electron beams in combination with very short interaction ranges of nanophotonic devices of ≈ 100 nm, leads to a negligible change in velocity. This does not mean that the actual energy-change is negligible. Energy changes of several eV can precisely be measured with modern spectrometers.

In conclusion, we can model EELS by a single electron beam with constant velocity, often referred to as No Recoil Approximation (NRA). The theoretical loss due to the electron-DUT interaction can further be described by the quantity

$$\Delta\mathcal{E} \;:=\; q\int_{-\infty}^{\infty} \mathbf{v}\cdot\mathbf{E}_{\mathrm{sca}}(\mathbf{r}_{\mathrm{elec}}(t),t)\,\mathrm{d}t. \tag{4.3.11}$$

Here, q is the charge of the electron, $\mathbf{v}$ the velocity of the electron and $\mathbf{r}_{\mathrm{elec}}(t)$ the position of the electron, i.e. its trajectory. The previous expression can be cast into

$$\Delta\mathcal{E} \;:=\; \int_{0}^{\infty} \hbar\omega\Gamma_{\mathrm{EELS}}\,\mathrm{d}\omega, \tag{4.3.12}$$

which now allows the definition of a electron energy loss probability

EELS-probability

$$\Gamma_{\mathrm{EELS}}(\omega) \;:=\; \frac{q\sqrt{2}}{\sqrt{\pi}\hbar\omega}\int_{-\infty}^{\infty} \Re\left\{\exp\left(i\omega t\right)\mathbf{v}\cdot\underline{\mathbf{E}}_{\mathrm{sca}}(\mathbf{r}_{\mathrm{elec}}(t),\omega)\right\}\,\mathrm{d}t. \tag{4.3.13}$$

Proof.

$$\begin{aligned}
\Delta\mathcal{E} &= q\int_{-\infty}^{\infty} \mathbf{v}\cdot\mathbf{E}_{\mathrm{sca}}(\mathbf{r}_{\mathrm{elec}}(t),t)\,\mathrm{d}t,\\
&= q\int_{-\infty}^{\infty} \mathbf{v}\cdot\Re\left\{\mathcal{F}^{-1}\left\{\underline{\mathbf{E}}_{\mathrm{sca}}(\mathbf{r}_{\mathrm{elec}}(t),\omega)\exp\left(i\omega t\right)\right\}\right\}\,\mathrm{d}t,\\
&= q\sqrt{\frac{2}{\pi}}\int_{-\infty}^{\infty}\int_{0}^{\infty} \mathbf{v}\cdot\Re\left\{\underline{\mathbf{E}}_{\mathrm{sca}}(\mathbf{r}_{\mathrm{elec}}(t),\omega)\exp\left(i\omega t\right)\right\}\,\mathrm{d}\omega\,\mathrm{d}t,\\
&= \int_{0}^{\infty} q\sqrt{\frac{2}{\pi}}\int_{-\infty}^{\infty} \mathbf{v}\cdot\Re\left\{\underline{\mathbf{E}}_{\mathrm{sca}}(\mathbf{r}_{\mathrm{elec}}(t),\omega)\exp\left(i\omega t\right)\right\}\,\mathrm{d}t\,\mathrm{d}\omega.
\end{aligned} \tag{4.3.14}$$

Here, we suppose that the integrals in time and angular frequency are formally exchangeable. □

Equation (4.3.13) gives rise to the frequency-dependent energy loss of an electron in the NRA.

Remark 4.3.1. *In simulations with a finite computational domain, the integral in* (4.3.13) *has to be truncated. This integration path has to be chosen such that it sufficiently accounts for all the scattered fields. The impact of the integration length will be studied in Section 5.2.5.*

The authors in [97, 153] have found increasing discrepancies between analytical Mie EELS spectra and DGTD simulations for beam velocities beyond $0.4c_0$*. On our opinion, the observed effect may be due to an erroneous formula for the electric and magnetic field of a moving charge in free-space. Using the correct formula* (2.7.33) *leads to a convergence of the DGTD results. See Section 5.2.5 for details.*

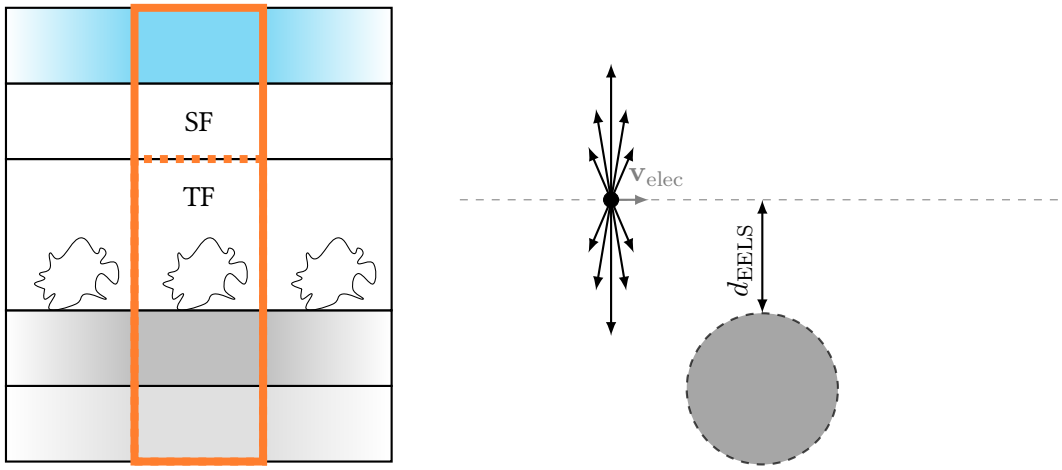

(a) Periodic unit cell setup. The unit cell contains a TF/SF-interface (dashed line).

(b) EELS-setup. The electron travels with the velocity $\mathbf{v}_{\mathrm{elec}}$ at the distance d_{EELS} to the surface of the nano-sphere.

Figure 4.7 | Periodic unit-cell and EELS-setup.

4.4 Optimization, inverse problems and uncertainty quantification

Optimization In the course of this thesis several optimization algorithms have been used. Although they are a key ingredient for the solution of the solution of the inverse problems in Section 6.1 and 6.2, the development and implementation of these algorithms was not part our work.

Almost all the optimization problems in the scope of this work are intrinsically derivative-free because the cost-functions rely on RCWA or DGTD simulations. Typical derivative-free algorithms among others are for example evolutionary algorithms (CMA-ES (CMA-ES)) [57], genetic algorithms [80], particle swarm [74], Nelder-Mead [130], simulated annealing [76] and pattern search [147].

The choice of the optimal algorithm for a given optimization problem is not always easy. Depending on the different attributes of the cost-function like its computational cost, its regularity and smoothness as well as the dimensionality of free parameters, an optimal a priori selection is not trivial.

Considering full-wave optical simulations as cost-functions, e.g. DGTD runs on a cluster computer, rapidly comes with simulation times of several hours per cost-function call. Classic optimization algorithms like CMA-ES or pattern search commonly require hundres of cost-function evaluations.

Modern meta-model based optimization algorithms like Gaussian-process models (Kriging) [17] in combination with derivative based optimization provide a lucrative and powerful alternative. Those methods build local meta-models around a local minimum in an adaptive way based on a Gaussian-process model.

Throughout this work, we predominantly rely on pattern-search and meta-model based optimization.

Inverse problems Section 6.1 and 6.2 are concerned with the solution of inverse problems. These inverse problems will be formulated as optimization problems. The arising optimization problems are tackled with pattern-search, meta-model based optimization and particle swarm methods.

UQ [1] In the context of numerical and applied mathematics or, accordingly, computational science and engineering, the term UQ [139] refers to a comparably new field of study which develops methods aim-

[1] With the kind permission from [120].

ing at quantifying the impact of input variability upon a computational model's output. We refer to the considered output as the QoI and denote it with q. The input parameters are denoted with $\mathbf{z} = (z_1, z_2, \ldots, z_N)$. The relation between inputs and QoI is denoted with f, such that $q = f(\mathbf{z})$, with $f : \mathbb{R}^N \to \mathbb{R}$. This notation assumes that q is a scalar quantity, however, the consideration of multiple real or complex QoI is also possible. In this context, f can be understood as an abstract representation of the underlying mathematical and computational model which produces a value of the QoI, given a set of input values. Moreover, f is assumed to be a completely deterministic function, i.e. the exact same q is produced for a fixed $\mathbf{z}$.

Due to input modeling uncertainties, e.g. stemming from measurement inaccuracies or manufacturing tolerances, we model $\mathbf{z}$ as a random vector defined on the probability space (Θ, Σ, P), such that $\mathbf{z} : \Theta \to \Gamma \subset \mathbb{R}^N$, and characterized by the Probability Density Function (PDF) $\varrho(\mathbf{z})$, $\varrho : \Gamma \to \mathbb{R}_+$. Assuming that $\mathbf{z}$ consists of mutually independent Random Variables (RVs) $z_1, z_2, \ldots, z_N$, the multivariate PDF is given as

$$\varrho(\mathbf{z}) = \prod_{n=1}^{N} \varrho_n(z_n), \tag{4.4.1}$$

where ϱ_n refers to the univariate PDF of the n-th RV. Then, the QoI $q = f(\mathbf{z})$ is itself a RV. Quantifying uncertainty with respect to q typically involves computing statistical measures, such as its expectation value, variance, higher order moments, PDF, quantiles, exceedance probabilities or sensitivity indices, to name a few.

We assume that f represents a complex computational model, such that modifications to the underlying software and/or numerical solvers are undesirable. For that reason, UQ studies must be performed in a black-box fashion. Moreover, we assume that the complexity and, accordingly, the execution time of a single model evaluation, corresponding to a single call of function f, is significantly higher than typical numerical operations. Then, the overall cost of a UQ study is dominated by the number of black-box model evaluations, respectively, function calls. Monte Carlo (MC) sampling [89] is the most commonly used method for black-box UQ studies. However, its slow convergence rate of $\mathcal{O}\left(M^{-0.5}\right)$, where M denotes the number of generated random samples and corresponding function calls, may lead to unacceptable computational costs. Under the further assumption that f is a smooth, ideally analytic, function with respect to $\mathbf{z}$, methods based on polynomial approximations of f may be employed [87, 163], in order to achieve algebraic or even exponential convergence rates. Such methods evaluate the QoI for a set of relatively few realizations of $\mathbf{z}$ and typically employ interpolation [3, 112, 164] or regression [7, 101, 100] schemes to construct the approximation. One such approach is the *stochastic collocation* method [3, 112, 164], which will be the method of choice in the context of the present work.

5 Simulations

Chapter 2 has provided a comprehensive overview of the underlying equations and their analytical solutions. Aiming for more general solutions for arbitrary geometries has constituted the numerical algorithms in Chapter 3. Carrying forward this reasoning to physical interpretations of numerically obtained solutions, we have established a set of physically interpretable observables in Chapter 4.

This Chapter now discusses implementation aspects, numerical convergence studies together with more complex validation examples, ensuring an error-free and robust software. Having a reliable DGTD code available, we investigate spherical dimer systems for plane wave excitations and EELS studies and High Performance Computing (HPC) aspects.

5.1 Implementation and third party software

This Chapter is supposed to provide a brief overview on the numerical implementation of Chapter 3 and 4 as well as the usage deployment of third party software. Figure 5.1 illustrates a typical workflow of our software. Starting with a geometry model, we create a computational mesh, i.e. triangles, tetrahedra or hexahedra, which will serve as a discretized computational domain. These steps are followed by the actual execution of the DGTD solver and the exploitation of the results in terms of visualization or further post-processing for physical or numerical interpretations.

5.1.1 Geometry model and meshing

A major part of the simulation examples of this work are based on the scripting input of GMSH [51] with https://www.opencascade.com/ (openCascade) engine extension. Depending on the individual meshing difficulties, we either directly use GMSH's mesh tool or Distene's MeshGems.

5.1.2 Optimization

Most optimization results rely on the https://team.inria.fr/acumes/software/ (Famosa) library or the https://fr.mathworks.com/products/optimization.html (Matlab) optimization toolbox.

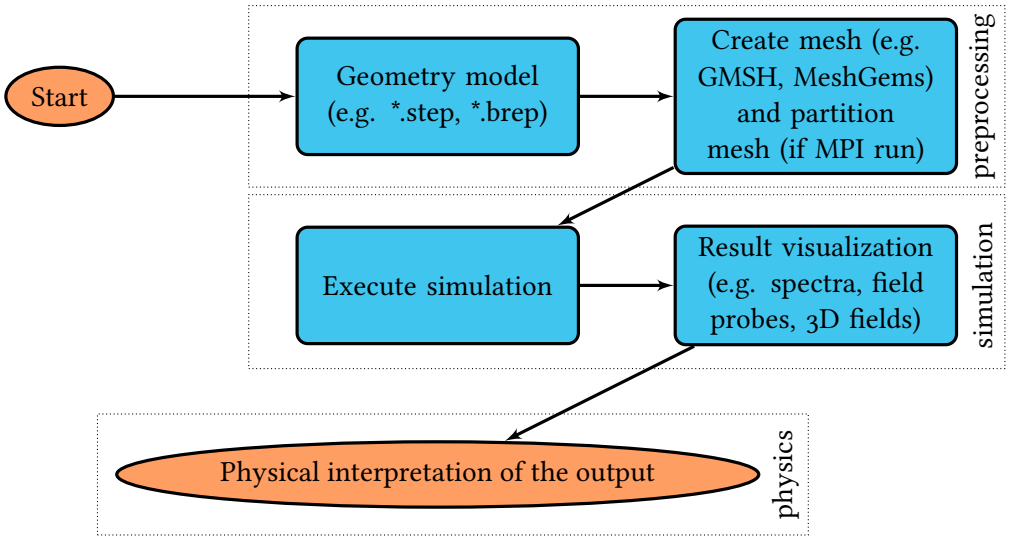

Figure 5.1 | DIOGENeS workflow.

5.1.3 Visualization

We have mainly used https://team.inria.fr/gamma3/project-presentation/gamma-software/ (Vizir) and https://www.paraview.org/ (Paraview) for mesh visualizations as well as for 2D and 3D simulation results.

5.1.4 2D implementation

Proof of principle tests have been first realized in an easy-to-manipulate 2D code. Key features of this code are:

- Affine triangular meshes
- Polynomial orders up to $\mathcal{P}_4$
- Leap-Frog and LSRK time integration
- Centered and upwind DGTD
- Local time stepping (not further detailed in this work) in the fashion of [118]
- PEC, PMC, ABC and hard-wall boundary conditions
- TF/SF-interfaces
- CS computation
- Field probes and 2D field visualization

5.1.5 3D implementation - DIOGENeS

Most of the relevant 3D development steps have been tested and eventually contributed to the DIOGENeS software suite. Important key features for this work are:

- Affine and curvilinear tetrahedral meshes

- Polynomial orders up to $\mathcal{P}_n$
- LSRK time integration
- Centered and upwind DGTD
- PEC, PMC, ABC, periodic, hard-wall and soft-wall boundary conditions
- TF/SF-interfaces
- SF source formulation
- CS, absorption, EELS computation
- Field probes and 3D field visualization
- MPI parallelization

5.2 Validation

This part deals with numerical results obtained with our 2D and 3D implementation of the proposed DGTD method. We start with different validation test cases ranging from numerical convergence rates to the importance of boundary conforming curvilinear elements for efficient simulations of scattering problems in nanophotonics.

5.2.1 2D Hydrodynamic test cavity and convergence study

We omit the convergence study of the 2D implementation. Interested readers may be referred to [134].

5.2.2 3D Hydrodynamic test cavity and convergence study

In order to validate our implementation of the previously presented DGTD solver we first perform a numerical convergence study. Here, we consider a simple test problem for which we have an analytical time-domain solution. This will be done for (2.5.1) when neglecting the ODE part. We propose to use the method of manufactured solutions, i.e. we artificially construct a solution that will satisfy (2.6.4) with a source term and hence allows us to determine the convergence rates. Inspired by [85, 134] we exploit the analytical eigenmode solution of the homogeneous Maxwell's and hydrodynamic equations on a rectangular cavity domain.

Manufactured solution of the coupled system We denote the eigenmode solutions for Maxwell's (2.7.2) equations and the hydrodynamic part (2.7.10) by $\mathbf{H}^{\text{art}}, \mathbf{E}^{\text{art}}$ and $\mathbf{J}^{\text{art}}, Q^{\text{art}}$ (see [134, 85] for details). We artificially fill this cavity with vacuum for Maxwell's equations and with a dispersive medium characterized by specific values of ω_{P} and β for the hydrodynamic Drude model while we neglect damping, i.e. $\gamma \equiv 0$ (which is not necessary). The resulting formulation of the coupled problem including the manufactured solution hence reads

$$\begin{aligned} \nabla \times \mathbf{E} + \mu_0 \partial_t \mathbf{H} &= 0, \\ \nabla \times \mathbf{H} - \varepsilon_0 \varepsilon_\infty \partial_t \mathbf{E} &= \mathbf{J} - \mathbf{J}^{\text{art}}, \\ \beta^2 \nabla Q - \partial_t \mathbf{J} &= -{\omega_{\text{P}}}^2 \varepsilon_0 (\mathbf{E} - \mathbf{E}^{\text{art}}), \\ \nabla \cdot \mathbf{J} - \partial_t Q &= 0. \end{aligned} \tag{5.2.1}$$

Table 5.1 | Number of tetrahedral for cubic cavity Mesh M1 is the coarsest and M5 is a systematically refined version of M1.

	M1	M2	M3	M4	M5
# Tets	48	384	3072	24576	196608

Table 5.2 | Hydrodynamic convergence rates. Numerically obtained convergence rates for the hydrodynamic test cavity solved by the DGTD method with centered fluxes (upper, $\mathcal{P}_0$ to $\mathcal{P}_4$) and upwind fluxes (lower, $\mathcal{P}_0$ to $\mathcal{P}_4$) and a LSRK time integration scheme. Mesh M1 is the coarsest mesh and M5 the most refined one.

	M1 $\rightarrow$ M2	M2 $\rightarrow$ M3	M3 $\rightarrow$ M4	M4 $\rightarrow$ M5
$\mathcal{P}_0$	-0.44	0.36	0.31	**0.09**
$\mathcal{P}_1$	-1.50	0.63	1.31	**2.04**
$\mathcal{P}_2$	4.43	4.08	2.15	**2.47**
$\mathcal{P}_3$	3.83	3.81	3.65	**3.01**
$\mathcal{P}_4$	5.13	3.66	4.89	**4.11**
$\mathcal{P}_0$	0.03	0.08	0.11	**0.13**
$\mathcal{P}_1$	0.12	0.77	2.29	**2.86**
$\mathcal{P}_2$	2.59	4.48	3.69	**3.06**
$\mathcal{P}_3$	5.68	4.19	3.96	**4.01**
$\mathcal{P}_4$	4.68	4.24	4.08	**4.07**

Let us define a time dependent error norm $||u - u^{\mathrm{a}}||^2_{\mathcal{L}^2(\Omega)}$ with $u \in \{\mathbf{H}, \mathbf{E}, \mathbf{J}, Q\}$ and $(\cdot)^{\mathrm{a}}$ being the analytical solution, on the domain Ω by

$$err = ||u - u^{\mathrm{a}}||^2_{\mathcal{L}^2(\Omega)} := \sum_{i \in \mathcal{N}_\Omega} ||u_i - u_i^{\mathrm{a}}||^2_{\mathcal{L}^2(\Omega_i)}. \tag{5.2.2}$$

The convergence rates are computed by comparing the evolution of the error norm while progressively refining the computational mesh. Starting with a coarse Mesh (M)1 and successively refining by two (i.e. h becomes $h/2$ at each refinement step) leads to a sixteen times finer mesh M5 (Table 5.1 shows the total number of tetrahedra). Simulations are run for 100 oscillation periods on each mesh, and for each polynomial order. Table 5.2 summarizes the convergence rates for the DGTD-LSRK scheme with centered fluxes. The results are in coherent [111] for the pure Maxwell operator and theoretical results of the DGTD method [44, 58, 86] as well as our results in Section 3. We obtain sub-optimal convergence rates for the centered scheme, i.e. n^{th} order for DGTD-$\mathcal{P}_n$ with n the polynomial order of the DG Ansatz space. For DGTD-$\mathcal{P}_n$ with upwind fluxes we obtain optimal convergence rates, which is even better than our theoretical result.

5.2.3 Mie scattering in 2D

Section 5.2.1 and 5.2.2 have shown the numerical convergence of the proposed DGTD scheme and hence confirmed the theoretical results in Section 3.1.

Realistic scattering problems are more complicated than simple rectangular cavity problems and require a set of more technical features like incident fields and radiation boundary conditions for the domain truncation. Of course, adding additional technical features bears the danger of implementation errors. We therefore want to assess more advanced test cases in order to add an additional validation stage and to obtain a first physical result.

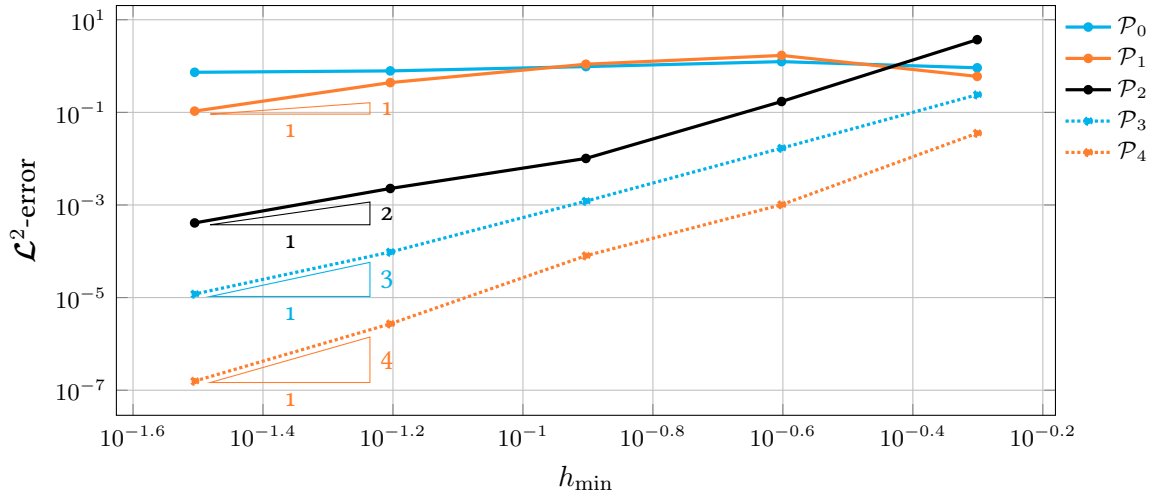

Figure 5.2 | $\mathcal{L}^2$-error for *centered* DG Maximum values of the L2-error for *centered fluxes* and a LSRK time integrator.

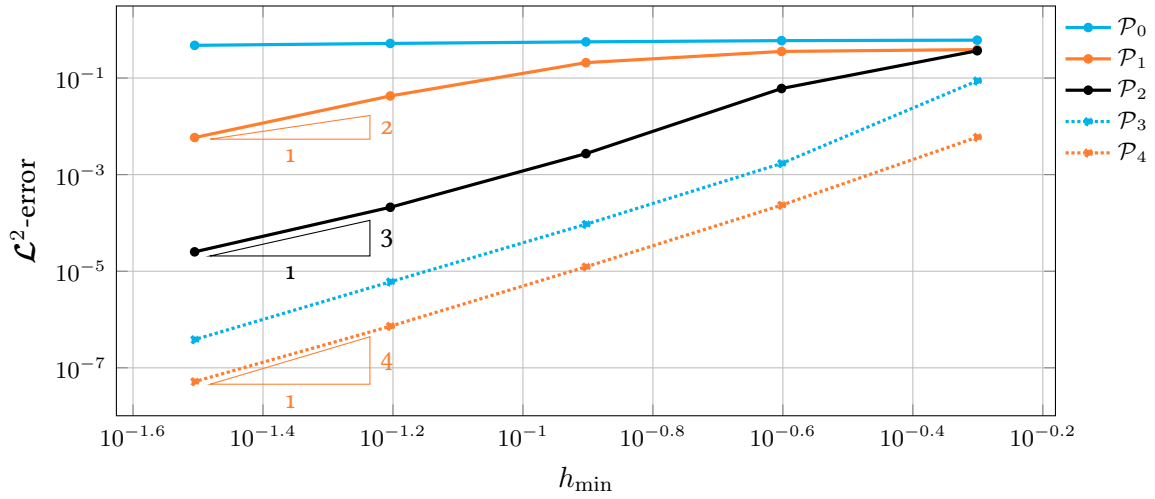

Figure 5.3 | $\mathcal{L}^2$-error for *upwind* DG Maximum values of the $\mathcal{L}^2$-error for *upwind fluxes* and a LSRK time integrator.

Our scenario of choice consists in the scattering of an infinitely long nano-rod, yielding a 2D setup due to its invariance along the rod axis. This scenario allows us to test our 2D DGTD implementation. Equivalent benchmarks of this kind have been carried out in recent works [61, 102].

We have performed multiple simulations on different (already very refined) affine triangular meshes. Figure 5.4 illustrates the different refinement levels of the gold nano-rod.

Remark 5.2.1. *Time-domain simulations have to ensure a sufficiently long simulation time in order to let all fields decay to (almost) zero. If this criterion is not respected, observables like CS or the volumic absorption may be erroneous due to an incorrect Fourier-transform.*

Table 5.3 summarizes the physical parameters and the simulation time we have used for the CS results in Figure 5.5.

The relatively high refinement is necessary due to the short wavelength of the bulk plasmons that appear for angular frequencies beyond the plasma angular frequency ω_P. Those bulk plasmon resonances

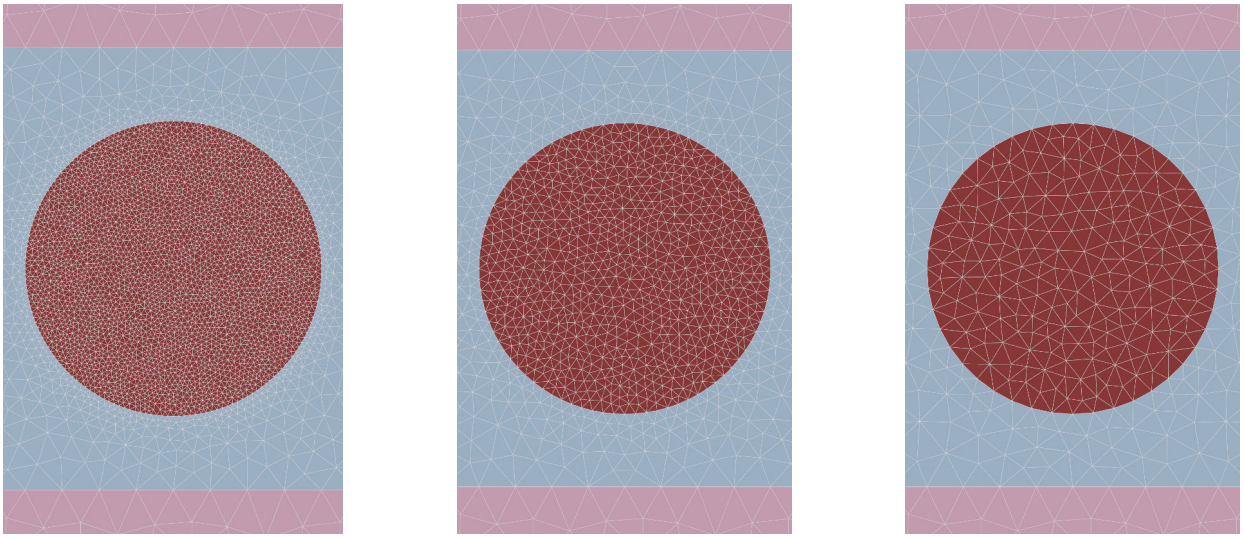

(a) M1 **(b)** M2 **(c)** M3

Figure 5.4 | Nano wire meshes. Each mesh mainly consists of a SF vacuum area (light red), a TF vacuum area (light blue), and the metallic circle (dark red). The extinction CS is computed on the TF/SF surface. The nano-wire's radius is $R = 2$ nm. M1 is already sufficiently refined and the CS spectra in Figure 5.5 for M2 and M3 are not distinguishable.

Table 5.3 | Simulation parameters

	ω_P	γ	β^2	R	$T_{\max}$
Run (R): 1	1.36e16 $1/s$	3.23e13 $1/s$	6.9738e11 m^2/s^2	2 nm	3.33e−14 s

do not exist if local dispersion models are employed. We refer to [106, 96] for comprehensive discussions. Figure 5.6 compares the field plots of a locally dispersive result and a simulation using the nonlocal hydrodynamic model. Bulk plasmons are only present in the nonlocal case (6^{th} bulk resonance).

5.2.4 Mie scattering in 3D

Section 5.2.3 has validated our 2D implementation and we now continue in the same way for the 3D implementation. The following discussion contains two main directions. First, we compare our numerical DGTD solution of a spherical scatterer with analytical Mie solutions for pure validation purposes. This study shows the performance of reasonably coarse affine tetrahedral meshes in combination with high order polynomial basis functions. Secondly, we investigate and show a significant performance increase due to curvilinear tetrahedra. The second part can be put into context as an applied continuation of Section 3.2.2.

The scattering of a single sphere in vacuum is a classic nanophotonics benchmark example. Beyond applications where the relatively simple result of an isolated sphere in vacuum already explains several physical effects, the scattering of a single sphere also comes with an analytical solution. This, of course, permits us to compare the performance of our method with so called Mie solutions. Gustav Mie has published his work on the scattering of spheres in vacuum in the early 20^{th} century [99] and his initial works have been extended to more complex material configurations [26], different coordinate systems [102] and even nonlocal dispersion laws [131, 20, 28].

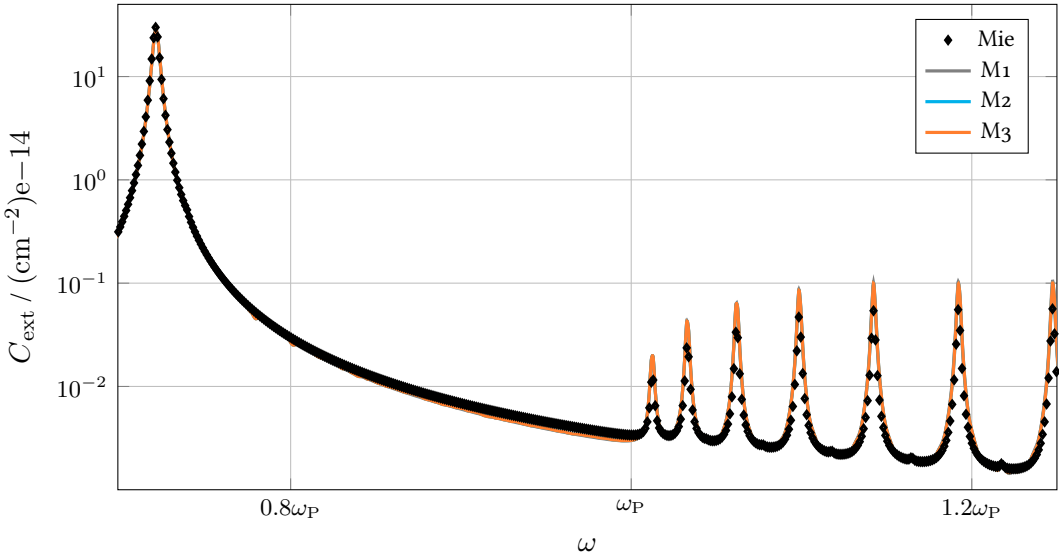

Figure 5.5 | Extinction CS of an infinitely long nanowire. Comparison of the analytical Mie solution and the numerical DGTD result with second order polynomials. $R = 2$ nm, $\omega_{\text{P}} = 13.6\text{e}15\ ^{rad}/_{\text{s}}$, $\gamma = 3.23\text{e}13\ ^{rad}/_{\text{s}}$ and $\beta = 0.835\text{e}6\ ^{m}/_{\text{s}}$. The here used meshes differ by means of the local mesh refinement inside the metallic regime. Here, M1 is the finest and M3 the most coarse mesh. M1 is already sufficiently refined and the CS spectra for M2 and M3 are not distinguishable.

From a more methodological point of view, the Mie sphere appears to be significantly more complex in comparison to the test problem of a cubic cavity that we have used for the convergence study in the previous section. Among others, the sphere involves the additional boundary condition (2.5.2) at the interface between the metallic sphere itself and the surrounding vacuum. Furthermore, it demands a free space approximation of the infinite vacuum. Regarding the free space approximations, we have used CFS-PMLs [6, 82] in order to minimize spurious reflections from the artificial domain truncation. Since such a setup forbids a direct imposition of the incident field, i.e. a pulsed plane wave in our case, via for example first order Silver-Müller radiation conditions [104], we use a TF/SF approach [143].

Affine elements and centered DG

As for this first 3D validation stage, we only rely on linear tetrahedral meshes and centered DG. It can thus be seen as the three dimensional analogue of Section 5.2.3. From a methodological point of view, only the time integration scheme has changed from a second order LF algorithm to a modern optimized LSRK scheme. Figure 5.8 depicts the extinction CS of a metallic nano-sphere.

Below the plasma frequency ω_{P}, local and nonlocal dispersion lead to similarly shaped extinction CS spectrum. This is not the case anymore for frequencies above ω_{P}. Nonlocality allows bulk plasmons, also referred to longitudinal modes [96], which are forbidden for Mie spheres consisting of locally dispersive metals.

In terms of the validation of our DGTD implementation (see Figure 5.8), we observe a fairly poor result for first order polynomial basis functions, i.e. DGTD$-\mathcal{P}_1$. Although the first resonance is relatively well observable, the second peak is already completely red-shifted with respect to the analytical solution. For higher frequencies, being equivalent to shorter wavelengths, the DGTD$-\mathcal{P}_1$ on the mesh in Figure 5.7 completely fails. Increasing the polynomial order to second order polynomials $\mathcal{P}_2$ yields an accurate solution of the first two resonances and also contains the first two bulk plasmon peaks. However, spurious solutions due to the centered fluxes within the DG scheme keeps a clear resonance detection inaccurate for

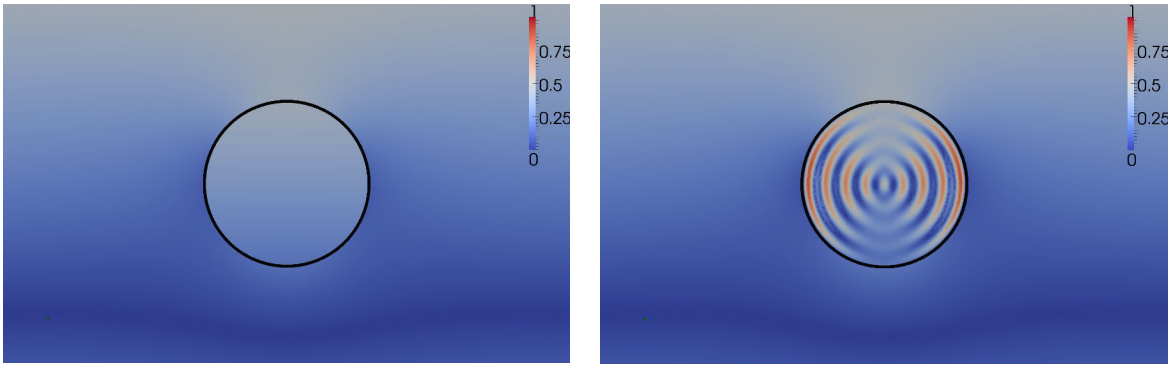

(a) Local dispersion **(b)** Nonlocal dispersion

Figure 5.6 | Nano-rod field plot. Field solutions of a dispersive nano-rod with a radius of 2 nm. The plots show the Fourier-transformed time-domain solution of $\left|\{\mathbf{E}\}_x\right|$ for the local and nonlocal dispersion model at $\omega = 1.963\omega_{\mathrm{P}}$.

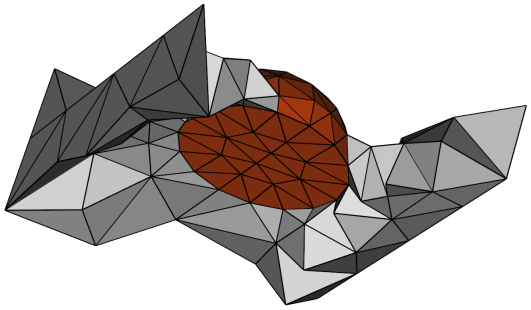

Figure 5.7 | Affine nano-sphere mesh. Red: Linear tetrahedra discretization of the sphere domain. Gray: Discretized surrounding vacuum domain.

the bulk plasmons. Allowing even higher order polynomials of order $\mathcal{P}_3$ leads to a very clean numerical solution, even for the bulk plasmons. As an intermediate result, we conclude:

- Classical centered DG for Maxwell's equations coupled to a linearized hydrodynamic dispersion model suffers from spurious solutions, being in line with well known results from the literature [54].
- Increasing the polynomial order of the basis functions and benefit from the flexible high order nature of the DGTD scheme for a fixed tetrahedral mesh, significantly improves the quality of the solution.

Accuracy and performance improvements due to upwind fluxes and curvilinear elements will be discussed in the following.

Curvilinear elements and upwind DG

We now investigate the surface approximation of a single sphere and its influence on the resulting extinction CS spectra [135]. Here, we compare different polynomial orders of the DG basis functions as well as the accuracy, and hence performance gain if curvilinear tetrahedra are used. Figure 5.9 shows the computational meshes we have used for this study. There are two topologically different meshes M1 and M2, shown in Figure 5.9 (a) and (c), respectively. Both meshes represent the same physical sphere and the

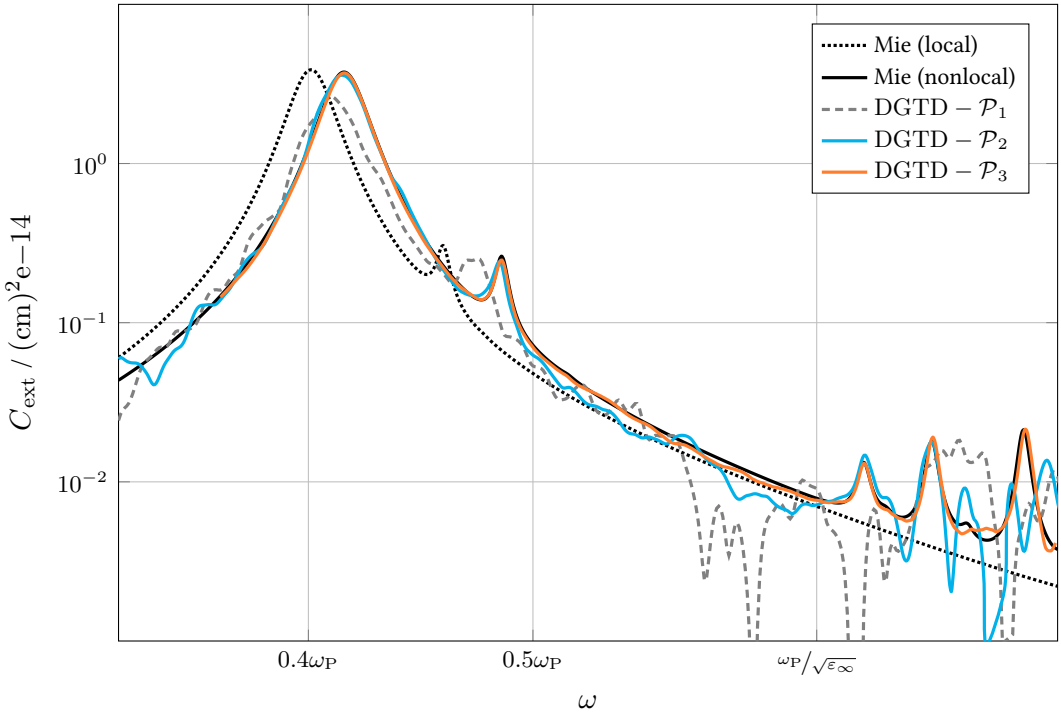

Figure 5.8 | Solution of a nonlocal Mie Sphere. Extinction CS spectra of the local an nonlocal Mie solution in comparison to the numerical Mie solution for polynomial expansions of order one to three.

geometrical misrepresentation of M1 (a) is quite obvious as the sphere hardly resembles a sphere at all - it rather represents a faceted particle. Performing an $h-$refinement leads to M2 (c) which visibly better approximates a sphere. Activating curvilinear elements gives curved versions of M1 and M2 as depicted in Figure 5.9 (b) and (d).

Using the same plane wave source, same boundary conditions and the same QoI, i.e. extinction CS, as before, we can obtain the extinction CS spectra in Figure 5.10 for the two different meshes on affine and curvilinear tetrahedra, respectively. Obviously, mesh M1 with affine tetrahedra leads to a very poor result, similarly for first order $\mathcal{P}_1$ and fourth order $\mathcal{P}_4$ polynomials as shown in Figure 5.10 (a). The $\mathcal{P}_1$ solution only reproduces the first resonance at about $0.675\omega_{\text{P}}$ although it is supposed to be at $0.7\omega_{\text{P}}$. Additionally, the second and third resonance of the Mie spectrum at about $0.825\omega_{\text{P}}$ and $0.875\omega_{\text{P}}$ are completely inobservable.

Increasing the polynomial order to $\mathcal{P}_4$ shifts the first resonance almost to the correct angular frequency, the second resonance now appears in the spectrum and is even relatively close to the correct resonance angular frequency. A third resonance seems to build up at $0.95\omega_{\text{P}}$ which would be quite far from the correct position if we relate it to the actual third resonance in the Mie spectrum. If we now switch to the curvilinear version of M1, the situation changes. The first resonance of the $\mathcal{P}_1$ solution is slightly shifted towards the correct value and the second resonance tends to build up.

However, both resonances positions are far off and the absolute as well as the relative amplitudes completely fail with respect to the Mie solution. Again, increasing the polynomial order to $\mathcal{P}_4$, the numerical solution significantly approaches the analytical Mie solution down to an error of 2.38%. Table 5.4 summarizes the errors of all runs.

Spatial $h-$refinement of the sphere, i.e. using M2, improves the situation of the affine mesh. Figure 5.10 (b) depicts the $\mathcal{P}_1$ spectrum now showing the first resonance at the correct frequency and the second

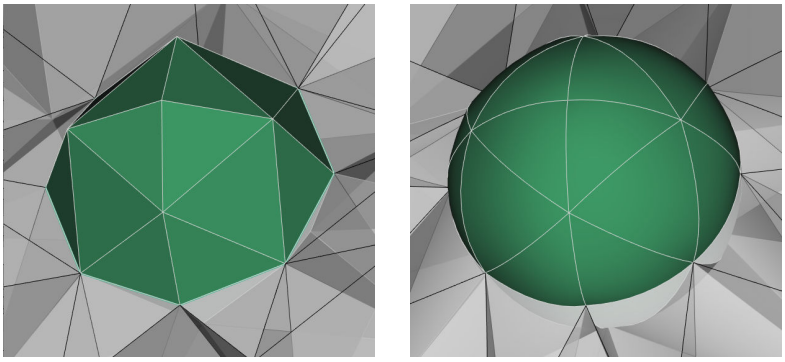

(a) Mesh M1 without high order cells. **(b)** Mesh M1 with quadratic cells.

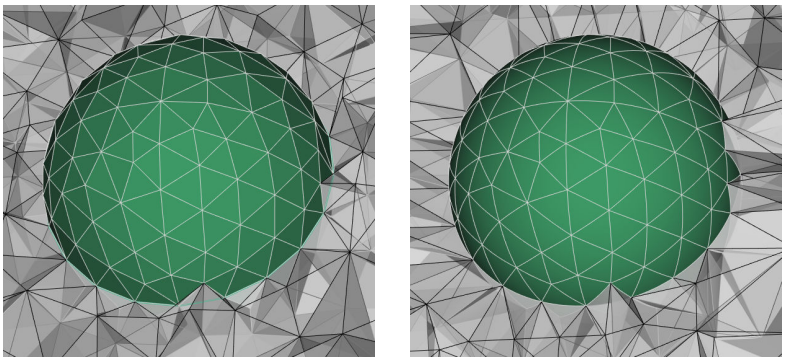

(c) Mesh M2 without high order cells. **(d)** Mesh M2 with quadratic cells.

Figure 5.9 | Four different discretization for a scattered sphere in vacuum. Figure (a) and (b) have the same number of elements and differ by the geometric representation order from linear to quadratic. Figure (c) is a refined version of (a) and (d) the high order version.

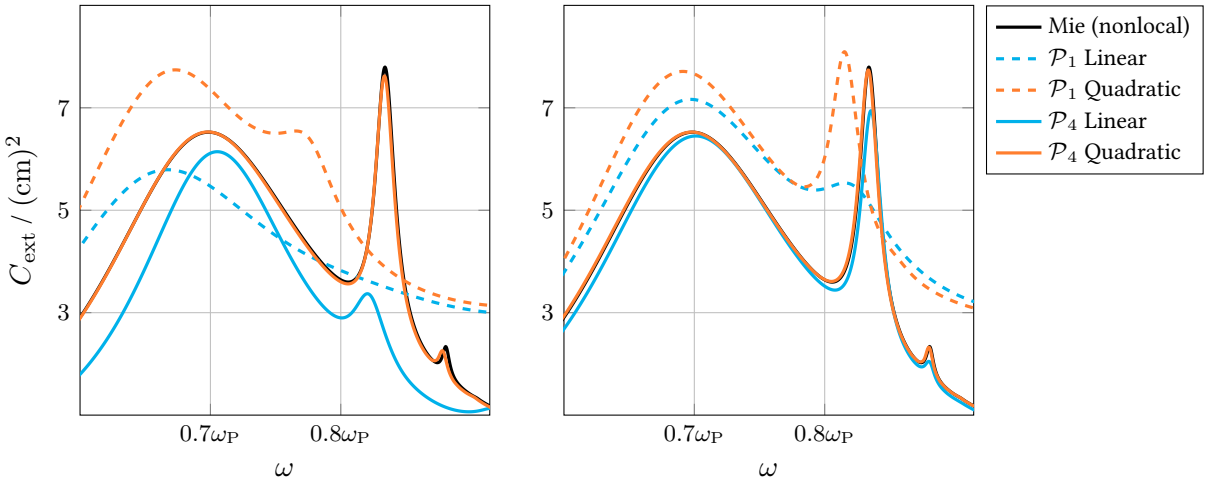

(a) M1 **(b)** M2

Figure 5.10 | Extinction cross-section spectra on mesh M1 and M2. Comparison of the extinction cross-section spectra of a metallic nano-sphere in dependence of the polynomial interpolation order $\mathcal{P}_n$ and the geometric mesh order, i.e. linear or quadratic mesh elements. The error in comparison to the Mie solution can be found in Table 5.4

Table 5.4 | Relative error of sphere simulations. The relative error is given with respect to the analytical nonlocal Mie solution.

	$\mathcal{P}_1$	$\mathcal{P}_2$	$\mathcal{P}_3$	$\mathcal{P}_4$
M1 – Linear	33.33%	29.95%	28.83%	28.80%
M1 – Quadratic	43.67%	18.51%	6.60%	2.38%
M2 – Linear	33.50%	11.07%	7.18%	5.34%
M2 – Quadratic	39.40%	10.07%	3.58%	0.96%

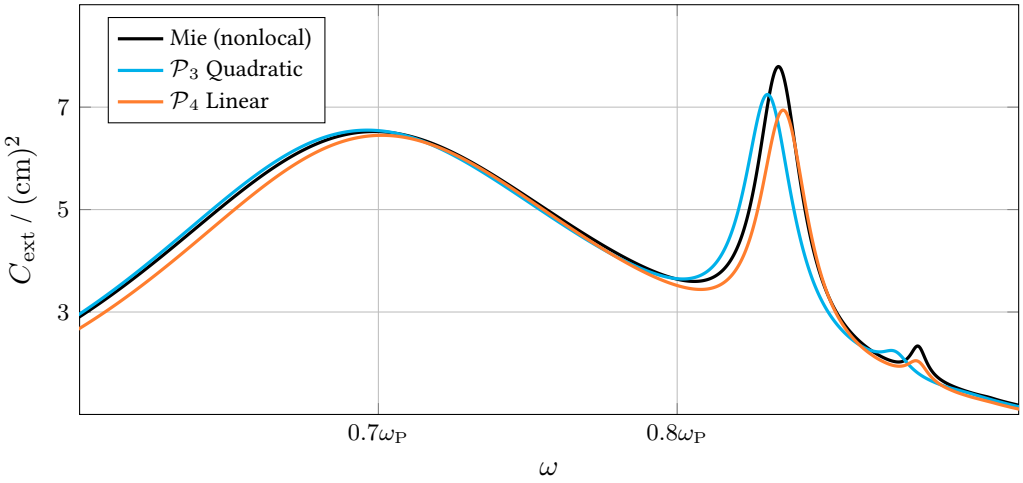

Figure 5.11 | Extinction cross-section spectra on mesh M1 and M2. Comparison of the extinction cross-section spectra of a metallic nanosphere in dependence of the polynomial interpolation order $\mathcal{P}_n$ and the geometric mesh order, i.e. linear or quadratic mesh elements. The error in comparison to the Mie solution can be found in Table 5.4

resonance that now builds up at $0.815\omega_{\text{P}}$ instead of $0.825\omega_{\text{P}}$. Although the positions of the resonances are relatively close to the exact solution, the amplitudes still differ heavily. The third resonance remains invisible for first order polynomials. If fourth order polynomials $\mathcal{P}_4$ on linear elements are used, the numerical solution already gets fairly close to the exact solution with an error of 5.45%. Activating curvilinear elements for $\mathcal{P}_1$ and $\mathcal{P}_4$, the numerical solutions with respect to the linear runs increase equally to M1 and the obtained error for $\mathcal{P}_4$ only is 0.96%.

Curvilinear simulations are intrinsically more costly than linear ones due to increased memory consumption, a reduced CFL condition and additional DoFs, see Section 3.2.2 for details, in comparison to the same run on a linear mesh. In order to present a fair comparison of a curvilinear solution on the coarse mesh M1 and the solution on an $h-$refined mesh M2 with linear elements, we choose the two runs with a similar error level, namely $\text{M1} - \mathcal{P}_3 - \text{curvilinear}$ and $\text{M2} - \mathcal{P}_4 - \text{linear}$. Figure 5.11 depicts the obtained spectra and Table 5.5 lists the statistics of both simulations (sequential as well as parallel).

Both meshes almost have the same amount of cells since the largest part of the domain consists of vacuum. While the sphere is discretized by 46 curved tetrahedra (M1), the $h-$refined mesh M2 needs 292 elements. This local refinement explains the little relative difference in the total amount of mesh cells and is at the same time close to a real world nanophotonics setup. Of course, the finer mesh M2 suffers from more mesh cells and even more severely from a time step due to a smaller characteristic mesh length h and an increased polynomial degree that changes the CFL condition [58]. This leads to an increased number of iterations in the time stepping scheme from 7060 for M1 to 90933 for M2. An average runtime

Table 5.5 | Performance comparison of sphere simulations. Sequential mesh and CPU statistics of the mesh M1 with curvilinear elements and a polynomial order $\mathcal{P}_3$ versus the refined mesh M2 with rectilinear elements and a polynomial order $\mathcal{P}_4$. The simulated spectra are depicted in Figure 5.11. The listed values only contain the actual mesh and do not contain ghost cells due to boundary conditions and domain decomposition for the parallel MPI runs. These runs have been performed on an Intel®Xeon®CPU E5-2630 v2 2.6 GHz machine with 64 GB RAM.

	$\mathrm{M1}-\mathrm{Quadratic}-\mathcal{P}_3$	$\mathrm{M2}-\mathrm{Linear}-\mathcal{P}_4$
$\mathcal{L}^2-$error (Mie)	6.6%	5.34%
# Cells	13827	14334
# Sphere cells	46	292
# HO cells	200	-
# Iterations	7060	90933
Memory	1481.5 MB	1980.4 MB
Time per 100 iterations	374 s	703 s
Total time in loop (sequ.)	26404 s	639259 s
Speedup	24.2	-

Timer per 100 iterations (parallel)	#proc	T[s]	T_{cpu}[s]	speedup	#proc	T[s]	T_{cpu}[s]	speedup
	2	186	372	2.0	2	380	740	1.9
	4	94	376	4.0	4	200	800	3.5
	8	50	400	7.5	8	105	840	6.7
	12	37	444	10.1	12	73	876	9.6

for 100 time stepping iterations of 374 s and 703 s for M1 and M2, respectively leads to a total simulation time of 7 h 20 mn and 177 h 34 mn which means a performance speedup of 24.2. In terms of memory, the $\mathrm{M1}-\mathcal{P}_3-\mathrm{curv}$ solution comes with more DoFs in comparison with a linear M1 run but still better performs in comparison to a $\mathrm{M2}-\mathcal{P}_4-\mathrm{lin}$ run by 75%.

If MPI parallelization is used (only within a single multi core node in this example) we obtain reasonably good scaling results. As depicted in Table 5.5 the scaling slightly breaks down at 12 sub domains for M1 and already at 8 sub domains for M2. This is due to the quite inhomogeneous load balancing of the computational cost of each cell type. This imbalance arises since the performed simulations contain different types of equations to be solved on each cell: purely Maxwell's equations in vacuum, Maxwell plus the hydrodynamic equation inside the sphere, CFS-PML cells, and boundary cells. Additionally, the TF/SF incident field and on-the-fly Fourier-transform of the extinction CS will add up to an even stronger imbalance. The systematic optimization of the load balancing will be part of a future work.

5.2.5 Validation of the scattered field formulation

Scattering of a Gaussian pulse

In order to validate the SF formulation with an incident Gaussian modulated plane wave (2.7.18), we compute the scattering CS of a metallic nano-sphere. The obtained results are compared with the analytical Mie solutions and results that have been obtained with the TF/SF formulation. Since the SF formulation is defined on volumes while the TF/SF formulation is surface based, we expect different results. Especially if the computational mesh is not sufficiently refined. Additionally, curvilinear elements might have a strong influence similarly to the results found in [153]. The simulation setup is depicted in Figure 4.1. However, for the SF formulation the TF/SF interface is only used for the CS calculation.

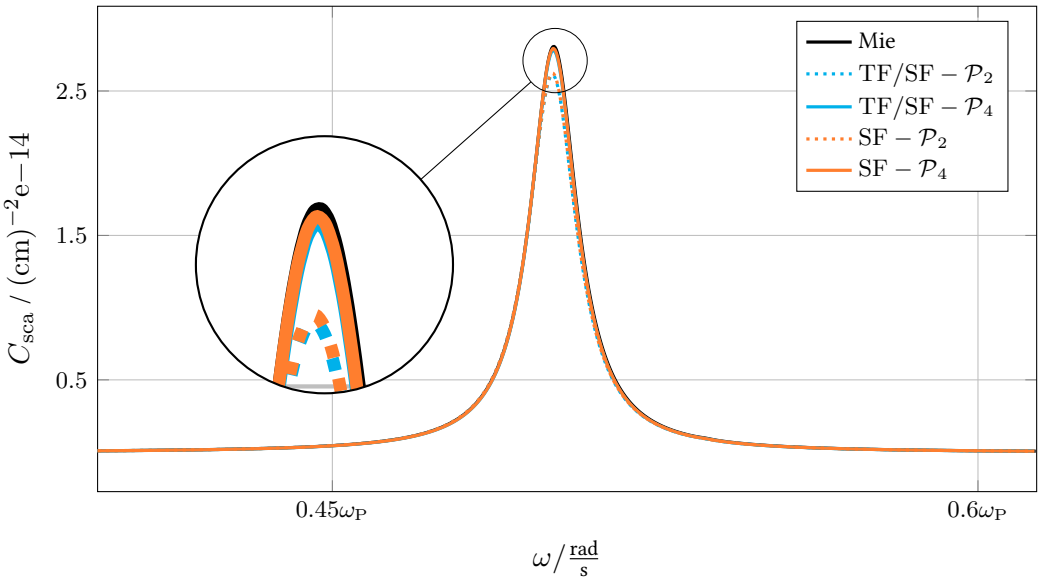

Figure 5.12 | Comparison of Mie, SF, and TF/SF. Comparison of the analytical Mie solution with two numerical results obtained by the DGTD with SF and TF/SF. The gold nano-sphere measures $R = 10$ nm with the material parameters $\omega_{\text{P}} = 1.1\text{e}16$ rad/s, $\gamma = 4.515\text{e}13$ rad/s and $\varepsilon_\infty = 3.74$. As slightly observable in the zoom, the SF formulation seems to perform better than the TF/SF formulation.

Figure 5.12 depicts the numerically computed scattering CS_{sca} obtained with the TF/SF and SF formulation in comparison with the analytical Mie solution. Obviously, the $\mathcal{P}_2$ solution obtained by the TF/SF and SF formulation are very close although not equal. Increasing the polynomial order to $\mathcal{P}_4$ yields a very good agreement of the numerical results in comparison to the analytical Mie solution.

Electron energy loss spectroscopy

We refer to Section 4.3.4 for details of the EELP calculation which is now validated (comparison to analytical Mie solutions [46]). Figure 5.14 and 5.15 show the numerical results of Γ_{EELS} for a single nano-sphere. Both figures show Γ_{EELS} for the same simulation setup but different Γ_{EELS} integration lengths.

EELS simulations can suffer from three main errors:

- A non-converged DGTD field solution because of a too coarse mesh;
- Too short integration time (erroneous Fourier-transform in (4.3.13));
- Insufficiently long integration length of the trajectory integral (4.3.13).

Here, we have used a sphere radius $R = 10\,\mathrm{nm}$, an impact factor of $d_{\mathrm{EELS}} = 2\,\mathrm{nm}$ and a beam velocity of $\mathbf{v}_{\mathrm{elec}} = 0.8c_0\mathbf{e}_z$. Figure 5.14 depicts Γ_{EELS} for a fixed integration length of $\pm 30\,\mathrm{nm}$. Successive mesh refinements lead to accuracy improvements of the numerically computed Γ_{EELS}. The different refinement stages from the most coarse mesh M1 up to the finest mesh M4 are shown in Figure 5.13. The DGTD solution seems to reach convergence for the meshes M3 and M4. Unfortunately, both meshes still cannot precisely reproduce the analytical Mie result.

Increasing the integration length to $\pm 60\,\mathrm{nm}$ lets the DGTD solution perfectly meet the analytical one (see Figure 5.15). As a conclusion, the integration length has to be sufficiently long in order to account for all the fields which are part of the electromagnetic interaction of the electron and the nano-particle.

Remark 5.2.2. *We have also tested integration lengths of* $\pm 90\,\mathrm{nm}$ *and* $\pm 120\,\mathrm{nm}$. *The influence on the computed* Γ_{EELS} *for integration lengths greater than* $\pm 60\,\mathrm{nm}$ *turns out to be negligible.*

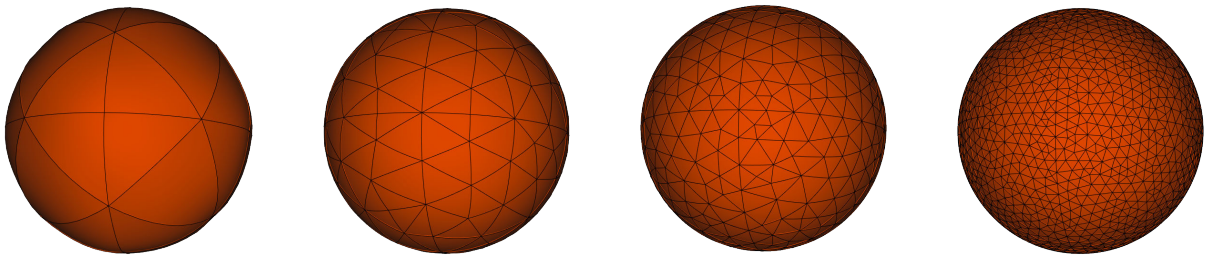

(a) M1 **(b)** M2 **(c)** M3 **(d)** M4

Figure 5.13 | Tetrahedral mesh of the nano-sphere EELS simulation. This figure shows the tetrahedral mesh in the vicinity of the nano-sphere.

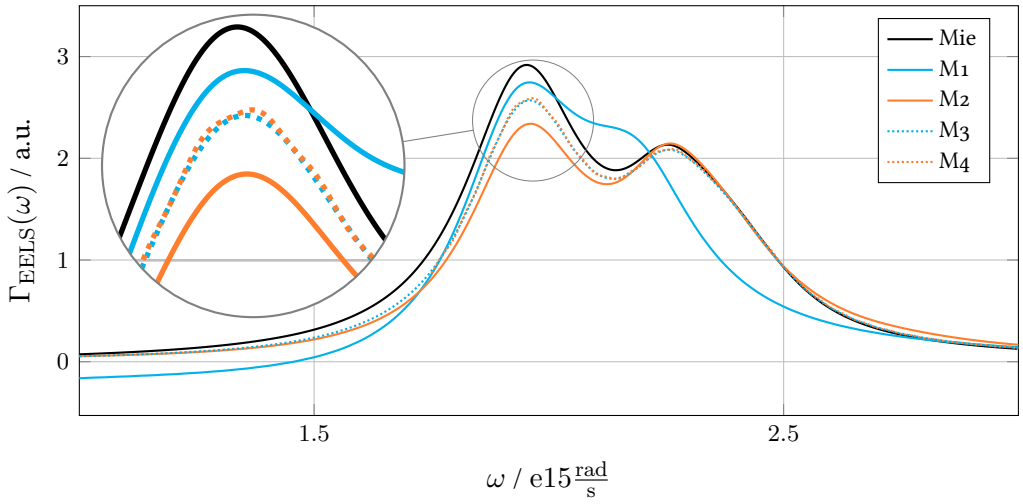

Figure 5.14 | EELS spectrum $\Gamma_{\mathrm{EELS}}(\omega)$ for a nano-sphere in vacuum with an impact parameter of $d_{\mathrm{EELS}} = 2\,\mathrm{nm}$. The curves vary in terms of an increasingly refined mesh M1, M2, M3, and M4. Here, the radius $R_{\mathrm{sphere}} = 10\,\mathrm{nm}$ and the integration length $\pm 30\,\mathrm{nm}$ for $\Gamma_{\mathrm{EELS}}(\omega)$.

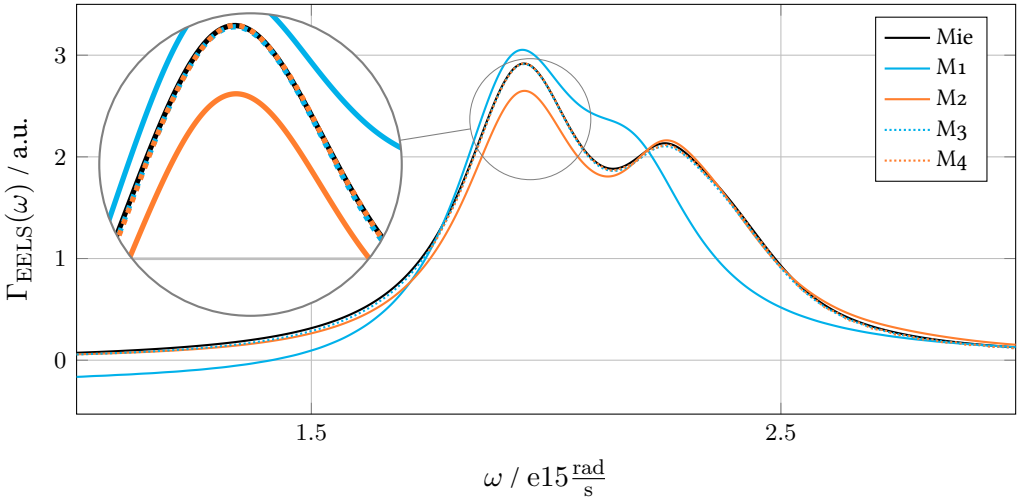

Figure 5.15 | EELS spectrum $\Gamma_{\mathrm{EELS}}(\omega)$ for a nano-sphere in vacuum with an impact parameter of $d_{\mathrm{EELS}} = 2$ nm. The curves vary in terms an increasingly refined mesh M1, M2, M3, and M4. Here, the radius $R_{\mathrm{sphere}} = 10$ nm and the integration length ± 60 nm for $\Gamma_{\mathrm{EELS}}(\omega)$.

Electron energy loss spectroscopy for penetrating beams

Assuming impact parameters $d_{\mathrm{EELS}} < 0$, i.e. an electron that travels *through* the sphere, leads to a singular source term in (2.7.33) and (2.7.34). In a discrete setting, e.g. FDTD or DGTD, a real singular field only arises if discrete electron trajectory $\mathbf{r}_{\mathrm{elec}}(t_i)$, with t_i being the $i-th$ time on the discrete time axis, coincides with the spatio-temporal computational grid. However, on computers with finite arithmetics, the evaluation of the source terms already leads to erroneous values for $\mathbf{d}(\mathbf{r}, t) > 0$ due to a limited machine precision (in our case 64-bit). Diehl et al. [34] have used an adaptive technique where they have slightly moved the electron trajectory in the $\mathbf{e}_z-$plane until the trajectory was sufficiently far away from the next DoF (in a given $x-y$ pixel).

Such an approach unfortunately *cannot* converge in a classical $h-$convergence sense. Imagining an initial mesh $\mathrm{M}_{\mathrm{init}}$ where this strategy finds an acceptable position under a constraint of the form

$$\begin{aligned} \text{find}: \quad & \mathbf{r}_{\mathrm{elec}} = \mathbf{r}_{\mathrm{elec},0} + \mathbf{v}_{\mathrm{elec}} t \quad \text{such that} \\ & |\mathbf{r}_{\mathrm{elec}}(t) - \mathbf{r}(\mathrm{DoF})| > \varepsilon_{\mathrm{min}}, \qquad \forall\, t \text{ and } \forall\, \mathrm{DoF}. \end{aligned} \tag{5.2.3}$$

A successive mesh refinement, e.g. h/i $i = 1, ..,$ will violate this constraint at some point. In other words, such an approach is doomed to fail in terms of numerical convergence.

Opting for a more robust method, we use a smeared out electron distribution that intrinsically avoids singularities. Section 2.7.7 has derived the free space solution of the electromagnetic field of a relativistic Gaussian electron. Using (2.7.43) and (2.7.45) instead of (2.7.33) and (2.7.34) circumvents singular fields in the source term of the SF formulation for penetrating beams, i.e. $d_{\mathrm{EELS}} < 0$.

We have successfully implemented the (2.7.33) and (2.7.34) in our DGTD framework. For $\mathbf{d}(\mathbf{r}, t) > 0$ and sufficiently small values of the Gaussian width σ, the point charge and Gaussian charge solution lead to the same Γ_{EELS} spectra (not detailed here).

Choosing a trajectory through a DUT on a sufficiently refined mesh (in order to account for an accurate field solution), forbids the use of (2.7.33) and (2.7.34) due the singularity. Unfortunately, our Gaussian electron approach is not a thorough solution. It turns out that we can accurately predict the parts of the

Γ_{EELS} spectrum which are linked to surfacic resonances. All bulk contributions, however, will logarithmically diverge with a decreasing Gaussian regularization parameter σ [47, 71]. This behavior can be observed in Figure 5.16. While the spectrum beyond 3.5e15 $^{rad}/_{\text{s}}$ is almost insensitive to the regularization parameter (surface contribution), the lower part of the spectrum significantly changes in dependence of σ. In other words, the regularized EELS approach evenly fails if used straightforwardly as presented in the scope of this work.

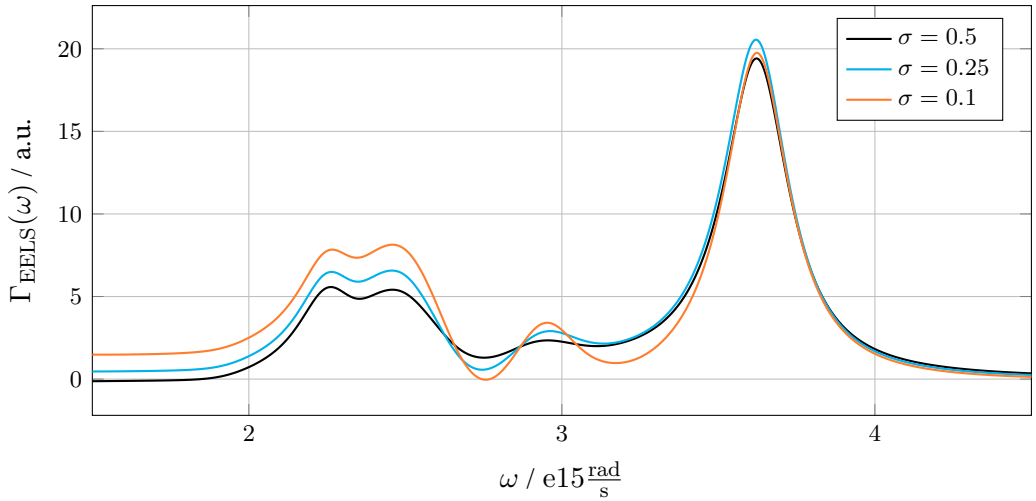

Figure 5.16 | EELS spectrum $\Gamma_{\text{EELS}}(\omega)$ for a Gaussian penetrating beam. The surface plasmon resonance at 3.7e15 $^{rad}/_{\text{s}}$ is not affected by σ while the bulk contribution slowly begins to diverge for decreasing σ. Here, the sphere's radius is $R_{\text{sphere}} = 10$ nm.

5.2.6 High performance computing aspects

A short performance study will complete the validation phase chapter. Aiming for a most realistic simulation setup that is representable in terms of common real world simulations, we study the performance behavior in the context of a nano-cube and a two-dimensional grating. The cube mesh is shown in Figure 6.30 and Table 5.6 contains further details on the mesh. Figure 5.17 illustrates the geometry of the grating setup and Table 5.7 provides details on the mesh topology.

Since DIOGENeS currently only supports MPI parallelization, the number of Central Processing Unit (CPU) is equivalent to the amount of sub domains, i.e. MPI ranks. Rankwise Symmetric multiprocessing (SMP) parallelization will be part of a future work. A pure MPI parallelization artificially increases the amount of DoF due to more ghost cells (artificial cells for the inter sub domain communication).

Nano-cube Figure 5.18 outlines the strong scaling result. We have tested the scaling behaviour for $\mathcal{P}_i$, $i = 1 \dots 4$ including curvilinear elements, local dispersion (auxiliary ODEs), nonlocal dispersion (auxiliary PDEs) and PMLs (auxiliary ODEs). The workload and memory consumption of each mesh cell strongly depends on the physical material, i.e. the underlying equation that has to be solved. Such supplementary informations are not yet exploited during the mesh partitioning and hence intrinsically lead to a sub optimal load balancing. Also, node-dependent performance inhomogeneities of the machine have not been taken into account either.

A fair scaling is observed up to 2 nodes (32 sub domains). Further increasing the amount of sub domains yields very poor scaling properties. Higher polynomials orders which lead to more DoFs per

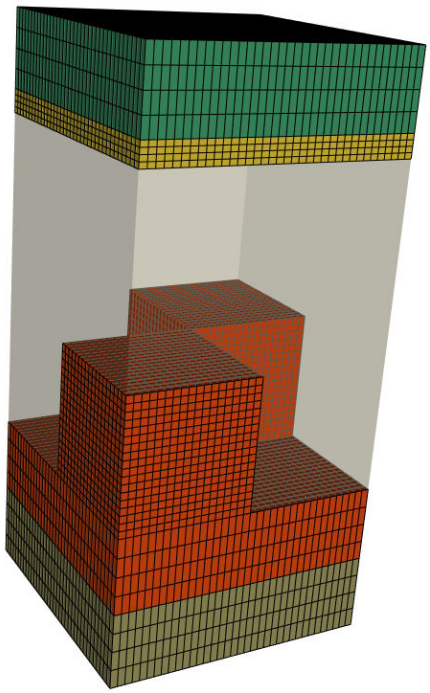

Figure 5.17 | Computational meshes of 2D grating. Brown: Si PML, red: Si substrate and grating, yellow: vacuum (SF zone), green: vacuum PML. The lateral faces are periodic boundary conditions.

Table 5.6 | Mesh statistics of nano-cube mesh. The statistics are for the initial mesh without ghost-cells.

# Cells	4026		
# Linear cells	573	# PML cells	166
# HO cells	3453	# Dielectric cells	1468
# Vacuum cells	1208	# Gen-disp + Nonlocal cells	1350

node on a fixed partitioning tend to improve the scaling. This confirms that we are in a situation of communication limited scaling where a higher workload per core creates a trend towards better scaling. We want to mention that for 64 sub domains the average number of cells per node is already 62 cells, if the partitioning was ideal.

Grating Figure 5.19 outlines the strong-scaling result. We have tested the scaling behaviour for $\mathcal{Q}_i$, $i = 1 \ldots 3$ including dielectrics, PMLs (auxiliary ODEs). Equivalent same sub-optimal partitioning arguments apply to the grating.

Despite a small offset (in the log scale), the grating case scales significantly better up to 128 cores. We observe a scaling breakdown for $\mathcal{Q}_1$ beyond 128 sub domains while $\mathcal{Q}_{2,3}$ still scale nicely up to 256 cores. This is due to the higher workload per core. Doubling the number of sub domains up to 512 eventually drops the scaling. We have to mention that each core only hosts 243 cells in average for 256 sub domains.

While the somewhat constant factor between the ideal scaling [1] and our results is order-independent, the scaling breakdown seems to appear at $\approx 10^2$ elements per node for the grating as well as for the cube.

[1] This factor might be due to the different computational costs for normal Maxwell cells and PML cells. Since the mesh is relatively homogeneous, there are many pure Maxwell or PML sub domains intrinsically having different workloads per rank.

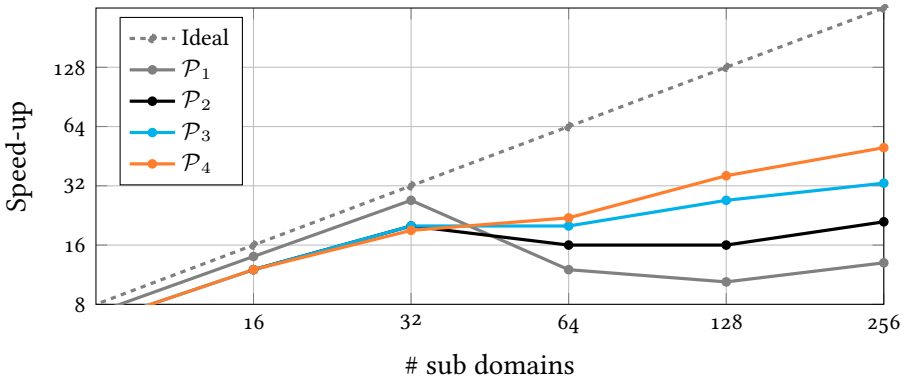

Figure 5.18 | MPI speedup for the nano-cube. The mesh statistics are depicted in Table 5.6. We have used the same mesh-partitioning for each $\mathcal{P}_i$. The speed-up is relative to 16 sub domains. This work was granted access to the HPC and visualization resources of "Centre de Calcul Interactif" hosted by "Université Nice Sophia Antipolis" (CICADA).

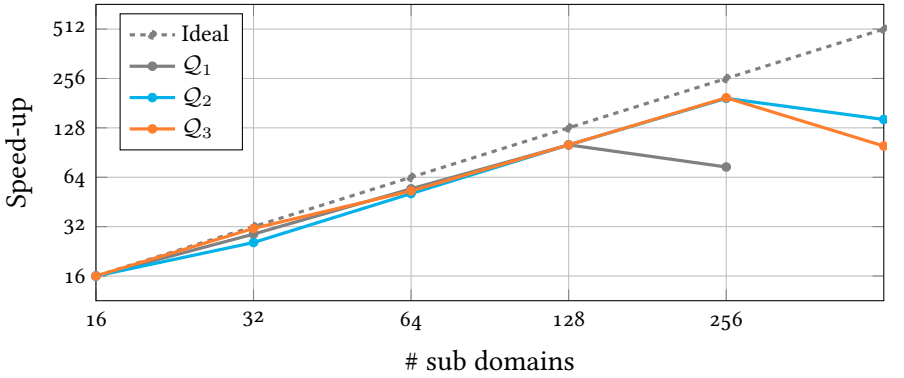

Figure 5.19 | MPI speedup for the grating. The mesh statistics are summarized in Table 5.6. We have used the same mesh-partitioning for each $\mathcal{Q}_i$. The speed-up is relative to 16 sub domains. This work was granted access to the HPC and visualization resources of "Centre de Calcul Interactif" hosted by "Université Nice Sophia Antipolis" (CICADA).

Although this estimation is very rough and heavily depends on the computational cost per cell, we can at least conclude an approximative partitioning limit. In other words, one MPI task should not host less than ≈ 150 cells.

Remark 5.2.3. *We are aware of the fact that these scaling results are far from usual HPC-standards. However, our scaling-study has been performed on two realistic test-cases and we hence consider them to be representative for a vast set of simulations. Also, we wanted to get a 'feeling' of how many elements per CPU are necessary for a reasonable scaling.*

Table 5.7 | Mesh statistics of grating mesh. The statistics are for the intial mesh without ghost-cells.

# Cells	62208		
# Linear cells	62208	# PML cells	10368
# HO cells	-	# Dielectric cells	22032
# Vacuum cells	40176	# Gen-disp + Nonlocal cells	0

5.3 Spherical dimer

Spherical dimers consist of two spheres being very close to each other, hence forming a gap system, see Figure 5.20 (a). Such dimers are well known to show high field enhancements due to the hybridized modes of the individual spheres that build up a so called gap plasmon. These field enhancements are of interest for e.g. Surface Enhanced Raman Scattering (SERS) [165].

Beyond the applicative aspects, the spherical dimer system is significantly more complicated for analytical solutions due to a lower symmetry level than single spheres. Breaking the symmetry of a single sphere by introducing a second sphere brings a second tuning parameter of the system - the gap size. For sufficiently small gaps, nonlocal effects are expected to occur, as has been recently theoretically shown for a fully retarded three dimensional dimer case [136].

5.3.1 Optical cross section simulation

For extinction CS simulations, in contrast to scattering CS, the absorption CS comes into play and the near field thus gains importance. A precise evaluation of the absorption CS, in turn, requires a well resolved near field which strongly depends on the surface approximation of the nano particles. We have used identical spheres with the radii $R_{\mathrm{Dimer}} = 10\ \mathrm{nm}$ and a gap of $\delta_{\mathrm{Dimer}} = 2\ \mathrm{nm}$ being sufficiently wide to neglect tunneling effects. Both spheres consist of gold with the material parameters $\omega_{\mathrm{P}} = 1.39\mathrm{e}16\ \mathrm{rad/s}$, $\gamma = 3.23\mathrm{e}13\ \mathrm{rad/s}$ and $\beta = 0.84\ {}^{m}\!/_{\mathrm{s}}$.

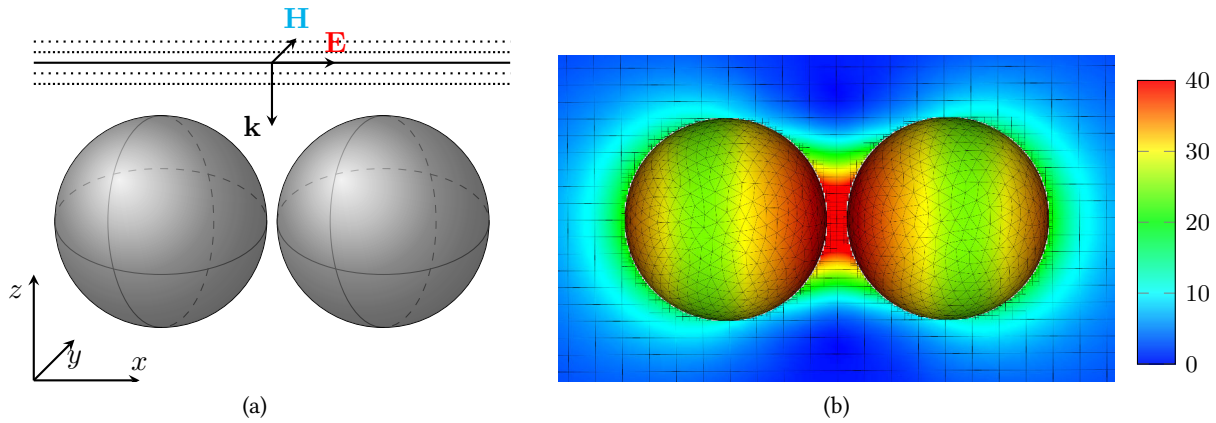

Figure 5.20 | Spherical dimer system. (a) sketches the dimer setup with an $\mathbf{e}_x$ polarized incident plane wave and (b) shows the 3D field distribution of the electric field on the dimer surface and on a cutting plane and along the dimer axis.

Numerical discussion: affine vs. curvilinear elements Figure 5.21 and 5.22 show the extinction CS spectra for simulations with local and nonlocal dispersion models on a mesh with affine tetrahedra and a converged reference spectrum obtained on a curvilinear mesh.

For *local* dispersion (see Figure 5.21), centered DGTD on affine tetrahedra obtains a reasonably good solution for frequencies below $0.56\omega_{\mathrm{P}}$. Spurious solutions dominate the extinction spectrum for centered fluxes. Using $\alpha = 1.0$, i.e. fully upwind fluxes, introduces numerical dissipation and damps spurious solutions. The resulting spectrum is very close to the reference solution.

The situation changes for *nonlocal* dispersion (see Figure 5.22). The solution with centered fluxes, i.e. $\alpha = 0$ in (3.1.8), barely shows dissipation and almost contains all the resonances as the reference solution. Unfortunately, the spectrum is heavily polluted by spurious oscillations which makes it extremely difficult

for the weaker resonances of amplitudes below $3\mathrm{e}{-15}\ \mathrm{cm}^{-2}$ to be correctly distinguished and detected. Switching to upwind fluxes, i.e. $\alpha = 1.0$ in (3.1.8), damps away all spurious solutions at the price of higher numerical dissipation making the detection of weak resonances impossible again.

If curvilinear elements are turned on now, i.e. the black curve in Figure 5.22, we indeed see that the previously discussed centered spectrum almost contains all correct resonances plus additional spurious modes. In contrast, the upwind solution smoothes out too strongly and at least two resonances are completely lost. Figure 5.24 (b) illustrates the computational mesh of the dimer system with the curvilinear elements.

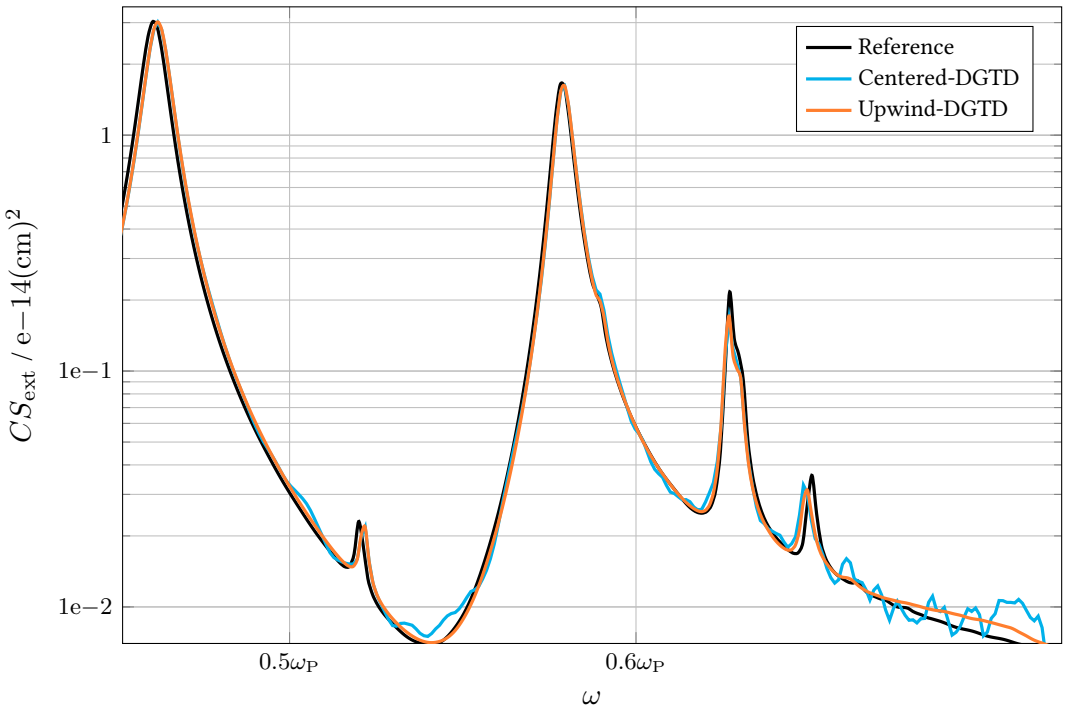

Figure 5.21 | Spherical dimer DGTD flux comparison (local). Comparison of the extinction CS spectra for a spherical dimer system on a linear mesh in dependence of the numerical flux choice. Black: the reference DGTD solution with curvilinear elements. Blue: DGTD with centered fluxes and linear mesh cells, and orange: DGTD with upwind fluxes and linear mesh cells.

Physical discussion: local vs. nonlocal dispersion Comparing a local dispersion model $\beta = 0$ with the nonlocal solution in Figure 5.24 (a) shows significant blue-shifts for all resonances. The resonances above $0.6\omega_{\mathrm{P}}$ are even shifted strong enough to lie on the next local resonance.

In terms of near field solution, Figure 5.23 depicts the electric field distribution inside the dimer and Figure 5.24 the field on the surface and in the gap. Regarding the field distribution inside the dimers, nonlocality leads to a stronger penetration of the field to the inside of the spheres. While locally dispersive dimers build out a nicely convex gap mode, nonlocality causes an almost parallel gap penetration layer. Additionally, nonlocality builds up a very thin penetration layer which is particularly strong on the rear side of the dimers. Such penetration effects and a more homogenous field (out-smearing) is not observable for local dispersion. Figure 5.24 confirms the previous inside observations. Nonlocality leads to field enhancements on the surface and widens the gap mode.

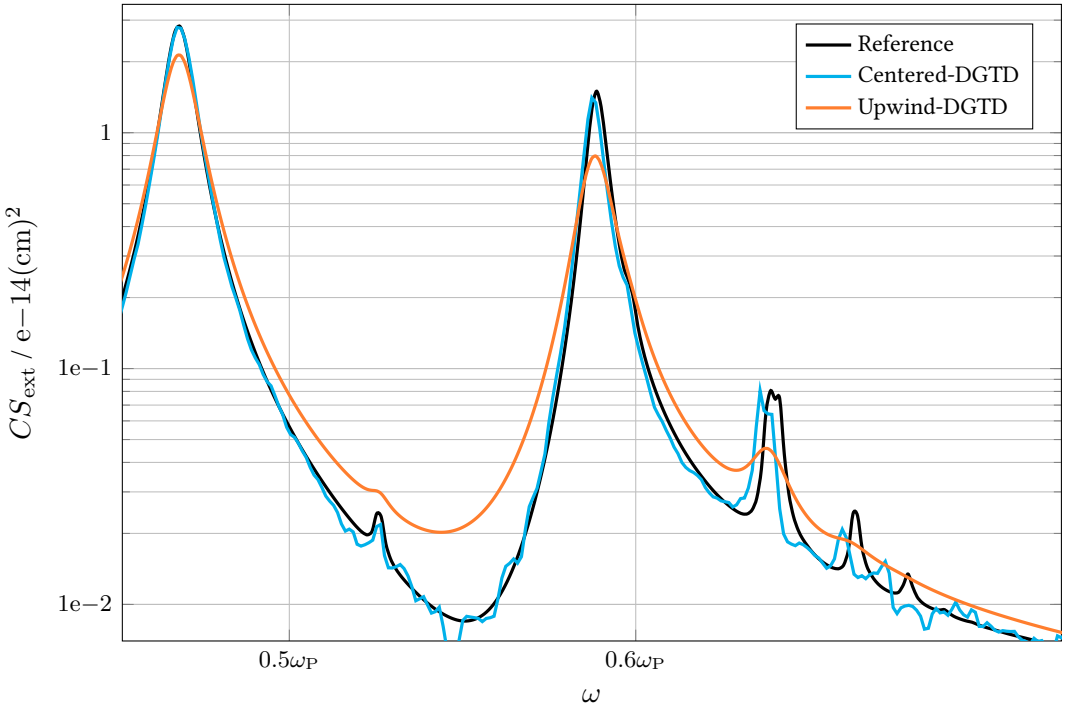

Figure 5.22 | Spherical dimer DGTD flux comparison (nonlocal). Comparison of the extinction CS spectra for a spherical dimer system on a linear mesh in dependence of the numerical flux choice. Black: the reference DGTD solution with curvilinear elements. Blue: DGTD with centered fluxes and linear mesh cells, and orange: DGTD with upwind fluxes and linear mesh cells.

In conclusion, nonlocality leads to blue-shifts in the CS spectra, even for relatively low βvalues of less than 1e6 m/s. Near field observations clearly show mode distortion in comparison to local dispersion models. Complementary simulation results are provided in section D.

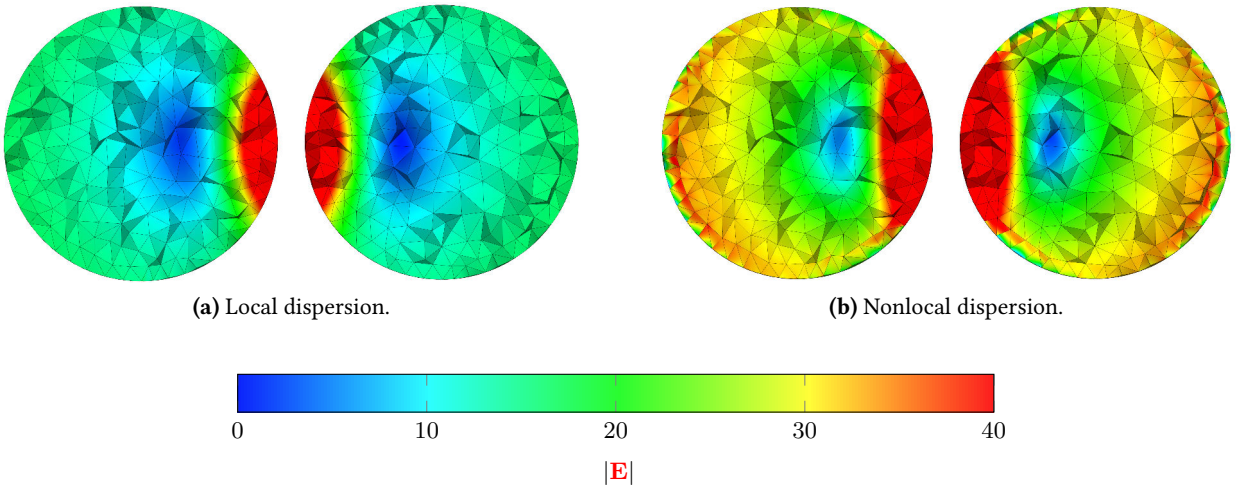

(a) Local dispersion.

(b) Nonlocal dispersion.

Figure 5.23 | Spherical dimer field plot at the third resonance (volume). Figure (a) shows the 3D field distribution of the electric field if a local dispersion model is employed. In (b) a nonlocal dispersion model is used. Nonlocality smears out vacuum-metal interface and builds up a 'penetration' layer. The discontinuities of the DGTD method are clearly visible.

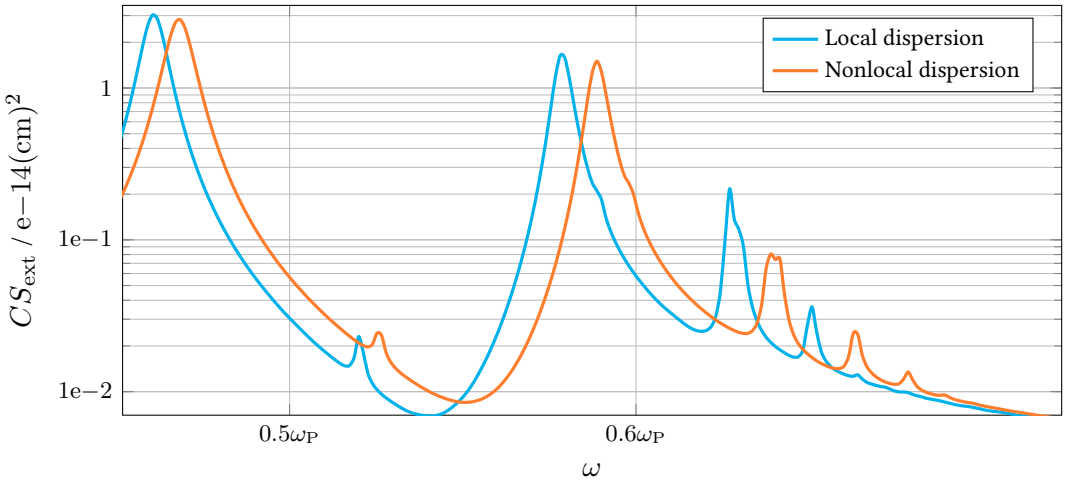

(a) Spherical dimer: local vs. nonlocal CS. Comparison of the extinction CS spectra of a spherical dimer system based on local on nonlocal dispersion models.

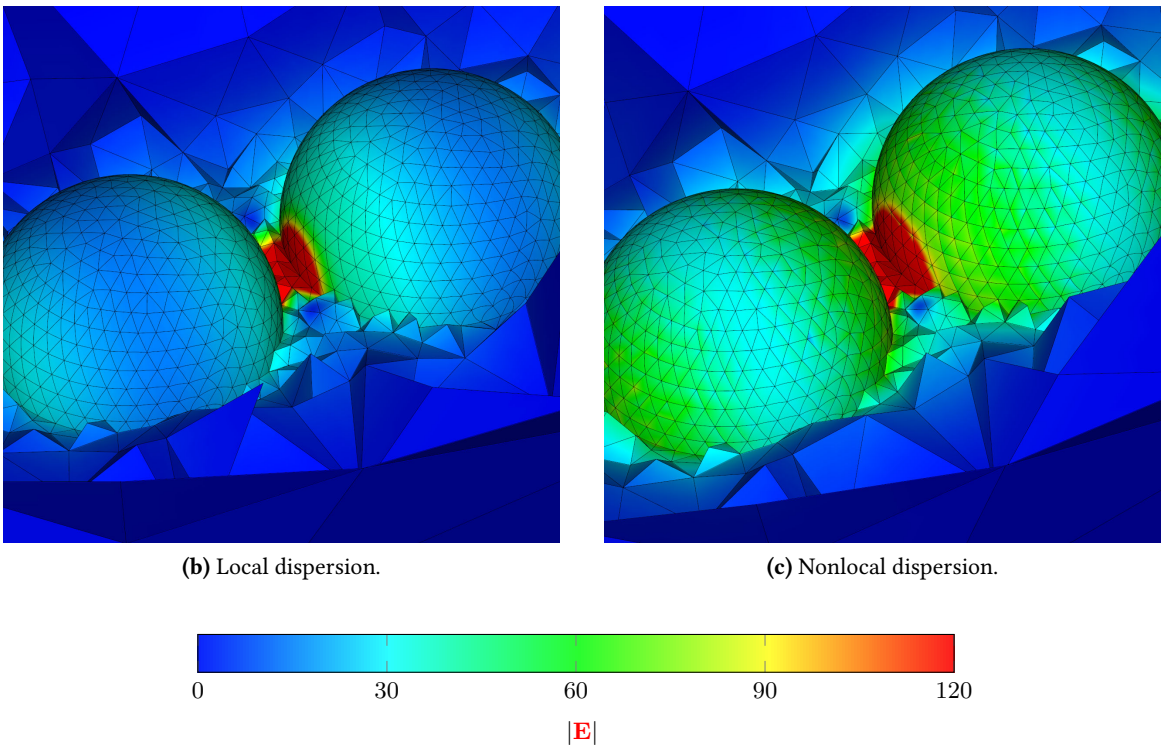

(b) Local dispersion.

(c) Nonlocal dispersion.

Figure 5.24 | Spherical dimer: local vs. nonlocal dispersion. A comparison of local an nonlocal extinction CS is shown in (a). Figure (b) shows the 3D field distribution at third resonance of the electric field if a local dispersion model is employed. In (c) a nonlocal dispersion model is used. Nonlocality widens the gap plasmon resonance due to stronger field enhancements.

6

Model calibration and experimental evidence

Differences between local and nonlocal dispersion models are still small. Especially for today's fabrication precisions, it remains a challenging task to find reliable structures where nonlocality is dominant over geometrical errors. Numerous theoretical studies [128, 103, 134] have been concerned with sphere based systems. However, these systems either require extremely small spheres of radii $\approx 2\ \mathrm{nm}$ or very small gap sizes in the dimer setup in order to be sensitive to nonlocality. Such small spheres appear to not be perfect spheres anymore since the atomic structure starts to cause faceted nano particles [127]. A promising experiment has been carried out in 2012 [24] where nonlocality was measured for spheres on a substrate. Despite the fact that the nonlocal model was able to accurately predict the measured data while the local model failed, the experimentalists had to tremendously decrease the gap size between the substrate and the sphere in order to obtain a sufficient impact of nonlocality. Gap sizes below $\approx 2\ \mathrm{nm}$ may be subject to tunneling which is not included in the nonlocal model.

Aspiring towards more experimental setups where nonlocality should be observed and clearly distinguishable from other effects like tunneling, we consider two promising structures. The first structure, a classical grating, presents a modern calibration approach of the nonlocal dispersion model. Calibrating the hydrodynamic dispersion model turns out to be fairly complicated if nonlocality wants to be properly distinguished from geometric uncertainties. Chapter 6.1 presents a calibration approach for well-known grating structures relying on the solution of inverse problems with state of the art meta-model based optimization and surrogate model based UQ analysis.

Afterwards, we benchmark our numerical results with experimental data. Our simulations of nanocubes show an excellent agreement and allow new interpretations and explanation of former experiments from Duke University [105]. This topic will be subject of Chapter 6.2.

6.1 Grating

This work has been realized in collaboration with Armel Pitelet at Institut Pascal, Clermont-Ferrand and Dimitris Loukrezis at TU-Darmstadt. The results have been published in [120]. We refer to [120] for a more thorough physical introduction and discussion. This chapter provides complementary details about the post-fabrication telemetry and the calibration of the nonlocal material parameter β.

6.1.1 Post-fabrication telemetry - solving an inverse problem

Nano gratings [144] strongly depend on the fabrication tolerances of the etching process and the layer-wise dielectric deposition technology. For our theoretical investigations, we will use an idealized geometric model of the grating structure based on three parameters d_{Grating}, a_{Grating}, h_{Grating} of the metallic structure and the height h_{Diel} of the dielectric. Figure 6.2 shows both setups, before and after the deposited dielectric.

Unfortunately, the fabrication tolerances of state-of-the-art nano processing still lead to a priori tolerances of about $\pm 5\ \mathrm{nm}$ for the etching process [84] and about $\pm 11\%$ [18] for the dielectric deposition. Modern electron beam etching is usually limited by the beam quality while the dielectric deposition depends on a layer-wise error, i.e. independent from layer to layer. In order to obtain the more accurate *geometric model*, we aim for a post-fabrication characterization, referred to as *geometric telemetry*.

Post-fabrication characterization is of particular importance for our study because nonlocality is a relatively small correction of the material model and its influence could be completely drowned in fabrication imperfections, i.e. tolerances. Trying to overcome this dilemma, we perform telemetry strategy, allowing to precisely determine the actual geometric parameters. The thereby found geometric model (see Figure 6.2) will subsequently be the starting point of our main study:

- Is the influence of nonlocality greater than that of geometric imperfections?
- If yes, can we extract the nonlocal material parameter β and hence calibrate the linearized hydrodynamic dispersion model with the proposed grating setup?

The geometric telemetry will be split up into two steps: step I which characterizes the metal geometry parameters d_{Grating}, a_{Grating}, h_{Grating} and step II providing the dielectric height h_{Diel}. A key ingredient of our strategy consists in the fact that we *do not* rely on nonlocal simulations at any time during step I and II. This is particularly important since the nonlocal material parameter β is still subject to ongoing discussions in the community [8, 128, 61, 24, 126]. *Thus, motivated by the lack of accuracy in the $\beta-$value, our final goal is to deploy a robust protocol that allows for the extraction, i.e. indirect measurement, of the nonlocal material parameter β.* This will be the last step after a successful determination of the geometry (step I and II) and in the following referred to as step III. Figure 6.1 illustrates the overall work-flow.

A SP propagating along an air-Ag (see Figure 6.2 (a)) interface is almost insensitive to nonlocality, while the TiO_2-Ag interface significantly increases the impact of spatial dispersion (see Figure 6.2 (b)), as discussed in the introduction and as depicted in Figure 1 in [120]. For this reason, it is beneficial to perform a first characterization step, *before* the TiO_2 deposition.

Telemetry goal An accurate knowledge of the entire geometry will eventually allow:

- A comparison of local and nonlocal simulations based on an accurate and realistic geometric model. This theoretical comparison checks whether the proposed grating structure is sufficiently sensitive in order to observe nonlocality experimentally. Here, a value for β will have to be assumed according to the literature [25].

- An UQ of the geometric uncertainty for the local and nonlocal simulation. This will show if uncertain geometries make the influence of nonlocality undetectable.
- The solution of an inverse problem in order to find the experimental and hence the real value of β.

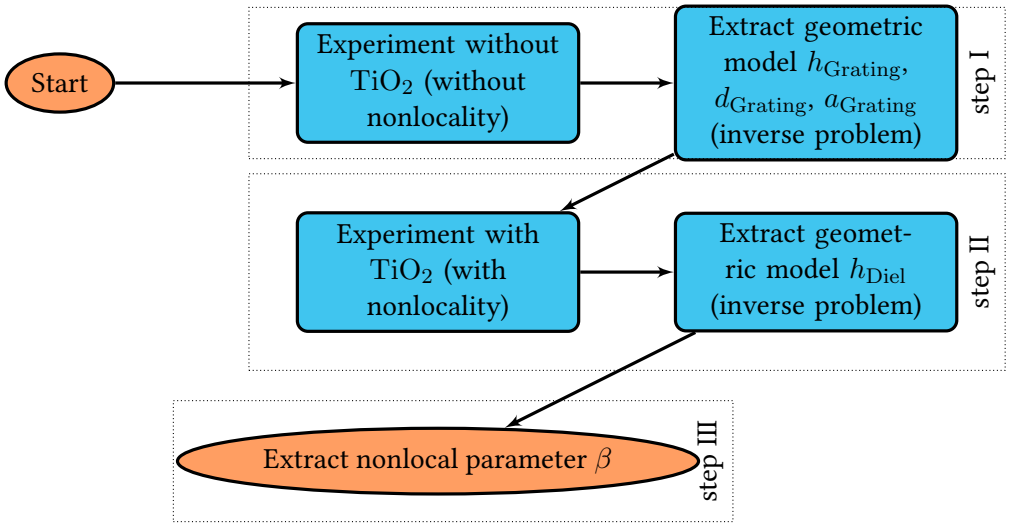

Figure 6.1 | Calibration of nonlocal dispersion model.

Remark 6.1.1. *As a first step, the presented study exclusively relies on theoretical results. We propose a robust telemetry strategy based on artificial measurement data, i.e. simulated spectra with added noise. Such a choice enables to sanity check, since the reference geometry is known. To the best of our knowledge, no experimental data, which would exactly meet our proposed strategy plan yet exists. We hope this work encourages experimentalists to realize the corresponding experiments.*

Step I and II - searching the grating's geometry Starting with step I and II, we require a numerical model that provides the reflectance spectrum. Grating structures with local dispersion, in a wisely chosen frequency range, can be efficiently solved by RCWA methods [93, 120]. According to the strategy outlined in Figure 6.1, we perform two 'artificial' fabrication (.a) and measurement (.b) sub-steps:

(I.a) Etch the grating into the Ag bulk layer and measure the reflectance (nonlocality absent);

(I.b) Find d_{Grating}, a_{Grating} and h_{Grating}, based on RCWA simulations (without nonlocality);

(II.a) Add the dielectric layer (TiO_2) and again measure the reflectance (nonlocality possible);

(II.b) Find h_{Diel}, based on RCWA[1] simulations (nonlocality possible).

Step I hence reads:

(i) Choose an reference set of geometric parameters $h_{\text{Grating}} = h_{G,\text{init}}$, $d_{\text{Grating}} = d_{\text{init}}$ and $a_{\text{Grating}} = a_{\text{init}}$;

(ii) Simulate the reflectance spectrum with RCWA (local dispersion). We call the result of this *first* simulation the *original* solution. Perturb the simulated reflectance by adding a white noise, referred to as artificial experimental data $R^{\text{local}}_{\text{measured}}$;

[1] We relied on a RCWA implementation of the Electromagnétisme et Nanophotonique de l'Institut Pascal team in Clermont-Ferrand.

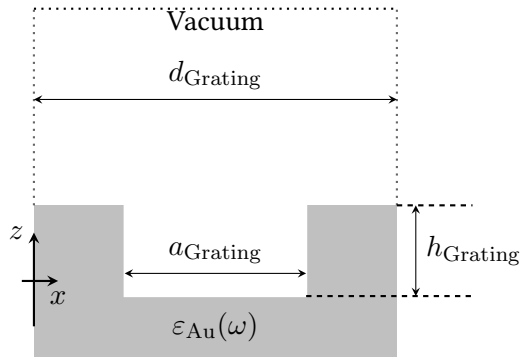

(a) Metallic grating without dielectric. Periodic metallic grating setup before dielectric deposition (nonlocality absent).

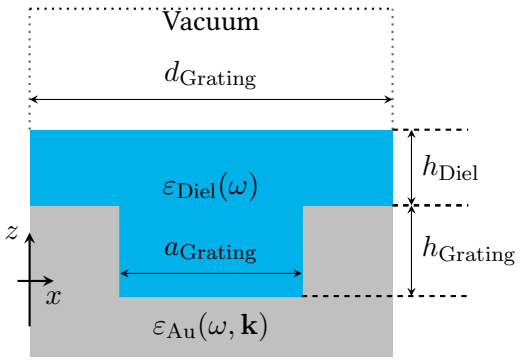

(b) Metallic grating with dielectric. Periodic grating setup with dielectric (TiO_2) finishing (nonlocality possible).

Figure 6.2 | Periodic grating. Two fabrication states of the metallo-dielectric grating. First, a periodic grating is etched into the silver ground layer, Figure (a). Then, the grating is filled up with TiO_2 and an additional homogeneous layer of the same material is topped on the structure, Figure (b). This allows spatial dispersion in the silver, i.e. $\varepsilon_{\text{Au}}(\omega)$ becomes $\varepsilon_{\text{Au}}(\omega, \mathbf{k})$.

(iii) Solve an inverse problem (formulated as an optimization problem) and find the fabricated geometry.

See Figure 6.3 for the corresponding flowchart.

Remark 6.1.2. *Step (i) and (ii) would be replaced by experimental results in the future.*

After the creation of the artificial measurement data, i.e. (i) and (ii), the inverse (optimization) problem reads

Inverse problem: find metallic geometry

$$\begin{aligned} \text{minimize} \quad & \left|\left| R^{\text{local}}_{\text{measured}} - R^{\text{local}}_{\text{optimized}} \right|\right|_{l^2} \\ \text{subject to} \quad & h_{\text{Grating}} \in [h_{\text{G,min}}, h_{\text{G,max}}] \\ & d_{\text{Grating}} \in [d_{\text{min}}, d_{\text{max}}] \\ & a_{\text{Grating}} \in [a_{\text{min}}, a_{\text{max}}]. \end{aligned} \tag{6.1.1}$$

Figure 6.4 shows the result of (6.1.1). We have tested two different optimization algorithms of the Matlab optimization toolbox, namely particle swarm and pattern search and INRIA's Famosa. Both algorithms from the Matlab optimization toolbox find fairly good solutions as depicted in Figure 6.5. Potential issues for the optimization process might be many local minima with similar error levels due to the high noise of the artificial measurement data. Such a situation makes it difficult to find the most 'realistic' minimum. Multiple local minima of the same level can be imagined as several parameter combinations of d_{Grating}, a_{Grating} and h_{Grating} yielding a similar error-level $\left|\left| R^{\text{local}}_{\text{measured}} - R^{\text{local}}_{\text{optimized}} \right|\right|_{l^2}$ in (6.1.1).

Remark 6.1.3. *We have performed multiple optimization runs with different algorithms: particle swarm, pattern search and metamodel (Kriging) based optimization, as well as different starting points for the pattern search. For Kriging, we rely on the Famosa optimization toolbox. The obtained results are not very sensitive to the choice of the optimization algorithm. In terms of computational costs, Kriging performs best, followed by*

pattern search and particle swarm seems to be less appropriate for this type of optimization problem. However, most results in the following discussion will be based on pattern search due to its robustness and higher efficiency for derivative-free medium-dimensional problems [53]. Although metamodel based optimization is faster, we have mainly used pattern search because of its availability in the Matlab Optimization Toolbox (this simplifies the reproducibility of our results for future experimentalists).

The cost-function calls are based on RCWA simulations and take approximately 10 *minutes for* 200 *frequency points without parallelization. Each frequency point is independent, leading to a linear scaling if parallelization was active.*

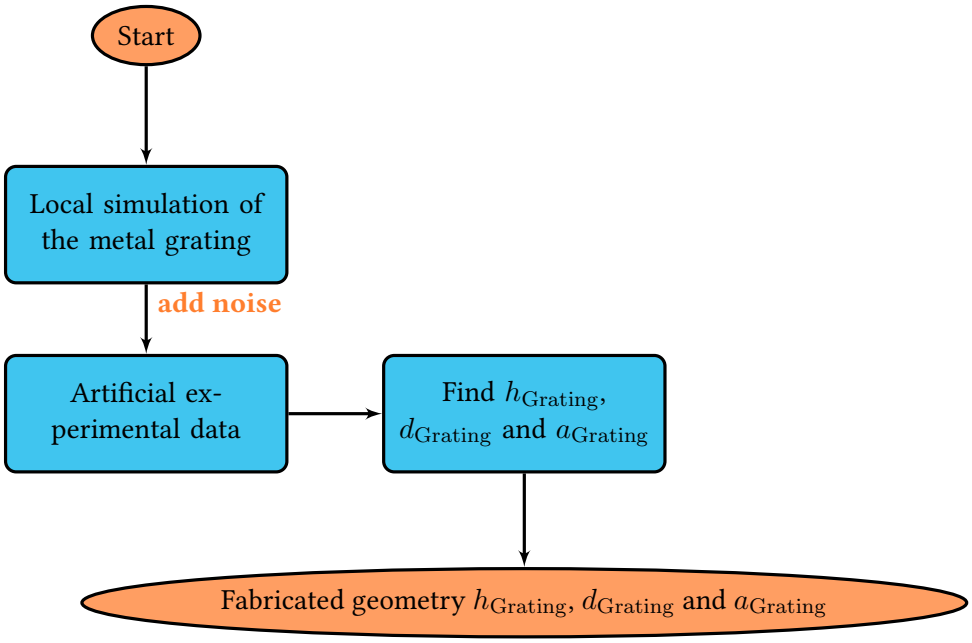

Figure 6.3 | Workflow of dielectric free grating. Schematic of step I. The pure metal grating in Figure 6.2 (a) will be free of nonlocal effects. Hence, we use a local simulation result and add a noise in order to get an artificial set of experimental data. Then, we search the three unknown geometric parameters (inverse problem).

Step II After adding the dielectric layer, a telemetry of h_{Diel} is carried out. There is now 5 different possible scenarios depending on the underlying material model of the 'measured' data, the material model of the simulations of the inverse problem and the amount of free geometric parameters. These 5 possibilities read:

A-1 Use the noisy *local* spectrum. Add h_{Diel} to the unknowns of the inverse problem (6.1.1) and solve

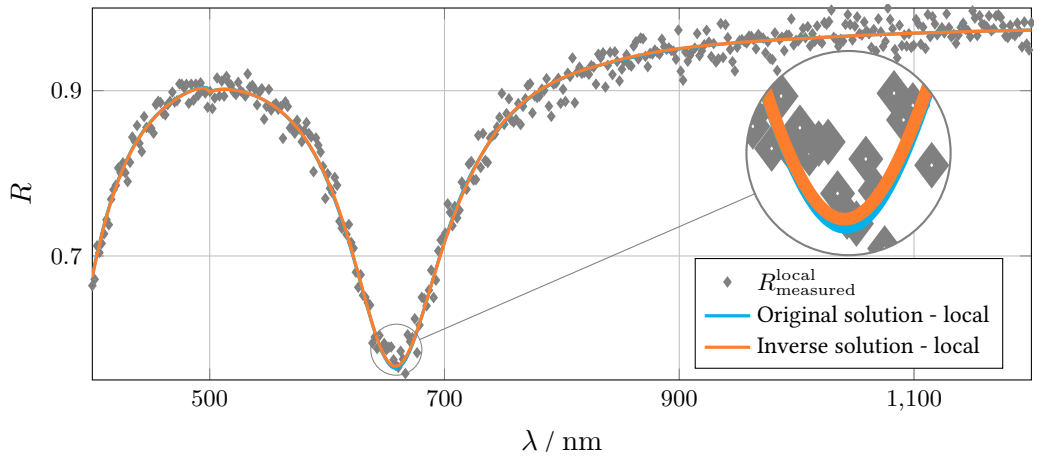

Figure 6.4 | Reflectance spectrum. Result of step I. An artificial white noise has been added to the original spectrum (in blue) obtained for $h_{\text{G,init}} = 68.0$ nm, $d_{\text{init}} = 500.00$ nm and $a_{\text{init}} = 166.67$ nm. In orange: The result of the inverse problem (6.1.1) with Matlab's pattern search. This spectrum corresponds to $h_{\text{Grating}} = 68.08$ nm, $d_{\text{Grating}} = 499.15$ nm and $a_{\text{Grating}} = 165.34$ nm. The constraint intervals are chosen to be $h_{\text{Grating}} \in [62, 73]$ nm, $d_{\text{Grating}} \in [495, 505]$ nm and $a_{\text{Grating}} \in [161, 171]$ nm, which is in accordance with the precision of the etching process.

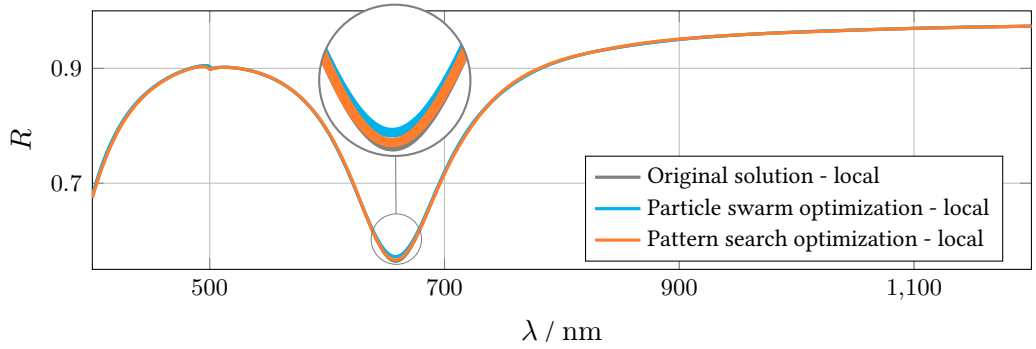

Figure 6.5 | Particle swarm vs. pattern search. Comparison of the original spectrum and the solution of the inverse problem. Here, we compare particle swarm optimization and pattern search for the solution of (6.1.1) (both based on local dispersion). The found geometric parameters for particle swarm are $h_{\text{Grating}} = 68.18$ nm, $d_{\text{Grating}} = 501.41$ nm and $a_{\text{Grating}} = 171.00$ nm. See Figure 6.4 for the pattern search results.

Inverse problem A-1

$$\begin{aligned} \text{minimize} \quad & \left|\left| R^{\text{local}}_{\text{measured}} - R^{\text{local}}_{\text{optimized}} \right|\right|_{l^2} \\ \text{subject to} \quad & h_{\text{Grating}} \in [h_{\text{G,min}}, h_{r,\text{max}}] \\ & d_{\text{Grating}} \in [d_{\text{min}}, d_{\text{max}}] \\ & a_{\text{Grating}} \in [a_{\text{min}}, a_{\text{max}}] \\ & h_{\text{Diel}} \in [h_{\text{Diel,min}}, h_{\text{Diel,max}}] \end{aligned} \tag{6.1.2}$$

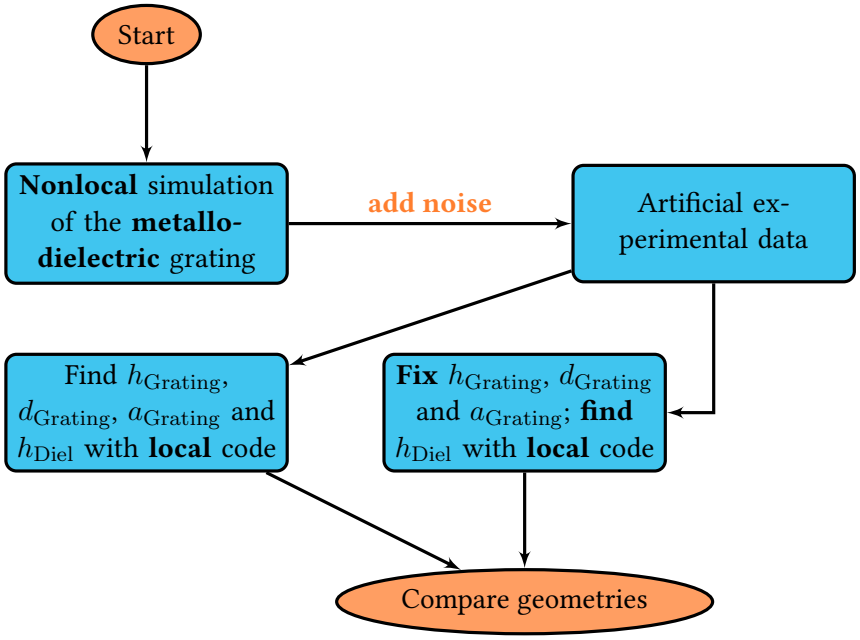

Figure 6.6 | Workflow of the metallo-dielectric grating. Schematic of step II B. Supposing nonlocality to be present in the real experiment as depicted in Figure 6.2 (b), we use a nonlocal simulation result of the metallo-dielectric grating. Adding an artificial measurement noise leads to the artificial nonlocal experimental data. The goal is to find h_{Diel}. We can either restart from scratch and leave all four parameters free or fix the already found parameters and search for h_{Diel} only.

A-2 Use the noisy *local* spectrum. However, fix d_{Grating}, a_{Grating} and h_{Grating} to the values of (6.1.1). Find h_{Diel} by solving

Inverse problem A-2

$$\begin{aligned} \text{minimize} \quad & \left|\left| R^{\text{local}}_{\text{measured}} - R^{\text{local}}_{\text{optimized}} \right|\right|_{l^2} \\ \text{subject to} \quad & h_{\text{Diel}} \in [h_{\text{Diel,min}}, h_{\text{Diel,max}}] \end{aligned} \tag{6.1.3}$$

B-1 Use the noisy *nonlocal* spectrum. Add h_{Diel} to the unknowns and solve

Inverse problem B-1

$$\begin{aligned} \text{minimize} \quad & \left|\left| R^{\text{nonlocal}}_{\text{measured}} - R^{\text{local}}_{\text{optimized}} \right|\right|_{l^2} \\ \text{subject to} \quad & h_{\text{Grating}} \in [h_{\text{G,min}}, h_{\text{G,max}}] \\ & d_{\text{Grating}} \in [d_{\text{min}}, d_{\text{max}}] \\ & a_{\text{Grating}} \in [a_{\text{min}}, a_{\text{max}}] \\ & h_{\text{Diel}} \in [h_{\text{Diel,min}}, h_{\text{Diel,max}}] \end{aligned} \tag{6.1.4}$$

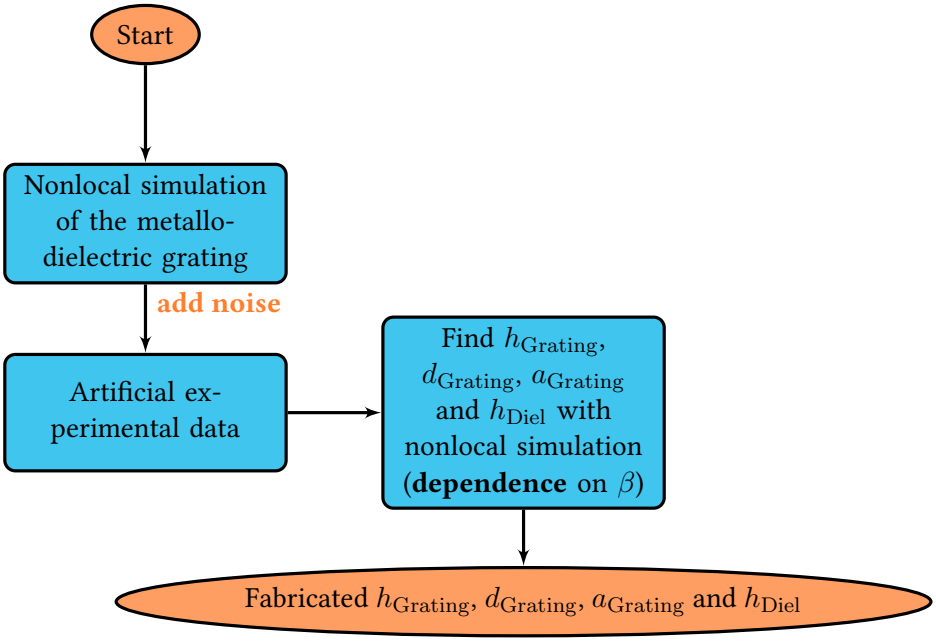

Figure 6.7 | Workflow of the metallo-dielectric free grating (nonlocal). Schematic for step II C. Similar steps as in Figure 6.6. However, here a nonlocal simulation tool is used to solve the inverse problem. This requires a precise knowledge of the nonlocal parameter β.

B-2 Use the noisy *nonlocal* spectrum and solve the optimization problem as stated in (6.1.1). However, fix the already found parameters for d_{Grating}, a_{Grating} and h_{Grating} (from step I) and optimize for h_{Diel} *only*

Inverse problem B-2

$$\begin{aligned} &\text{minimize} && \left|\left| R^{\text{nonlocal}}_{\text{measured}} - R^{\text{local}}_{\text{optimized}} \right|\right|_{l^2} \\ &\text{subject to} && h_{\text{Diel}} \in [h_{\text{Diel,min}}, h_{\text{Diel,max}}] \end{aligned} \tag{6.1.5}$$

C Use the noisy *nonlocal* spectrum and solve the optimization problem as stated in (6.1.1), add h_{Diel} but use a *nonlocal* model for $R_{\text{optimized}}$ in (6.1.1)

Inverse problem C

$$\begin{aligned} &\text{minimize} && \left|\left| R^{\text{nonlocal}}_{\text{measured}} - R^{\text{nonlocal}}_{\text{optimized}} \right|\right|_{l^2} \\ &\text{subject to} && h_{\text{Diel}} \in [h_{\text{Diel,min}}, h_{\text{Diel,max}}]. \end{aligned} \tag{6.1.6}$$

Indeed, a combination of these scenarios gives rise to multiple indications for nonlocality. We will chronologically discuss each step in the following.

Remark 6.1.4. *The nonlocal simulation for $R^{\text{nonlocal}}_{\text{measured}}$ relies on a nonlocal DGTD simulation.*

A-1 Figure 6.8 shows the result for an artificial measurement based on a local dispersion model, compared to the solution of the inverse problem that is equally based on a local simulation. This strategy finds the same values for h_{Grating}, d_{Grating}, a_{Grating} as (6.1.1) and additionally $h_{\text{Diel}} = 84.82$ nm. Leading to an absolute error of 0.18 nm ($h_{\text{Diel,init}} = 85$ nm).

A highly accurate result of the inverse problem can be explained by the fact that the artificial measurement data is based on the *same* physical model (local dispersion).

A-2 Strategy A-2 leads to $h_{\text{Diel}} = 85.45$ nm being very close to the result in A-1. We refer to the discussion of A-1.

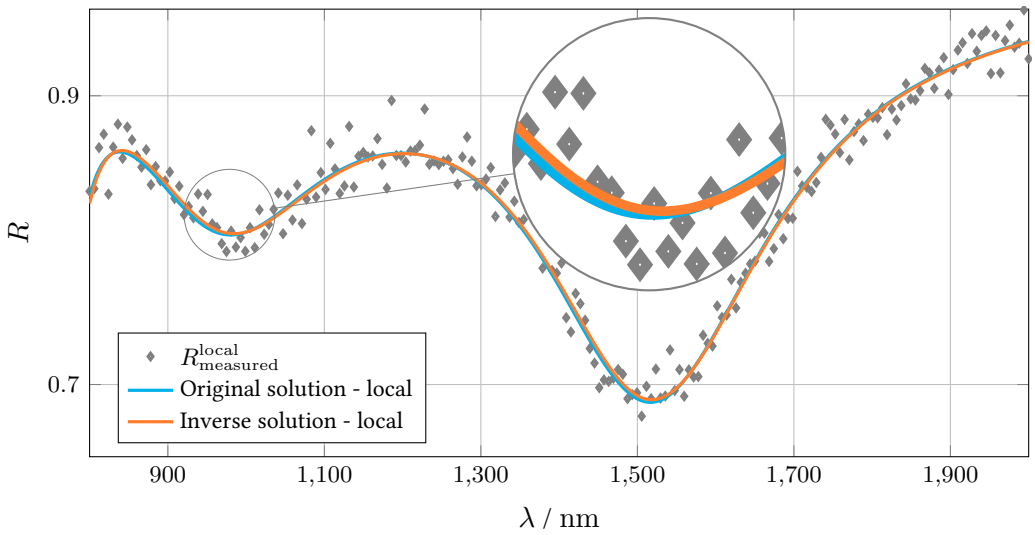

Figure 6.8 | Reflectance spectrum. Result of step II A-1 and A-2. An artificial white noise has been added to the original local dispersion spectrum (in blue) obtained for $h_{\text{G,init}} = 68.0$ nm, $d_{\text{init}} = 500.0$ nm, $a_{\text{init}} = 166.67$ nm, and $h_{\text{Diel,init}} = 85$ nm . In orange: the result of (6.1.2). The spectrum corresponds to $h_{\text{Grating}} = 68.01$ nm, $d_{\text{Grating}} = 502.19$ nm, $a_{\text{Grating}} = 166.91$ nm and $h_{\text{Diel}} = 85.45$ nm. The constraint intervals are chosen to be $h_{\text{Grating}} \in [62, 73]$ nm, $d_{\text{Grating}} \in [495, 505]$ nm, $a_{\text{Grating}} \in [161, 171]$ nm and $h_{\text{Diel}} \in [75, 95]$ nm, which is in accordance with the precision of the fabrication process. If we fix the previously obtained values of h_{Grating}, d_{Grating} and a_{Grating} from Figure 6.4 and hence solve (6.1.3), we obtain $h_{\text{Diel}} = 84.82$ nm. The resulting spectra are almost identical and we omit displaying the result of A-2.

B-1 If nonlocality was present in reality, the measured spectrum will be affected as soon as the dielectric is deposited. Using a reflectance result from a simulation (based on nonlocal dispersion) allows a theoretical investigation of that case. This is equivalent to the left branch in Figure 6.6. According to the small visual difference between the artificial reflectances $R^{\text{local}}_{\text{measured}}$ and $R^{\text{nonlocal}}_{\text{measured}}$ as shown in Figure 6.13, we expected a low impact of nonlocality on the solution of (6.1.4) compared to (6.1.2). Nonlocality seemingly causes a small deviation compared to the local curve and the noise finally blurs the difference completely.

This, however, is not the case. Solving the inverse problem (6.1.4) does not yield the correct geometric parameters d_{Grating}, a_{Grating}, h_{Grating} and h_{Diel}. Keeping the same fabrication uncertainty intervals as before, (6.1.4) finds $d_{\text{Grating}} = 499.71$ nm, $a_{\text{Grating}} = 161.00$ nm, $h_{\text{Grating}} = 67.23$ nm and $h_{\text{Diel}} = 85.96$ nm. Here, the optimizer reached the lower constraint value of the interval bound of h_{Grating}, see Figure 6.9. Artificially increasing the interval bounds, i.e. exceeding the a priori fabrication uncertainty, leads to $d_{\text{Grating}} = 491.08$ nm, $a_{\text{Grating}} = 158.15$ nm, $h_{\text{Grating}} = 67.36$ nm and $h_{\text{Diel}} = 85.99$ nm. It seems that the optimization process tried to compensate nonlocality by tweaking the values of a_{Grating}

and h_{Grating}. Nevertheless, the 'wrong' (local dispersion) model still yields reasonably good results for d_{Grating} and a_{Grating}.

This allows us to conclude an intermediate result. If *nonlocality is not* present in the measurement, the inverse problems (6.1.1), (6.1.2) as well as (6.1.3) will find the *same* geometric parameters for d_{Grating}, a_{Grating}, h_{Grating} *and* an accurate value for h_{Diel}.

Contrarily, if *nonlocality is* present, the inverse problem (6.1.4) will not confirm the already found values from (6.1.1). Especially, the parameters a_{Grating} and h_{Grating} seem to be particularly sensitive to this effect. Since the deposition of the dielectric does not affect the metallic geometry (step I), we have hereby found a *first hint* for nonlocality.

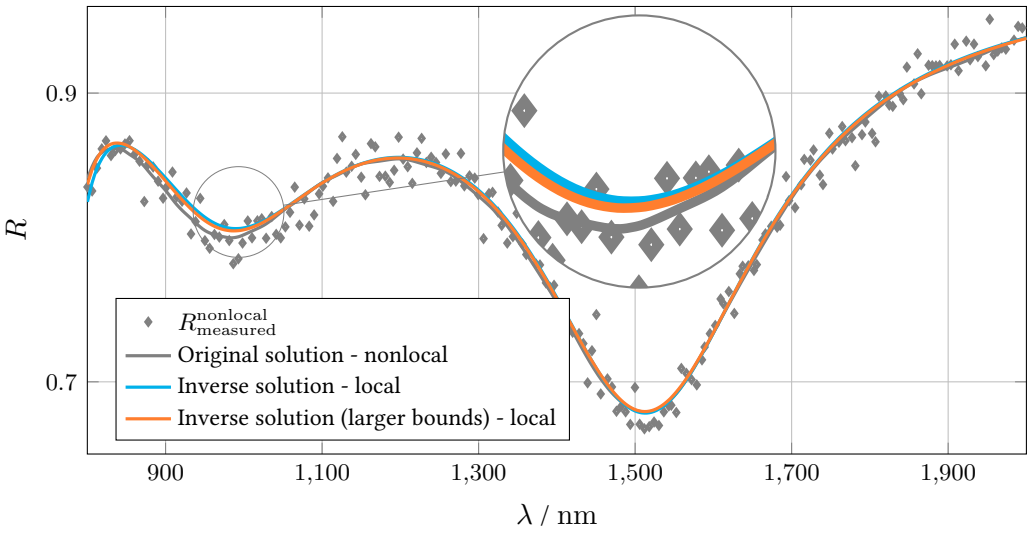

Figure 6.9 | Reflectance spectrum. Result of step II B-1. Gray diamonds: $R^{\text{nonlocal}}_{\text{measured}}$ corresponds to the *nonlocal* spectrum (gray line) with $h_{\text{G,init}} = 68.0$ nm, $d_{\text{init}} = 500.0$ nm, $a_{\text{init}} = 166.67$ nm, and $h_{\text{Diel,init}} = 85$ nm . In blue: the result of the inverse problem (6.1.4). The spectrum is based on $h_{\text{Grating}} = 67.23$ nm, $d_{\text{Grating}} = 499.71$ nm, $a_{\text{Grating}} = 161.00$ nm and $h_{\text{Diel}} = 85.96$ nm. The constraint intervals are chosen to be $h_{\text{Grating}} \in [62, 73]$ nm, $d_{\text{Grating}} \in [495, 505]$ nm, $a_{\text{Grating}} \in [161, 171]$ nm and $h_{\text{Diel}} \in [75, 95]$ nm, which is in accordance with the precision of the fabrication process. In orange: the same result as the blue curve for larger constraint intervals $h_{\text{Grating}} \in [57, 78]$ nm, $d_{\text{Grating}} \in [490, 510]$ nm, $a_{\text{Grating}} \in [156, 176]$ nm and $h_{\text{Diel}} \in [70, 100]$ nm. Optimization finds $h_{\text{Grating}} = 67.36$ nm, $d_{\text{Grating}} = 491.08$ nm, $a_{\text{Grating}} = 158.15$ nm and $h_{\text{Diel}} = 85.99$ nm.

B-2 Reusing the already obtained results for h_{Grating}, d_{Grating}, a_{Grating}in (6.1.1) for the metal geometry, yields (6.1.5) (similar to A-2 but with nonlocal measurement data). This is equivalent to the right branch in Figure 6.6. Still, the underlying simulation model for the inverse problem (6.1.5) remains *local* and is hence 'wrong' with respect to the artificial (nonlocal dispersion model) measurement data.

However, solving the inverse problem (6.1.5) based on local simulations, yields $h_{\text{Diel}} = 84.83$ nm (see Figure 6.10), being very close to the original value of 85.00 nm. In contrast to B-1, where all 4 parameters were free, the found value for h_{Diel} is now significantly more accurate.

In other words, if *nonlocality is present* in the measurement, B-1 (nonlocal measurement) finds different values for the metal structure and than A-1 and A-2 (local measurements). As a matter of fact, B-2 seems to realize a well working manner to find the unknown dielectric height h_{Diel}, only relying on locally dispersive simulations (although being the 'wrong' model). This circumvents any assumption on a nonlocal dispersion model during step I and II.

Remark 6.1.5. *We cannot provide a thorough explanation why this works. A possible reason may be that the metal geometry dictates the overall shape of the reflectance curve. Although nonlocality modifies the reflectance, the dielectric height cannot compensate this impact. This further means:* nonlocality is not interchangeable with the dielectric height. *A proper sensitivity analysis will be part of a future work.*

Furthermore, even if the impact of nonlocality (compare reflectances in Figure 6.13) is not directly visible in the measured spectrum for $\lambda \in [800, 2000]$ nm, it clearly becomes observable through the geometric parameters, obtained by the solution of concatenated inverse problems (step I + II).

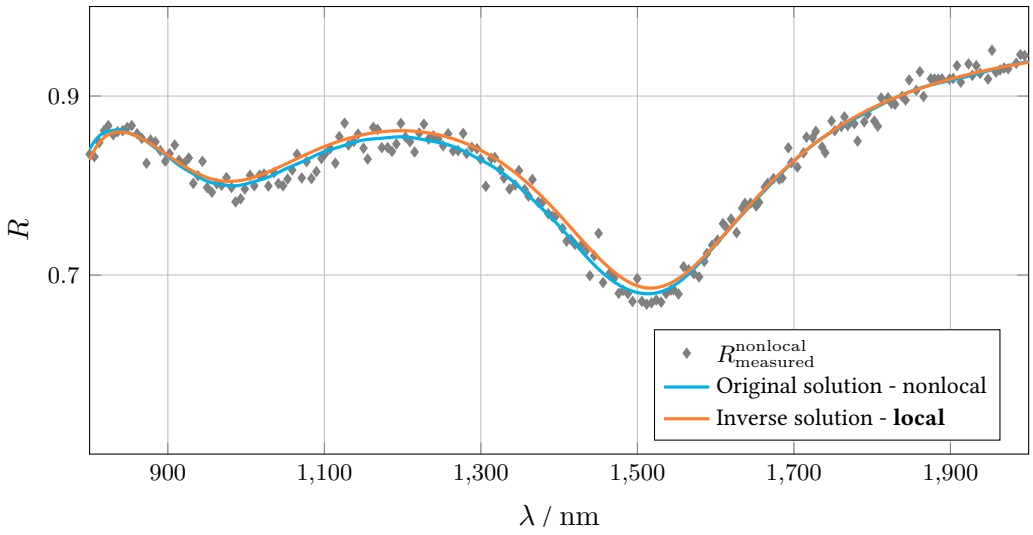

Figure 6.10 | Reflectance spectrum. Result of step II B-2. Gray: $R^{\text{nonlocal}}_{\text{measured}}$ corresponds to the original *nonlocal* spectrum (in blue) for $h_{\text{G,init}} = 68.0$ nm, $d_{\text{init}} = 500.0$ nm, $a_{\text{init}} = 166.67$ nm, and $h_{\text{Diel,init}} = 85$ nm . Orange: the result of the inverse problem (6.1.5). We have fixed the first three values of h_{Grating}, d_{Grating} and a_{Grating} according to Figure 6.4 and find $h_{\text{Diel}} = 84.83$ nm. The constraint interval is chosen to be $h_{\text{Diel}} \in [75, 95]$ nm, which is in accordance with the precision of the fabrication process. The positive off-set of the local solution with comparison to the initial nonlocal reference spectrum is in line with our simulations, where nonlocality slightly decreases the reflectance.

C Figure 6.7 and system (6.1.6) have not been tackled within the scope of this work because we want to avoid any assumptions on the nonlocal model for the geometric telemetry step.

Telemetry result Step I and II provide the final geometry

Geometric telemetry result

$$\begin{aligned} h_{\text{Grating}} &= 68.08 \text{ nm}, \\ d_{\text{Grating}} &= 499.15 \text{ nm}, \\ a_{\text{Grating}} &= 165.34 \text{ nm}, \\ h_{\text{Diel}} &= 84.83 \text{ nm}, \end{aligned} \tag{6.1.7}$$

of the metallo-dielectric grating in Figure 6.2.

Table 6.1 | Uncertain parameters extracted from procedure B-2.

Parameter	$\overline{z}$	δ_z	Units
h_{G}	68.082	0.1	(nm)
d_{G}	499.156	1.0	(nm)
a_{G}	165.36	1.5	(nm)
h_{D}	84.83	0.3	(nm)

6.1.2 Nonlocal dispersion - distinction from geometric uncertainty and model calibration

The geometric telemetry has lead to the fabricated geometries in Table 6.1. This has paved the way for two further studies:

(1) An a priori comparison of local and nonlocal reflectance spectra, assuming a β-value from literature. Here, we have used $\beta = 1.35\text{e}6$ $\mathrm{m/s}$.

(2) A similar strategy as for the geometric telemetry in order to extract β from the measurement data. (step III)

(1) - Geometric uncertainty vs. nonlocality We use the UQ study results in order to estimate $\pm 2\sigma$ intervals around the optimized local reflectance curve, where $\sigma = \sqrt{\mathbb{V}[R]}$ refers to the standard deviation. The results corresponding to each resonance area are presented in Figure 6.11 and Figure 6.12 (in blue), respectively. Since the nonlocal DGTD simulations are too expensive for an UQ of the same kind as we have performed local model, we rely on a min-max study. Here, min-max represents solver calls for all interval bound combinations (in orange) as depicted in the corresponding figures.

According to Figure 6.12 (a), a clear measurement of the first resonance is almost impossible due to the small difference between the local and nonlocal curves. Nevertheless, the second resonance (see Figure 6.12 (b)) is significantly more sensitive to nonlocality and stays distinguishable. For the sake of robustness, we have also performed simulations with the lowest physically acceptable value for $\beta = 0.85\text{e}6$ $\mathrm{m/s}$ [61], which still guarantees a blueshift of 5 nm for the second resonance, i.e. stronger than the geometric uncertainty. A parameter sweep on β is depicted in Figure 6.14. Physically acceptable values for β may lie between $\beta_{\min} \approx 0.85\text{e}6$ $\mathrm{m/s}$ [61] and $\beta_{\max} \approx 1.4\text{e}6$ $\mathrm{m/s}$ [128].

(2) - Model calibration (step III) Knowing the geometry and estimating the impact of nonlocality to be greater than geometric uncertainties, we now want to extract the nonlocal material parameter β. We proceed in the same way as for the geometric telemetry. However, instead of searching the geometry parameters d_{Grating}, a_{Grating}, h_{Grating} and h_{Diel}, we are now interested in β. The corresponding inverse problem, formally cast into an optimization problem, reads

Calibration of the nonlocal dispersion model: find β

$$\begin{aligned} &\text{minimize} && \left|\left| R^{\text{nonlocal}}_{\text{measured}} - R^{\text{nonlocal}}_{\text{optimized}} \right|\right|_{l^2} \\ &\text{subject to} && \beta \in [\beta_{\min}, \beta_{\max}]. \end{aligned} \tag{6.1.8}$$

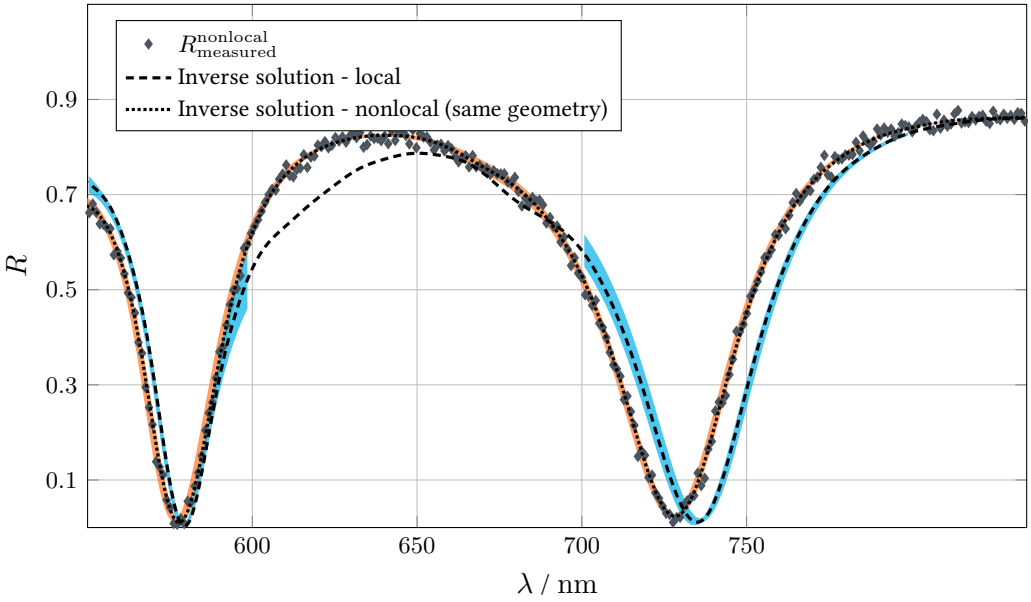

Figure 6.11 | Local vs. nonlocal grating. Comparison of the local and nonlocal reflectance. The positions of the local resonances are at 579 nm and 735 nm and the nonlocal ones at 577 nm and 728 nm. This leads a blue-shift of 2 nm and 7 nm, respectively. In blue: the $\{R\} \pm 2\sigma$ area, being an output of the UQ analysis based on stochastic polynomials. In orange: the min-max intervals of the reflectance for all interval bound combinations of the uncertain geometric parameters $h_{\text{Grating}} \in \{67.98, 68.18\}$ nm, $d_{\text{Grating}} \in \{498.15, 500.15\}$ nm, $a_{\text{Grating}} \in \{163.86, 166.86\}$ nm and $h_{\text{Diel}} \in \{84.69, 85.31\}$ nm.

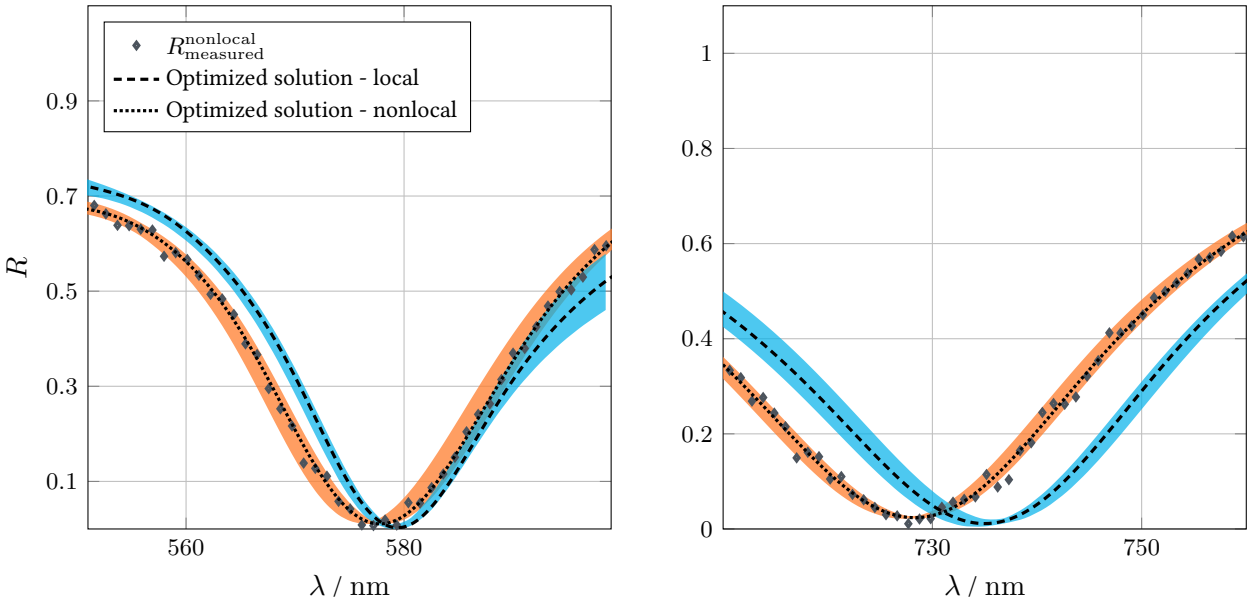

(a) Zoom on first resonance. **(b) Zoom on second resonance.**

Figure 6.12 | Local vs. nonlocal grating (Zoom). Zoom on the resonances in Figure 6.11.

Obviously, the solution of (6.1.8) requires nonlocally dispersive simulations. Since our RCWA neither handles the whole spectrum $\lambda \in [550, 2000]$ nm nor considers nonlocal dispersion, we have to rely on DGTD [135].

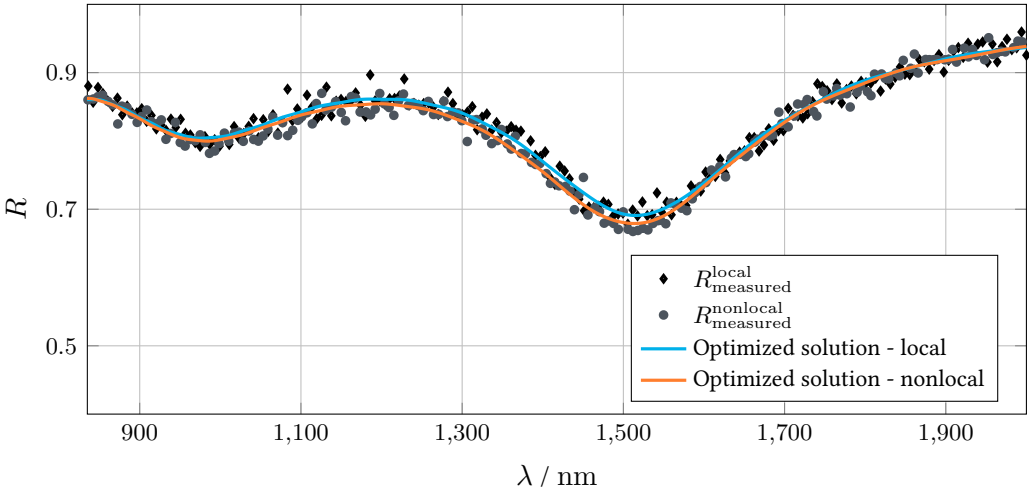

Figure 6.13 | Local vs. nonlocal grating. Comparison of the local and nonlocal reflectance at wavelengths $\lambda \in [800, 2000]$ nm. In black and gray, the artificially obtained experimental data for the local and nonlocal dispersion model, respectively. The distinction between both sets of measurement points is almost impossible. Blue: Reflectance of the metallo-dielectric grating based on the parameters found in B-2 and *local* dispersion. Orange: Reflectance of the metallo-dielectric grating based on the parameters found in B-2 and *nonlocal* dispersion.

The geometric size of the structure in combination with very small effective wavelengths already requires very fine meshes with respect to the free-space wavelength. Additionally, the interaction range of nonlocal effects is in the range of several nano-meters at the metallo-dielectric interface and also needs to be well resolved. The size of the computational domain and the necessary mesh-refinements lead to $\approx 10^7$ DoFs. Since we work in time-domain, the combination of small mesh cells (strong constraint for explicit time integration, i.e. CFL-condition) and a long plasmon lifetime due to periodic boundary conditions, lead to $\approx 120,000$ time-step iterations. In summary, one broad-band simulation takes about 640 CPU hours. Employing MPI-parallelization reduces the actual simulation times to 5-10h on 4-6 nodes (16 cores per node) of the Occigen cluster [56]. The solution of the inverse problem as stated in (6.1.8) can be significantly accelerated by meta-model based optimization algorithms. We have used the Kriging meta-model (Gaussian process model) implementation of the FAMOSA [37] optimization toolbox.

Physically acceptable values for β may lie between $\beta_{\text{min}} \approx 0.85\text{e}6$ m/s [61] and $\beta_{\text{max}} \approx 1.4\text{e}6$ m/s [128]. Figure 6.15 shows the result of (6.1.8). We find $\beta_{\text{inverse}} = 1.385\text{e}6$ m/s which is reasonably close to the $\beta_{\text{init}} = 1.35\text{e}6$ m/s (value for $R^{\text{nonlocal}}_{\text{measured}}$).

6.1.3 Optical near-field of the grating - local vs. nonlocal dispersion

We conclude this chapter with 2D solutions of the electric field. Figure 6.16 shows the Fourier-transformed fields at $\lambda_{\text{res},1} = 577$ nm and $\lambda_{\text{res},2} = 728$ nm. A high coupling-efficiency of the normally incident plane wave with the surface plasmon at λ_{res}, i.e. $R(\lambda_{\text{res}}) < 2\%$, leads to a very plane wave-like field at a certain height above the dielectric. This observation is also confirmed by almost vanishing fields in the SF-domain above the TF/SF-interface. These observations apply for both, local and nonlocal dispersive simulations.

Zooming-in to the metallo-dielectric surface in the vicinity of the grating reveals sub-tile differences between local and nonlocal dispersion. Figure 6.17 compares the near-field at $\lambda_{\text{res},1}$ of a local and nonlocal simulation. The local simulation clearly respects the metallo-dielectric interface. The magnitude of the electric field $|\mathbf{E}|$ jumps exactly at the transition from the metal to the dielectric. For nonlocal dispersion,

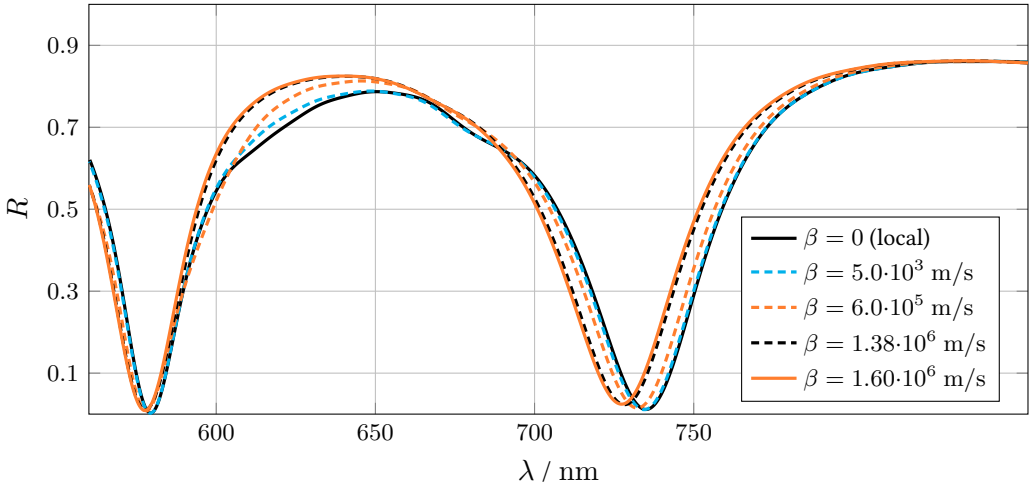

Figure 6.14 | Local to nonlocal dispersive grating. Comparison of the reflectance curve in dependence of an increasing β factor. Starting from a purely local dispersion model up to physically acceptable values of β.

however, we can observe a thin penetration layer and a smoother field distribution. Especially, the upper corner experiences an increased field inside the metal. Additionally, nonlocality seems to smooth the field singularities that appear in vicinity of the corners. Those field-singularities are well known to be problematic for numerical methods at material corners. Although our linearized hydrodynamic fluid-model only allows a first order perturbation of the electron density, it already leads to a significantly smoother surface transition at the metallo-dielectric interface. Our results are in line with theoretical investigations in [9]. Equivalent interpretations apply to the second resonance $\lambda_{\mathrm{res},2}$ (see Figure 6.18).

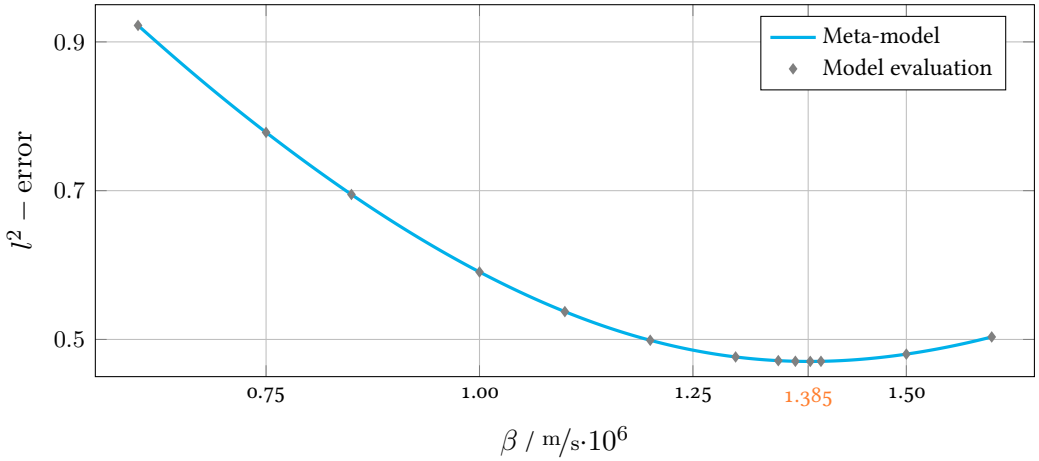

Figure 6.15 | Find beta. Meta-model based optimization of (6.1.8). Blue: Kriging meta-model of the l^2-error. Gray: cost function calls of that calibrate the meta-model. The minimum is found to be $\beta_{\text{inverse}} = 1.385\text{e}6\ ^{m}/_{s}$, which is very close to the initial value of $\beta_{\text{init}} = 1.35\text{e}6^{m}/_{s}$.

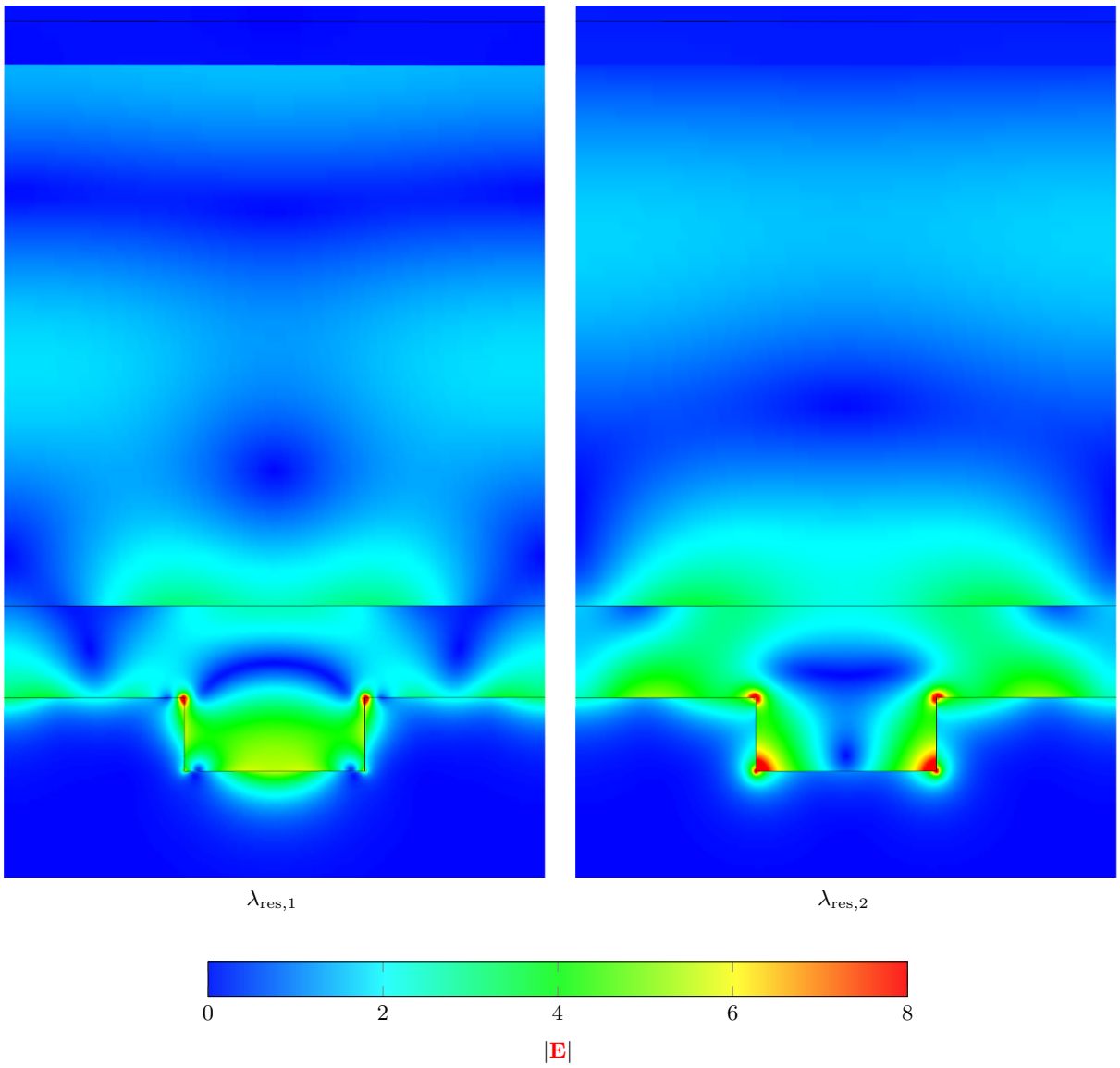

Figure 6.16 | Field solution at grating resonances. From the top to the bottom: PML-domain (not displayed), SF-domain, TF-domain, vacuum-TiO_2 interface, metallic grating. The high coupling efficiency of the incident plane wave and the surface plasmonic mode is remarkably obvious (almost no field in the SF domain). We quantify this by the very plane-wave like wavefront above the grating. In other words, the grating couples almost all the incident energy into the surface plasmon. This is perfectly in line with with the almost vanishing reflectance of about 1% and 2% for the first and second resonance, respectively.

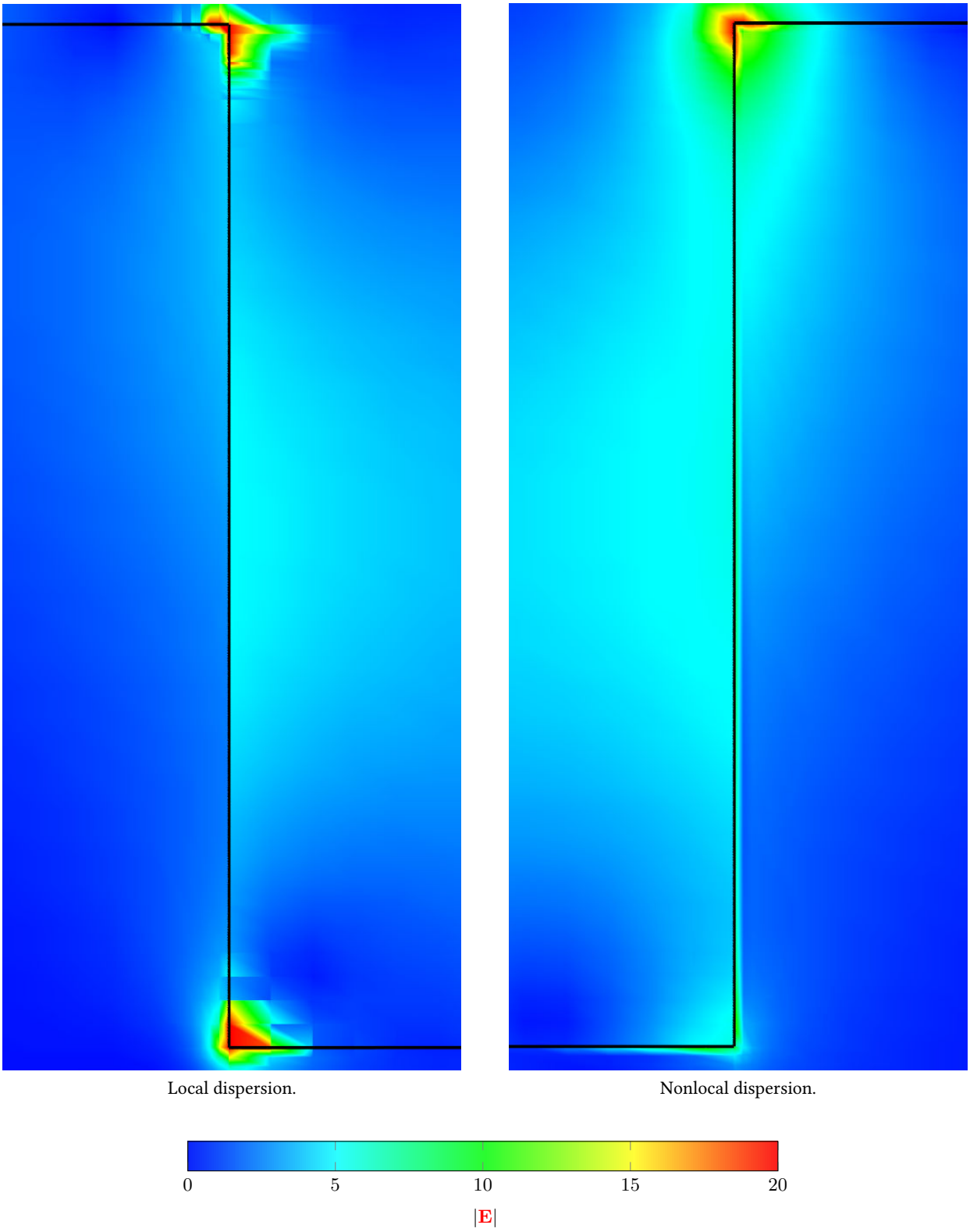

Figure 6.17 | Field solution at grating resonances $\lambda_{\mathrm{res},1}$ (zoom). First resonance. Nonlocality allows a very think penetration layer at the metallo-dielectric interface. Additionally, the field singularities at the corners are weakened and almost completely disappear for the lower corner.

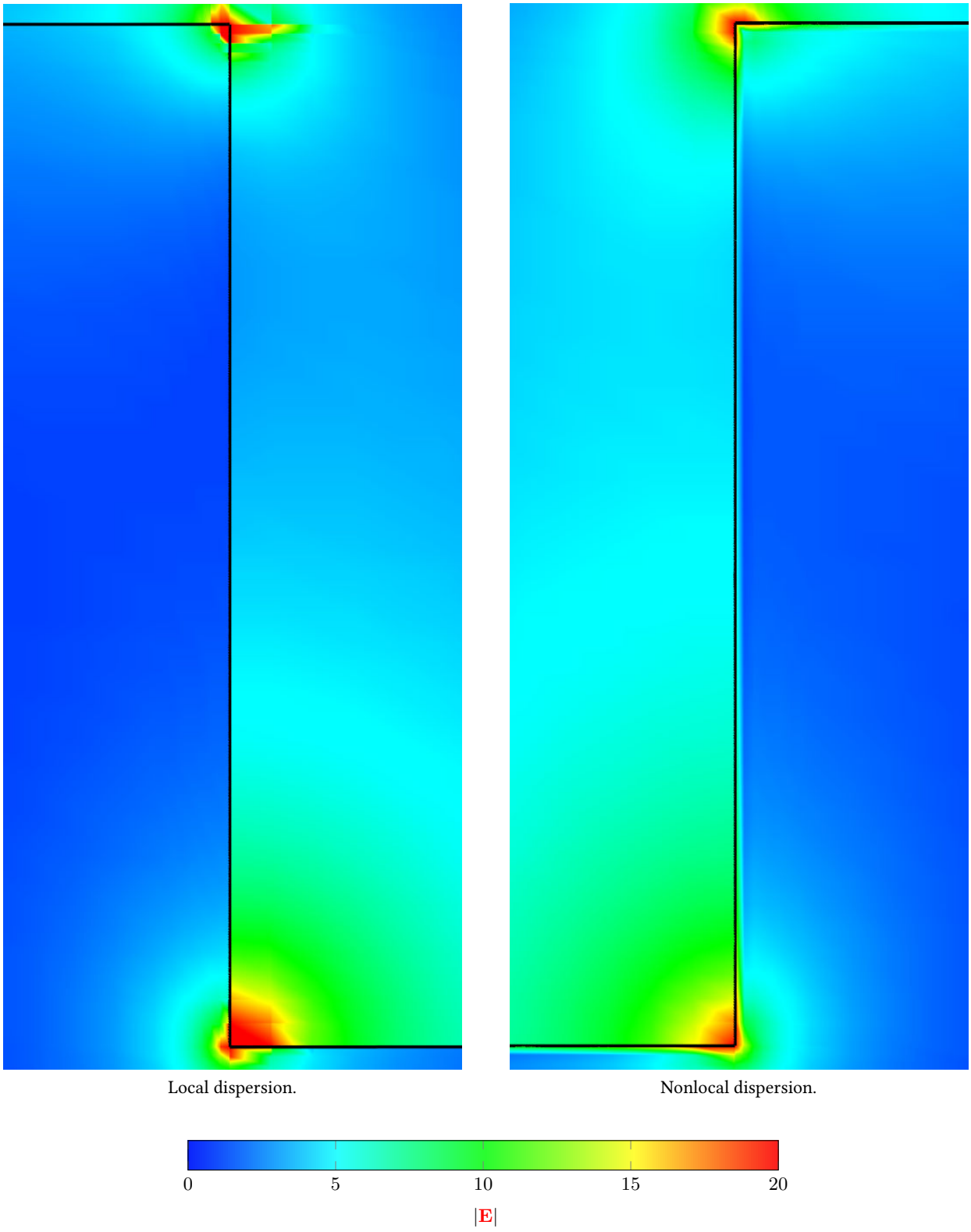

Local dispersion. Nonlocal dispersion.

Figure 6.18 | Field solution at grating resonances $\lambda_{\mathrm{res},2}$ (zoom). Second resonance. Nonlocality allows a very think penetration layer at the metallo-dielectric interface. Additionally, the field singularities at the corners are weakened.

6.2 Nano-cubes

Why are we interested in nano-cubes? Surface plasmons at metallo-dielectric interfaces can be sensitive to nonlocality. Figure 6.19 (a) depicts an gold-dielectric interface. Following standard derivations [96, 106], the dispersion relation of the surface plasmon reads

$$\frac{\kappa_z}{\varepsilon_\mathrm{d}} + \frac{\kappa_\mathrm{t}}{\varepsilon} = \xi, \qquad \text{with} \quad \xi := \frac{\{\mathbf{k}\}_x^2 \left(\frac{1}{\varepsilon} - \frac{1}{1+\chi_b}\right)}{\sqrt{\{\mathbf{k}\}_x^2 + \frac{{\omega_\mathrm{P}}^2}{\beta^2}\left(\frac{1}{\chi_f} + \frac{1}{1+\chi_b}\right)}} \tag{6.2.1}$$

Here, ε is the local permittivity contribution of the metal, ε_d the permittivity of the dielectric, $\kappa_z = \sqrt{\{\mathbf{k}\}_x^2 - \varepsilon_\mathrm{d} {k_0}^2}$, $\kappa_\mathrm{t} = \sqrt{\{\mathbf{k}\}_x^2 - \varepsilon {k_0}^2}$, and $\chi_{b,f}$ are consistent with Chapter 2. Equation (6.2.1) is well known from local dispersion theory if $\beta = 0$, i.e. $\xi = 0$. Figure 6.20 (a) depicts the dispersion relation of a surface plasmon. Obviously, nonlocality has a negligible impact. Considering a metal-dielectic-metal gap structure as shown in Figure 6.19 (b) with the gap height h yields the dispersion relation for the symmetric mode

$$\frac{\kappa_z}{\varepsilon_\mathrm{d}} \tanh \frac{\kappa_z h}{2} + \frac{\kappa_t}{\varepsilon} = \xi. \tag{6.2.2}$$

We refer to [106] for details and conclude two important statements from (6.2.2):

- The impact of nonlocality on the symmetric mode scales with $\{\mathbf{k}\}_x$;
- Decreasing gap sizes lead to very high $\{\mathbf{k}\}_x$ and thus to an increased sensitivity to nonlocality (see Figure 6.20 (b));
- Nonlocality kicks in at gap sizes smaller than $\approx 5\,\mathrm{nm}$ since $\{\mathbf{k}\}_x$ reaches considerably high values.

Motivated by these theoretical predictions for infinite gap structures, we propose the well-known nano-cube setup to study the influence of nonlocal dispersion on gap plasmons. Nano-cubes are famous for the high fabrication accuracy due to the underlying chemical process. Application wise, nano-cubes have been used for extreme Purcell factor devices [1], imaging based on meta surface pixels [141], molecule sensoring [66], perfect absorbers [2], ultrafast emission sources [62] and many more.

In the scope of this work, we want to investigate the resonance position of the gap plasmon for very small gaps. By this means, we study the discrepancy between local and nonlocal simulations. In order to build a reliable geometric model, we first perform a post-fabrication telemetry, which leads to accurate geometrical parameters of the nano-cube. This telemetry is based on the experimental data in [105]. As a major result, we are able to explain the discrepancies between local simulations and measured resonance positions by a significant impact of nonlocal dispersion for gap sizes of about $3.1\,\mathrm{nm}$. This result is based on a 3D simulation with nonlocal dispersion models.

6.2.1 Metamodel-based telemetry

Unfortunately, microscopy techniques cannot provide sufficiently accurate information about the geometric parameters of our model cube, see Figure 6.21. The optical response of nano-cubes is very sensitive to the actual cube size that is mainly determined by the cube roundings, the thickness of the dielectric shell and the length of the cube. This makes an accurate knowledge of the geometry absolutely necessary. From a modeling point of view, we first have to calibrate our geometric model of Figure 6.21 (b). Relying

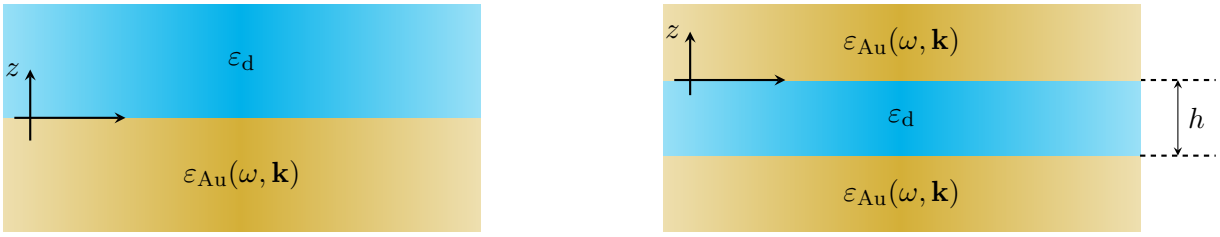

(a) Interface between gold and air.

(b) Dielectric slit in a metal bulk.

Figure 6.19 | Surface and gap plasmon geometry.

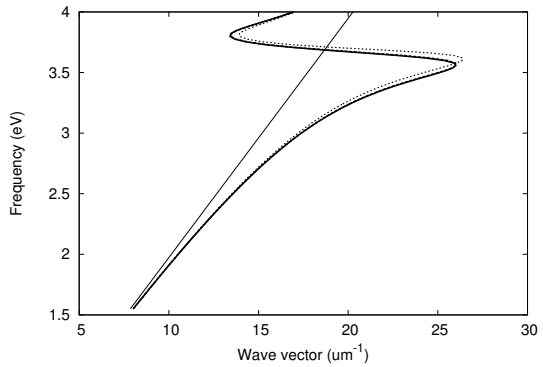

(a) Dispersion relation (ω as a function of $\{\mathbf{k}\}_x$) for a surface plasmon at the interface between silver and air. The local description (thick solid curve) can almost not be distinguished from the nonlocal description (thick dashed curve, almost identical with the thick solid curve). In order to illustrate the effect of nonlocality, we show here (dotted line) the impact of an exaggerated nonlocality (β multiplied by ten). The thin solid curve is $\omega = \{\mathbf{k}\}_x c_0$.

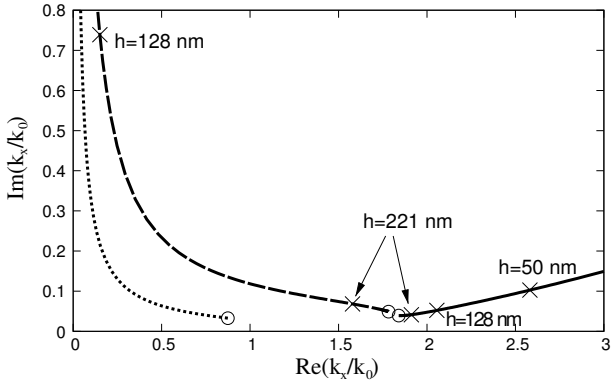

(b) Trajectory in the complex plane of the quantity ${}^{\{\mathbf{k}\}_x}/_{k_0}$ for three different waveguided modes (solide line: first even mode; dashed line: first odd mode ; dotted line: second even mode) when the width of the metal goes from 380 nm (circles) to 10 nm. The permittivity of the metal is taken equal to the permittivity of gold at 608 nm, $\sigma \approx -10.01 + i1.44$ Intermediate thickness of 221 nm (when the real part of the index of the odd mode becomes smaller than 1.58, so that the coupled plasmon picture becomes less relevant), 128 nm (when the odd mode can be considered non-propagative, and the coupled plasmon picture is not relevant any more) and 50 nm are indicated on the curves.

Figure 6.20 | Surface and gap plasmon. Figures with courtesy of [106].

on a well established local dispersion model for silver and gold, we will perform a calibration procedure for gap widths, where nonlocality is negligible. In the following, we only rely on the gap plasmon resonance position. Based on theoretical results in the literature [106], nonlocality is expected to be of minor importance for gap sizes larger than 5 nm. The term gap size has to be understood as the gap between two metals, where the gap is usually filled by a dielectric material. According to the schematic in Figure 6.21, the gap size would be $\delta_{\mathrm{Gap}} = \delta_{\mathrm{Diel}} + \delta_{\mathrm{Shell}}$. Assuming the cube fabrication process to be sufficiently robust, we want to find a radius r_{Ag}, a shell thickness δ_{Shell} and a cube length l_{Cube} independent of δ_{Diel}. (Robust here means that these parameters are constant for the fabrication of different samples with varying dielectric heights δ_{Diel}.) Once these parameters have been found, a variation of the dielectric layer δ_{Diel} will be performed, equivalent to the study in [105].

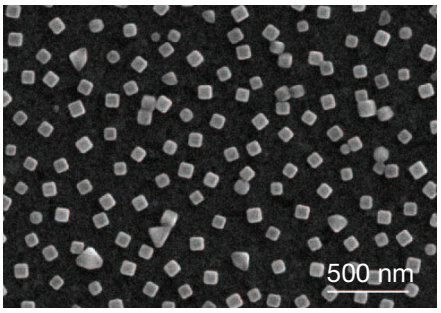

(a) Scanning electronic microscopy images of the silver nano-cubes. Here, the surface coverage is 17.1%. Courtesy of [105].

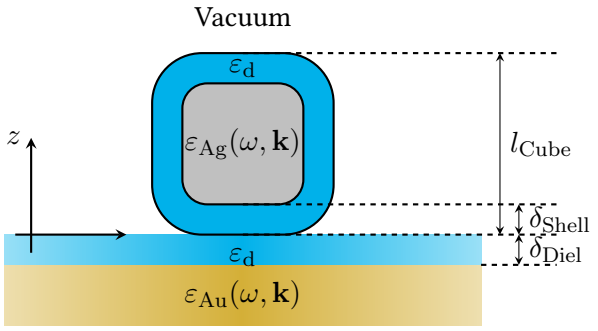

(b) The nano-cube setup consists of an infinite gold ground layer, a dielectric spacer of height δ_{Diel} and the cube surrounded by vacuum. Realistic cubes are wrapped in a dielectric shell layer of size δ_{Shell}. We define l_{Cube} as the total length of the cube, including the dielectric shell. The rounding radii of the inner and outer cube are denoted by r_{Ag} and r_{Diel}, respectively.

Figure 6.21 | Nano-cube. Figure (a) shows a Scanning Electronic Microscopy (SEM) image of the fabricated nano-cubes [105] at Duke university, (b) defines the modeled geometry.

Indirect measurement of the cube geometry Finding the geometric parameters can be understood as an inverse problem because we know the solution, i.e. the measured gap resonance position of the nano-cube, and we aim to find the cube geometry that leads to these resonances.

Here, we tackle the inverse problem by an optimization of the gap resonance positions. This means, we try to find an optimal data set $\{r_{\mathrm{Ag}}, \delta_{\mathrm{Shell}}, l_{\mathrm{Cube}}\}$ in order to optimally fit the experimental data. In other words, we want to find a global minimum of the discrepancy between the measured and simulated resonance positions.

Such a procedure will require a significant amount of cost function evaluations, i.e. simulation runs. Depending on the cube geometry and the numerical simulation algorithm, this may be restrictively costly. As an example, a full wave 3D DGTD simulations in the time-domain of this nano-cube setup takes about 45 minutes on a modern parallel machine [56]. Figure 6.31 illustrates an example of the computational mesh. A key ingredient for rounded nano-cube simulations is the capability to accurately treat the rounded corners and edges. Since DGTD is a special FE type method, we can employ isoparametric curvilinear tetrahedra, well suited for rounded geometries (see Section 3.2.2). Alternatively, standard Cartesian based methods like FDTD would have to massively refine the global mesh in order to obtain a sufficient local spatial sampling, i.e. discretization of the rounded geometry. Details on the computational are postponed to the end of this chapter and we now want to focus on the solution of the inverse problem first.

In order to speed up the optimization procedure of the inverse problem, we will construct a *surrogate* model of the gap plasmon resonance position λ_{res}. The overall workflow is depicted in Figure 6.22.

Surrogate model

> igi-global.com *"A surrogate model is a model that approximates a more complex, higher order model and used in place of the complex model (hence the term surrogate). The reason is usually that the complex model is too computationally expensive to use directly, hence the need for a faster approximation. It is also known as a response surface model or a metamodel."*

For this study, different surrogate models are potentially applicable. For instance, one could imagine a single surrogate model, which completely approximates the whole absorption spectrum of the cube.

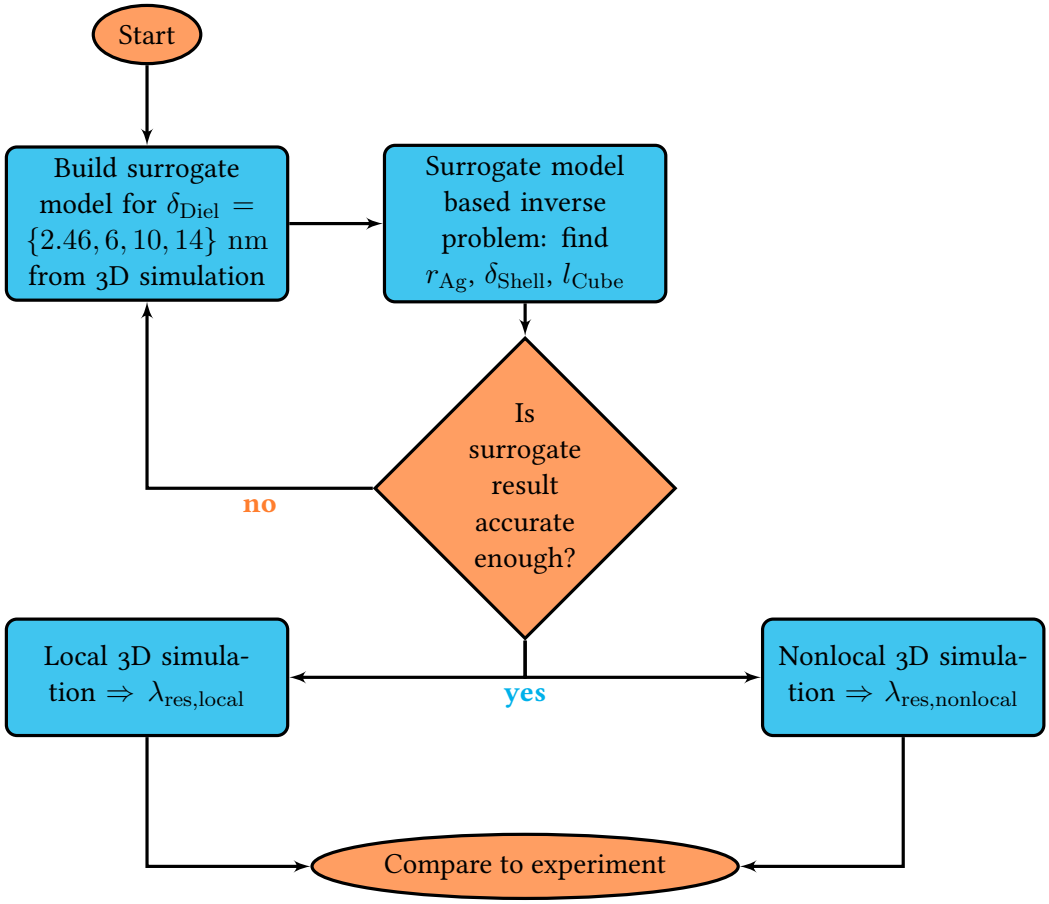

Figure 6.22 | Surrogate model based optimization. First, a surrogate model of the resonance position is built. Based on this surrogate model, we find the cube geometry r_{Ag}, δ_{Shell} and l_{Cube}. This surrogate model result is cross checked with a 3D simulation. If these simulations confirm the result, we assume the found geometry to be reliable and investigate the smaller gap sizes. Local and nonlocal simulations are performed for the smaller gap sizes and compared to the experimental data.

However, each surrogate model is ideally based on a functional behaviour that mimics the QoI dependency (linear, exponential, etc.) on the model parameters (geometry, material, etc.). Here, we only know the resonance position as a function of the dielectric height δ_{Diel} (for a finite number of values δ_{Diel}. Furthermore, we do not have any a priori knowledge about the δ_{Diel} dependency of the resonance position, i.e. $\lambda_{\mathrm{res}} = f(\delta_{\mathrm{Diel}})$ is unknown. For small perturbations, the gap resonance is assumed to depend almost linearly[2] on $\{r_{\mathrm{Ag}}, \delta_{\mathrm{Shell}}, l_{\mathrm{Cube}}\}$. We hence propose to build independent and linear surrogate models for each δ_{Diel}.

Due to the fact that we have only 5 samples for different heights $\delta_{\mathrm{Diel}} = \{0.6, 2.46, 6.0, 10.0, 14.0\}$ nm from [105], the available data set is very limited. In consequence, we have decided to base our geometric telemetry on the four thickest dielectrics $\delta_{\mathrm{Diel}} = \{2.46, 6.0, 10.0, 14.0\}$ nm where nonlocality should be of minor importance since the overall gap size is $\delta_{\mathrm{Gap}} = \delta_{\mathrm{Diel}} + \delta_{\mathrm{Shell}}$.

In summary, each of the dielectric heights δ_{Diel}, where nonlocality is negligible, will have its 'own' surrogate model. These surrogate models will rely on simulations based on a local dispersion model and will be independent of δ_{Diel}. Since future experiments may provide a richer sampling of the dielectric height, we consider N samples of δ_{Diel} in the following and later restrict our considerations to $N = 4$.

[2] Changing the cube is equivalent to change the cavity size.

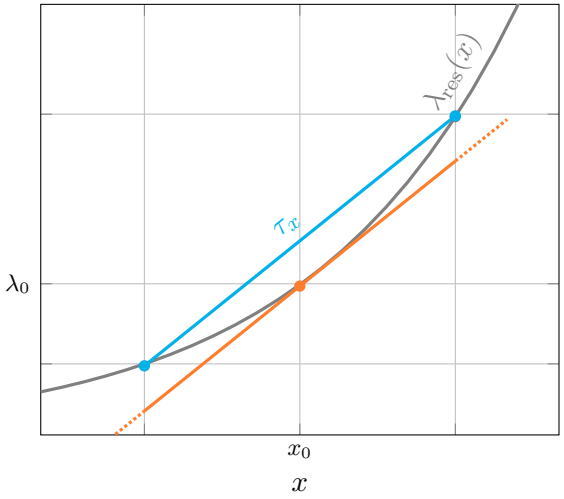

Figure 6.23 | Linear meta model. The linear meta model of the function $\lambda_{\mathrm{res}}(x)$ requires three function evaluations. One at the interval center, and two at the interval boundaries in order to obtain the approximated finite difference gradient τ_x. For visualization reasons, we have simplified the model to the 1D case.

The linear surrogate models of each gap plasmon resonance position for all dielectric heights δ_{Diel} can be cast into one vector

$$\begin{aligned} \boldsymbol{\lambda}_{\mathrm{res}}(r_{\mathrm{Ag}}, \delta_{\mathrm{Shell}}, l_{\mathrm{Cube}}) &= \boldsymbol{\lambda}_0 + \boldsymbol{\tau}_{r_{\mathrm{Ag}}} \Delta_{r_{\mathrm{Ag}}} + \boldsymbol{\tau}_{\delta_{\mathrm{Shell}}} \Delta_{\delta_{\mathrm{Shell}}} + \boldsymbol{\tau}_l \Delta_{l_{\mathrm{Cube}}} \\ &:= \boldsymbol{\lambda}_0 + \mathbb{A}\boldsymbol{\Delta} \end{aligned} \tag{6.2.3}$$

where we have defined

$$\begin{aligned} \mathbb{A} &:= \begin{bmatrix} \boldsymbol{\tau}_{r_{\mathrm{Ag}}} & \boldsymbol{\tau}_{\delta_{\mathrm{Shell}}} & \boldsymbol{\tau}_l \end{bmatrix}, \\ \boldsymbol{\Delta} &:= \begin{bmatrix} r_{\mathrm{Ag}} - r_{\mathrm{Ag},0} \\ \delta_{\mathrm{Shell}} - \delta_{\mathrm{Shell},0} \\ l_{\mathrm{Cube}} - l_{\mathrm{Cube},0} \end{bmatrix}. \end{aligned} \tag{6.2.4}$$

Here, $\boldsymbol{\lambda}_{\mathrm{res}}, \boldsymbol{\lambda}_0, \boldsymbol{\tau}_{r_{\mathrm{Ag}}}, \boldsymbol{\tau}_{\delta_{\mathrm{Shell}}}, \boldsymbol{\tau}_{l_{\mathrm{Cube}}} \in \mathbb{R}^N$ and the matrix $\mathbb{A} \in \mathbb{R}^{N\times 3}$. We omit SI units in the following. All geometric dimensions, if not further indicated, are to be considered in nm except for the $\mathbb{A}$, which is dimensionless.

The linear metamodel in (6.2.3) now needs to be calibrated to the experimental data from [105], being exactly the first step in Figure 6.22. We perform one simulation at the mean to determine λ_0 and compute τ_i with $i \in \{r_{\mathrm{Ag}}, \delta_{\mathrm{Shell}}, l_{\mathrm{Cube}}\}$, using the simulations at the interval bounds. These slopes are shifted to the mean point (see Figure 6.23).

In this sense, we now set $N = 4$ and define an interval mean $\boldsymbol{\lambda}_0$ at $\{r_{\mathrm{Ag}} = 5.0, \delta_{\mathrm{Shell}} = 3.5, l_{\mathrm{Cube}} = 72.5\}$ and symmetric intervals for the finite difference gradients in $\mathbb{A}$, i.e. $r_{\mathrm{Ag}} = 5 \pm 2.5$, $\delta_{\mathrm{Shell}} = 3.5 \pm 1.5$

and $l_{\text{Cube}} = 72.5 \pm 7.5$. Eventually, local dispersion 3D DGTD simulations at all of these samples lead to

$$\begin{aligned} \boldsymbol{\lambda}_0 &= \begin{bmatrix} 616.8 \\ 641.2 \\ 684.1 \\ 768.9 \end{bmatrix}, \\ \mathbb{A} &= \begin{bmatrix} -5.97 & -10.63 & 3.87 \\ -6.68 & -14.85 & 4.39 \\ -8.59 & -24.23 & 5.23 \\ -11.16 & -49.10 & 6.85 \end{bmatrix}, \end{aligned} \tag{6.2.5}$$

which concludes the first step of our workflow in Figure 6.22.

Surrogate model based inverse problem Having a surrogate model available, we now want to find the combination of r_{Ag}, δ_{Shell} and l_{Cube} that optimally fit with the measured resonance position

$$\boldsymbol{\lambda}_{\text{res,exp}} = \begin{bmatrix} 580.7 \\ 606.9 \\ 655.1 \\ 734.7 \end{bmatrix}. \tag{6.2.6}$$

This step can be formally cast into a constrained optimization problem of the form

Inverse problem: find cube geometry

$$\begin{aligned} \lambda_{\text{optimized}} &= \operatorname{argmin} ||\boldsymbol{\lambda}_{\text{res,exp}} - \boldsymbol{\lambda}_{\text{res}}(r_{\text{Au}}, \delta_{\text{Shell}}, l_{\text{Cube}})||_{l^2} \\ \text{subject to} \quad r_{\text{Au}} &\in [2.0, 8.0] \\ \delta_{\text{Shell}} &\in [2.0, 6.0] \\ l_{\text{Cube}} &\in [60.0, 85.0]. \end{aligned} \tag{6.2.7}$$

To solve this optimization problem, we have used Matlab's pattern search. Applying the optimization algorithm yields $r_{\text{Ag, optimal}} = 7.0$ nm, $\delta_{\text{Shell, optimal}} = 2.5$ nm and $l_{\text{Cube, optimal}} = 65.0$ nm. We have rounded the actually obtained values and cross checked that the rounding has a negligible impact. These values are in line with previous expectations from microscopy images. Figure 6.24 compares the measured data with the metamodel based resonance positions. We have also cross-checked the metamodel results with full wave 3D DGTD simulations, which corresponds to step three in Figure 6.22. The obtained negligible errors in the range of less than 0.2 nm or $\approx 0.03\%$. In consequence, we consider our metamodel to be sufficiently accurate and proceed with the subsequent steps in Figure 6.22.

Remark 6.2.1. *As for our case, a linear surrogate model appeared to be sufficient. We were thus not obliged to make the 'no'-loop in Figure 6.22. If this was necessary, a more complicated surrogate model might be required. We have not investigated this within the here presented study. Possible directions could be Kriging or stochastic collocation methods [94].*

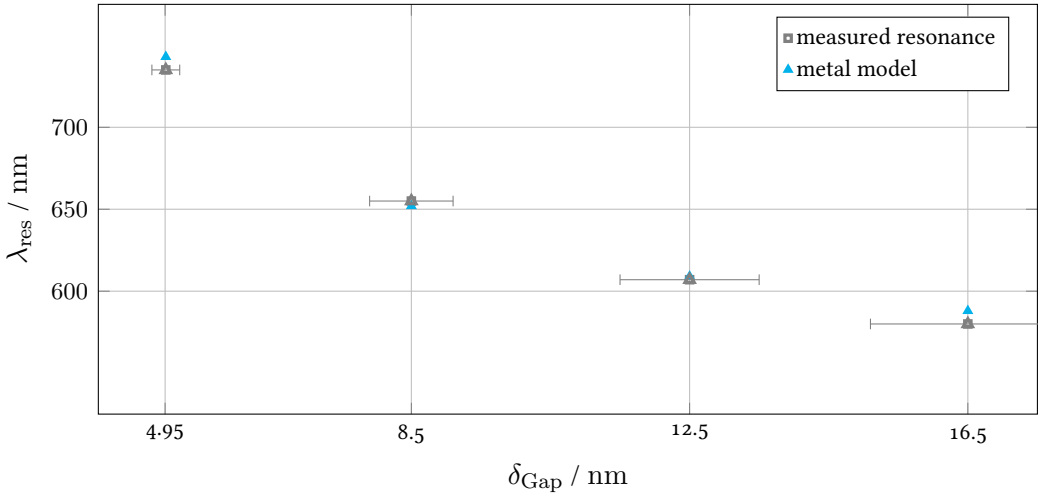

Figure 6.24 | Metal model based gap plasmon resonance. The optimized parameters are $r_{\mathrm{Ag,\,optimal}} = 7.0$ nm, $\delta_{\mathrm{Shell,\,optimal}} = 2.5$ nm and $l_{\mathrm{Cube,\,optimal}} = 65.0$ nm. The worst error of the meta model compared to a 3D simulation is of the order of 0.2 nm. The error bars are due to fabrication tolerances of the dielectric spacer as detailed in the text.

6.2.2 Local vs. nonlocal dispersion - comparison to experimental results

The initial purpose of the nano-cube setup was to demonstrate nonlocal effects for very small gap sizes. We have proposed a metamodel-based telemetry, helping to find a realistic set of geometric parameters for the cube model of Figure 6.21.

If we now decrease the gap size, the local simulation results should start to red-shift with respect to the measured data. This effect is supposed to increase with a decreasing gap size due to a stronger coupling of the gap plasmon to nonlocality. Following theoretical investigations in [106], nonlocality starts to be important for gap sizes $\delta_{\mathrm{Gap}} = \delta_{\mathrm{Shell}} + \delta_{\mathrm{Diel}} \leq 5$ nm. We will proceed in two steps:

- Run a 3D full wave simulation for $\delta_{\mathrm{Diel}} = \{2.46\ \mathrm{nm},\ 0.6\ \mathrm{nm}\}$ with a local dispersion model
- Repeat the same simulations with a nonlocal dispersion model.

Figure 6.25 depicts the resonance positions, resulting from both simulation series and the measured values.

Local vs. nonlocal simulations Figure 6.25 compares local and nonlocal DGTD simulations of the nano-cube system. From a purely theoretical or simulation point of view, nonlocality is almost negligible for $\delta_{\mathrm{Gap}} \geq 12.5$ nm. At $\delta_{\mathrm{Gap}} = 16.5$ nm, both models lead to the same result. Decreasing the dielectric height slowly introduces a blue-shift of the resonance position due to nonlocality. While it remains fairly low for $\delta_{\mathrm{Gap}} = 8.5$ nm, the blue-shift starts to be observable at $\delta_{\mathrm{Gap}} = 4.96$ nm and is clearly distinguishable for $\delta_{\mathrm{Gap}} = 3.1$ nm.

Figure 6.26 compares a simulated local and nonlocal spectrum for $\delta_{\mathrm{Gap}} = 3.1$ nm. While the first resonance, which can be identified as the surface plasmon, does only shift about ≈ 3 nm, the second resonance shifts by ≈ 31 nm. As nonlocality is significantly stronger for gap modes, we can identify the second resonance with the gap plasmon that is the one we are interested in.

Simulation vs. experiment Figure 6.25 also compares the experimental data with simulations based on local and nonlocal dispersion models. A good agreement of the three largest gaps is not surprising, since we have based the calibration of our geometric model on those measured resonances. However, for

$\delta_{\mathrm{Gap}} = 5.96\ \mathrm{nm}$, the model still seems to work very well. Further decreasing the gap size now leads to a red-shifted simulation result with respect to the measured data, if local dispersion is employed. Adding nonlocality accounts for the necessary blue-shift and leads to a very good agreement of the simulation result with the measured data. Also, the uncertainty of the dielectric height δ_{Diel} decreases for a decreasing spacer thickness, leading to a very small uncertainty interval at $\delta_{\mathrm{Diel}} = 0.6\ \mathrm{nm}$.

Fabrication error and geometry precision The measured gap resonances in Figure 6.25 depend on the dielectric spacer δ_{Diel}. As a matter of fact, the fabrication of the dielectric space is done by a many layer process. Each deposited layer is supposed to be $0.045\ \mathrm{nm}$ thick and suffers from an absolute thickness error of $0.005\ \mathrm{nm}$. Since each layer is completely independent of the previous one, we can estimate a worst case fabrication uncertainty of

$$\Delta_{\mathrm{fabrication,max}} = \frac{0.005}{0.045}\delta_{\mathrm{Diel}}, \tag{6.2.8}$$

which corresponds to the error bars in Figure 6.25. This explains why the measured resonances in do not perfectly fit with our model. Every parameter set that better fits the resonance of the thickest height $\delta_{\mathrm{Diel}} = 14.0\ \mathrm{nm}$ systematically leads to a higher error for $\delta_{\mathrm{Diel}} = \{6.0, 10.0\}\ \mathrm{nm}$. Furthermore, the resonance at $\delta_{\mathrm{Diel}} = 2.46\ \mathrm{nm}$ will be completely off. We interpret it like this:

(i) The shape of $\lambda_{\mathrm{res}}(\delta_{\mathrm{Diel}})$ is dominated by r_{Ag}, δ_{Shell} and l_{Cube};

(ii) The larger error of the resonance position for $\delta_{\mathrm{Diel}} = 14.0\ \mathrm{nm}$ might be due to the fabrication error. This means, the actual dielectric height is probably not exactly $14.0\ \mathrm{nm}$. Since this error decreases for smaller spacers and the cube size does not change for different spacer heights, we trust in the found cube geometry.

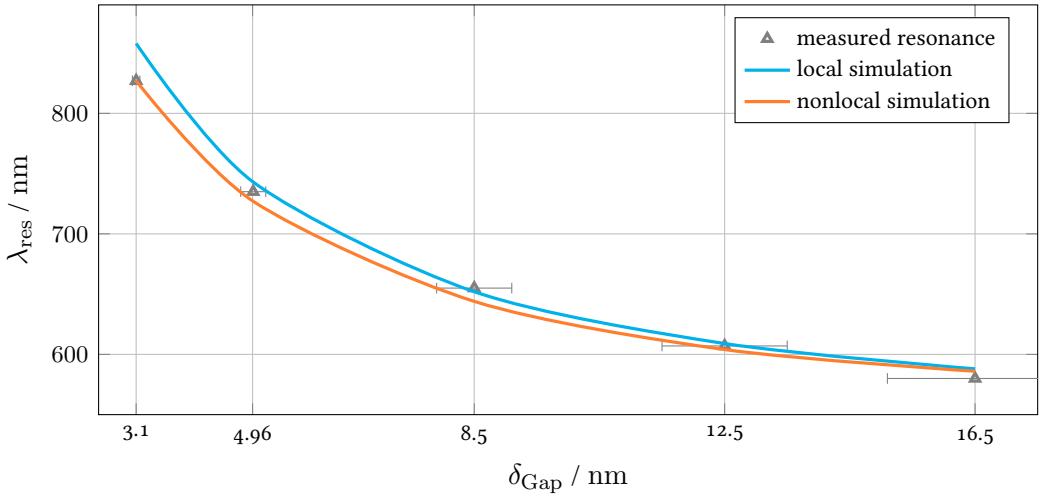

Figure 6.25 | Gap plasmon resonance for different cube lengths. Gray: Measured resonance position. The error bars show the a priori fabrication tolerance of the dielectric spacer δ_{Diel}. Blue: Result of a local full wave 3D DGTD simulation. Orange: Result of a nonlocal full wave 3D DGTD simulation with $\beta = 1.35\mathrm{e}6\ \mathrm{m/s}$. The error bars are due to fabrication tolerances of the dielectric spacer as detailed in the text.

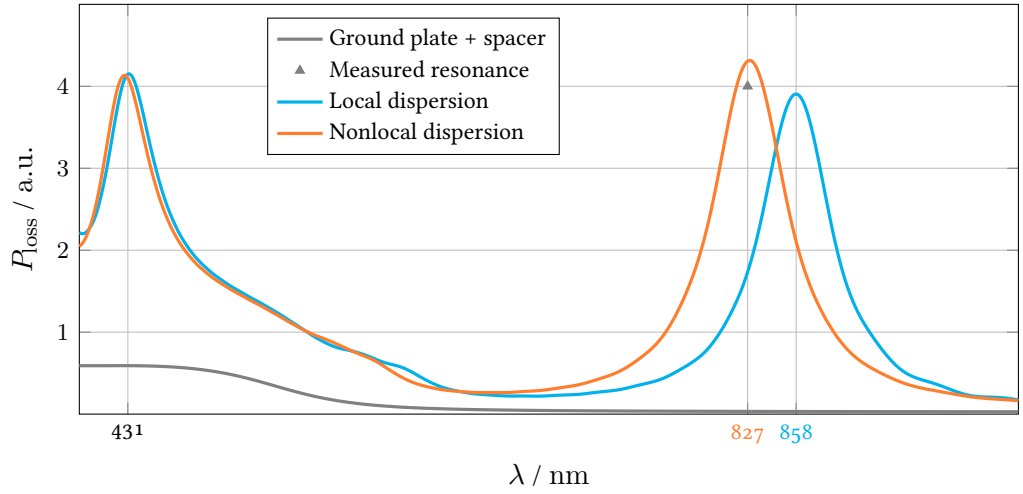

Figure 6.26 | Local vs. nonlocal nano cube absorption. Cube size: $r_{\text{Ag}} = 7.0$ nm, $\delta_{\text{Shell}} = 2.5$ nm, $l_{\text{Cube}} = 65.0$ nm and $\delta_{\text{Diel}} = 0.6$ nm. Nonlocality causes a blue shift of ≈ 31 nm for the gap resonance. The overall dielectric gap between the metals is $\delta_{\text{Diel}} + \delta_{\text{Shell}} = 3.1$ nm wide. As a reference, the gray line shows the absorption of the same setup if the cube and the dielectric shell are considered as vacuum, leading to a one dimensional multilayer refraction problem.

6.2.3 Appropriate domain truncation - the influence of a finite dielectric slab

Modeling a nano-cube in a numerical simulation comes with several difficulties. In the following, we want to highlight more technical aspects of our 3D DGTD simulations, especially concerning the domain truncation.

Periodic unit cell Our first attempts were based on periodic boundary conditions, i.e. a nano-cube in a periodic unit cell. However, imposing periodic boundaries in x and y direction leads to an infinite grating of equivalent nano-cubes. Grating modes can hence arise and couple to the gap plasmon. Mode overlaps and mode repulsion due to the periodic modeling error might be significant. On the other hand, decreasing the periodicity length will forbid grating modes but increases the direct mutual coupling of the cubes, in the fashion of cube dimers [79]. Figure 6.27 and Figure 6.28 outline the absorption spectra for different dielectric heights δ_{Diel} of a cube in a periodic unit cell.

Obviously, the spectra in the Figures 6.27 and 6.28 show the surface plasmon resonance at about 450 nm similar as for the single nano-cube in Figure 6.26. Screening the spectra to longer wavelengths surprisingly now shows two resonances. We identify the first peak (i) at ≈ 530 nm as the grating mode and the second peak (ii) as the gap resonance. This is justified by

(i.a) A unit cell size of 500 nm in x and y direction;

(i.b) A very low gap size dependency of the first resonance;

(ii.a) A very strong dependency on the gap size δ_{Diel}.

A closer look at Figure 6.28 reveals an interesting fact for increasing gap sizes. Once the gap resonance approaches ≈ 570 nm, it seems to experience an insuperable barrier. Even further, the gap resonance pushes the grating mode to higher frequencies, what we define as resonance repulsion.

This reasoning completes our arguments: we cannot use a periodic unit cell approach for our study.

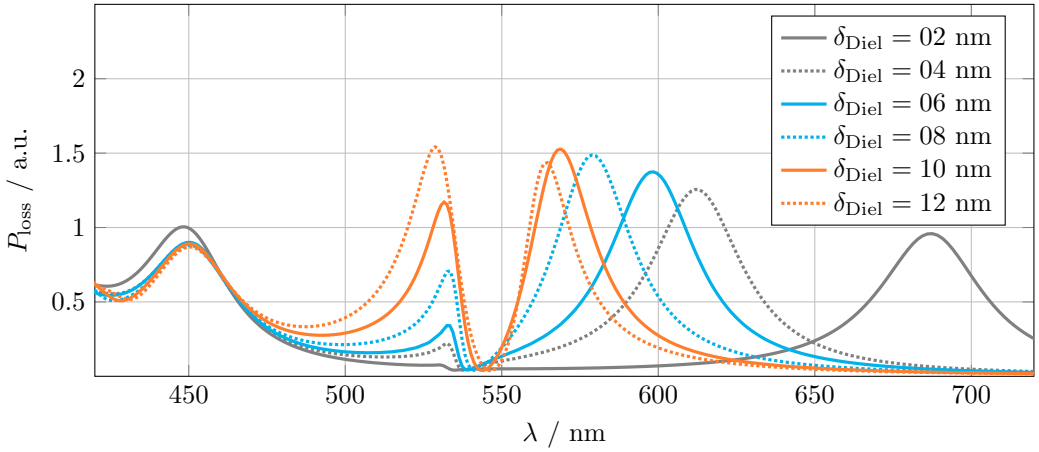

Figure 6.27 | Volumic absorption of the periodic cube. Part one. Cube size: $r_{\text{Ag}} = 3.0$ nm, $\delta_{\text{Shell}} = 3.0$ nm, $l_{\text{Cube}} = 50.0$ nm $l_{\text{Periodic}} = 500.0$ nm , and varying dielectric height δ_{Diel}.

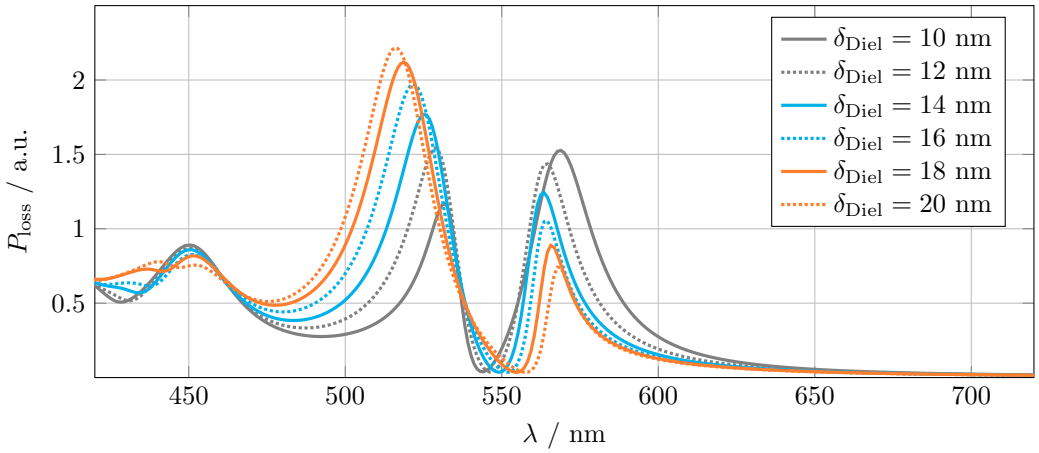

Figure 6.28 | Volumic absorption of the periodic cube. Part two. Cube size: $r_{\text{Ag}} = 3.0$ nm, $\delta_{\text{Shell}} = 3.0$ nm, $l_{\text{Cube}} = 50.0$ nm $l_{\text{Periodic}} = 500.0$ nm , and varying dielectric height δ_{Diel}.

Infinite substrate and single cube Aiming to overcome the limitations we have discussed previously, we want to propose a proper single nano-cube simulation setup. This requires two key ingredients:

(i) CFS-PMLs, easily accepting arbitrary materials;

(ii) TF/SF surfaces inside the PML zone, allowing a true incident plane wave.

Figure 6.30 (a) shows an example mesh including the PML domain and the TF/SF interface. As a matter of fact, if the TF/SF is not continued in the PML region, the incident field is wrong. This is due to a missing field on the PML side of the interface between PMLs and the inner domain. In other words, imposing the field only in the inner domain, causes spurious diffraction at the domain-PML interface.

We want to conclude this discussion with a third aspect. Decreasing the dielectric height δ_{Diel} leads to a very flat sheet. As can be seen in Figure 6.30 (a), the aspect ratio of the tetrahedra in the dielectric PML zone becomes extreme. One possibility is a local refinement, which dramatically increases the number of elements. Alternatively, the dielectric slab can be considered to be finite around the cube, as depicted in Figure 6.30 (b). This obviously changes the physical setup. However, a numerical experiment shows

a fairly small impact for $\delta_{\text{Diel}} \leq 2.5$ nm, see Figure 6.29. Larger dielectric sizes show an increasing discrepancy. Since the dielectric is finite, the surface plasmon experiences a cavity in propagation direction, which impacts the system response. In conclusion, the dielectric spacer can be modeled as a finite layer, if the δ_{Diel} is sufficiently small.

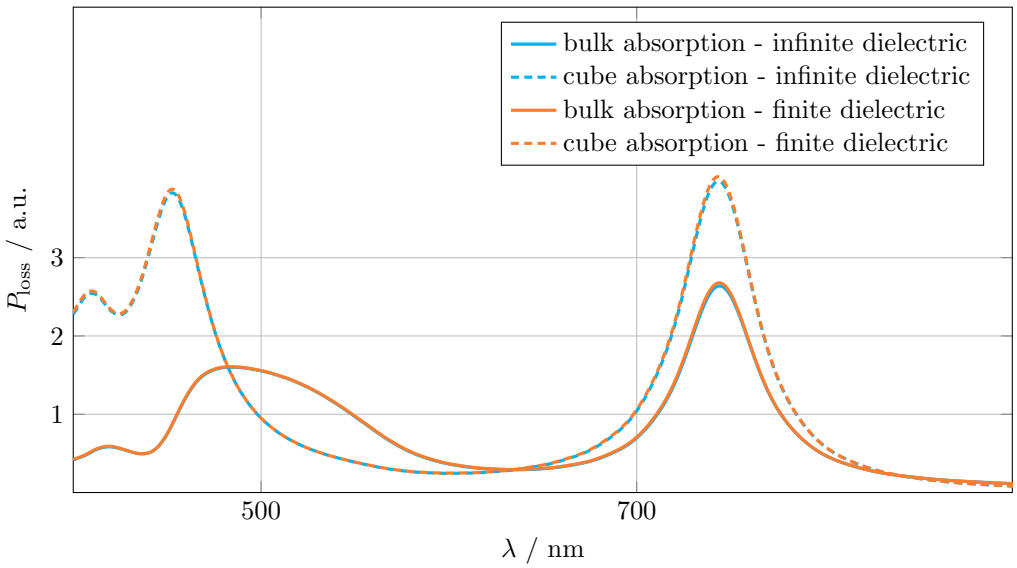

Figure 6.29 | Infinite vs. finite dielectric. Cube length $r_{\text{Ag}} = 7.0$ nm, $\delta_{\text{Shell}} = 2.5$ nm, $l_{\text{Cube}} = 65.0$ nm and $\delta_{\text{Diel}} = 2.5$ nm and local dispersion. Comparison of the absorption in different zones for a finite and infinite dielectric spacer.

6.2.4 Optical near field of the gap plasmon - local vs. nonlocal dispersion

Figure 6.32 illustrates 3D solutions of the Fourier-transformed electric and magnetic field at the gap resonance. We observe a significantly higher penetration of the magnetic field **H** into the metallic part of the shell-cube as well as the metal substrate when nonlocality is activated. Also, the mode is less confined in the center of the gap compared to the locally dispersive solution. This result is in line with our findings in Chapter 5.3.

The **E** field in contrast, gets screened from the bulk and yields an extreme field enhancement at the metallo-dielectric interface. Additionally, the highest fields concentrate in the outer half of the gap. Thin penetration layers due to nonlocality have theoretically been predicted [119] and also appear for metallo-dielectric gratings (see Figures 6.17 and 6.18 in Chapter 6.1).

Time-domain videos of the magnetic and electric field (see link) show a 'rotating' behaviour. Turning here means that the plasmon runs in anti-clockwise circles seen from above. This can be interpreted as a wave which gets reflected at the cube walls in x- and y-direction. We identify this wave with the localized gap plasmon.

6.2.5 Concluding remarks

This chapter has proposed a surrogate model-based telemetry strategy based in order to obtain the fabricated cube dimension (inverse problem). Based on this geometric characterization, we have decreased the gap size between the gold substrate and the silver cube and have compared numerical simulations which either employ local or nonlocal dispersion models. As a theoretical result, the influence of nonlocality exceeds the experimental error bars for gap sizes below 3.1 nm. Additionally, our *nonlocal* simulations

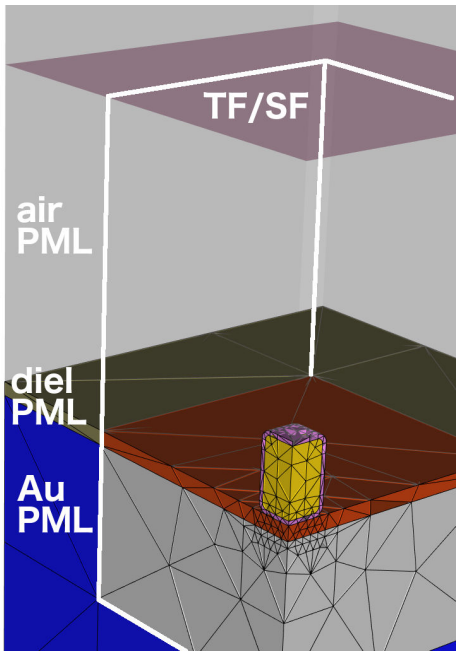

(a) Computational mesh with infinite dielectric, including PMLs and TF/SF surface. The TF/SF surface continues in the PML region.

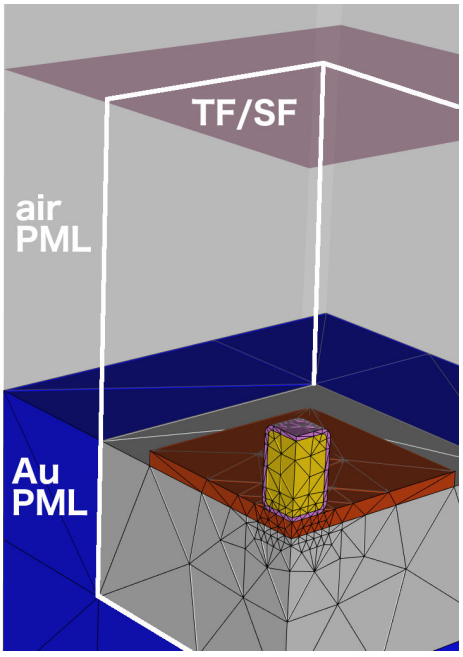

(b) Computational mesh with finite dielectric. Here, the dielectric does not continue inside the PML region.

Figure 6.30 | Finite vs. infinite dielectric mesh.

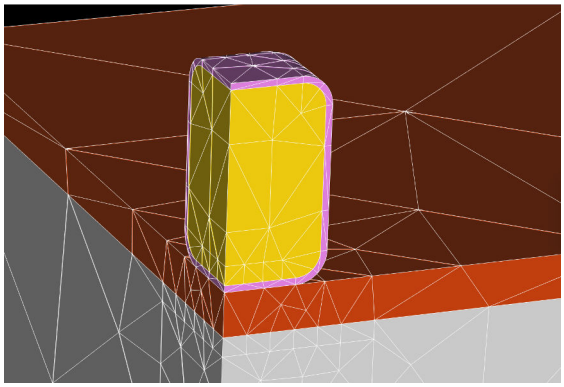

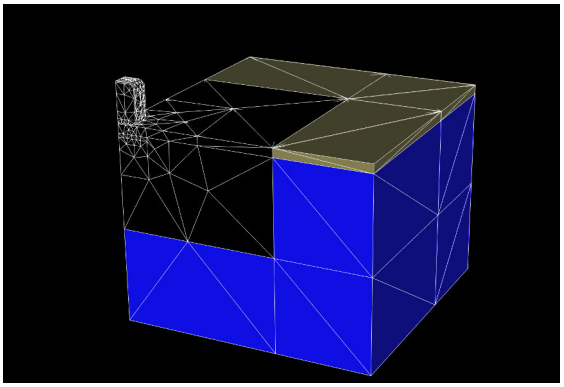

Figure 6.31 | Triangulation of nano-cube. Curvilinear mesh of the single nano-cube setup. The cube length is $l_{\mathrm{Cube}} = 65\,\mathrm{nm}$, the radius of the metallic domain is $r_{\mathrm{Ag}} = 7\,\mathrm{nm}$, the thickness of the dielectric shell is $\delta_{\mathrm{Shell}} = 2.5\,\mathrm{nm}$ and the thickness of the dielectric slab is $\delta_{\mathrm{Diel}} = 14\,\mathrm{nm}$. Left: the nano-cube with its different materials, right: the PML domain truncation.

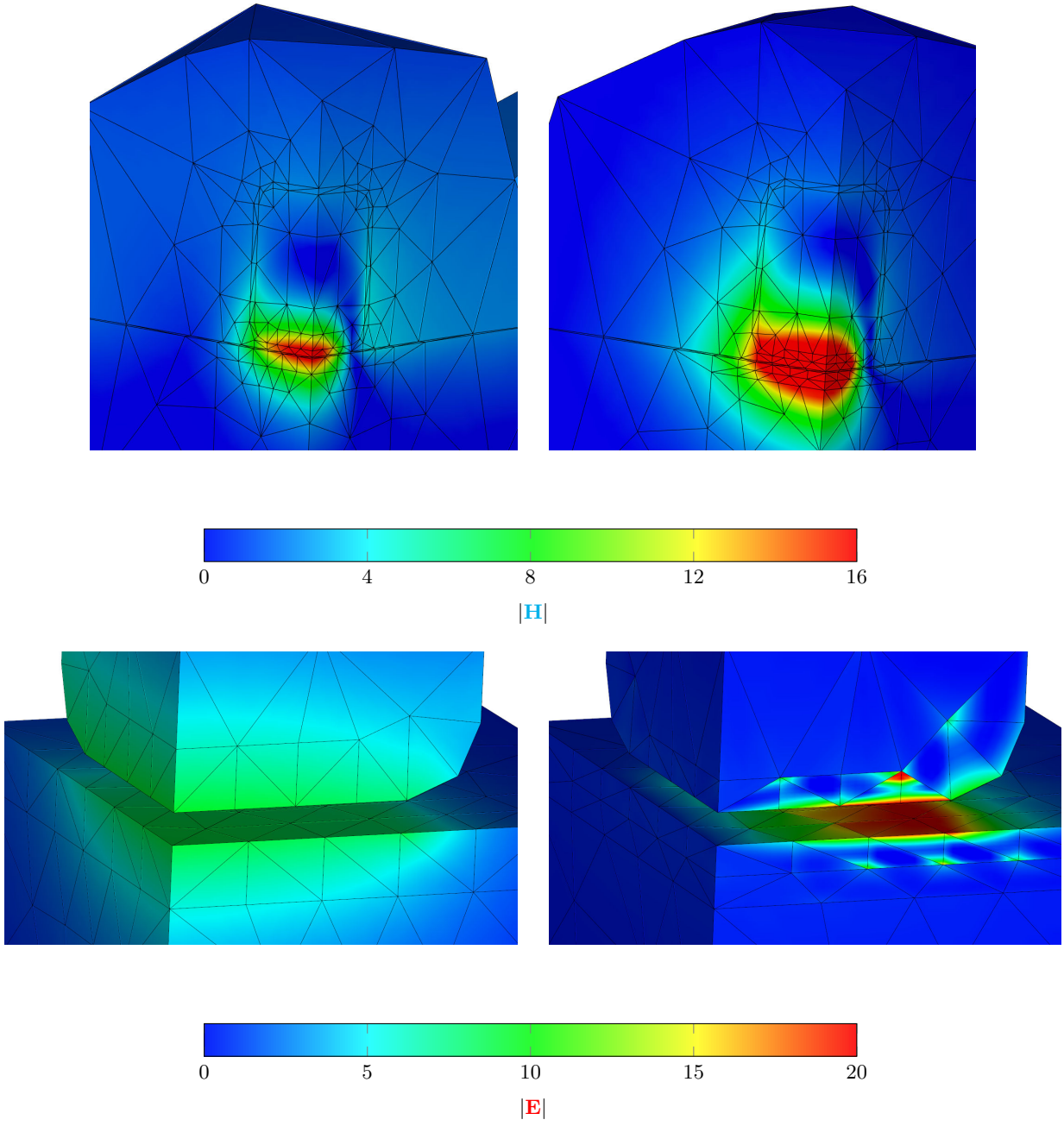

Figure 6.32 | Field solution at cube gap resonance. Cube with gap size $\delta_{\mathrm{Diel}} = 0.6\ \mathrm{nm}$ comparison of the local (left) and the nonlocal (right) dispersion model. Nonlocality allows the **H** field to be significantly spread into the metallic zone of the cube and the substrate. The **E** field penetrates less into the bulk but builds up an intense field region at the metal-dielectric interfaces of the cube and the bulk. The gap mode is more confined in the 'outer' half of the gap. (These results have used DGTD $-\ \mathcal{P}_4$ on curvilinear elements. The visualization employs affine tetrahedra.)

are able to explain the discrepancy between the experiment and *local* simulations [105] for very small gap sizes.

7 Conclusions and outlook

Today's high-tech fabrication processes have opened the field to plasmonic structures where local dispersion laws are not sufficient anymore and nonlocal dispersion models are required. This thesis has proposed and analyzed simulation strategies for these models. Furthermore, we have assessed the developed tools with respect to real world examples.

Theoretical considerations First, it was necessary to develop a material model for metals in nanophotonics, which would be able to include the nonlocal response of the free electrons as well as the bound electron contribution.

In order to do so, we started from continuous Maxwell's equations in non-vacuum domains. The material descriptions were first kept arbitrary and their response was cast into the polarization and magnetization. We have recalled several classical electrodynamic results, which have served as a toolbox throughout the course of this thesis.

Subsequently, we have considered unmagnetized materials and have focused our work on modeling the materials' polarization. A clear priority has been put on the modeling of metals in a sub-wavelength nanophotonic setup where the skin-depth is usually comparable to or larger than the device's geometry. Within this modeling step, two different origins of polarization have been identified: the contribution of the bound electrons and the response of the quasi-free valence electrons. While the bound electrons can accurately be modeled with a temporal dispersion relation (local dispersion), the free electrons require a more complicated model if certain conditions appear. Such a condition is attained if the plasmonic wave vector's magnitude becomes very high and its effective wavelength approaches the mean free path length of the free electrons. In this case, a mutual coupling of the electrons gains importance and the system response becomes nonlocal (temporal and spatial dispersion). The overall model hence consists of Maxwell's equations, which are strongly coupled to a system of ODEs for the local contribution and a system of PDEs for the nonlocal part.

In order to gain a deeper understanding of the underlying model, we have reviewed the well posedness of the system and studied its hyperbolicity. We found that the new system is still hyperbolic, that it

benefits from an energy principle and that it well describes physical phenomena such as electron density waves, often referred to as bulk plasmons. It is clear that Maxwell's equations alone do not admit such solutions.

Realistic nanophotonic devices are beyond the capabilities of analytical solutions. For this reason, it was necessary to develop an accurate numerical algorithm for the solution of the underlying model equations on arbitrary geometries.

Aiming for a numerical algorithm that is able to solve our model on complex geometries with high accuracy and efficiency, we have decided to discretize our model with a DGTD method. The definition of a numerical flux is necessary in order to account for the arising discontinuities at the mesh cell interfaces due to the local finite element approximation space. We defined this flux as the solution of a local Riemann problem. This provided the building blocks for the definition of a global weak form. We then continued with proofing stability and convergence properties of the semi-discrete scheme before choosing an appropriate time discretization.

The accurate modelling of the material interfaces is crucial and must be considered in the design of the numerical method in order to render it efficient. We thus provided a short intermezzo discussing mappings between a reference element and affine and curvilinear elements. Curvilinear meshes have turned out to be a key ingredient for efficient nanophotonics simulations and especially for nonlocal dispersion models. Performance studies were tackled in the simulations chapter. At this stage, we have outlined the increased implementation complexity of curvilinear elements in a DGTD framework compared to affine meshes.

Beyond the spatial discretization of the PDE system, an appropriate time integration scheme is required for the time discretization. The resulting fully-discrete scheme obviously has to be investigated in terms of numerical stability and convergence. Here, we have proposed three different time discretization schemes for the semi-discrete weak form. Our analysis started with a second order LF time integration scheme due to its simplicity. A fully-discrete stability result of this scheme has been provided, yielding a CFL type stability criterion. In order to exploit the high-order nature of DGTD we have extended the time discretization to fourth-order RK methods. Here, we have used used a classic RK_4 scheme for the stability and convergence analysis. For our implementation, we chose an optimized fourth-order RK variant with lower storage requirements than the original ($LSRK_4$).

Practical considerations Simulations of complex realistic nanophotonic devices require more than a basic numerical scheme in order to solve the underlying PDE. Such additional components are for example sophisticated source formulations, domain truncation techniques, and observables. Furthermore, modern algorithms for optimization and UQ round off the ensemble of useful add-ons.

We have recalled the TF/SF and SF source formulation techniques, which are particularly useful for scattering problems in combination with PMLs. In this thesis, we have focused on CFS-PMLs. These are highly flexible if materials are present inside the PML region, at the price of implementing a more complicated split flux formulation.

In order to treat EELS simulations within this DGTD framework, we had to employ a special field source, namely the SF formulation. This SF source formulation in combination with CFS-PMLs has turned out to be inappropriate in the time-domain. We have rigorously explained where an intuitive use leads to an incorrect formulation and provided the correct formulation as a result. However, this approach still remains impractical in the time-domain. Tackling this challenge, we have developed an alternative to SF-CFS-PMLs, which consists of a TF/SF formulation in combination with CFS-PMLs. This approach has proven to work very well for certain classes of problems and has been extensively used in the chapters concerned with numerical results.

The physical interpretation and technical exploitation of our simulations did require observables that are derived in a post-treatment from the actual field solution. We defined various observables, which complete the considered practical aspects of a simulation tool. Additionally, we have briefly outlined the techniques and algorithms we have used for optimizations, the solution of inverse problems and UQ.

Implementation, validation and benchmarks In order to study nonlocal effects in complex real world applications, we wanted to provide a user friendly and robust software.

All the models, formulations and observables have been implemented in the parallel 3D software suite DIOGENeS and are now available for further usage. First tests on the nonlocal dispersion model have also been implemented in a 2D code featuring local time stepping, which is not described in this manuscript.

Thorough validations and benchmarks have been presented. In particular, the performance gain due to curvilinear elements is of significant importance. Mie scattering has been used as an ultimate validation and performance test, as this allows to test multiple solver components against analytical solutions. Our numerical results concluded with the simulation of a spherical dimer system. This study has been conducted in collaboration with Matthias Moeferdt and Kurt Busch [136]. The dimer simulations have confirmed the need for curvilinear elements, coherent with the benchmarks for individual spheres. Furthermore, they revealed physical insights regarding the impact of nonlocal dispersion models on the spectra of the dimer system.

Physical considerations After successfully developing our simulation tool, we wanted to exploit its access to nonlocal dispersion models. Fortunately, we had the opportunity to collaborate with leading specialists in the field. These collaborations have lead to new insights into the nature of nonlocal dispersion.

Our first study proposes a calibration technique of the nonlocal material parameter β. This work has been conducted in collaboration with Armel Pitelet, Antoine Moreau, Dimitrios Loukrezis, and Herbert DeGersem [120]. We have shown that surface plasmons are sensitive to spatial dispersion, which previously has not been commonly known in the literature. This is only the case if an interface between a metal and a high permittivity dielectric is considered. As a first result, we have discovered that the optical response of metallic structures surrounded by a high refractive index medium will only be accurately described if spatial dispersion is taken into account. We have relied on grating couplers where an observation of spatial dispersion via its optical response, i.e. a resonance blueshift of up to 7 nm (around 1% of the wavelength), is now theoretically predicted. Finally, in order to ensure the usefulness of such an experiment, we have proposed a full procedure to carefully characterize the geometrical parameters of the structure after fabrication. This has been achieved by a concatenation of inverse problems. Furthermore, we have solved an inverse problem in order to estimate the hydrodynamic weighting parameter β. Our main result here is that effects due to spatial dispersion can in no way be confused with effects due to variations in the geometrical parameters of the grating. The signature of nonlocality is thus unique.

Our second study has investigated nonlocal effects on the plasmonic gap resonance of nano-cubes. We have provided accurate geometric parameters of the actually fabricated nano-cubes through the solution of an inverse problem. Furthermore, we have compared our simulation results with experimental data, which are perfectly in line for gap sizes $> 5\,\mathrm{nm}$. For smaller gap sizes, however, our local simulations and previous simulations at Duke university are clearly redshifted with respect to the measurements. Considering a nonlocal dispersion model for the nano-cube has led to a very good agreement for all gap sizes, even the smallest ones. This agreement of experiment and theory has provided a second experimental setup beyond nano-spheres where nonlocality has been measured.

Achievements The main achievements and scientific contributions of this thesis are:

- A theoretical study of the continuous Maxwell-hydrodynamic system;
- The proposition of a DGTD formulation for this system and its numerical stability [134] and convergence analysis;
- The demonstration of significant performance improvements for curvilinear elements compared to linear meshes in the context of the linearized fluid model[1] [135];
- An investigation of SF-CFS-PMLs in the time-domain and a workaround with TF/SF-CFS-PMLs;
- The proposition of a post-fabrication telemetry for metallo-dielectric gratings and a theoretical prediction of the experimental observations. Special attention was given to geometric uncertainties and whether their influence exceeds the impact of nonlocality [120];
- The accurate 3D simulation of silver nano-cubes and the demonstration of experimental evidence by means of blueshifts on the gap-plasmon [133];
- The extension of the DIOGENeS software by the numerical treatment of the linearized hydrodynamic equations, isoparametric curvilinear elements and MPI parallelization [135].

Future research topics The work presented in this thesis could be extended in multiple directions. In terms of modeling, one may consider:

- The Generalized nonlocal optical response (GNOR) model [91], which is an extension of the linear hydrodynamic model. Section A.1 sketches the model and provides an energy result;
- Spill-out models [23]. Such models are already significantly more complicated since they numerically struggle when the background electron density tends to zero. Further, the initial electron density is not easy to compute for complex structures. Section A.2 outlines a weak formulation;
- A nonlinear hydrodynamic model [102] as a relatively easy extension towards nonlinear effects;
- Kerr-nonlinearities as a significantly more complicated setup [43].

In terms of numerics, several algorithmic extensions are promising candidates for further efficiency improvements:

- More advanced time stepping schemes like local time steps [118] or hybrid explicit/implicit schemes [32] in order to account for the very small mesh cells that are required for an appropriate solution of nonlocal effects;
- An extension to p-adaptivity [154] or hp-adaptivity [137];
- A hybrid mesh DGTD scheme [88], especially for the PMLs;
- Diffuse Interface Methods [145];
- The exciting field of Trefftz methods [38].

[1] Here, we fixed the error level and used different mesh refinements for the linear and curvilinear meshes.

A

Future directions

Here, we sketch two possible directions for more advanced material models in the context of linearized nonlocal dispersion models.

A.1 Generalized nonlocal optical response

Mortensen et al. [162] have proposed a refined version of the linearized fluid model. The so-called GNOR model extend our linearized hydrodynamic model by an additional diffusion term. While the proposed model is derived in frequency-domain, we want to study it in time-domain and investigate elementary properties like energy conservation. In order to prepare the formulation of a DGTD framework it is convenient to introduce the auxiliary variables Q and R avoiding the "violation of the variational crime" [138]. After simple re-arrangements the GNOR model reads

$$\begin{aligned} \partial_t \mathbf{J} &= D\nabla(R) + \tilde{\beta}^2 \nabla Q - \gamma \mathbf{J} + {\omega_\mathrm{P}}^2 \varepsilon_0 \mathbf{E}, \\ \partial_t Q &= \nabla \cdot \mathbf{J}, \\ R &= \nabla \cdot \mathbf{J}. \end{aligned} \tag{A.1.1}$$

Here, $\tilde{\beta}^2 = \beta^2 + \gamma D$ with the diffusion constant D. The weak form for sufficiently regular test functions $\boldsymbol{\phi}$ is straightforward and follows

$$\begin{aligned} < \partial_t \mathbf{J}, \boldsymbol{\phi} > &= D < \nabla(\nabla \cdot \mathbf{J}), \boldsymbol{\phi} > + \tilde{\beta}^2 < \nabla Q, \boldsymbol{\phi} > \\ &\quad -\gamma < \mathbf{J}, \boldsymbol{\phi} > + {\omega_\mathrm{P}}^2 \varepsilon_0 < \mathbf{E}, \boldsymbol{\phi} >, \\ \partial_t < Q, \boldsymbol{\phi} > &= < \nabla \cdot \mathbf{J}, \boldsymbol{\phi} > . \end{aligned} \tag{A.1.2}$$

Energy First, we investigate the energy evolution in time. Physically speaking, the overall energy must not increase in the absence of source terms. Similar steps for appropriate functions in order to evaluate $\partial_t \mathcal{E}$ apply and lead to

$$\begin{aligned} < \partial_t \mathbf{J}, \mathbf{J} > &= D < \nabla(\nabla \cdot \mathbf{J}), \mathbf{J} > + \tilde{\beta}^2 < \nabla Q, \mathbf{J} > \\ &\quad -\gamma < \mathbf{J}, \mathbf{J} > + {\omega_\mathrm{P}}^2 \varepsilon_0 < \mathbf{E}, \mathbf{J} > . \end{aligned} \tag{A.1.3}$$

All terms are analogous to the nonlocal Drude model except for $< \nabla(\nabla \cdot \mathbf{J}), \mathbf{J} >$. We thus have to show its negativity $< \nabla(\nabla \cdot \mathbf{J}), \mathbf{J} > \leq 0$. Integration by parts yields

$$\begin{aligned} \int_\Omega \nabla(\nabla \cdot \mathbf{J}) \cdot \mathbf{J} &= \int_\Omega \nabla \cdot ((\nabla \cdot \mathbf{J})\mathbf{J}) - (\nabla \cdot \mathbf{J})(\nabla \cdot \mathbf{J}), \\ &= \int_\Omega \nabla \cdot ((\nabla \cdot \mathbf{J})\mathbf{J}) - ||\nabla \cdot \mathbf{J}||^2_{\boldsymbol{\mathcal{L}}^2(\Omega)}, \end{aligned} \tag{A.1.4}$$

but

$$\begin{aligned} \int_\Omega \nabla \cdot ((\nabla \cdot \mathbf{J})\mathbf{J}) &= \int_{\partial\Omega} (\nabla \cdot \mathbf{J})\mathbf{J} \cdot \mathbf{n} \\ &= 0, \end{aligned} \tag{A.1.5}$$

due to the boundary condition (2.5.3).

Numerics GNOR has been successfully implemented in the Comsol Multiphysics FEM framework [109] and more recently in the context of Hybrid Discontinuous Galerkin (HDG) methods [91]. Since GNOR does not introduce additional differential operator nor complicates the linear hydrodynamic Drude model by more than an additional **grad div**-term, we do not expect significant difficulties for a numerical treatment with DGTD.

A.2 Electron spill-out model

Within the derivations in Chapter 2.4.3 and 2.4.4 we have assumed a constant background electron density which sharply drops to zero at the metal boundary. Extremely small and perfectly round particles may, however, be subject to spill-out effects and tunneling as has been shown recently. We refer to [23] for thorough derivations and physical interpretations. Varying background electron densities $n_0(\mathbf{r})$ lead to a more complicated pressure term in (2.4.6) since the gradient $\nabla n_0(\mathbf{r}) \neq 0$ does not vanish anymore. The linearized spill-out equation in time-domain reads

$$\nabla \left(\frac{\delta G_\eta[n]}{\delta n} \right)_1 \frac{q_{\text{elec}}}{m_{\text{elec}}} \underbrace{-(\partial_{tt} + \gamma\partial_t) n_0^{-1} \mathbf{P} + \varepsilon_0 {\omega_{\text{P}}}^2 n_0^{-1} \mathbf{E}}_{=:\mathbf{A}(t)} = 0, \tag{A.2.1}$$

with

$$G_\eta[n] = T^{\text{TF}} + T^{\text{W}} + E^{\text{LDA}}_{\text{XC}} \tag{A.2.2}$$

and

$$\begin{aligned} \left(\frac{\delta T^{\text{TF}}}{\delta n} \right)_1 &= (E_h a_0^2) \frac{10}{9} c_{\text{TF}} n_0^{-1/3} n_1, \\ \left(\frac{\delta T^{\text{W}}}{\delta n} \right)^{\text{W}}_1 &= (E_h a_0^2) \frac{1}{4} \left(\frac{\nabla n_0 \cdot \nabla n_1}{n_0^2} + \frac{\nabla^2 n_0}{n_0^2} n_1 - \frac{|\nabla n_0|^2}{n_0^3} n_1 - \frac{\nabla^2 n_1}{n_0} \right), \\ \left(\frac{\delta E^{\text{LDA}}_{XC}}{\delta n} \right)^{\text{XC}}_1 &= (E_h) \left(-a_0 \frac{4}{9} c_{\text{x}} n_0^{-2/3} n_1 + a_0^3 \mu_c'[n_0] n_1 \right). \end{aligned} \tag{A.2.3}$$

Vectorial and scalar test functions respectively from the spaces $\boldsymbol{\phi} \in (\boldsymbol{\mathcal{L}}^2(\Omega))^3$ and $\varphi \in \boldsymbol{\mathcal{L}}^2(\Omega)$ yield the weak gradient of density functional

$$\left\langle \nabla \left(\frac{\delta G_\eta[n]}{\delta n} \right)_1, \boldsymbol{\phi} \right\rangle_\Omega = \left\langle \left(\frac{\delta G_\eta[n]}{\delta n} \right)_1 \boldsymbol{\phi}, \mathbf{n} \right\rangle_{\partial\Omega} - \left\langle \left(\frac{\delta G_\eta[n]}{\delta n} \right)_1, \nabla\boldsymbol{\phi} \right\rangle_\Omega, \tag{A.2.4}$$

Now, the weak terms of the individual contributions

$$\left\langle \nabla \left(\frac{\delta T^{\mathrm{TF}}}{\delta n} \right)_1, \boldsymbol{\phi} \right\rangle_\Omega = (E_h a_0^2) \frac{10}{9} c_{\mathrm{TF}} \left(\left\langle n_0^{-1/3} n_1 \boldsymbol{\phi}, \mathbf{n} \right\rangle_{\partial\Omega} - \left\langle n_0^{-1/3} n_1, \nabla\boldsymbol{\phi} \right\rangle_\Omega \right), \tag{A.2.5}$$

$$\begin{aligned} \left\langle \nabla \left(\frac{\delta T^{\mathrm{W}}}{\delta n} \right)_1, \boldsymbol{\phi} \right\rangle_\Omega = (E_h a_0^2) \frac{1}{4} \quad & \left(\left\langle \frac{\nabla n_0 \cdot \nabla n_1}{n_0^2} \boldsymbol{\phi}, \mathbf{n} \right\rangle_{\partial\Omega} - \left\langle \frac{\nabla n_0 \cdot \nabla n_1}{n_0^2}, \nabla\boldsymbol{\phi} \right\rangle_\Omega \right. \\ & + \left\langle \frac{\nabla^2 n_0}{n_0^2} n_1 \boldsymbol{\phi}, \mathbf{n} \right\rangle_{\partial\Omega} - \left\langle \frac{\nabla^2 n_0}{n_0^2} n_1, \nabla\boldsymbol{\phi} \right\rangle_\Omega \\ & - \left\langle \frac{|\nabla n_0|^2}{n_0^3} n_1 \boldsymbol{\phi}, \mathbf{n} \right\rangle_{\partial\Omega} + \left\langle \frac{|\nabla n_0|^2}{n_0^3} n_1, \nabla\boldsymbol{\phi} \right\rangle_\Omega \\ & \left. - \left\langle \frac{\nabla^2 n_1}{n_0} \boldsymbol{\phi}, \mathbf{n} \right\rangle_{\partial\Omega} + \left\langle \frac{\nabla^2 n_1}{n_0}, \nabla\boldsymbol{\phi} \right\rangle_\Omega \right), \end{aligned} \tag{A.2.6}$$

$$\begin{aligned} \left\langle \left(\frac{\delta E_{XC}^{\mathrm{LDA}}}{\delta n} \right)_1^{\mathrm{XC}}, \boldsymbol{\phi} \right\rangle_\Omega = (E_h) \quad & \left(-a_0 \frac{4}{9} c_{\mathrm{x}} \left(\left\langle n_0^{-2/3} n_1 \boldsymbol{\phi}, \mathbf{n} \right\rangle_{\partial\Omega} - \left\langle n_0^{-2/3} n_1, \nabla\boldsymbol{\phi} \right\rangle_\Omega \right) \right. \\ & \left. + a_0^3 \left(\langle \mu_c'[n_0] n_1 \boldsymbol{\phi}, \mathbf{n} \rangle_{\partial\Omega} - \langle \mu_c'[n_0] n_1, \nabla\boldsymbol{\phi} \rangle_\Omega \right) \right). \end{aligned} \tag{A.2.7}$$

The total system hence reads

$$\begin{aligned} (E_h a_0^2) \frac{10}{9} c_{\mathrm{TF}} \quad & \left(\left\langle n_0^{-1/3} \frac{1}{q_{\mathrm{elec}}} Q \boldsymbol{\phi}, \mathbf{n} \right\rangle_{\partial\Omega} - \left\langle n_0^{-1/3} \frac{1}{q_{\mathrm{elec}}} Q, \nabla\boldsymbol{\phi} \right\rangle_\Omega \right) \\ + (E_h a_0^2) \frac{1}{4} \quad & \left(\left\langle \frac{\nabla n_0}{n_0^2} \cdot \boldsymbol{\xi} \boldsymbol{\phi}, \mathbf{n} \right\rangle_{\partial\Omega} - \left\langle \frac{\nabla n_0}{n_0^2} \cdot \boldsymbol{\xi}, \nabla\boldsymbol{\phi} \right\rangle_\Omega \right. \\ & + \left\langle \frac{\nabla^2 n_0}{n_0^2 q_{\mathrm{elec}}} Q \boldsymbol{\phi}, \mathbf{n} \right\rangle_{\partial\Omega} - \left\langle \frac{\nabla^2 n_0}{n_0^2 q_{\mathrm{elec}}} Q, \nabla\boldsymbol{\phi} \right\rangle_\Omega \\ & - \left\langle \frac{|\nabla n_0|^2}{n_0^3 q_{\mathrm{elec}}} Q \boldsymbol{\phi}, \mathbf{n} \right\rangle_{\partial\Omega} + \left\langle \frac{|\nabla n_0|^2}{n_0^3 q_{\mathrm{elec}}} Q, \nabla\boldsymbol{\phi} \right\rangle_\Omega \\ & \left. - \left\langle \frac{1}{n_0} \nu \boldsymbol{\phi}, \mathbf{n} \right\rangle_{\partial\Omega} + \left\langle \frac{1}{n_0} \nu, \nabla\boldsymbol{\phi} \right\rangle_\Omega \right) \\ + (E_h) \quad & \left(-a_0 \frac{4}{9} c_{\mathrm{x}} \left[\left\langle n_0^{-2/3} \frac{1}{q_{\mathrm{elec}}} Q \boldsymbol{\phi}, \mathbf{n} \right\rangle_{\partial\Omega} - \left\langle n_0^{-2/3} \frac{1}{q_{\mathrm{elec}}} Q, \nabla\boldsymbol{\phi} \right\rangle_\Omega \right] \right. \\ & \left. + a_0^3 \left[\left\langle \mu_c'[n_0] \frac{1}{q_{\mathrm{elec}}} Q \boldsymbol{\phi}, \mathbf{n} \right\rangle_{\partial\Omega} - \left\langle \mu_c'[n_0] \frac{1}{q_{\mathrm{elec}}} Q, \nabla\boldsymbol{\phi} \right\rangle_\Omega \right] \right) \\ & + \frac{m_{\mathrm{elec}}}{q_{\mathrm{elec}}} \langle \mathbf{A}, \boldsymbol{\phi} \rangle_\Omega = 0. \end{aligned} \tag{A.2.8}$$

with

$$\begin{aligned}
\partial_t \langle Q, \varphi \rangle_\Omega &= \langle \mathbf{J}\varphi, \mathbf{n} \rangle_{\partial\Omega} - \langle \mathbf{J}, \nabla\varphi \rangle_\Omega, \\
\langle \boldsymbol{\xi}, \boldsymbol{\phi} \rangle_\Omega &= \frac{1}{q_{\text{elec}}} \langle Q\boldsymbol{\phi}, \mathbf{n} \rangle_{\partial\Omega} - \langle Q, \nabla\boldsymbol{\phi} \rangle_\Omega, \\
\langle \nu, \varphi \rangle_\Omega &= \langle \boldsymbol{\xi}\varphi, \mathbf{n} \rangle_{\partial\Omega} - \langle \boldsymbol{\xi}, \nabla\varphi \rangle_\Omega, \\
\langle \mathbf{A}, \boldsymbol{\phi} \rangle_\Omega &= -\partial_t \langle n_0^{-1}\mathbf{J}, \boldsymbol{\phi} \rangle_\Omega - \gamma \langle n_0^{-1}\mathbf{J}, \boldsymbol{\phi} \rangle_\Omega + \varepsilon_0 {\omega_\text{P}}^2 \langle n_0^{-1}\mathbf{E}, \boldsymbol{\phi} \rangle_\Omega,
\end{aligned} \tag{A.2.9}$$

where we have used

$$\begin{aligned}
\partial_t Q &= \nabla \cdot \mathbf{J}, \\
\boldsymbol{\xi} &= \frac{1}{q_{\text{elec}}} \nabla Q, \\
\nu &= \nabla \cdot \boldsymbol{\xi}.
\end{aligned} \tag{A.2.10}$$

Finally, the boundary conditions

$$\begin{aligned}
\mathbf{n} \cdot \mathbf{J}|_{\partial\Omega} &= 0, \\
\partial_\mathbf{n} Q|_{\partial\Omega} &= 0, \\
\mathbf{n} \cdot \boldsymbol{\xi}|_{\partial\Omega} &= 0, \\
\partial_\mathbf{n} \nu|_{\partial\Omega} &= 0,
\end{aligned} \tag{A.2.11}$$

conclude the weak form of the spill-out model. Equivalent to the derivations in Chapter 3, an appropriate trace definition is required. This will be subject of a future work. Allowing a variation of $n_0(\mathbf{r})$ leads to numerical difficulties. Imagining the situation where $n_0 \to 0$ and equation (A.2.3) and its weak counterpart face a division by zero. Ciraci et al. [23] have introduced a cut-off criterion which detects a threshold value of n_0 and switches the material model if n_0 undergoes a defined value.

Remark A.2.1. *The application of spill-out models comes with a second challenge. A central argument of the model is the varying background electron density $n_0(\mathbf{r})$ which has consequently to be known. This is not trivial for arbitrary geometries. The authors and given references in [23] discuss several possibilities the accompanying approximations for fairly easy geometries like spheres and dimers. Aiming for more complex 3D structures will at least require a solution of a nonlinear Laplace-problem.*

B

Conventions

B.1 Coordinate system

We have used the polar coordinate system according to Figure B.1.

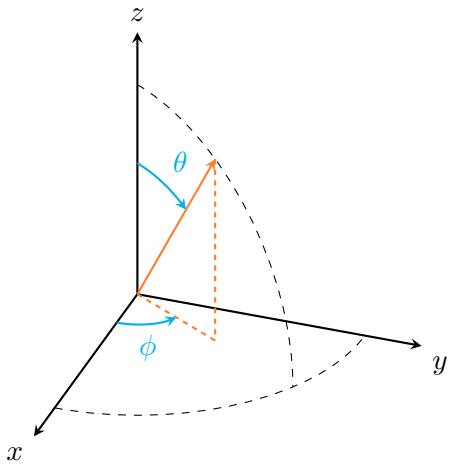

Figure B.1 | Spherical coordinates system. With kind permission from [153].

C Materials

C.1 Gold

Figure C.1 and Table C.1 specify the Au material fit of the Brendel-Bormann (BB)-model.

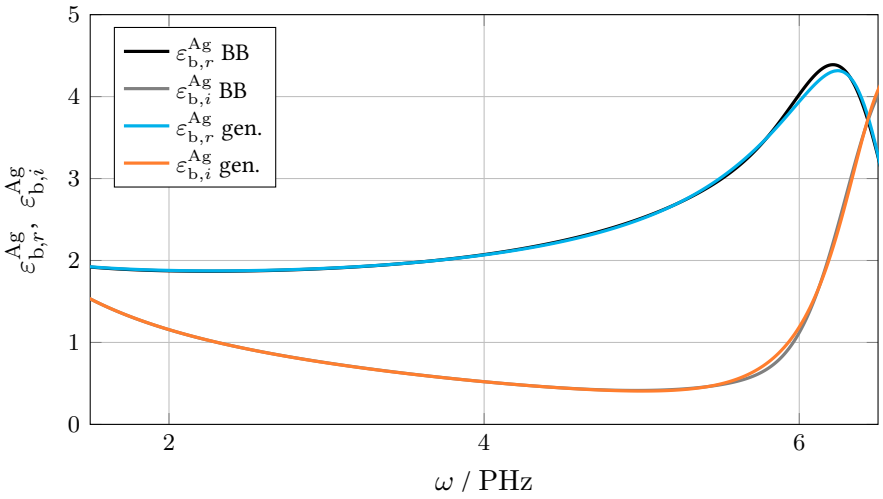

Figure C.1 | Real and imaginary part of Ag's bound permittivity. Black: ε_{r} and ε_{i} respectively are the real and imaginary part of the experimentally motivated BB model [123]. Colored: the fitted permittivity with our generalized dispersion model [153]. The corresponding fitting coefficients can be found in Table C.1.

Table C.1 | Fit parameters of Ag. Coefficients of the generalized dispersion model (2.4.5) with $\varepsilon_\infty = 1.0$ fitted to the BB permittivity of Ag. Figure C.1 depicts the original BB model and the fitted result. $\omega_P = 1.2403e16$ Hz and $\gamma = 7.4444e13$Hz.

i	c_i [Hz^2]	d_i [Hz]	e_i [Hz^2]	f_i [Hz]
1	0.1213021E+33	0.1933339E+06	0.5968192E+33	0.2543320E+18
2	0.2151872E+32	0.1165294E+16	0.4277860E+32	0.8377380E+15
3	0.6448077E+33	0.1095568E+06	0.3148161E+32	0.2885543E+18
4	0.8549296E+31	0.8121876E+15	0.6063455E+32	0.9921510E+15

D

Spherical Dimer

We provide a collection of simulation results for the spherical dimer system. More precisely, different incident polarizations have been tested in combination with varying flux formulations and material laws on. Further, we have also compared affine meshes and curvilinear elements respectively for plane waves and EELS excitations.

D.1 Linear elements

Simulations on affine meshes, centered and upwind DGTD, absorption, scattering and extinction cross section for the polarizations:

- $(\{\mathbf{k}\}_z, \{\mathbf{E}\}_x)$: Figures D.1, D.2, and D.3;
- $(\{\mathbf{k}\}_z, \{\mathbf{E}\}_y)$: Figures D.4, D.5, and D.6;
- $(\{\mathbf{k}\}_x, \{\mathbf{E}\}_y)$: Figures D.7, D.8, and D.9.

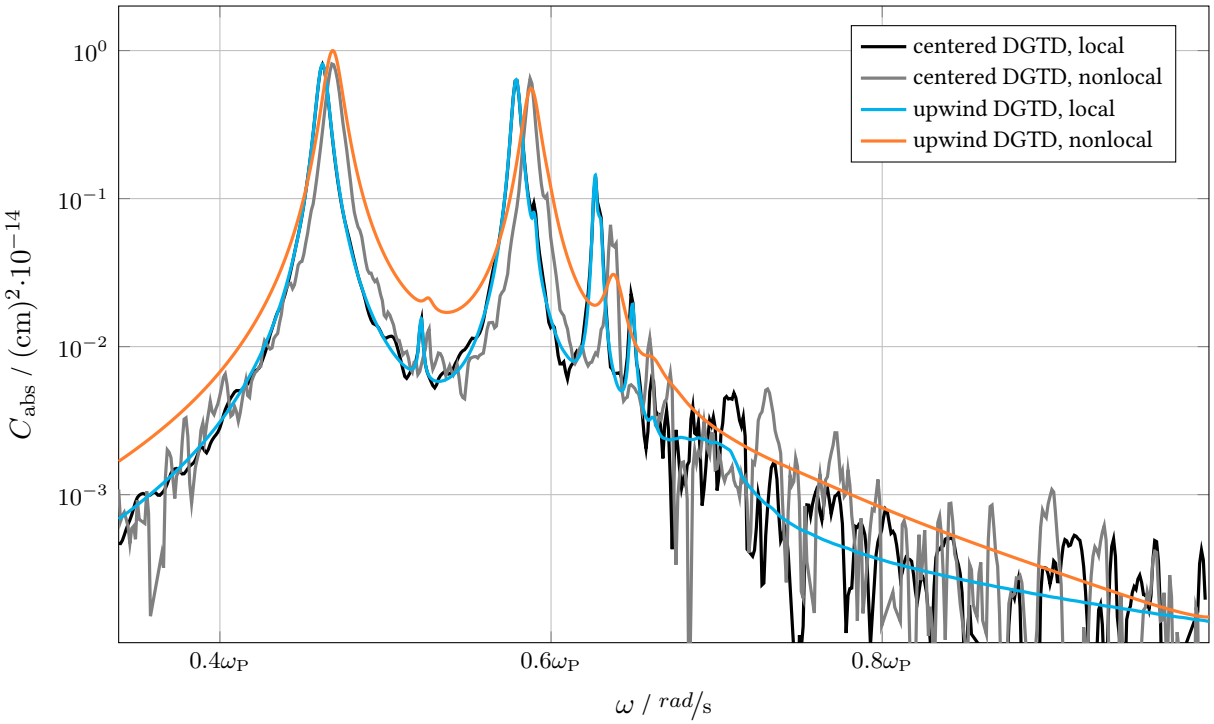

Figure D.1 | Logarithmic absorption CS of dimer ($\{\mathbf{k}\}_z$, $\{\mathbf{E}\}_x$).

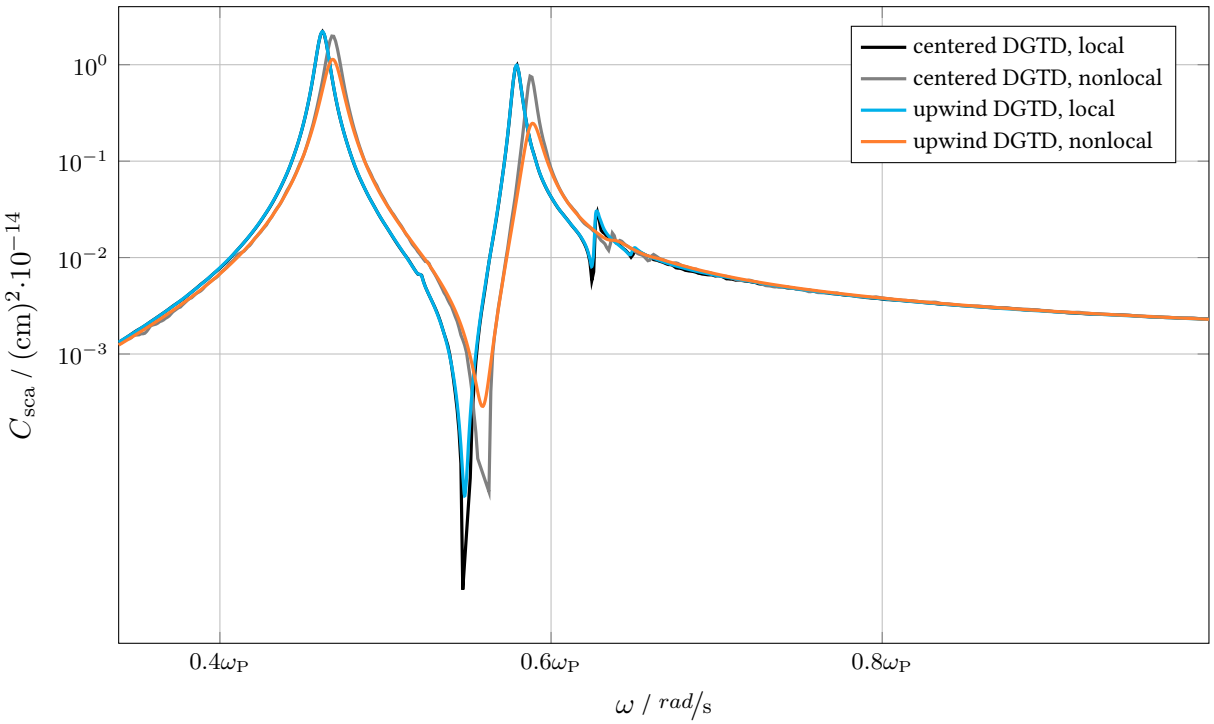

Figure D.2 | Logarithmic scattering CS of dimer ($\{\mathbf{k}\}_z$, $\{\mathbf{E}\}_x$).

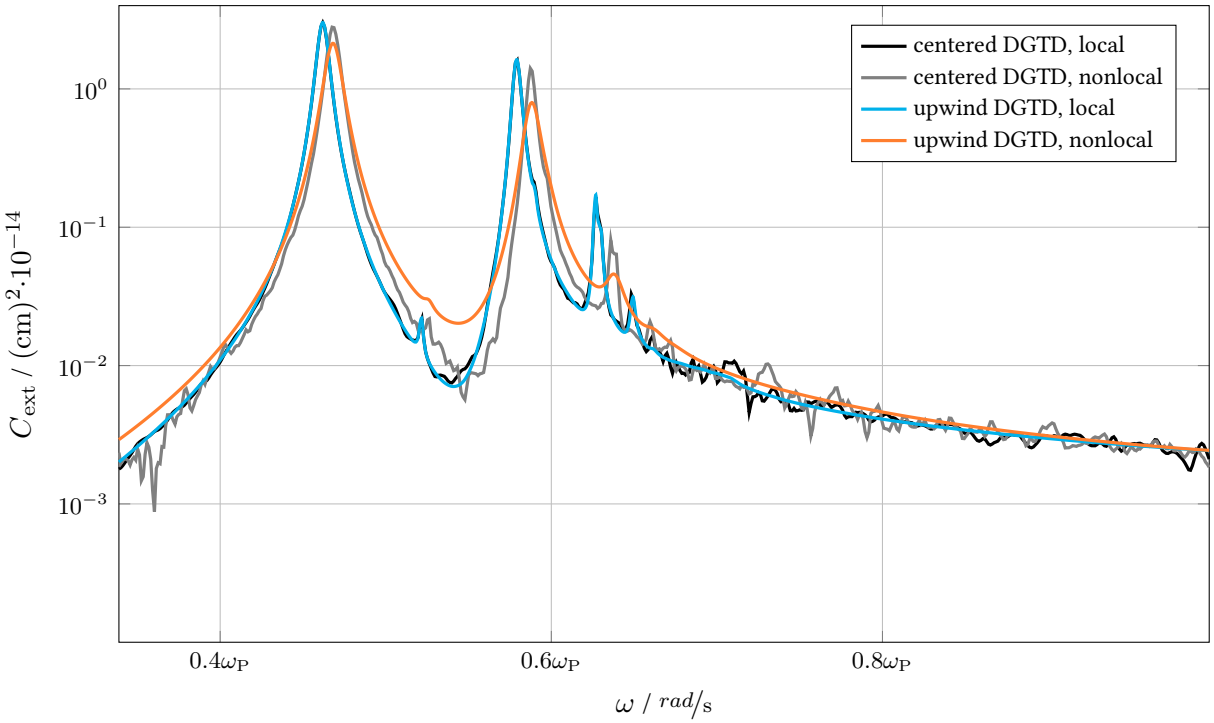

Figure D.3 | Logarithmic extinction CS of dimer ($\{\mathbf{k}\}_z$, $\{\mathbf{E}\}_x$).

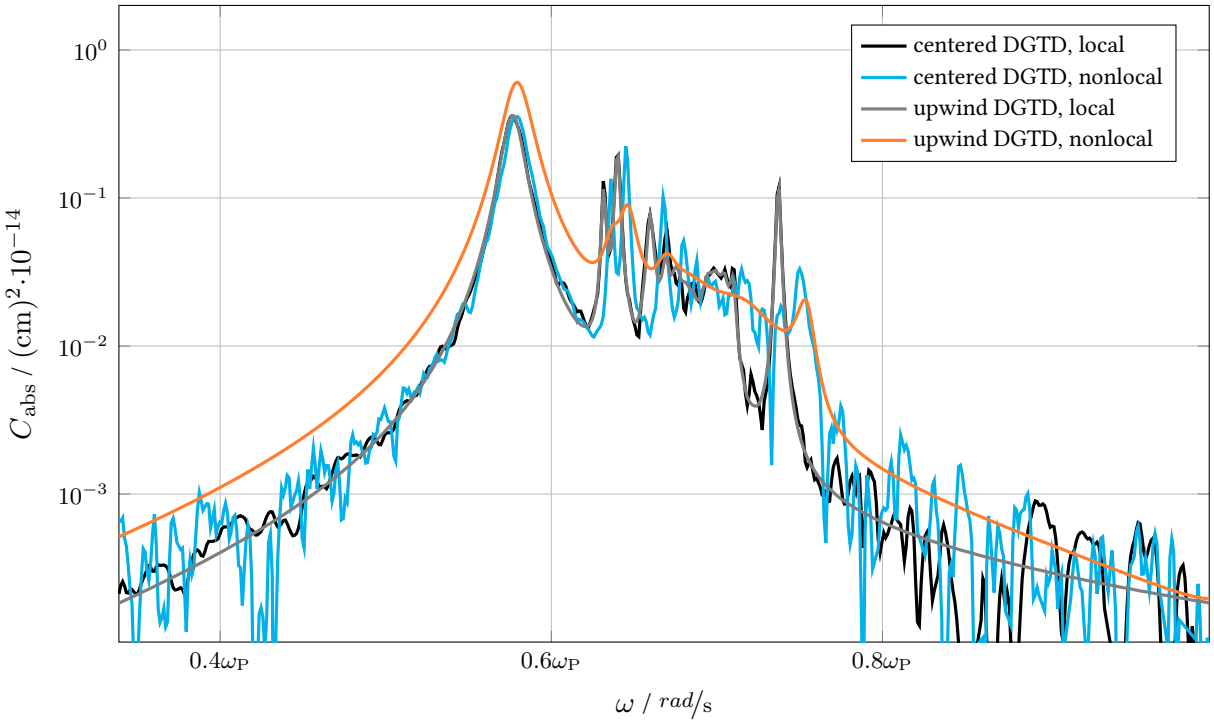

Figure D.4 | Logarithmic absorption CS of dimer ($\{\mathbf{k}\}_z$, $\{\mathbf{E}\}_y$).

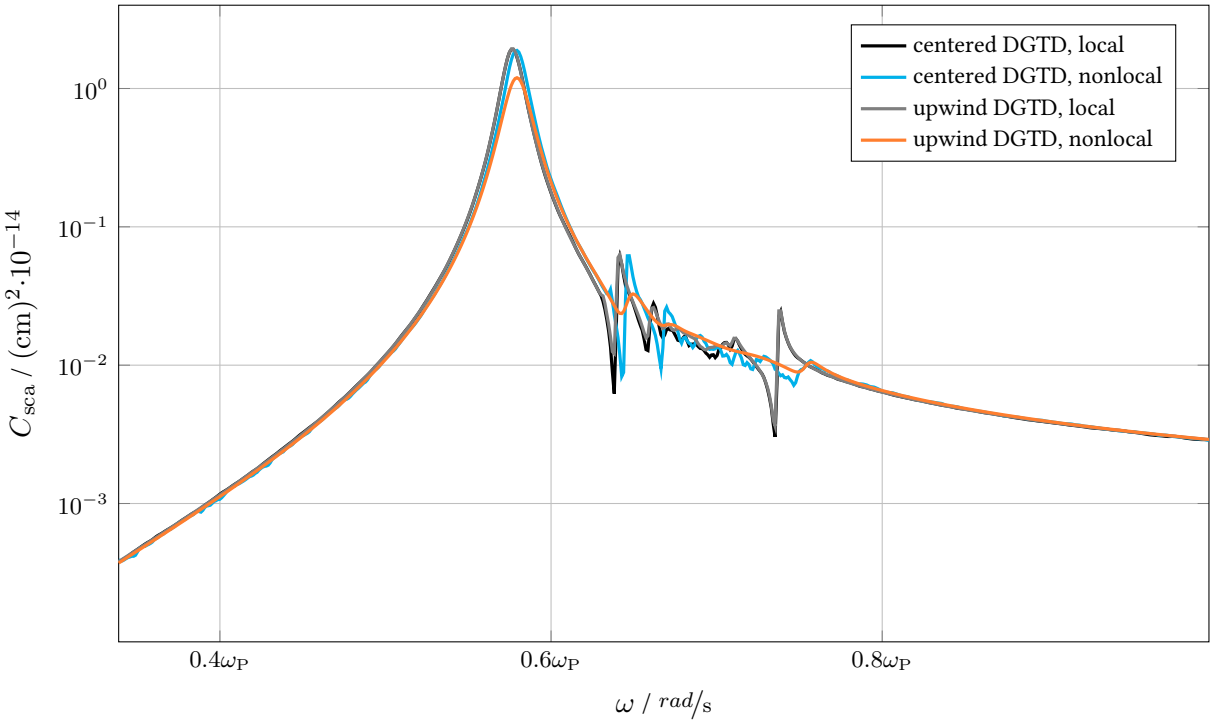

Figure D.5 | Logarithmic scattering CS of dimer ($\{\mathbf{k}\}_z$, $\{\mathbf{E}\}_y$).

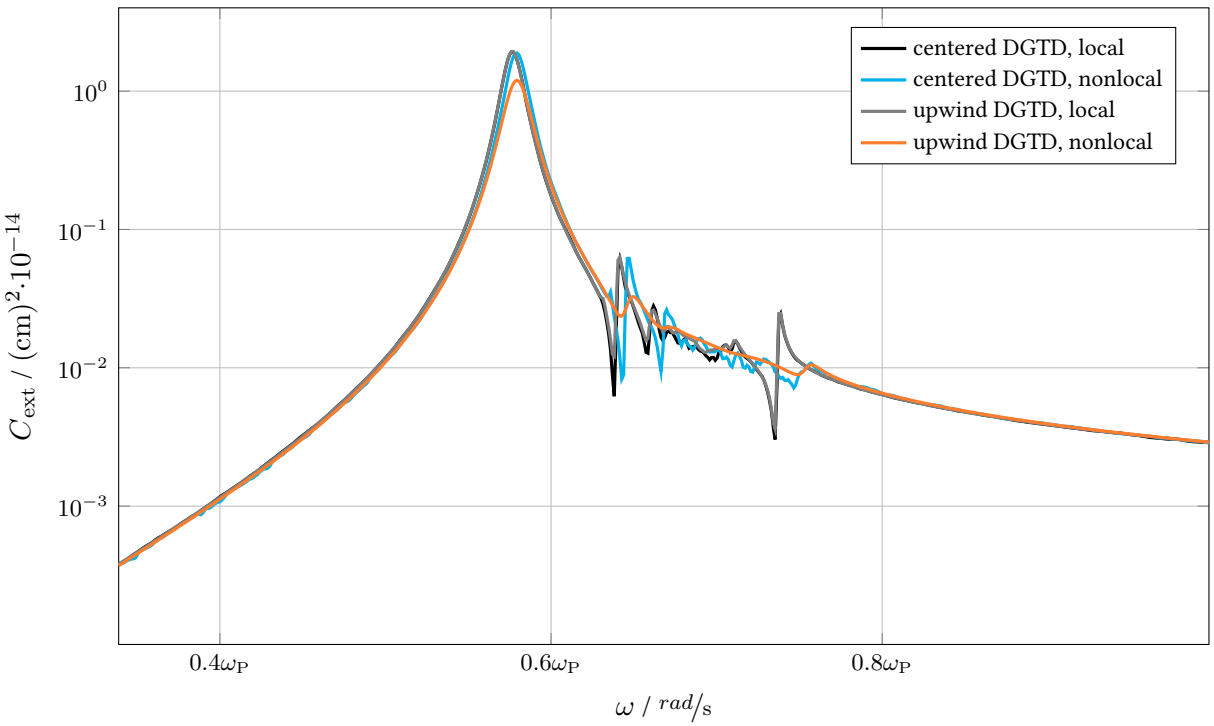

Figure D.6 | Logarithmic extinction CS of dimer ($\{\mathbf{k}\}_z$, $\{\mathbf{E}\}_y$).

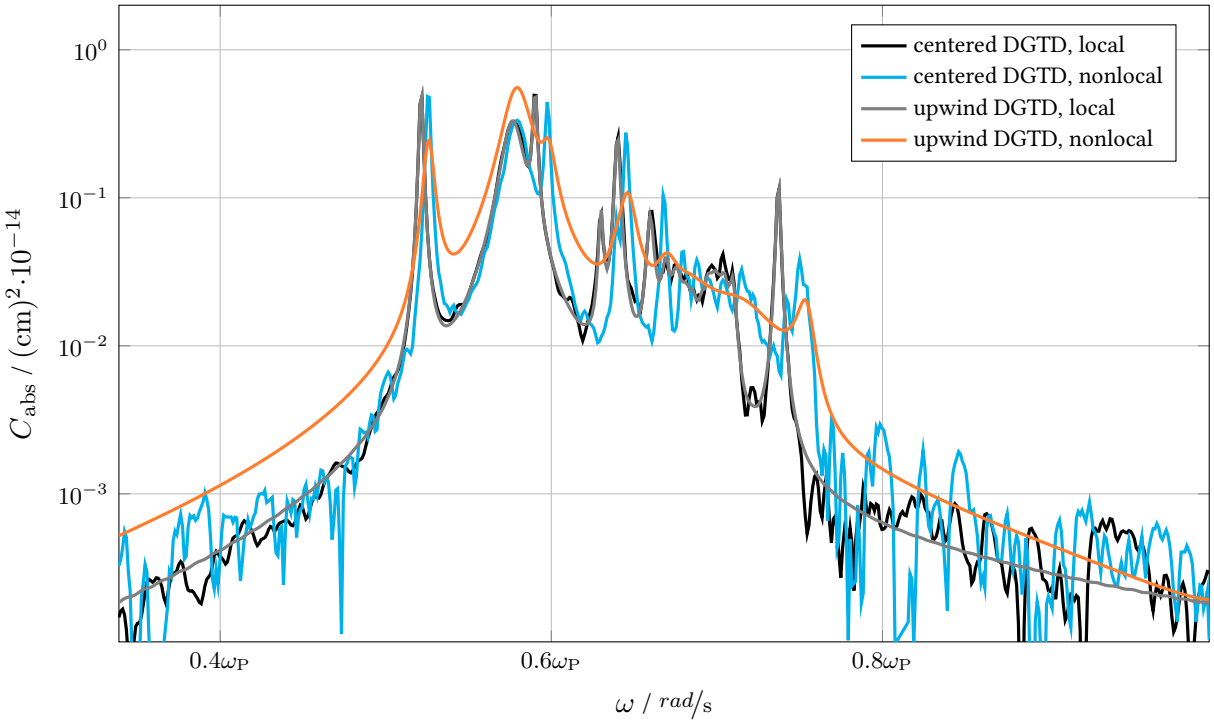

Figure D.7 | Logarithmic absorption CS of dimer ($\{\mathbf{k}\}_x$, $\{\mathbf{E}\}_y$).

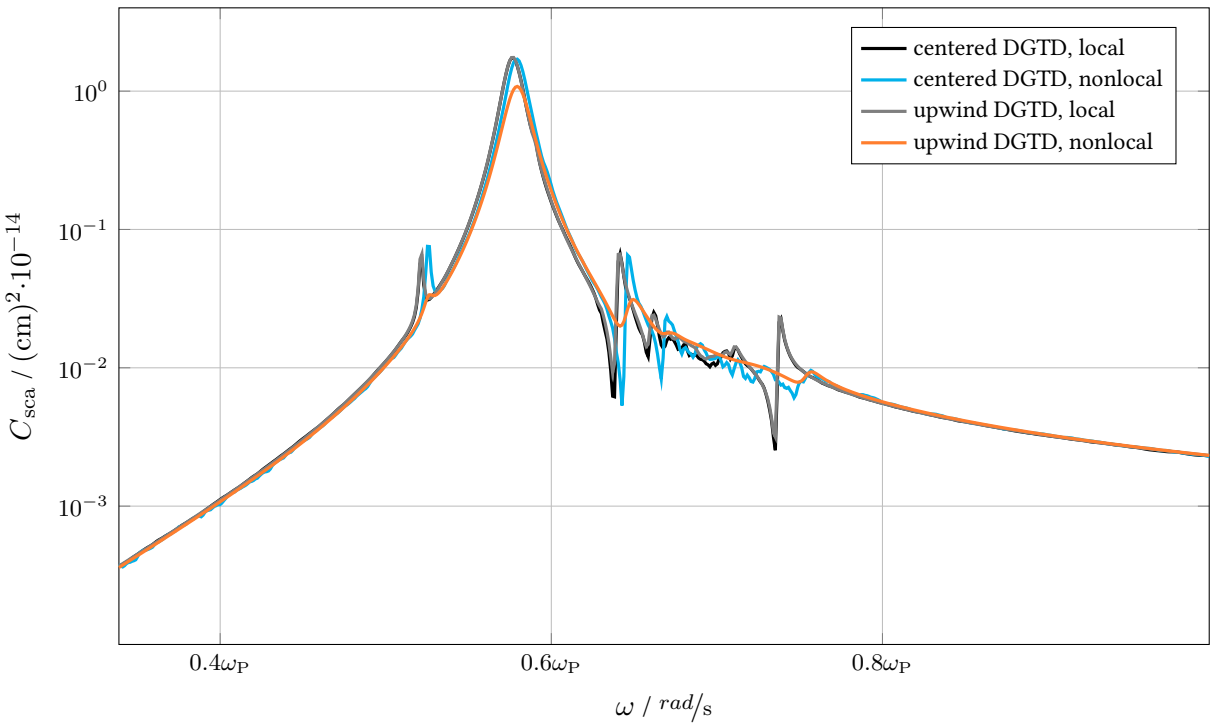

Figure D.8 | Logarithmic scattering CS of dimer ($\{\mathbf{k}\}_x$, $\{\mathbf{E}\}_y$).

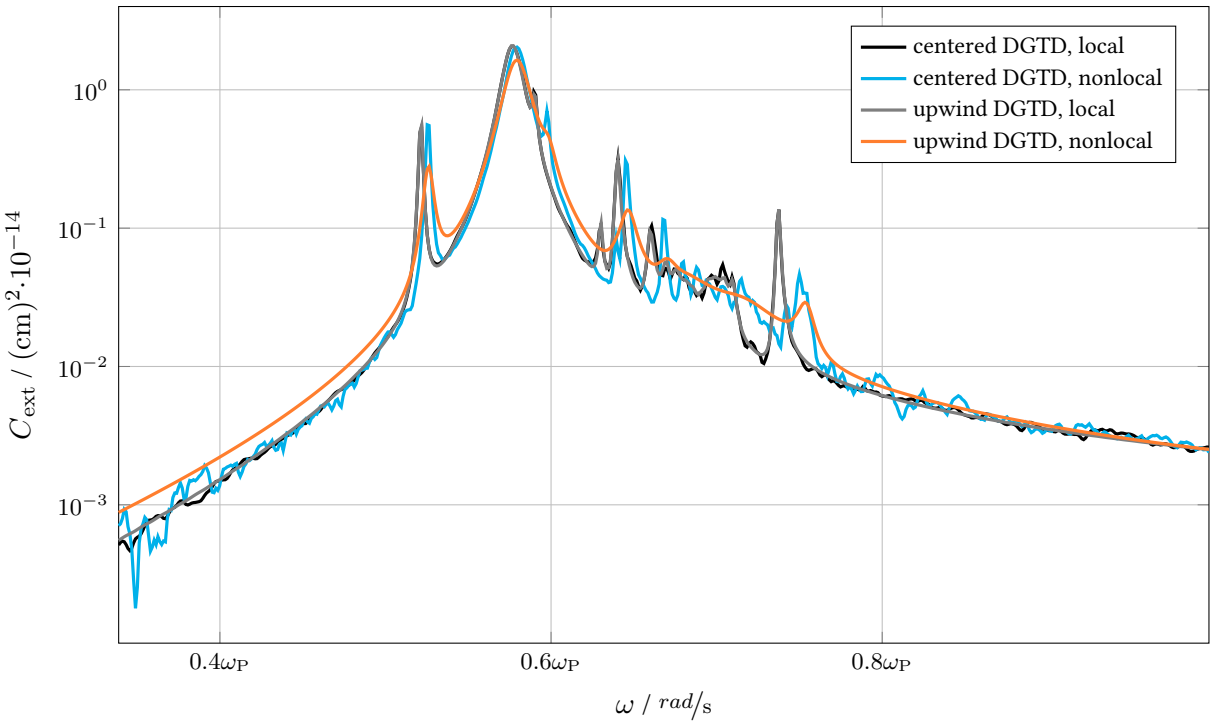

Figure D.9 | Logarithmic extinction CS of dimer ($\{\mathbf{k}\}_x$, $\{\mathbf{E}\}_y$).

D.2 Curvilinear elements

Comparison of local vs. nonlocal dispersion models for the scattering (Figure D.12), absorption (Figure D.12) and extinction (Figure D.10) cross section.

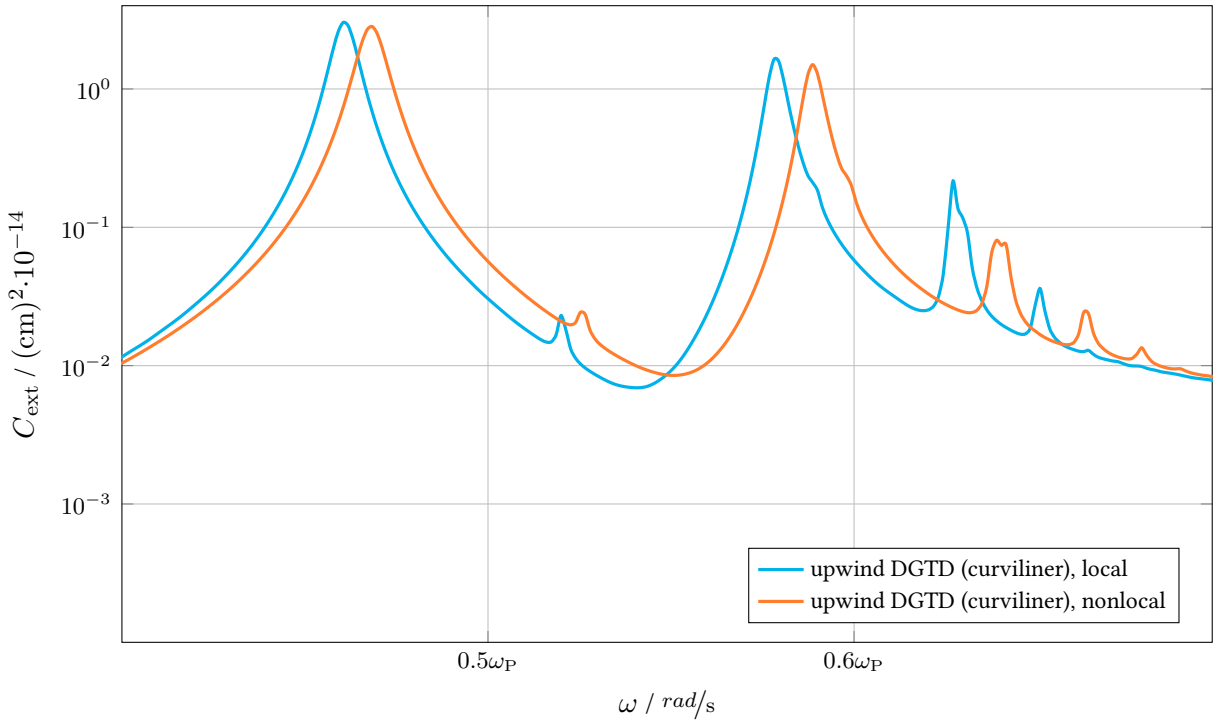

Figure D.10 | Logarithmic extinction CS of dimer ($\{\mathbf{k}\}_x$, $\{\mathbf{E}\}_y$).

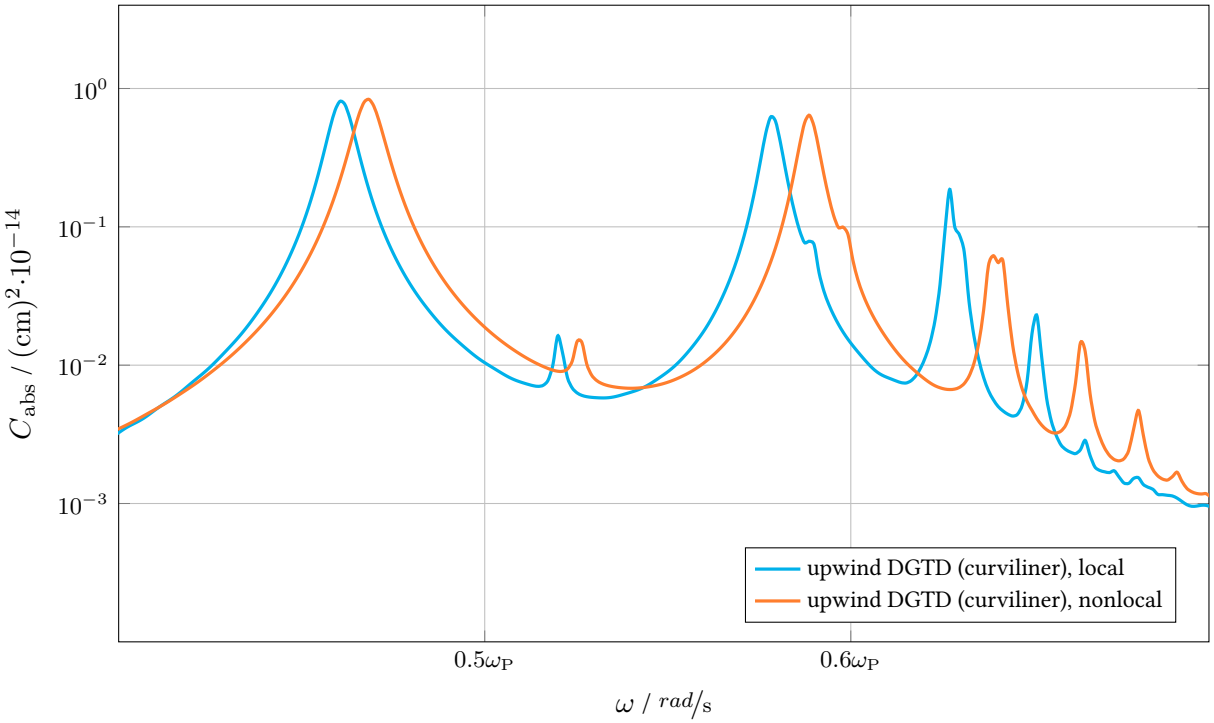

Figure D.11 | Logarithmic absorption CS of dimer ($\{\mathbf{k}\}_x$, $\{\mathbf{E}\}_y$).

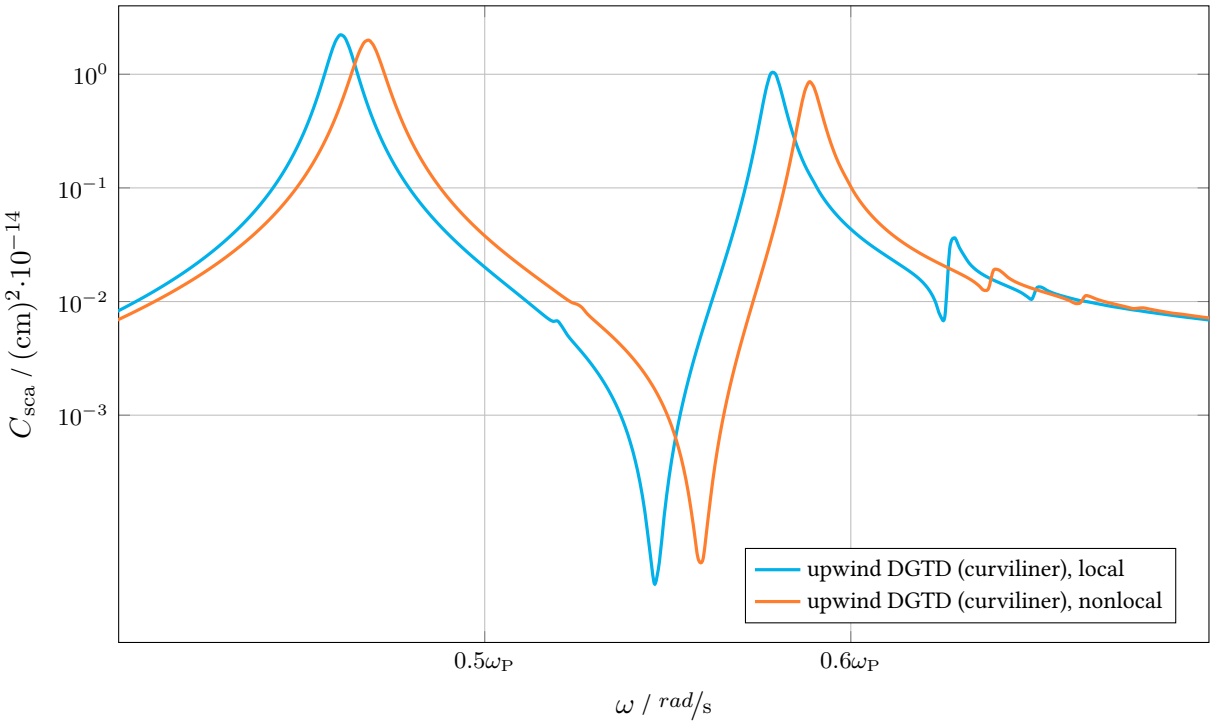

Figure D.12 | Logarithmic scattering CS of dimer ($\{\mathbf{k}\}_x$, $\{\mathbf{E}\}_y$).

D.3 EELS-simulations

Comparison of local vs. nonlocal dispersion models as well as extinction spectra vs. EELS signals of the spherical dimer system. The electron beam travels at center through the gap. The spectra are respectively in Figures D.13, D.14 and D.15.

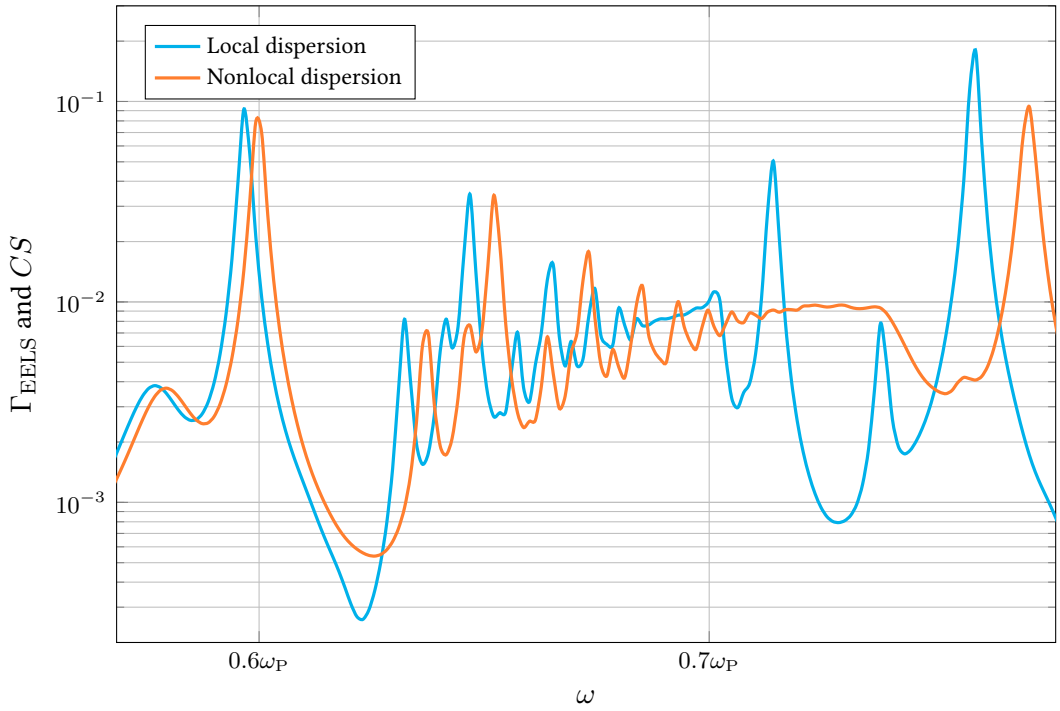

Figure D.13 | Spherical dimer: Comparison of local and nonlocal EELS.

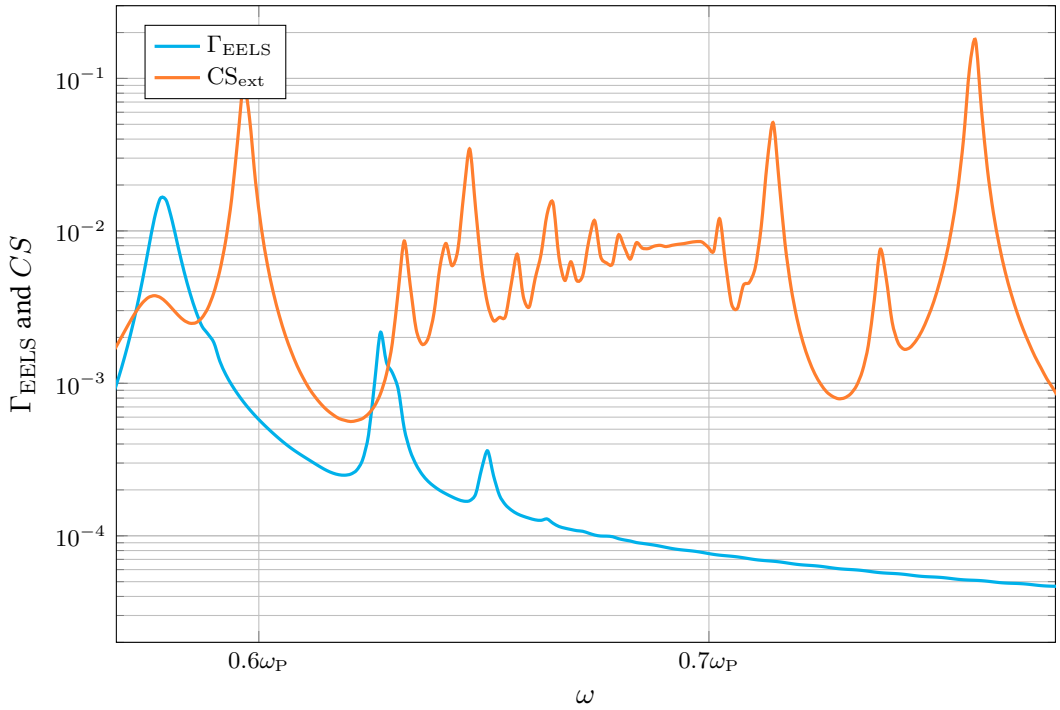

Figure D.14 | Spherical dimer: Comparison of local EELS and CS. The EELS spectrum is significantly richer than the CS spectrum. Most EELS resonances are dark-modes with respect to the incident plane wave in Figure 5.20 (a).

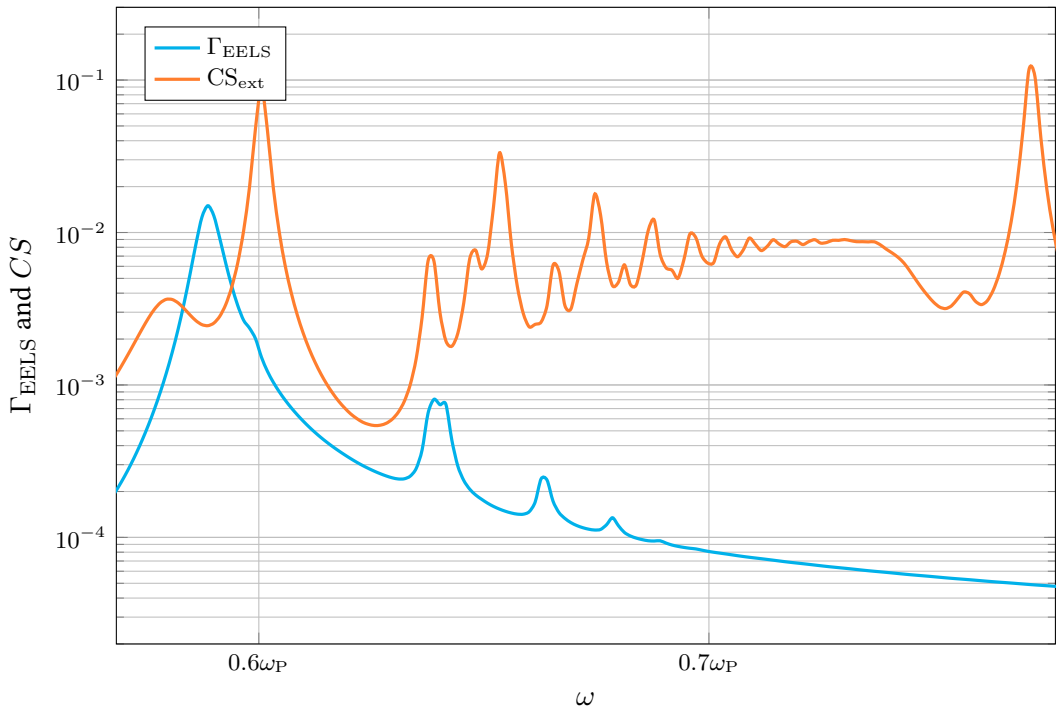

Figure D.15 | Spherical dimer: Comparison of nonlocal EELS and CS. The EELS spectrum is significantly richer than the CS spectrum. Most EELS resonances are dark-modes with respect to the incident plane wave in Figure 5.20 (a).

Index

This list of symbols contains all symbols that occur in multiple sections. Local variables and definitions generally not contained.

Symbols

Mathematics

α	Upwind factor of numerical flux
C	Generic constant independant of Δt and h
$\mathcal{C}$	Space of continuous functions
$\mathcal{D}$	Functional space, see analysis of well posedness
$\mathbf{e}$	Unit vector
$\mathcal{F}$	Rankine Hugeniot $\mathcal{F}$
$\boldsymbol{\mathcal{F}}$	Numerical trace operator
$F(\omega)$	Function in the spectral domain
$f(t)$	Function in the time-domain
$\mathbf{G}$	Auxiliary PML current
h	Characteristic mesh size
$\mathcal{H}$	Hilbert space
$\boldsymbol{\mathcal{H}}$	Vectorial Hilbert space
$\mathbf{I}$	Identity matrix
$\boldsymbol{\mathcal{I}}$	Differential operator of Maxwell's equations + dispersion models including source terms
$\boldsymbol{\mathcal{K}}$	Operator containing the source terms of Maxwell's equations + dispersion models
$\boldsymbol{\mathcal{L}}$	Differential operator of Maxwell's equations + dispersion models
L	Linear operator
$\mathbf{\Lambda}$	Matrix containing physical parameters of Maxwell's equations + dispersion models

$\boldsymbol{\lambda}$	Eigenvalues of the hyperbolic system
$\boldsymbol{\mathcal{L}}$	Vectorial function space
$\mathcal{L}$	Functional space
$\mathcal{L}^1$	Functional space $\mathcal{L}^1$
$\mathbb{N}$	Set of positive integers
$\mathbf{n}$	Normal vector
ν	Rescaled velocity $\nu = v/c_0$
Ω	Computational Domain
$\boldsymbol{\phi}$	Test function
$\boldsymbol{\psi}_{\tau_i}$	Mapping between the reference and physical element
$\mathcal{P}$	Approximation space of Lagrange polynomials on tetrahedra
$\boldsymbol{\mathcal{Q}}$	Matrix of physical parameters for the conservative form
$\mathcal{Q}$	Approximation space of Lagrange polynomials on hexahedra
$\mathbb{R}$	Set of real numbers
s	Coordinate stretching for PML
σ	Standard deviation
T	Final time
t	time coordinate
$\boldsymbol{\Theta}$	DG DoF vector
$\boldsymbol{\vartheta}$	Vector of vectors $= \{\mathbf{E}, \mathbf{H}, \mathbf{J}, Q\}$
$\mathcal{V}$	Volume
V	Functional space
$\mathbb{V}$	Vectorial approximation space
$\mathbf{V}$	Vectorial approximation space
$\mathcal{W}$	Flux for Rankine Hugeniot condition
$\mathbf{W}$	Vectorial discrete solution
W	Discrete solution
(x', y', z', t')	Cartesian axis and time in the moving frame
(x, y, z, t)	Cartesian axis and time in the laboratory frame
$\mathcal{F}$	Fourier transform

Physics

$\mathbf{A}$	Arbitrary vector
$\mathbf{B}$	Magnetic flux density field vector
β	Material parameter β of the linearized hydrodynamic model

c_0	Velocity of light in vacuum
χ	Susceptibility
c_r	Correction of the velocity of light in a medium $c_r = 1/\sqrt{\mu_r \varepsilon_\infty}$
$\mathbf{D}$	Electric displacement field vector
$\mathbf{E}$	Electric field vector
$\mathcal{E}$	Energy
ε	Permittivity
ε_L	Drude permittivity (local dispersion)
$\mathbf{F}$	Lorentz force
G	Energy functional of the nonlinear hydrodynamic model
γ	Damping frequency of the Drude and linearized hydrodynamic model
$\mathbf{H}$	Magnetic field vector
$\mathbf{J}$	Current density field vector
$\mathbf{k}$	Wave vector
$\mathbf{M}$	Magnetic polarization vector
m	Mass
μ	Permeability
n	Electron density
ω_P	Plasma frequency
$\mathbf{P}$	Electric polarization vector
q	Electric charge
Q	Charge density of the linearized hydrodynamic model
R	Radius
ρ	Electric charge density
$\mathbf{S}$	Poynting vector
σ	Surface charge
T	Energy functional (kinetic or von Weiszäcker contribution)
$\mathbf{v}$	Velocity
v_F	Fermi velocity
w	Energy density
$\mathbf{x}$	Displacement of an electron relative to its initial position
Y	Admittance
Z	Impedance

Sources and Observables

A	Absorption coefficient
$\mathbf{d}(\mathbf{r}, t)$	Distance vector from point $\mathbf{r}$ to electron position $\mathbf{r}_e(t)$ of an incident electron. $\mathbf{d}(\mathbf{r}, t) := \mathbf{r}_e(t) - \mathbf{r}(t)$
CS	Cross section
d_{EELS}	EELS impact parameter
erf	Error function, integral of the Gaussian function
γ	Relativistic factor $\gamma := \frac{1}{\sqrt{1 - \left(\frac{\lvert\mathbf{v}\rvert}{c_0}\right)^2}}$
Γ_{EELS}	EELS probability
H	Spherical Hankel function of the first kind
J	Spherical Bessel function of the first kind
K	Separation constant
k_0	Free space wave number $k_0 := \omega/c_0$
ω_{c}	Central frequency
P	Power
R	Reflection coefficient
s	Piecewise function splitting parameter for Gaussian electron beam
σ	Sigma environment of a Gaussian signal
T	Transmission coefficient

Acronyms

2D	Two Dimensional
3D	Three Dimensional
ABC	First Order Absorbing Boundary Condition
BB	Brendel-Bormann
BEM	Boundary Element Method
BREP	Boundary Representation
CAD	Computer Aided Design
CFL	Courant Friedrichs Lewy
CFS	Complex Frequency Shifted
CICADA	This work was granted access to the HPC and visualization resources of "Centre de Calcul Interactif" hosted by "Université Nice Sophia Antipolis"
CL	Cathodoluminescence
CMA-ES	CMA-ES
CPU	Central Processing Unit
CS	Cross Section

DFT	Density functional theory
DG	Discontinuous Galerkin
DGTD	Discontinuous Galerkin Time-Domain
DIOGENeS	Software developed at Inria Sophia Antipolis-Méditerannée
Distene	www.meshgems.com
DoF	Degree of Freedom
DUT	Device Under Test
EEGS	Electron Energy Gain Spectroscopy
EELP	Electron Energy Loss Probability
EELS	Electron Energy Loss Spectroscopy
Famosa	https://team.inria.fr/acumes/software/
FDTD	Finite Differences Time-Domain
FE	Finite Element
FEM	Finite Element Method
FIT	Finite Integration Technique
FV	Finite Volume
FVM	Finite Volume Method
GMSH	http://gmsh.info/
GNOR	Generalized nonlocal optical response
HDG	Hybrid Discontinuous Galerkin
HPC	High Performance Computing
HW	Hard Wall
IGA	Isogeometric Analysis
LF	Leap-Frog
LHS	Left Hand Side
LSRK	Low Storage Runge-Kutta
M	Mesh
Matlab	https://fr.mathworks.com/products/optimization.html
MC	Monte Carlo
MPI	Message Passing Interface
NRA	No Recoil Approximation
NURBS	Non-Uniform Rational Basis Spline
ODE	Ordinary Differential Equation
openCascade	https://www.opencascade.com/
Paraview	https://www.paraview.org/
PDE	Partial Differential Equation

PDF	Probability Density Function
PEC	Perfect Electrical Conductor
PMC	Perfect Magnetic Conductor
PML	Perfectly Matched Layer
QoI	Quantity of Interest
R	Run
RCWA	Rigorous Coupled Wave Analysis
RHS	Right Hand Side
RK	Runge-Kutta
RV	Random Variable
SEM	Scanning Electronic Microscopy
SERS	Surface Enhanced Raman Scattering
SF	Scattered Field
SHG	Second Harmonic Generation
SMP	Symmetric multiprocessing
SPP	Surface Plasmon Polariton
SW	Soft Wall
TF	Total Field
TF/SF	Total Field / Scattered Field
UPML	Uniaxial Perfectly Matched Layer
UQ	Uncertainty Quantification
UV	Ultra Violet
Vizir	https://team.inria.fr/gamma3/project-presentation/gamma-software/
w.l.o.g.	Without Loss Of Generality

List of Figures

List of Tables

Bibliography

[1] G. M. Akselrod, C. Argyropoulos, T. B. Hoang, C. Ciracì, C. Fang, J. Huang, D. R. Smith, and M. H. Mikkelsen. Probing the mechanisms of large Purcell enhancement in plasmonic nanoantennas. *Nature Photonics*, 8(11):835–840, 2014.

[2] G. M. Akselrod, J. Huang, T. B. Hoang, P. T. Bowen, L. Su, D. R. Smith, and M. H. Mikkelsen. Large-Area Metasurface Perfect Absorbers from Visible to Near-Infrared. *Advanced Materials*, 27(48):8028–8034, 2015.

[3] I. Babuska, F. Nobile, and R. Tempone. A Stochastic Collocation Method for Elliptic Partial Differential Equations with Random Input Data. *SIAM Review*, (2):317–355, 2010.

[4] C. Balanis. *Antenna Theory: Analysis and Design*, volume 28. Wiley, 2012.

[5] J.-P. Berenger. A perfectly matched layer for the absorption of electromagnetic waves. *Journal of Computational Physics*, 114(2):185–200, 1994.

[6] J.-P. Bérenger. *Perfectly Matched Layer (PML) for Computational Electromagnetics*. Morgan & Claypool, 2007.

[7] G. Blatman and B. Sudret. Adaptive Sparse Polynomial Chaos Expansion Based on Least Angle Regression. *J. Comput. Physics*, 230(6):2345–2367, 2011.

[8] A. D. Boardman. *Electromagnetic Surface Modes*. John Wiley & Sons, 1982.

[9] A. S. Bonnet-Ben Dhia, C. Carvalho, and P. Ciarlet. Mesh requirements for the finite element approximation of problems with sign-changing coefficients. *Numerische Mathematik*, pages 1–38, 2017.

[10] Z. Bontinck, J. Corno, H. De Gersem, S. Kurz, A. Pels, S. Schöps, F. Wolf, C. de Falco, J. Dölz, R. Vázquez, and U. Römer. Recent Advances of Isogeometric Analysis in Computational Electromagnetics. *arXiv:1709.06004v1*, 2017.

[11] S. Burger, R. Köhle, L. Zschiedrich, W. Gao, F. Schmidt, R. März, and C. Nölscher. Benchmark of FEM, waveguide, and FDTD algorithms for rigorous mask simulation. In *SPIE 5992, 25th Annual BACUS Symposium on Photomask Technology*, number 599216, 2005.

[12] S. Burger, L. Zschiedrich, J. Pomplun, and F. Schmidt. JCMsuite: An Adaptive FEM Solver or Precise Simulations in Nano-Optics. In *Integrated Photonics and Nanophotonics Research and Applications*, Boston, Massachusetts, 2008. Optical Society of America.

[13] E. Burman, A. Ern, and M. A. Fernández. Explicit Runge–Kutta Schemes and Finite Elements with Symmetric Stabilization for First-Order Linear PDE Systems. *SIAM Journal on Numerical Analysis*, 48(6):2019–2042, 2010.

[14] K. Busch, M. König, and J. Niegemann. Discontinuous Galerkin methods in nanophotonics. *Laser and Photonics Reviews*, 5(6):773–809, 2011.

[15] J. C. Butcher. *Numerical Methods for Ordinary Differential Equations*. John Wiley & Sons, 2008.

[16] M. H. Carpenter and C. A. Kennedy. Fourth-order 2N-storage Runge-Kutta schemes. *Nasa Technical Memorandum*, 109112(TM 109112):1–26, 1994.

[17] P. Chandrashekarappa and R. Duvigneau. Radial basis functions and kriging metamodels for aerodynamic optimization. *INRIA Research Report*, (March):1–40, 2007.

[18] Y. Chen. Nanofabrication by electron beam lithography and its applications: A review. *Microelectronic Engineering*, 135:57–72, 2015.

[19] W. C. Chew and W. H. Weedon. A 3D perfectly matched medium from modified maxwell's equations with stretched coordinates. *Microwave and Optical Technology Letters*, 7(13):599–604, 1994.

[20] T. Christensen, W. Yan, S. Raza, A. P. Jauho, N. A. Mortensen, and M. Wubs. Nonlocal response of metallic nanospheres probed by light, electrons, and atoms. *ACS Nano*, 8(2):1745–1758, 2014.

[21] P. Ciarlet and C. Scheid. Title. *submitted*.

[22] J.-P. Cioni, L. Fezoui, and H. Steve. Approximation des équations de maxwell par des schemas décentrés en éléments finis. Technical report, Technical report, INRIA, 2006.

[23] C. Ciracì and F. Della Sala. Quantum hydrodynamic theory for plasmonics: Impact of the electron density tail. *Physical Review B*, 93(20):1–14, 2016.

[24] C. Ciracì, R. T. Hill, J. J. Mock, Y. Urzhumov, A. I. Fernández-Domínguez, S. A. Maier, J. B. Pendry, A. Chilkoti, and D. R. Smith. Probing the ultimate limits of plasmonic enhancement. *Science*, 337(6098):1072–1074, 2012.

[25] C. Ciracì, J. B. Pendry, and D. R. Smith. Hydrodynamic model for plasmonics: A macroscopic approach to a microscopic problem. *ChemPhysChem*, 14(6):1109–1116, 2013.

[26] D. K. Cohoon. An exact solution of mie type for scattering by a multilayer anisotropic sphere. *Journal of Electromagnetic Waves and Applications*, 3(5):421–448, 1989.

[27] T. J. Cui, D. Smith, and R. Liu. *Metamaterials - Theory, Design, and Applications*. Springer, 2010.

[28] C. David and F. J. García De Abajo. Spatial nonlocality in the optical response of metal nanoparticles. *Journal of Physical Chemistry C*, 115(40):19470–19475, 2011.

[29] J. Defrance, C. Lemaître, R. Ajib, J. Benedicto, E. Mallet, R. Pollès, J.-p. Plumey, M. Mihailovic, E. Centeno, C. Ciracì, D. Smith, and A. Moreau. Moosh: A Numerical Swiss Army Knife for the Optics of Multilayers in Octave/Matlab. *Journal of Open Research Software*, 4(1), 2016.

[30] A. Deinega and I. Valuev. Subpixel smoothing for conductive and dispersive media in the finite-difference time-domain method. *Optics Letters*, 32(23):3429–3431, 2007.

[31] G. Demèsy, F. Zolla, A. Nicolet, M. Commandré, and C. Fossati. The finite element method as applied to the diffraction by an anisotropic grating. *Optics Express*, 15(26):18089, 2007.

[32] S. Descombes, S. Lanteri, and L. Moya. Locally implicit time integration strategies in a discontinuous galerkin method for maxwell's equations. *Journal of Scientific Computing*, 56(1):190–218, 2013.

[33] D. A. Di Pietro and A. Ern. *Mathematical Aspects of Discontinuous Galerkin Methods*, volume 3. Springer, 2011.

[34] R. Diehl. *Analysis of Metallic Nanostructures by a Discontinuous Galerkin Time-Domain Maxwell Solver on Graphics Processing Units*. PhD thesis, KIT, 2012.

[35] F. Dimroth, M. Grave, P. Beutel, U. Fiedeler, C. Karcher, T. N. D. Tibbits, E. Oliva, G. Siefer, M. Schachtner, AlexanderWekkeli, A. Bett, R. Krause, M. Piccin, N. Blanc, C. Drazek, E. Guiot, B. Ghyselen, T. Salvetat, A. Tauzin, T. Signamarcheix, A. Dobrich, T. Hannappel, and K. Schwarzburg. Waferbondedfour-junction GaInP/GaAs//GaInAsP/GaInAs concentrator solar cells with 44.7% efficiency. *Progress in photovoltaics: research and applications*, 22:277–282, 2014.

[36] P. Drude. Zur Elektronentheorie der Metalle. *Annalen der Physik*, 354(6):710–724, 1916.

[37] R. Duvigneau. FAMOSA, http://www-sop.inria.fr/members/Regis.Duvigneau/soft_famosa.html.

[38] H. Egger, F. Kretzschmar, S. M. Schnepp, and T. Weiland. A space-time discontinuous Galerkin Trefftz method for time dependent Maxwell's equations. *SIAM J. Sci. Comput.*, 37(5):689–711, 2015.

[39] R. Eymard, T. Gallouët, and R. Herbin. Finite volume methods. In *Handbook of Numerical Analysis*, volume 7, pages 713–1018. 2000.

[40] H. Fahs. Improving accuracy of high-order discontinuous Galerkin method for time-domain electromagnetics on curvilinear domains. *International Journal of Computer Mathematics*, 88(10):2124–2153, 2011.

[41] A. Farjadpour, D. Roundy, A. Rodriguez, M. Ibanescu, P. Bermel, J. D. Joannopoulos, S. G. Johnson, and G. W. Burr. Improving accuracy by subpixel smoothing in the finite-difference time domain. *Optics Letters*, 31(20):2972–2974, 2006.

[42] R. P. Feynman, R. B. Leighton, and M. Sands. *The Feynman Lectures on Physics, Vol. II: The New Millennium Edition: Mainly Electromagnetism and Matter*, volume 24. 2010.

[43] L. Fezoui and S. Lanteri. Discontinuous Galerkin methods for the numerical solution of the nonlinear Maxwell equations in 1d. Technical Report hal-01114155, 2015.

[44] L. Fezoui, S. Lanteri, S. Lohrenengel, and S. Piperno. Convergence and stability of a discontinuous Galerkin time-domain method for the 3D heterogeneous Maxwell equations on unstructured meshes. *ESAIM: Mathematical Modelling and Numerical Analysis*, 39:1149–1176, 2005.

[45] B. Gallinet, J. Butet, and O. J. Martin. Numerical methods for nanophotonics: Standard problems and future challenges. *Laser and Photonics Reviews*, 9(6):577–603, 2015.

[46] F. García de Abajo. Relativistic energy loss and induced photon emission in the interaction of a dielectric sphere with an external electron beam. *Physical Review B*, 59(4):3095–3107, 1999.

[47] F. J. García De Abajo. Optical excitations in electron microscopy. *Reviews of Modern Physics*, 82(1):209–275, 2010.

[48] P. Genevet and F. Capasso. Holographic optical metasurfaces: a review of current progress. *Reports on Progress in Physics*, 78(2):024401, 2015.

[49] P. Genevet, F. Capasso, F. Aieta, M. Khorasaninejad, and R. Devlin. Recent advances in planar optics: from plasmonic to dielectric metasurfaces. *Optica*, 4(1):139, 2017.

[50] C. Geuzaine, A. Johnen, J. Lambrechts, J. F. Remacle, and T. Toulorge. The generation of valid curvilinear meshes. *Notes on Numerical Fluid Mechanics and Multidisciplinary Design*, 128:15–39, 2015.

[51] C. Geuzaine and J.-F. Remacle. Gmsh: a three-dimensional finite element mesh generator with built-in pre-and post-processing facilities. *International Journal for Numerical Methods in Engineering 79(11)*, 0:1309–1331, 2009.

[52] V. Giannini, A. I. Fernández-Domínguez, S. C. Heck, and S. A. Maier. Plasmonic nanoantennas: Fundamentals and their use in controlling the radiative properties of nanoemitters. *Chemical Reviews*, 111(6):3888–3912, 2011.

[53] P. E. Gill, W. Murray, and M. H. Wright. *Practical Optimization*. Academic Press, 1981.

[54] E. Gjonaj, T. Lau, and T. Weiland. Conservation properties of the discontinuous galerkin method for maxwell equations. *2007 International Conference on Electromagnetics in Advanced Applications, ICEAA'07*, (3):356–359, 2007.

[55] G. Granet. Efficient implementation of B-spline modal method for lamellar gratings. *Journal of the Optical Society of America A*, 31(2):332, 2014.

[56] (Grant2017-A0030610263). This work was performed using HPCresources from GENCI-CINES.

[57] N. Hansen. The CMA evolution strategy: A comparing review. *Studies in Fuzziness and Soft Computing*, 192:75–102, 2006.

[58] J. S. Hesthaven and T. Warburton. *Nodal Discontinuous Galerkin Methods*. Springer, 2008.

[59] A. Hille, R. Kullock, S. Grafström, and L. M. Eng. Improving nano-optical simulations through curved elements implemented within the discontinuous Galerkin method computational. In *Journal of Computational and Theoretical Nanoscience*, volume 7, pages 1581–1586, 2010.

[60] A. Hille, M. Moeferdt, C. Wolff, C. Matyssek, R. Rodríguez-Oliveros, C. Prohm, J. Niegemann, S. Grafström, L. M. Eng, and K. Busch. Second Harmonic Generation from Metal Nano-Particle Resonators: Numerical Analysis on the Basis of the Hydrodynamic Drude Model. *Journal of Physical Chemistry C*, 120(2):1163–1169, 2016.

[61] K. R. Hiremath, L. Zschiedrich, and F. Schmidt. Numerical solution of nonlocal hydrodynamic Drude model for arbitrary shaped nano-plasmonic structures using Nédélec finite elements. *Journal of Computational Physics*, 231(17):5890–5896, 2012.

[62] T. B. Hoang, G. M. Akselrod, C. Argyropoulos, J. Huang, D. R. Smith, and M. H. Mikkelsen. Ultrafast spontaneous emission source using plasmonic nanoantennas. *Nature Communications*, 6, 2015.

[63] U. Hohenester and A. Trügler. MNPBEM - A Matlab toolbox for the simulation of plasmonic nanoparticles. *Computer Physics Communications*, 183(2):370–381, 2012.

[64] Http://www.lumerical.com/tcad-products/fdtd/. Lumerical Inc.

[65] Y. Huang, J. Li, and W. Yang. Theoretical and numerical analysis of a non-local dispersion model for light interaction with metallic nanostructures. *Computers and Mathematics with Applications*, 72(4):921–932, 2016.

[66] Z. Huang, G. Meng, Q. Huang, B. Chen, F. Zhou, X. Hu, Y. Qian, H. Tang, F. Han, and Z. Chu. Polyacrylic acid sodium salt film entrapped Ag-nanocubes as molecule traps for SERS detection. *Nano Research*, 7(8):1177–1187, 2014.

[67] T. J. Hughes, J. A. Cottrell, and Y. Bazilevs. Isogeometric analysis: CAD, finite elements, NURBS, exact geometry and mesh refinement. *Computer Methods in Applied Mechanics and Engineering*, 194(39-41):4135–4195, 2005.

[68] J. D. Jackson. *Classical Electrodynamics Third Edition*. John Wiley & Sons, 1999.

[69] A. Johnen, J. F. Remacle, and C. Geuzaine. Geometrical validity of curvilinear finite elements, 2013.

[70] P. B. Johnson and R. W. Christy. Optical constants of the noble metals. *Physical Review B*, 6(12):4370–4379, 1972.

[71] S. Kadkhodazadeh, T. Christensen, M. Beleggia, N. A. Mortensen, and J. B. Wagner. The Substrate Effect in Electron Energy-Loss Spectroscopy of Localized Surface Plasmons in Gold and Silver Nanoparticles. *ACS Photonics*, 4(2):251–261, 2017.

[72] K. W. Kark. *Antennen und Strahlungsfelder*. Vieweg Teubner, 2011.

[73] M. Kauranen, A. V. Zayats, J. W. Jarrett, T. Zhao, J. S. Johnson, X. Liu, P. F. Nealey, R. A. Vaia, K. L. Knappenberger, J. Butet, P.-F. Brevet, O. J. F. Martin, X. Liu, S. Biswas, J. W. Jarrett, E. Poutrina, A. Urbas, K. L. Knappenberger, R. A. Vaia, P. F. Nealey, X. Liu, J. W. Jarrett, D. Brown, V. Pustovit, A. Urbas, K. L. Knappenberger, P. F. Nealey, R. A. Vaia, H. Aouani, M. Rahmani, M. Navarro-Cía, and S. a. Maier. Nonlinear plasmonics. *Nature Photonics*, 9(11):737–748, 2015.

[74] J. Kennedy. Particle Swarm Optimization BT - Encyclopedia of Machine Learning. pages 760–766. Springer US, Boston, MA, 2010.

[75] D. I. Ketcheson. Highly Efficient Strong Stability-Preserving Runge–Kutta Methods with Low-Storage Implementations. *SIAM Journal on Scientific Computing*, 30(4):2113–2136, 2008.

[76] S. Kirkpatrick, C. D. Gelatt, and M. P. Vecchi. Optimization by Simulated Annealing. *Science*, 220(4598):671–680, 1983.

[77] C. Kittel. *Introduction to Solid State Physics*. Wiley, 2010.

[78] H. Klingbeil, U. Laier, and D. Lens. RF Cavities BT - Theoretical Foundations of Synchrotron and Storage Ring RF Systems. pages 173–224. Springer International Publishing, Cham, 2015.

[79] D. Knebl, A. Hörl, A. Trügler, J. Kern, J. R. Krenn, P. Puschnig, and U. Hohenester. Gap plasmonics of silver nanocube dimers. *Physical Review B*, 93(8):1–5, 2016.

[80] A. Konak, D. W. Coit, and A. E. Smith. Multi-objective optimization using genetic algorithms: A tutorial. *Reliability Engineering and System Safety*, 91(9):992–1007, 2006.

[81] M. König. *Discontinuous Galerkin Methods in Nanophotonics*. PhD thesis, 2011.

[82] M. König, C. Prohm, K. Busch, and J. Niegemann. Stretched-coordinate PMLs for Maxwell's equations in the discontinuous Galerkin time-domain method. *Optics Express*, 19(5):4618, 2011.

[83] P. Lalanne and G. M. Morris. Highly improved convergence of the coupled-wave method for TM polarization. *Journal of the Optical Society of America A*, 13(4):779, 1996.

[84] E. Langereis, S. B. S. Heil, H. C. M. Knoops, W. Keuning, M. C. M. van de Sanden, and W. M. M. Kessels. In situ spectroscopic ellipsometry as a versatile tool for studying atomic layer deposition. *Journal of Physics D: Applied Physics*, 42(7):073001, 2009.

[85] S. Lanteri and C. Scheid. Convergence of a discontinuous Galerkin scheme for the mixed time-domain Maxwell's equations in dispersive media. *IMA Journal of Numerical Analysis*, 33(2):432–459, 2013.

[86] S. Lanteri, C. Scheid, and J. Viquerat. Analysis of a generalized dispersive model coupled to a DGTD method with application to nanophotonics. *SIAM J. Numer. Anal.*, 39(3):831–859, 2017.

[87] O. Le Maitre and O. Knio. *Spectral Methods for Uncertainty Quantification: With Applications to Computational Fluid Dynamics*. Scientific Computation. Springer Netherlands, 2010.

[88] R. Léger, J. Viquerat, C. Durochat, C. Scheid, and S. Lanteri. A parallel non-conforming multi-element DGTD method for the simulation of electromagnetic wave interaction with metallic nanoparticles. *Journal of Computational and Applied Mathematics*, 270:330–342, 2014.

[89] C. Lemieux. *Monte Carlo and Quasi-Monte Carlo Sampling*. Springer Series in Statistics. Springer, Dordrecht, 2009.

[90] L. Li. Field singularities at lossless metal–dielectric arbitrary-angle edges and their ramifications to the numerical modeling of gratings. *Journal of the Optical Society of America A*, 29(4):593, 2012.

[91] L. Li, S. Lanteri, N. A. Mortensen, and M. Wubs. A hybridizable discontinuous Galerkin method for solving nonlocal optical response models. *Computer Physics Communications*, 219:99–107, 2017.

[92] J. Lin, J. Dellinger, P. Genevet, B. Cluzel, F. De Fornel, and F. Capasso. Cosine-gauss plasmon beam: A localized long-range nondiffracting surface wave. *Physical Review Letters*, 109(9):1–5, 2012.

[93] H. Liu and P. Lalanne. Microscopic theory of the extraordinary optical transmission. *Nature*, 452(7188):728–731, 2008.

[94] D. Loukrezis, U. Römer, and H. De Gersem. Numerical Comparison of Leja and Clenshaw-Curtis Dimension-Adaptive Collocation for Stochastic Parametric Electromagnetic Field Problems. *arXiv:1712.07223*, pages 1–20, 2017.

[95] Y. Luo, E. D. Ahmadi, K. Shayan, Y. Ma, K. S. Mistry, C. Zhang, J. Hone, J. L. Blackburn, and S. Strauf. Purcell-enhanced quantum yield from carbon nanotube excitons coupled to plasmonic nanocavities. *Nature Communications*, 8(1), 2017.

[96] S. A. Maier. *Plasmonics: Fundamentals and applications.* Springer, 2007.

[97] C. Matyssek, J. Niegemann, W. Hergert, and K. Busch. Computing electron energy loss spectra with the Discontinuous Galerkin Time-Domain method. *Photonics and Nanostructures - Fundamentals and Applications*, 9(4):367–373, 2011.

[98] J. M. McMahon, S. K. Gray, and G. C. Schatz. Nonlocal optical response of metal nanostructures with arbitrary shape. *Physical Review Letters*, 103(9):3–6, 2009.

[99] G. Mie. Beiträge zur Optik trüber Medien, speziell kolloidaler Metalllösungen. In *Annalen der Physik*. 1908.

[100] G. Migliorati, F. Nobile, E. von Schwerin, and R. Tempone. Approximation of Quantities of Interest in Stochastic PDEs by the Random Discrete L2 Projection on Polynomial Spaces. *SIAM J. Scientific Computing*, 35(3), 2013.

[101] G. Migliorati, F. Nobile, E. von Schwerin, and R. Tempone. Analysis of Discrete L2 Projection on Polynomial Spaces with Random Evaluations. *Foundations of Computational Mathematics*, 14(3):419–456, 2014.

[102] M. Moeferdt. *Nonlocal and Nonlinear Properties of Plasmonic Nanostructures Within the Hydrodynamic Drude Model.* PhD thesis, HU Berlin, 2017.

[103] M. Moeferdt, T. Kiel, T. Sproll, F. Intravaia, and K. Busch. Plasmonic modes in nanowire dimers: A study based on the hydrodynamic Drude model including nonlocal and nonlinear effects. *Physical Review B*, 97(7), 2018.

[104] P. Monk. *Finite element methods for Maxwell's equations.* Oxford Science Publications, 2003.

[105] A. Moreau, C. Ciracì, J. J. Mock, R. T. Hill, Q. Wang, B. J. Wiley, A. Chilkoti, and D. R. Smith. Controlled-reflectance surfaces with film-coupled colloidal nanoantennas. *Nature*, 492(7427):86–89, 2012.

[106] A. Moreau, C. Ciracì, and D. R. Smith. Impact of nonlocal response on metallodielectric multilayers and optical patch antennas. *Physical Review B - Condensed Matter and Materials Physics*, 87(4):1–12, 2013.

[107] N. A. Mortensen. Nonlocal formalism for nanoplasmonics: Phenomenological and semi-classical considerations. *Photonics and Nanostructures - Fundamentals and Applications*, 11(4):303–309, 2013.

[108] N. A. Mortensen, S. Raza, M. Wubs, T. Søndergaard, and S. I. Bozhevolnyi. Generalized nonlocal optical response in nanoplasmonics. *arXiv:1312.7190*, (May), 2013.

[109] N. A. Mortensen, S. Raza, M. Wubs, T. Søndergaard, and S. I. Bozhevolnyi. A generalized non-local optical response theory for plasmonic nanostructures. *Nature Communications*, 5, 2014.

[110] J. Niegemann. *High-Order Methods for Solving Maxwell's Equations in the Time-Domain.* PhD thesis, KIT, 2009.

[111] J. Niegemann, R. Diehl, and K. Busch. Efficient low-storage Runge-Kutta schemes with optimized stability regions. *Journal of Computational Physics*, 231(2):364–372, 2012.

[112] F. Nobile, R. Tempone, and C. G. Webster. A Sparse Grid Stochastic Collocation Method for Partial Differential Equations with Random Input Data. *SIAM J. Numerical Analysis*, 46(5):2309–2345, 2008.

[113] R. L. Olmon, B. Slovick, T. W. Johnson, D. Shelton, S. H. Oh, G. D. Boreman, and M. B. Raschke. Optical dielectric function of gold. *Physical Review B - Condensed Matter and Materials Physics*, 86(23), 2012.

[114] A. F. Oskooi, C. Kottke, and S. G. Johnson. Accurate finite-difference time-domain simulation of anisotropic media by subpixel smoothing. *Optics Letters*, 34(18):2778–2780, 2009.

[115] S. T. Park and A. H. Zewail. Photon-induced near-field electron microscopy: Mathematical formulation of the relation between the experimental observables and the optically driven charge density of nanoparticles. *Physical Review A - Atomic, Molecular, and Optical Physics*, 89(1):1–10, 2014.

[116] L. Piazza, T. Lummen, E. Quiñonez, Y. Murooka, B. Reed, B. Barwick, and F. Carbone. Simultaneous observation of the quantization and the interference pattern of a plasmonic near-field. *Nature Communications*, 6:6407, 2015.

[117] L. Piegl and W. Tiller. *The NURBS book*, volume 53. Springer, 2013.

[118] S. Piperno. Symplectic local time-stepping in non-dissipative DGTD methods applied to wave propagation problems. *ESAIM: Mathematical Modelling and Numerical Analysis*, 40(5):815–841, 2006.

[119] A. Pitelet, É. Mallet, E. Centeno, and A. Moreau. Fresnel coefficients and Fabry-Perot formula for spatially dispersive metallic layers. *Physical Review B*, 96(4):1–5, 2017.

[120] A. Pitelet, N. Schmitt, D. Loukrezis, C. Scheid, H. De Gersem, and A. Moreau. Revealing spatial dispersion with grating coupler. *Physical Review B*, submitted, 2018.

[121] J. Pomplun, S. Burger, L. Zschiedrich, and F. Schmidt. Adaptive Finite Element Method for Simulation of Optical Nano Structures. 3434(10):3419–3434, 2007.

[122] A. W. Powell, D. M. Coles, R. A. Taylor, A. A. Watt, H. E. Assender, and J. M. Smith. Plasmonic Gas Sensing Using Nanocube Patch Antennas. *Advanced Optical Materials*, 4(4):634–642, 2016.

[123] A. D. Rakic, A. B. Djurisic, J. M. Elazar, and M. L. Majewski. Optical properties of metallic films for vertical-cavity optoelectronic devices. *Applied optics*, 37(22):5271–5283, 1998.

[124] S. Raza. *Probing Plasmonic Nanostructures with electron energy-loss spectroscopy*. PhD thesis, 2014.

[125] S. Raza, S. I. Bozhevolnyi, M. Wubs, and N. A. Mortensen. Nonlocal optical response in metallic nanostructures. (4):1–19, 2014.

[126] S. Raza, S. Kadkhodazadeh, T. Christensen, M. Di Vece, M. Wubs, N. A. Mortensen, and N. Stenger. Multipole plasmons and their disappearance in few-nanometre silver nanoparticles. *Nature Communications*, 6:8788, 2015.

[127] S. Raza, N. Stenger, S. Kadkhodazadeh, S. V. Fischer, N. Kostesha, A. P. Jauho, A. Burrows, M. Wubs, and N. A. Mortensen. Blueshift of the surface plasmon resonance in silver nanoparticles studied with EELS. *Nanophotonics*, 2(2):131–138, 2013.

[128] S. Raza, G. Toscano, A. P. Jauho, M. Wubs, and N. A. Mortensen. Unusual resonances in nanoplasmonic structures due to nonlocal response. *Physical Review B - Condensed Matter and Materials Physics*, 84(12), 2011.

[129] W. H. Reed and T. R. Hill. Triangular mesh methods for the neutron transport equation. *Triangular mesh methods for the neutron transport equation*, Technical(LA-UR-73-479):1–23, 1973.

[130] L. M. Rios and N. V. Sahinidis. Derivative-free optimization: a review of algorithms and comparison of software implementations. *Journal of Global Optimization*, 56(3):1247–1293, 2013.

[131] R. Ruppin. Optical properties of a plasma sphere. *Physical Review Letters*, 31(24):1434–1437, 1973.

[132] R. Ruppin. Extinction properties of thin metallic nanowires. *Optics Communications*, 190(1-6):205–209, 2001.

[133] N. Schmitt, S. Lanteri, and A. Moreau. Experimental evidence of spatial dispersion for nano-cube gap plasmons. *in preparation*, 2018.

[134] N. Schmitt, C. Scheid, S. Lanteri, A. Moreau, and J. Viquerat. A DGTD method for the numerical modeling of the interaction of light with nanometer scale metallic structures taking into account non-local dispersion effects. *Journal of Computational Physics*, 316:396–415, 2016.

[135] N. Schmitt, C. Scheid, J. Viquerat, and S. Lanteri. Simulation of three-dimensional nanoscale light interaction with spatially dispersive metals using a high order curvilinear DGTD method. *Journal of Computational Physics*, submitted, 2018.

[136] N. Schmitt, J. Viquerat, C. Scheid, S. Lanteri, M. Moeferdt, and K. Busch. A 3D Discontinuous Galerkin Time-domain Method for Nano Plasmonics with a Nonlocal Dispersion Model. *PIERS 2017 Proceedings for IEEE Xplore*, 2017.

[137] S. M. Schnepp. Error-driven dynamical hp-meshes with the Discontinuous Galerkin Method for three-dimensional wave propagation problems. *Journal of Computational and Applied Mathematics*, 270:353–368, 2014.

[138] C.-w. Shu. An analysis of three different formulations of the discontinuous Galerkin method for diffusion equations. *Mathematical Models and Methods in Applied Science*, 13(3):395–413, 2003.

[139] R. C. Smith. *Uncertainty Quantification - Theory, Implementation, and Applications.* Computational science and engineering. SIAM, 2014.

[140] G. A. Sotiriou, F. Starsich, A. Dasargyri, M. C. Wurnig, F. Krumeich, A. Boss, J. C. Leroux, and S. E. Pratsinis. Photothermal killing of cancer cells by the controlled plasmonic coupling of silica-coated Au/Fe2O3 nanoaggregates. *Advanced Functional Materials*, 24(19):2818–2827, 2014.

[141] J. W. Stewart, G. M. Akselrod, D. R. Smith, and M. H. Mikkelsen. Toward Multispectral Imaging with Colloidal Metasurface Pixels. *Advanced Materials*, 29(6), 2017.

[142] I. Strout. *Boundary Representation Modelling Techniques.* Springer, 2006.

[143] A. Taflove and S. C. Hagness. *Computational Electrodynamics: The Finite-Difference Time-Domain Method, Third Edition.* 2005.

[144] D. Taillaert, F. Van Laere, M. Ayre, W. Bogaerts, D. Van Thourhout, P. Bienstman, and R. Baets. Grating couplers for coupling between optical fibers and nanophotonic waveguides. *Japanese Journal of Applied Physics*, 45(8 A):6071–6077, 2006.

[145] M. Tavelli, M. Dumbser, D. E. Charrier, L. Rannabauer, T. Weinzierl, and M. Bader. A simple diffuse interface approach on adaptive Cartesian grids for the linear elastic wave equations with complex topography. *arXiv:1804.09491*, 2018.

[146] J. Tiggesbäumker, L. Köller, K. H. Meiwes-Broer, and A. Liebsch. Blue shift of the Mie plasma frequency in Ag clusters and particles. *Physical Review A*, 48(3):1749–1752, 1993.

[147] V. Torczon. On the convergence of pattern search algorighms. *SIAM J. OPTIM.*, 7(1):1–25, 1997.

[148] G. Toscano, J. Straubel, A. Kwiatkowski, C. Rockstuhl, F. Evers, H. Xu, N. A. Mortensen, and M. Wubs. Resonance shifts and spill-out effects in self-consistent hydrodynamic nanoplasmonics. *Nature Communications*, 6:7132, 2015.

[149] A. Trügler, U. Hohenester, and F. J. G. de Abajo. Plasmonics simulations including nonlocal effects using a boundary element method approach. *International Journal of Modern Physics B*, 31(24), 2017.

[150] P. J. van der Houwen. Explicit Runge-Kutta formulas with increased stability boundaries. *Numerische Mathematik*, 20(2):149–164, 1972.

[151] J. T. van Wijngaarden and J. T. van Wijngaarden. Cathodoluminescence Imaging Spectroscopy on Plasmonic Structures. (August 2004):47, 2005.

[152] A. Vial, A. S. Grimault, D. Macías, D. Barchiesi, and M. Lamy De La Chapelle. Improved analytical fit of gold dispersion: Application to the modeling of extinction spectra with a finite-difference time-domain method. *Physical Review B - Condensed Matter and Materials Physics*, 71(8), 2005.

[153] J. Viquerat. *Simulation of electromagnetic waves propagation in nano-optics with a high-order discontinuous Galerkin time-domain method.* PhD thesis, 2016.

[154] J. Viquerat and S. Lanteri. Simulation of near-field plasmonic interactions with a local approximation order discontinuous Galerkin time-domain method. *Photonics and Nanostructures - Fundamentals and Applications*, 18:43–58, 2016.

[155] J. Viquerat and C. Scheid. A 3D curvilinear discontinuous Galerkin time-domain solver for nanoscale light-matter interactions. *Journal of Computational and Applied Mathematics*, 289:37–50, 2015.

[156] J. Waxenegger, A. Trügler, and U. Hohenester. Plasmonics simulations with the MNPBEM toolbox: Consideration of substrates and layer structures. *Computer Physics Communications*, 193:138–150, 2015.

[157] T. Weiland. Eine Methode zur Loesung der Maxwellschen Gleichungen fuer sechs- komponentige Felder auf diskreter Basis. *Electronics and Communication*, 31(3):116–120, 1977.

[158] T. Weiland. Time domain electromagnetic field computation with finite difference methods. *International Journal of Numerical Modelling: Electronic Networks, Devices and Fields*, 9(4):295–319, 1996.

[159] A. Wiener, H. Duan, M. Bosman, A. P. Horsfield, J. B. Pendry, J. K. Yang, S. A. Maier, and A. I. Fernández-Domínguez. Electron-energy loss study of nonlocal effects in connected plasmonic nanoprisms. *ACS Nano*, 7(7):6287–6296, 2013.

[160] C. H. Wilcox. An expansion theorem for electromagnetic fields. *Communications on Pure and Applied Mathematics*, 9(2):115–134, 1956.

[161] J. H. Williamson. Low-storage Runge-Kutta schemes. *Journal of Computational Physics*, 35(1):48–56, 1980.

[162] M. Wubs and N. A. Mortensen. Nonlocal Response in Plasmonic Nanostructures. In *Quantum Plasmonics*, volume 37, pages 761–767. 2012.

[163] D. Xiu. *Numerical Methods for Stochastic Computations: A Spectral Method Approach*. Princeton University Press, Princeton, NJ, USA, 2010.

[164] D. Xiu and J. S. Hesthaven. High-Order Collocation Methods for Differential Equations with Random Inputs. *SIAM J. Scientific Computing*, 27(3):1118–1139, 2005.

[165] H. X. Xu, E. J. Bjerneld, M. Käll, and L. Börjesson. Spectroscopy of single hemoglobin molecules by surface enhanced Raman scattering. *Phys. Rev. Lett.*, 83:4357–4360, 1999.

[166] K. S. Yee. Numerical Solution of Initial Boundary Value Problems Involving Maxwell's Equations in Isotropic Media. *IEEE Transactions on Antennas and Propagation*, 14(3):302–307, 1966.

[167] J. X. Zhao. Numerical and Analytical Formulizations of the Extended Mie Theory for Solving the Sphere Scattering Problem. *Journal of Electromagnetic Waves and Applications*, 20(7):967–983, 2006.

Scientific contributions

Journal publications

- *Experimental evidence of spatial dispersion for nano cube gap plasmons*; N. Schmitt, A. Moreau, S. Lanteri, in preparation
- *Simulating 3D periodic structures at oblique incidences with discontinuous Galerkin time-domain methods: theoretical and practical considerations*; J. Viquerat, N. Schmitt, C. Scheid, submitted
- *Influence of spatial dispersion on surface plasmons and grating couplers*; A. Pitelet, N. Schmitt, D. Loukrezis, E. Centeno, C. Scheid, H. De Gersem, C. Ciraci, A. Moreau, submitted
- *Simulation of three-dimensional nanoscale light interaction with spatially dispersive metals using a high order curvilinear DGTD method*; N. Schmitt, C. Scheid, J. Viquerat and S. Lanteri, Journal of Computational Physics, 373: 210-229, 2018
- *A 3D Discontinuous Galerkin Time-domain Method for Nano Plasmonics with a Nonlocal Dispersion Model*; N. Schmitt, J. Viquerat, C. Scheid, S. Lanteri, M. Moeferdt, and K. Busch., PIERS 2017 Proceedings IEEE-Explore, 2792-2799, 2017
- *A DGTD method for the numerical modeling of the interaction of light with nanometer scale metallic structures taking into account non-local dispersion effects*; N. Schmitt, C. Scheid, S. Lanteri, A. Moreau and J. Viquerat, Journal of Computational Physics, 316: 396-415, 2016

Oral presentations

- TEMF Numerik Seminar 2018, Darmstadt, Germany
- KWT 2017, Riezlern, Austria
- Plasmonica 2017, Lecce, Italy
- PIERS 2017, Saint Petersburg, Russia
- INRIA team evaluation 2017, Paris, France
- Colloque LJAD 2016, Barcelonette, France
- META 2016, Malaga, Spain
- KWT 2016, Riezlern, Austria

Posters

- EMF 2018, Darmstadt, Germany
- GdR Ondes 2018, Paris, France
- NANOP 2017, Barcelona, Spain
- PIQUE 2017, Nice, France
- School of Plasmonics 2016, Cortona, Italy
- NanoPhoton 2016, Sophia-Antipolis, France
- TEMF poster session 2015, Darmstadt, Germany